



Forschungszentrum Karlsruhe
in der Helmholtz-Gemeinschaft

Wissenschaftliche Berichte
FZKA 7187

**Contributions to the
29th International Cosmic Ray Conference,
Pune, India, 2005**
by **Forschungszentrum Karlsruhe**
Institut für Kernphysik
and **Universität Karlsruhe**
Institut für Experimentelle Kernphysik

J. Blümer, R. Engel, A. Haungs (Editors)
Institut für Kernphysik

Dezember 2005

Forschungszentrum Karlsruhe

in der Helmholtz-Gemeinschaft

Wissenschaftliche Berichte

FZKA 7187

Contributions to the 29th International Cosmic Ray
Conference, Pune, India, 2005

by

Forschungszentrum Karlsruhe

Institut für Kernphysik

and

Universität Karlsruhe

Institut für Experimentelle Kernphysik

Johannes Blümer, Ralph Engel, Andreas Haungs (Editors)

Institut für Kernphysik

Forschungszentrum Karlsruhe GmbH, Karlsruhe

2005

Als Manuskript gedruckt
Für diesen Bericht behalten wir uns alle Rechte vor

Forschungszentrum Karlsruhe GmbH
Postfach 3640, 76021 Karlsruhe

Mitglied der Hermann von Helmholtz-Gemeinschaft
Deutscher Forschungszentren (HGF)

ISSN 0947-8620

urn:nbn:de:0005-071870

ABSTRACT

This report is a compilation of contributions of institutes of the Forschungszentrum Karlsruhe and University Karlsruhe to the International Cosmic Ray Conference (ICRC) held in Pune, India this year. These contributions have been made in close collaboration with many national and international universities and institutes. The compilation provides a review of the corresponding scientific activities of the issuing institutes. It also gives an overview of the status and scientific results of the air shower experiments **KASCADE-Grande**, the **Pierre Auger Project**, and the new radio antenna array **LOPES**, which is complemented by a number of articles on related physics subjects such as air shower simulation and direct cosmic ray measurements.

The scientific results presented in these articles have been obtained within and with the support of the Centre of Excellence for Particle and Astroparticle Physics (**CETA**, <http://www.ceta.uni-karlsruhe.de/>) and the Virtual Institute for High-Energy Radiation from the Cosmos (**VIHKOS**, <http://www-ik.fzk.de/~vihkos/>). VIHKOS is an association of 2 Helmholtz research centres, 3 Max Planck institutes and 13 universities with the aim of supporting the interaction and integration of research centres and universities for the investigation of astrophysical questions related to cosmic ray physics.

KASCADE-Grande (**KA**rlsruhe **S**hower **C**ore and **A**rray **DE**tector with the extension **Grande**) is a multi-detector set-up on the site of the Forschungszentrum Karlsruhe. The different detector systems allow the reconstruction of a large set of observables for each measured air shower providing comprehensive information for the analyses. The main aim of the experiment is the determination of the primary energy spectrum and mass composition of cosmic rays in the knee region, i.e. at primary energies of 100 TeV - 1 EeV. The results of the initial experiment KASCADE establish the fact that the knee at a few PeV is dominated by light primaries, whereas the flux of heavy primaries shows no knee in the energy region up to 50 PeV. The extension of KASCADE to **KASCADE-Grande** for measurements of cosmic rays in the energy region above 50 PeV up to 1 EeV lead to first results after one year of data taking, which were presented at the conference.

The **LOPES** project addresses investigation of radio emission from extensive air showers with the aim to establish this detection technique as a suitable new method for measuring high-energy cosmic rays. LOPES consists of an array of 30 dipole antennas which measure in the frequency range of 40 to 80 MHz in coincidence with KASCADE-Grande. First, very promising experimental results as well as theoretical studies of the possible emission processes in the radio frequency range were reported at the ICRC 2005.

The southern part of the **Pierre Auger Observatory** is presently under construction in the Province Mendoza, Argentina. It will consist of a 3000 km² array of 1600 water Cherenkov detectors and 24 fluorescence telescopes. The Auger experiment is designed to measure cosmic rays of ultra-high energy, e.g. above 10 EeV with the aim of investigating the energy spectrum, type and origin of these elusive particles. The Karlsruhe research groups are mainly involved in the construction of the fluorescence detectors, including the DAQ electronics and in data analysis. Reports of the first results underline the unique capabilities of the Auger observatory. Contributions of the Karlsruhe groups discuss the monitoring

atmospheric conditions as well as various data analysis aspects ranging from the search for photons at ultra-high energy over fluorescence signal calculations to various approximations for the Cherenkov light emission of air showers.

The contributions of the Karlsruhe groups to the ICRC 2005 also include reports on recent additions, improvements of the **CORSIKA** (**CO**smic **R**ay **S**imulation for **K**ascade and **A**uger) simulation package and model tests by comparing their predictions with accelerator data. Other articles discuss the use of a new simulation technique, called hybrid simulations, in which Monte Carlo methods are combined with the numerical treatment of cascade equations for the simulation of showers.

In addition to the collaboration works of the KASCADE-Grande and Auger groups the many individual, cosmic ray related contributions are also compiled in this volume. They cover a wide range, including results of experiments concerning cosmic rays of lower energies (**TRACER**), dark matter search by analysing low energy gamma-rays by satellite measurements, and performance studies of detectors for the space experiment **AMS**.

**Beiträge zur 29th International Cosmic Ray Conference (ICRC), Pune, India, 2005 des
Forschungszentrums Karlsruhe, Institut für Kernphysik und der
Universität Karlsruhe, Institut für experimentelle Kernphysik**

ZUSAMMENFASSUNG

Der vorliegende Bericht fasst Beiträge zur zweijährlich stattfindenden internationalen Konferenz zur kosmischen Strahlung (ICRC 2005) zusammen, die von den herausgebenden Instituten des Forschungszentrums und der Universität Karlsruhe in enger Zusammenarbeit mit weiteren nationalen und internationalen Universitäten und Instituten entstanden sind. Die Beiträge der beteiligten Institute konzentrieren sich dabei auf den wissenschaftlichen Stand der Luftschauer-Experimente **KASCADE-Grande** mit **LOPES** und des **Pierre Auger-Projektes**, ergänzt durch eine Reihe von weiteren Beiträgen zu relevanten Themenbereichen, auch in Energiebereichen der kosmischen Strahlung, die mit direkten Messungen zugänglich sind.

Alle hier vorgestellten Aktivitäten der beteiligten Institute sind sowohl in das Exzellenzzentrum **CETA** (Centrum für Elementarteilchenphysik und Astroteilchenphysik <http://www.ceta.uni-karlsruhe.de/>) der Universität Karlsruhe, als auch in **VIHKOS** (Virtuelles Institut für Hochenergiestrahlungen aus dem Kosmos <http://www-ik.fzk.de/~vihkos/>) eingebettet. VIHKOS ist eine gemeinsame Einrichtung von 2 Helmholtz-Zentren, 3 Max-Planck-Instituten und 13 deutschen Universitäten zur gemeinsamen Erforschung bedeutender astrophysikalischer Fragen mit Hilfe der Messung hochenergetischer kosmischer Strahlung.

KASCADE-Grande (**K**ARlsruhe **S**hower **C**ore and **A**rray **D**Etector mit der Erweiterung **Grande**) ist ein Multi-Detektor-Aufbau auf dem Gelände des Forschungszentrums Karlsruhe. Die unterschiedlichen Detektorsysteme erlauben die Rekonstruktion einer großen Anzahl von Observablen pro Ereignis. Das Hauptziel des Experimentes ist die Bestimmung des primären Energiespektrums und der Elementzusammensetzung der kosmischen Strahlung im Energiebereich des ‚Knies‘ (100 TeV – 1 EeV). Die Ergebnisse des ursprünglichen KASCADE-Experimentes zeigen nun, dass das Knie durch die leichte primäre Komponente dominiert wird und das Spektrum der schweren Teilchen kein Knie im Energiebereich bis 50 PeV aufweist. Nach einem Jahr der Datennahme konnte bei der Konferenz über erste Ergebnisse von **KASCADE-Grande**, der Erweiterung des KASCADE Experimentes zur Messung der kosmischen Strahlung im Energiebereich von 50 PeV bis 1 EeV, berichtet werden.

Das Ziel des **LOPES** Projektes ist die Untersuchung der Emission von Radiostrahlung während der Luftschauerentwicklung in der Atmosphäre, sowie die Etablierung dieser Nachweisteknik als neue Messmethode kosmischer Strahlung höchster Energien. LOPES besteht aus einem Feld von 30 Dipolantennen, die Radiostrahlung in einem Frequenzbereich von 40 bis 80 MHz in Koinzidenz mit KASCADE-Grande messen. Auf der ICRC 2005 wurden erste spektakuläre Resultate von LOPES, sowie theoretische Studien zum Mechanismus der Radioemission in Luftschauer vorgestellt.

Der Aufbau des Südteiles des **Pierre Auger-Observatoriums** wird momentan in Argentinien fertig gestellt. Es besteht aus einem 3000 km² großem Array aus 1600 Wasser-Cherenkov-Tanks und 24 Fluoreszenzdetektoren. Das Auger-Experiment wird das Energiespektrum, die Herkunft und die Art der höchstenergetischsten kosmischen Teilchen über 10 EeV messen. Die Karlsruher Forschungsgruppen leisten einen signifikanten Anteil am Bau und Betrieb der Fluoreszenzteleskope, sowie an der Analyse der ersten Daten. Die Beiträge in diesem Bericht widmen sich dem Monitoring der Atmosphäre während der Fluoreszenzmessungen, sowie ersten Daten-Analysen, dem Anteil primärer Photonen in der kosmischen Strahlung, und Untersuchungen zur Erzeugung des Fluoreszenz- und Cherenkov-Lichtes in der Luftschauerentwicklung.

Über Erweiterungen, Verbesserungen und mithilfe von Beschleunigerdaten durchgeführte Tests des Luftschauersimulationsprogrammes **CORSIKA** (**CO**smic **R**ay **S**imulation for **K**ASCADE and **A**uger) wird berichtet. Weitere Artikel diskutieren die Benutzung einer neuen Simulationstechnik, der so genannten Hybrid-Technik, die durch Verbindung von analytischen und Monte Carlo-Methoden eine wesentlich schnellere Simulation der Luftschauerentwicklung ermöglicht, was vor allem bei hohen Primärenergien an Bedeutung gewinnt.

Zusätzlich zu den kollaborativen Arbeiten an den KASCADE-Grande und Auger Experimenten werden weitere relevante Themen zur kosmischen Strahlung diskutiert. Dies beinhaltet sowohl Messungen und Analysen von Experimenten zur kosmischen Strahlung niederer Energien (**TRACER**), die Suche nach dunkler Materie durch Analyse von mit Satelliten gemessener niederenergetischer Gammastrahlung, als auch Studien zu Detektoreigenschaften für ihre Anwendung im Rahmen des Raumfahrtexperiments **AMS**.

CONTENTS

KASCADE-Grande

Composition and Energy Spectra of Elemental Groups around the Knee: Results from KASCADE H. Ulrich et al., KASCADE Collaboration	1
Operation, Calibration and Accuracy of the Grande array of the KASCADE-Grande experiment A. Chiavassa et al., KASCADE-Grande Collaboration	5
Shower Size Reconstruction at KASCADE-Grande R. Glasstetter et al., KASCADE-Grande Collaboration	9
Muon Size Spectrum measured by KASCADE-Grande J. van Buren et al., KASCADE-Grande Collaboration	13
Studies of different LDFs for primary energy estimation and mass discrimination of cosmic rays by the EAS lateral charged particle distribution as observed by KASCADE-Grande H. Rebel, O. Sima et al., KASCADE-Grande Collaboration	17
Event - by - event studies of the discriminative features of the LDF of charged EAS particles: observable correlations and non –parametric analyses of multivariate distributions I.M. Brancus et al., KASCADE-Grande Collaboration	21
A self-triggered, high-resolution data acquisition system for the KASCADE-Grande experiment M. Brüggemann et al., KASCADE-Grande Collaboration	25
Hadrons in a calorimeter measured in air showers and at an accelerator S. Plewnia et al., KASCADE-Grande Collaboration	29
Investigation of Hadronic Interaction Models with the KASCADE-Grande Hadron Calorimeter J. Milke et al., KASCADE-Grande Collaboration	33
The influence of properties of individual hadronic interactions on the development of extensive air showers J.R. Hörandel et al., KASCADE-Grande Collaboration	37
Muon Density Measurements with KASCADE-Grande A. Haungs et al., KASCADE-Grande Collaboration	41
Analysis of Muon Production Heights using KASCADE parameters R. Obenland et al., KASCADE-Grande Collaboration	45
Muon Tracking In KASCADE-Grande: CORSIKA Simulation Study J. Zabierowski et al., KASCADE-Grande Collaboration	49
Approach to elemental energy spectra of cosmic rays by correlation curves method I. Lebedev et al., KASCADE Collaboration	53

LOPES

LOPES30: A digital antenna array for measuring high-energy cosmic ray air showers S. Nehls et al., LOPES Collaboration	57
Detection of radio pulses from extensive air showers A. Horneffer et al., LOPES Collaboration	61
First determination of the reconstruction resolution of an EAS radio detector A.F. Badea et al., LOPES Collaboration	65
Remote event analyses of LOPES-10 A.F. Badea et al., LOPES Collaboration	69
Radio emission of highly inclined cosmic ray air showers measured with LOPES J. Petrovic et al., LOPES Collaboration	73
Electric field influence on the radio emission of air showers S. Buitink et al., LOPES Collaboration	77
A Cosmic Ray Trigger for LOFAR S. Lafebre, A. Nigl et al., LOPES Collaboration	81
Fluctuations in the EAS radio signal derived with improved Monte Carlo simulations based on CORSIKA T. Huege et al., LOPES Collaboration	85
Simulations and parametrisation of radio emission from cosmic ray air showers T. Huege, H. Falcke	89
Simulation Cherenkov and Synchrotron Radio Emission in EAS R. Engel, N. Kalmykov, A.A. Konstantinov	93

Air shower simulation and related

Hadronic Interactions in QGSJET-II: Physics and Results S. Ostapchenko, D. Heck	97
Extensive Air Shower Simulation Program CONEX: Matching Monte Carlo and Numerical Methods M. Alekseeva, T. Bergmann, V. Chernatkin, R. Engel, D. Heck, N. Kalmykov, S. Ostapchenko, T. Pierog, K. Werner	101
Dependence of the longitudinal shower profile on the characteristics of hadronic multiparticle production T. Pierog, M. Alekseeva, T. Bergmann, V. Chernatkin, R. Engel, D. Heck, N.N. Kalmykov, S. Ostapchenko, M. Unger, and K. Werner	105
Hadronic multiparticle production in extensive air showers and accelerator experiments C. Meurer, J. Blümer, R. Engel, A. Haungs, M. Roth	109
Monte Carlo simulations and semianalytical parameterisations of the atmospheric muon flux controlled by muon charge ratio measurements performed with WILLI detector I.M. Brancus, B. Mitrica, A. Bercuci, G. Toma, J. Wentz, H. Rebel, M. Duma	113

The Pierre-Auger-Experiment

Upper limit on the primary photon fraction from the Pierre Auger Observatory M. Risse for the Pierre Auger Collaboration	117
Atmospheric Profiles at the Southern Pierre Auger Observatory and their Relevance to Air Shower Measurement J. Blümer, R. Engel, D. Gora, P. Homola, B. Keilhauer, H. Klages, J. Pekala, M. Risse, M. Unger, B. Wilczynska, H. Wilczynski for the Pierre Auger Collaboration	121
Validation of the Real and Simulated Data of the Pierre Auger Fluorescence Telescopes A. Ewers, H. Geenen, K.-H. Kampert, L. Perrone, S. Robbins, V. Scherini, M Unger for the Pierre Auger Collaboration	125
Impact of a new Cherenkov light parameterisation on the reconstruction of shower profiles from Auger hybrid data F. Nerling, J. Blümer, R. Engel, M. Unger for the Pierre Auger Collaboration	129
Lateral width of shower image in the Auger fluorescence detector H. Barbosa, V. de Souza, C. Dobrigkeit, R. Engel, D. G´ora, D. Heck, P. Homola, H. Klages, G. Medina-Tanco, J.A. Ortiz, J. Pekala, M. Risse, B. Wilczynska, and H. Wilczynski for the Pierre Auger Collaboration	133
Universality of the lateral distribution of energy deposit in extensive air showers D. Gora, R. Engel, D. Heck, P. Homola, H. Klages, J. Pekala, M. Risse, B. Wilczynska, and H. Wilczynski	137
Atmospheric multiple scattering of fluorescence and Cherenkov light from air shower J. Pekala, D. Gora, P. Homola, M. Risse, B. Wilczynska, H. Wilczynski	141
Parameterisation of Cherenkov light production in high-energy showers F. Nerling, J. Blümer, R. Engel, M. Risse	145
Variability of atmospheric depth profiles B. Wilczynska, D. Gora, P. Homola , B. Keilhauer, H. Klages, J. Pekala, M. Risse, H. Wilczynski	149
Nitrogen fluorescence yield in dependence on atmospheric conditions B. Keilhauer, R. Engel, H. Klages, T. Waldenmaier	153
Measurement of the Air Fluorescence Yield with the AirLight Experiment T. Waldenmaier, J. Blümer, B. Keilhauer, H. Klages, S. Klepser	157
Top-Down Reconstruction of Ultrahigh Energy Air Showers F. Schüssler, J. Blümer, R. Engel, M. Unger	161
Measurement of the lateral distribution function of UHECR air showers with the Auger Observatory D. Barnhill, P. Bauleo, M.T. Dova, J. Harton, R. Knapik, J. Knapp, J. Lee, M. Mancenido, A.G. Mariazzi, I.C. Maris, D. Newton, M. Roth, T. Schmidt, A.A. Watson for the Pierre Auger Collaboration	165
The Offline Software Framework of the Pierre Auger Observatory S. Argiro, S.L.C. Barroso, S. Dagoret-Campagne, J. Gonzalez, L. Nellen, T. Paul, T. Porter, L. Prado Jr., M. Roth, R. Ulrich and D. Veberic for the Pierre Auger Collaboration	169

Derivation of upper limit on the photon fraction using the highest-energy AGASA cosmic rays M. Risse, P. Homola, R. Engel, D. Gora, D. Heck, J. Pekala, B. Wilczynska, and H. Wilczynski	173
Contributions of the Pierre Auger Collaboration (abstracts only)	177
Further articles	
An analysis of super-high energy cosmic-ray propagation in the Galaxy J.R. Hörandel, N.N. Kalmykov, A.V. Timokhin	189
Energy Spectra of Heavy Cosmic Ray Nuclei from 0.5 GeV/amu to 10,000 GeV/amu P.J. Boyle, M. Ave, F. Gahbauer, C. Höppner, J. Hörandel, M. Ichimura, D. Müller, A. Romero-Wolf, S. Wakely	193
The Response of the TRACER Detector: Design, Calibrations and Measurements C. Höppner, M. Ave, P. Boyle, F. Gahbauer, J. Hörandel, M. Ichimura, D. Müller, A. Romero-Wolf, S. Wakely	197
Measurements with TRACER: Discussion of Results and Future Prospects D. Müller, M. Ave, P.J. Boyle, F. Gahbauer, C. Höppner, J. Hörandel, M. Ichimura, A. Romero-Wolf, S. Wakely	201
Antarctic Balloon Flight and Data Analysis of TRACER A. Romero-Wolf, M. Ave, P. Boyle, F. Gahbauer, C. Höppner, J. Hörandel, M. Ichimura, D. Müller, S. Wakely	205
Solar modulation of cosmic rays in the energy range from 10 to 20 GeV I. Braun, J. Engler, J.R. Hörandel, J. Milke	209
Egret excess of diffuse galactic gamma rays as tracer of Dark Matter C. Sander	213
The performance of the AMS-02 Transition Radiation Detector M. Schmanau on behalf of the AMS-02 TRD collaboration	221
Collaborations lists	225

Composition and energy spectra of elemental groups around the knee: Results from KASCADE

H. Ulrich^b, T. Antoni^a, W.D. Apel^b, F. Badea^{b,1}, K. Bekk^b, A. Bercuci^c, J. Blümer^{b,a},
H. Bozdog^b, I.M. Brancus^c, A. Chilingarian^d, K. Daumiller^b, P. Doll^b, R. Engel^b, J. Engler^b,
F. Feßler^b, H.J. Gils^b, R. Glasstetter^{a,2}, A. Haungs^b, D. Heck^b, J.R. Hörandel^a,
K.-H. Kampert^{a,b,2}, H.O. Klages^b, G. Maier^{b,3}, H.J. Mathes^b, H.J. Mayer^b, J. Milke^b,
M. Müller^b, R. Obenland^b, J. Oehlschläger^b, S. Ostapchenko^{b,4}, M. Petcu^c, H. Rebel^b,
A. Risse^e, M. Risse^b, M. Roth^a, G. Schatz^b, H. Schieler^b, J. Scholz^b, T. Thouw, J. van Buren^b
A. Vardanyan^d, A. Weindl^b, J. Wochele^b, J. Zabierowski^e, S. Zagromski^b

(a) Institut für Experimentelle Kernphysik, Universität Karlsruhe, 76021 Karlsruhe, Germany

(b) Institut für Kernphysik, Forschungszentrum Karlsruhe, 76021 Karlsruhe, Germany

(c) National Institute of Physics and Nuclear Engineering, 7690 Bucharest, Romania

(d) Cosmic Ray Division, Yerevan Physics Institute, Yerevan 36, Armenia

(e) Soltan Institute for Nuclear Studies, 90950 Lodz, Poland

(1) on leave of absence from Nat. Inst. of Phys. and Nucl. Engineering, Bucharest, Romania

(2) now at Fachbereich Physik, Universität Wuppertal, 42097 Wuppertal, Germany

(3) now at University Leeds, LS2 9JT Leeds, United Kingdom

(4) on leave of absence from Moscow State University, 119899 Moscow, Russia

Presenter: H. Ulrich for KASCADE collaboration (holger.ulrich@ik.fzk.de), ger-ulrich-H-abs1-he12-oral

A composition analysis of KASCADE air shower data is performed by means of unfolding the two-dimensional electron-muon number spectrum in energy spectra of 5 elemental groups. The results of the analysis are based on a vast number of Monte Carlo simulations with the two different high-energy hadronic interaction models QGSJet and SIBYLL. For both models the light elemental groups show a distinctive knee feature, causing the knee in the all particle spectrum at around 4 PeV, whereas heavy primaries do not. The relative abundancies of the elemental groups show a large model dependence. Moreover, the description of the data by the simulations shows to be imperfect and sensitive to the characteristics of the interaction model used.

1. Introduction

The origin of the knee in the cosmic ray energy spectrum (a steepening of the spectrum at ≈ 4 PeV) is still not convincingly explained. To discriminate between different proposals for its origin it is necessary to obtain information about the energy spectra of individual elements or at least elemental groups of primary cosmic rays.

The KASCADE experiment [1], especially designed for air shower measurements in the knee region, aims at this question. A major component is the field array whose main reconstructed observables are the electron number N_e and the truncated muon number N_μ^{tr} which are used in this analysis. The latter one is the number of muons with distances to the shower core between 40 m and 200 m. Information about the reconstruction and the measurement procedures are given in Ref. [1]. The accessible energy range covers the knee, the effective measurement time added up to 900 days.

The presented analysis makes use of unfolding algorithms, which are applied to the measured two-dimensional frequency spectrum of $\lg N_e$ and $\lg N_\mu^{tr}$. Since such an analysis depends crucially on air shower simulations, the analysis is performed twice using different hadronic interaction models for their generation. This approach also gives a lower limit of the uncertainties due to the modelling of the hadronic interactions.

2. Outline of the analysis

Starting point of the analysis is the correlated frequency distribution of $\lg N_e$ and $\lg N_\mu^{tr}$ displayed in Fig. 1 (left panel). The lower boundaries in $\lg N_e$ and $\lg N_\mu^{tr}$ were chosen in a way to minimize influences from efficiencies. Considered zenith angles range from 0° to 18° . The content N_j of each cell can be written as

$$N_j = C \sum_{A=1}^{N_A} \int_{-\infty}^{+\infty} \frac{dJ_A}{d \lg E} p_A(\lg N_{e,j}, \lg N_{\mu,j}^{tr} | \lg E) d \lg E. \quad (1)$$

C is a normalizing constant (time, aperture), the sum is carried out over all primary types with mass A , and p_A describes the probability for an EAS with primary energy $\lg E$ to be measured and reconstructed with shower sizes $\lg N_e$ and $\lg N_\mu^{tr}$. This probability consists of the shower fluctuations s_A , efficiencies ϵ_A , and reconstruction properties r_A . For sake of simplicity the integration over cell area and solid angle is omitted in Eqn. 1 but of course accounted for in the analysis. The data histogram of Fig. 1 (left) is therefore interpreted as a system of coupled integral equations. For the analysis the primary particles H, He, C, Si, and Fe were chosen as representatives for five mass groups. The probability distributions s_A , ϵ_A , and r_A were determined by Monte Carlo simulations using CORSIKA[2] 6.018 with the low energy interaction model GHEISHA[3] (corrected version of 2002) and the two high energy interaction models QGSJet[4] (2001 version) and SIBYLL[5] (version 2.1). In order to solve the equation system unfolding methods were applied. Three different algorithms were used to cross-check systematic uncertainties. Details of the analysis and the used unfolding methods can be found in Ref. [6].

3. Results and conclusions

In the upper part of Fig. 2 the results for the spectra of light elements (left) and heavy elements (right) of the QGSJet based analysis are shown, in the lower part the corresponding spectra using SIBYLL simulations. The resulting all particle spectra for both cases are shown in the right panel of Fig. 1. The shaded bands in the figures represent an estimate of the methodical uncertainties.

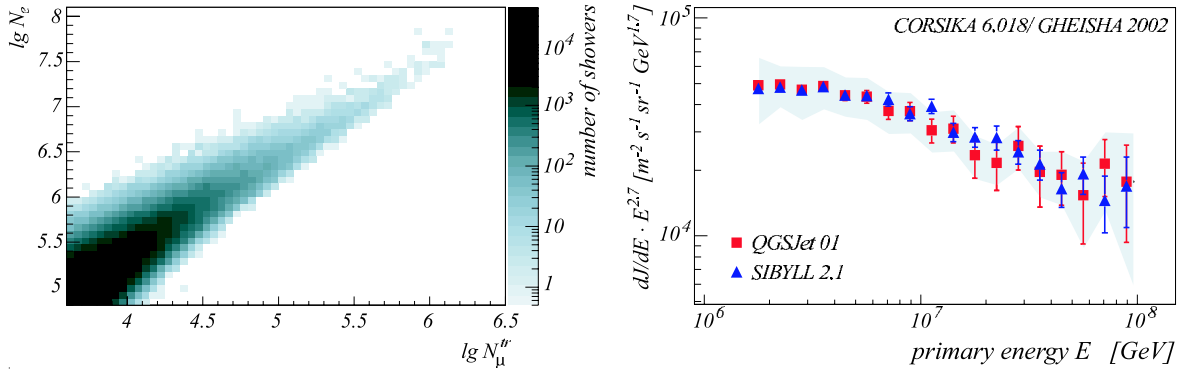


Figure 1. Left: Two-dimensional shower size spectrum as measured by KASCADE. The range in $\lg N_e$ and $\lg N_\mu^{tr}$ is chosen to avoid influences of inefficiencies. Right: Result for the all particle energy spectrum using QGSJet01 and SIBYLL 2.1 simulations. The shaded band represents the estimated systematic uncertainties for the QGSJet solution, being of the same order as for the SIBYLL solution.

The all particle energy spectrum shows a knee at ≈ 4 PeV for both results and inside the statistical uncertainties the results coincide. The decrease of light elements across the knee, i.e. the occurrence of knee-like features in the light element spectra is also revealed independent of the used simulation code. In contrast the spectra of Si and Fe differ significantly and look quite unexpected. This can be understood by judging the ability of the simulations to describe the data. Fig. 3 (upper row) shows the distribution of residuals of a χ^2 -comparison between data and forward folded (according to Eqn. 1) solutions. For both interaction models the overall value of χ^2 p.d.f. is about 2.4 and strong systematic effects are found in the distribution of the residuals. These systematics reflect properties of the used interaction models and are not caused by improper understanding of reconstruction or detector simulation.

To demonstrate the kind of these deviations a comparison between the measured and the $\lg N_e$ -distribution resulting from forward folding for two fixed $\lg N_\mu^{tr}$ bins are displayed in the lower row of Fig. 3. It turns out that both interaction models fail to reproduce the overall correlation between $\lg N_e$ and $\lg N_\mu^{tr}$ as observed in the data. In the case of QGSJet simulations the predictions are incompatible with the data in the low energy regime (simulations look too heavy), for SIBYLL incompatibility occurs at higher energies (simulations look too light). Summarizing the results of this analysis the knee in the all particle spectrum is due to kinks in the light element spectra resulting in a heavier composition above the knee. A more specific statement seems inappropriate since neither QGSJet nor SIBYLL describe the measured data consistently over the whole measurement range. The analysis is ongoing, using the new version of QGSJet and other high and also low energy interaction models, e.g. replacing GHEISHA by FLUKA [7] in the simulations.

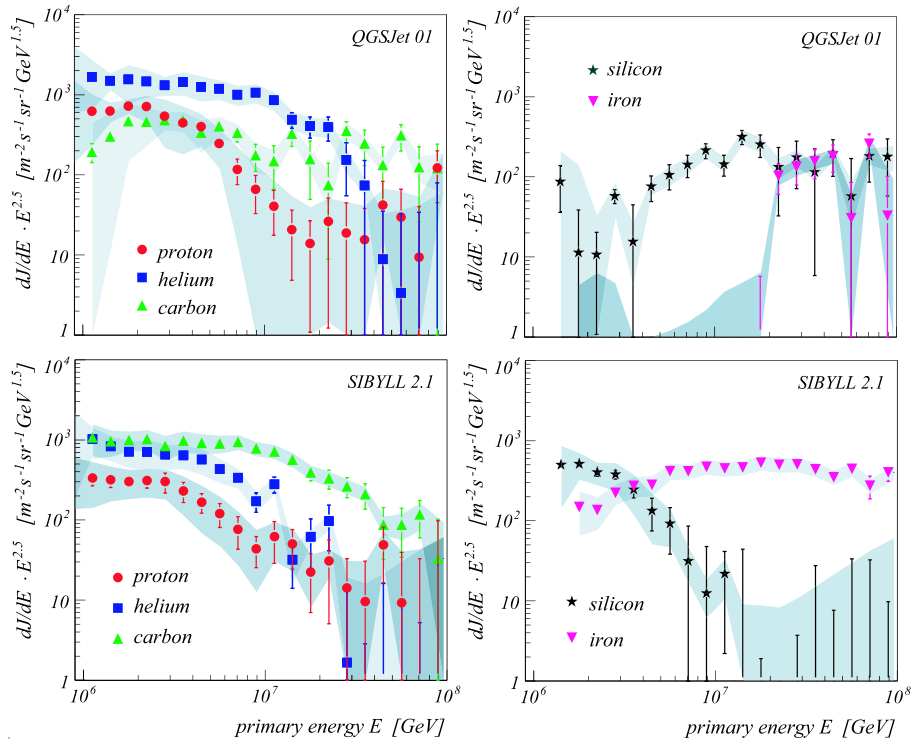


Figure 2. Results for the energy spectra, H, He, C in left column, Si and Fe in right column. Upper row: QGSJet01 hypothesis; lower row: SIBYLL 2.1 hypothesis. The shaded bands indicate methodical uncertainties.

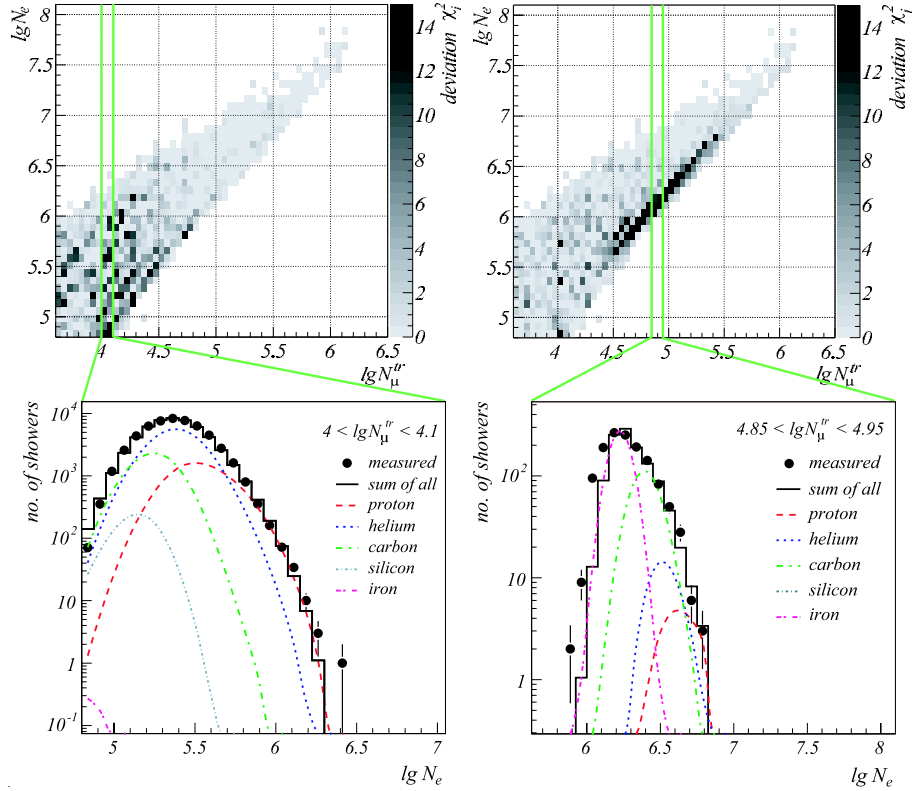


Figure 3. Upper part: Distribution of deviations between data and forward folded solution for QGSJet (left) and SIBYLL (right). Lower part: Example of insufficient description of measured data for fixed $\lg N_\mu^{tr}$ bins; left panel for QGSJet, right panel for SIBYLL.

References

- [1] T. Antoni et al. (KASCADE collaboration), *Nucl. Instr. and Meth.* **A 513**, 490 (2003).
- [2] D. Heck et al., Forschungszentrum Karlsruhe, Report FZKA 6019 (1998).
- [3] H. Fesefeldt, Report PITHA-85/02, RWTH Aachen (1985).
- [4] N.N. Kalmykov and S.S. Ostapchenko, *Phys. Atom. Nucl.* **56**, 346 (1993).
- [5] R. Engel et al., *Proc. 26th Int. Cosmic Ray Conf.* Salt Lake City (USA) **1**, 415 (1999).
- [6] T. Antoni et al. (KASCADE collaboration), *Astropart. Phys.*, in press (2005); astro-ph/0505413
- [7] A. Fassò et al., *FLUKA: Status and Prospective of Hadronic Applications*, Proc. Monte Carlo 2000 Conf., Lisbon, Oct. 23-26, 2000, A. Kling et al. (Eds.), Springer (Berlin) 955 (2001); www.fluka.org

Operation, Calibration and Accuracy of the Grande array of the KASCADE-Grande experiment

A. Chiavassa^d, T. Antoni^a, W.D. Apel^b, F. Badea^{b,1}, K. Bekk^b, A. Bercuci^c, M. Bertaina^d, J. Blümer^{b,a}, H. Bozdog^b, I.M. Brancus^c, M. Brüggemann^e, P. Buchholz^e, K. Daumiller^b, F. Di Pierro^d, P. Doll^b, R. Engel^b, J. Engler^b, F. Feßler^b, P.L. Ghia^f, H.J. Gils^b, R. Glasstetter^g, C. Grupen^e, A. Haungs^b, D. Heck^b, J.R. Hörandel^a, K.-H. Kampert^g, H.O. Klages^b, Y. Kolotaev^e, G. Maier^{b,2}, H.J. Mathes^b, H.J. Mayer^b, J. Milke^b, B. Mitrica^c, C. Morello^f, M. Müller^b, G. Navarra^d, R. Obenland^b, J. Oehlschläger^b, S. Ostapchenko^{b,3}, S. Over^e, M. Petcu^c, T. Pierog^b, S. Plewnia^b, H. Rebel^b, A. Risse^h, M. Roth^a, H. Schieler^b, J. Scholz^b, O. Sima^c, M. Stümpert^a, G. Toma^c, G.C. Trinchero^f, H. Ulrich^b, S. Valchierotti^d, J. van Buren^b, W. Walkowiak^e, A. Weindl^b, J. Wochele^b, J. Zabierowski^h, S. Zagromski^b, D. Zimmermann^e

(a) Institut für Experimentelle Kernphysik, Universität Karlsruhe, 76021 Karlsruhe, Germany

(b) Institut für Kernphysik, Forschungszentrum Karlsruhe, 76021 Karlsruhe, Germany

(c) National Institute of Physics and Nuclear Engineering, 7690 Bucharest, Romania

(d) Dipartimento di Fisica Generale dell'Università, 10125 Torino, Italy

(e) Fachbereich Physik, Universität Siegen, 57068 Siegen, Germany

(f) Istituto di Fisica dello Spazio Interplanetario, INAF, 10133 Torino, Italy

(g) Fachbereich Physik, Universität Wuppertal, 42097 Wuppertal, Germany

(h) Soltan Institute for Nuclear Studies, 90950 Lodz, Poland

¹ on leave of absence from Nat. Inst. of Phys. and Nucl. Engineering, Bucharest, Romania

² now at University Leeds, LS2 9JT Leeds, United Kingdom

³ on leave of absence from Moscow State University, 119899 Moscow, Russia

Presenter: A. Chiavassa (achiavas@to.infn.it), ita-chiavassa-A-abs1-he13-oral

The KASCADE-Grande experiment is in continuous and stable data taking since the beginning of 2004. The Grande array, made of 37 plastic scintillators detectors (10 m² each) placed at a distance of 140 m from each other, has been set up to cover a surface (~ 0.5 km²) big enough to study the primary cosmic rays in the 10¹⁶-10¹⁸ eV energy range. We present the status of the Grande array and discuss the calibration procedures and the accuracies achieved in the particle density measurements. Energy deposits (in 4 cm thick scintillators) are measured from ~ 5 MeV to $\sim 5 \times 10^4$ MeV, allowing us to cover the dynamic range required to study the primary cosmic rays in the range previously mentioned. A comparison of the showers parameters reconstructed by the Grande and by the KASCADE arrays is shown.

1. Introduction

The KASCADE-Grande experiment[1] has been set up to study primary cosmic rays in the energy range from 10¹⁶ to 10¹⁸ eV, its main goal is the detection of the knee of the iron component. This observation would confirm the hypothesis that explains the knee of the primary cosmic rays spectrum with astrophysical motivations, and its existence is expected by the measurements of the KASCADE[2] and EASTOP[3] experiments.

The experiment is located at the Forschungszentrum Karlsruhe, Germany, where, beside the existing KASCADE [4] array, two new detector set ups (Grande and Piccolo) have been installed. The experiment is able

to sample different components of Extensive Air Showers (electromagnetic, muonic and hadronic) with high accuracy and covering a surface of 0.5 km^2 .

2. The Grande array

The Grande array[5] is made by 37 stations of plastic scintillation detectors, 10 m^2 surface (divided into 16 individual scintillators) and 4 cm thick. The distance between detectors is in average 137 m and they are located in a hexagonal grid (see fig.1). All 16 scintillators are viewed by a high gain photomultiplier (for timing and low particle density measurements), the four central ones are additionally viewed by a low gain one (for high particle density).

For triggering stations are arranged in 18 clusters of hexagonal shape with six detectors surrounding a central one. The minimum trigger requirement is the coincidence of the central and three neighbouring stations in one hexagon. The trigger rate is 5 Hz, the stability of the array is shown in figure 2 where the distribution of the number of counts (in 10 minutes bins) after the correction for the pressure variations is shown. The standard deviation of the distribution is ~ 1.1 times the standard deviation of a poissonian distribution, thus the non poissonian fluctuations are equal to 46% of the poissonian ones.

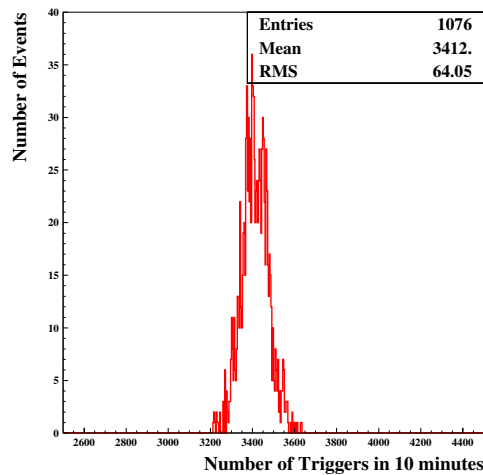
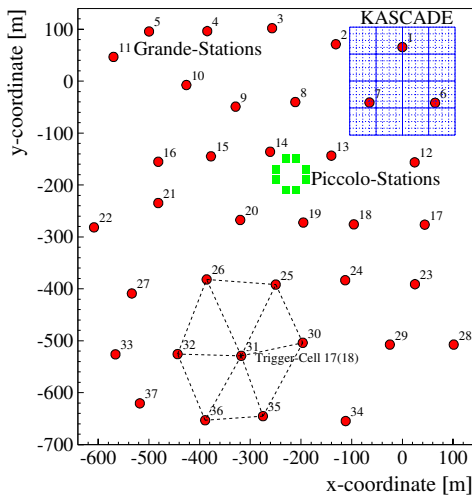


Figure 1. Layout of the KASCADE-Grande experiment **Figure 2.** Distribution of the number of events, in 10 minutes bins, after the correction for the pressure coefficient.

The analog signals of the high gain photomultipliers are fed into a charge amplifier, then are shaped and reach the maximum amplitude after $8 \mu\text{s}$, the output is split in two channels that go through a final amplification. The higher densities are measured using the low gain photomultipliers whose signals follow the same electronic chain (without being split in two signals).

To calibrate the peak sensing ADC we use a circuit that inject into the shaper-amplifiers a charge that is measured both by peak and charge sensing ADC. The charge values span over the whole peak ADC range, the curves obtained allow us to convert each peak ADC count into a charge ADC count.

The ADC value (in charge ADC scale) corresponding to the peak of the single particle spectrum is measured in each station during run time. In fact each EAS event ($\nu \sim 5$ Hz) is followed by three triggers given by a station in single mode ($\nu \sim 2000$ Hz), in this way we can measure the spectrum (15000 events) of each station every eight hours. This operation allows us to determine, for each run longer than ~ 36 hours, the peak position with a precision of $\sim 3\%$. Using a simulation of single muons crossing the detectors we proof that the energy deposit corresponding to the peak of the single particle spectrum is 8.5 MeV.

Three stations of the Grande array are located (see fig.1) inside the e/γ detectors of the KASCADE experiment allowing a check of the previously described calibration method by comparing the energy deposit in a Grande station with the mean energy deposit of the four e/γ detectors that are located around it. Only events that have the core located at about 100 m distance from the Grande station are selected. In this way the KASCADE detectors, that are separated by 13 m from each other, are at a distance from the core where the lateral distribution of particles in the EAS is flat and the mean value of their energy deposit can be compared with the Grande stations one.

As the Grande and the e/γ KASCADE detectors are surrounded by different materials and as they do not have the same thickness, we expect that the energy deposits, even if they are crossed by the same number of particles, are not equal. Figure 4 shows the measured energy deposits in the two detectors (full squares) compared with those expected by a full shower (CORSIKA) and detector (CRES) simulation (open circles).

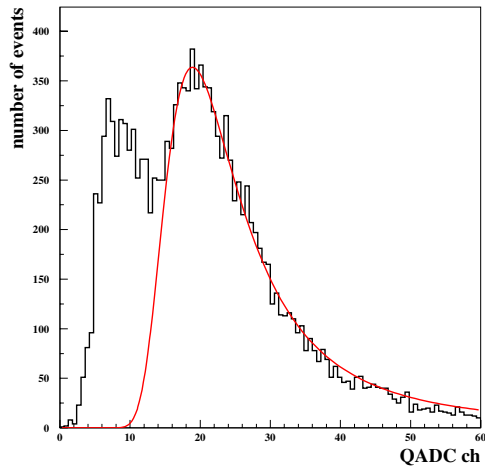


Figure 3. Single particle spectrum measured in station 5. The line shows the result of a Landau fit.

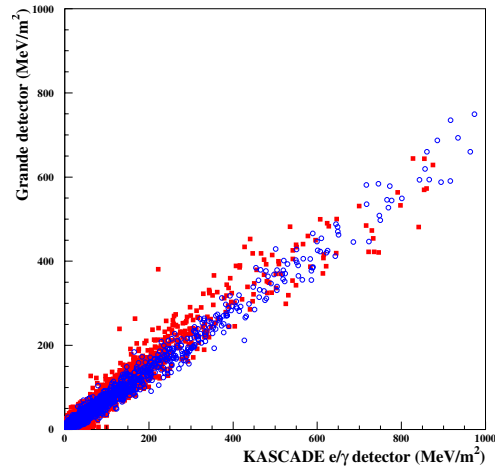


Figure 4. Comparison of the energy deposit measured (full squares) and expected from a full simulation (open circles) in the KASCADE e/γ and Grande detectors.

We also compare the shower parameters reconstructed, for the same events, by the Grande and by the KASCADE e/γ arrays separately. We select events with the core located inside both arrays and reconstructed by both of them. This is obtained requiring that: the maximum energy deposit in the Grande detectors is measured by station 7 (i.e. the center of the Grande trigger cluster located inside the KASCADE array, see fig.1); the core position, measured by KASCADE, is located inside a circle of 90 m radii centered in the middle of the array; $0.4 < s_{Grande} < 1.4$ (i.e. events with a good reconstruction) and $\text{Log Ne}_{KASCADE} > 5.6$ (i.e. Grande efficiency near to one).

The distribution of the differences of the x (red solid line) and y (blue dashed line) coordinates of the core position are shown in figure 5. It can be seen that the mean value of the differences, on both coordinates, between two arrays is lower than 2 m and that the standard deviation of the distribution is about 12 m. As the errors on the core location for the KASCADE array[4] are, at these energies, ~ 2 m we can say that this width is mainly due to the resolution of the Grande array that can be so evaluated being less than 12 m. Figure 6 shows the scatter plot of the shower size measured by the two arrays. This is dominated by the statistical uncertainties on the Grande reconstruction, that are (in the range $6.0 < \text{Log} N_e_{KASCADE} < 6.1$) about 25%. Possible systematic uncertainties and their origin are under investigation.

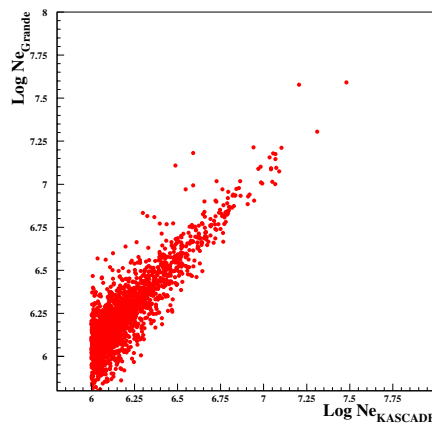
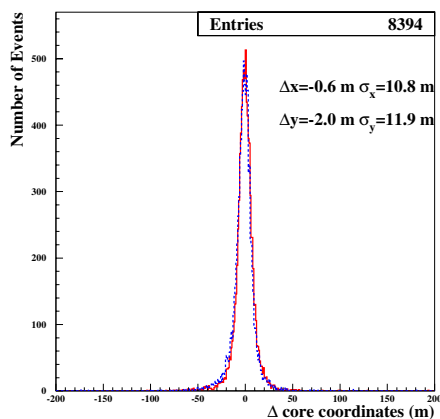


Figure 5. Distribution of the difference of the coordinates of the core position (x solid line and y dashed line) measured by the KASCADE and the Grande arrays.

Figure 6. Scatter plot of the shower size measured by the Grande array vs the one measured by the KASCADE array

3. Conclusions

The Grande array is in continuous and stable data taking since January 2004. We have described the procedure used to calibrate the analog signals; comparing the energy deposits in the KASCADE and Grande detectors with the expectations from a complete shower simulation, we can conclude that the calibrations of the two arrays are coherent with each other. We have also reported the results of the event reconstruction obtained independently with the two arrays, showing that the resolution on the core coordinates of the Grande array is around 12 m reaching the value foreseen in the experiment proposal.

References

- [1] A. Haungs et al. KASCADE-Grande Collab., Proc of 28th ICRC, Tsukuba (2003) 2, 985.
- [2] T. Antoni et al. KASCADE Coll., To appear in Astroparticle Physics (2005).
- [3] M. Aglietta et al. EAS-TOP Coll., Astrop. Phys. 21, 583 (2004).
- [4] T. Antoni et al KASCADE Coll., Nucl. Instr. and Meth. A 513, 490 (2003).
- [5] A. Chiavassa et al. KASCADE-Grande Coll., Proc of the 28th ICRC, Tsukuba (2003).

Shower Size Reconstruction at KASCADE-Grande

R. Glasstetter^a, T. Antoni^b, W.D. Apel^c, F. Badea^{c,1}, K. Bekk^c, A. Bercuci^d, M. Bertaina^e, J. Blümer^{c,b}, H. Bozdog^c, I.M. Brancus^d, M. Brüggemann^f, P. Buchholz^f, A. Chiavassa^e, K. Daumiller^c, F. Di Pierro^e, P. Doll^c, R. Engel^c, J. Engler^c, F. Feßler^c, P.L. Ghia^g, H.J. Gils^c, C. Grupen^f, A. Haungs^c, D. Heck^c, J.R. Hörandel^b, K.-H. Kampert^a, H.O. Klages^c, Y. Kolotaev^f, G. Maier^{c,2}, H.J. Mathes^c, H.J. Mayer^c, J. Milke^c, B. Mitrica^d, C. Morello^g, M. Müller^c, G. Navarra^e, R. Obenland^c, J. Oehlschläger^c, S. Ostapchenko^{c,3}, S. Over^f, M. Petcu^d, T. Pierog^c, S. Plewnia^c, H. Rebel^c, A. Risse^h, M. Roth^b, H. Schieler^c, J. Scholz^c, O. Sima^d, M. Stümpert^b, G. Toma^d, G.C. Trinchero^g, H. Ulrich^c, S. Valchierotti^e, J. van Buren^c, W. Walkowiak^f, A. Weindl^c, J. Wochele^c, J. Zabierowski^h, S. Zagromski^c, D. Zimmermann^f

(a) *Fachbereich Physik, Universität Wuppertal, 42097 Wuppertal, Germany*

(b) *Institut für Experimentelle Kernphysik, Universität Karlsruhe, 76021 Karlsruhe, Germany*

(c) *Institut für Kernphysik, Forschungszentrum Karlsruhe, 76021 Karlsruhe, Germany*

(d) *National Institute of Physics and Nuclear Engineering, 7690 Bucharest, Romania*

(e) *Dipartimento di Fisica Generale dell'Università, 10125 Torino, Italy*

(f) *Fachbereich Physik, Universität Siegen, 57068 Siegen, Germany*

(g) *Istituto di Fisica dello Spazio Interplanetario, INAF, 10133 Torino i.i. CNR, Italy*

(h) *Soltan Institute for Nuclear Studies, 90950 Lodz, Poland*

¹ *on leave of absence from Nat. Inst. of Phys. and Nucl. Engineering, Bucharest, Romania*

² *now at University Leeds, LS2 9JT Leeds, United Kingdom*

³ *on leave of absence from Moscow State University, 119899 Moscow, Russia*

Presenter: Karl-Heinz Kampert (kampert@uni-wuppertal.de), ger-kampert-K-abs2-he13-oral

The KASCADE-Grande experiment consists of a large scintillator array for the detection of charged particles from extensive air showers in the primary energy range $10^{16} - 10^{18}$ eV. In combination with the KASCADE muon detectors it provides the means to investigate the possible existence of an iron knee and the change in composition due to extragalactic cosmic rays expected to become more dominant in that energy range. The performance of the apparatus and shower reconstruction methods will be presented on the basis of detailed Monte Carlo simulations. After approximately one year of data taking we present lateral distributions of the charged shower component and the reconstructed 2-dimensional shower size spectrum.

1. Experimental Setup

The combined KASCADE and KASCADE-Grande Experiment [1], located on the site of the Forschungszentrum Karlsruhe (110m a.s.l.), consists of various detector components [2] for measuring the particles of extensive air showers in the primary energy range from $10^{14} - 10^{18}$ eV. The measurement at the upper part of that energy range is possible due to a large scintillator array covering an area of approx. 700×700 m². It comprises 37 stations located on a hexagonal grid with an average distance of 140 m to each other for the measurement of the charged shower component. Each of the detector stations is equipped with 16 4 cm thick plastic scintillator sheets covering a total area of 10 m² per station. With the present setup the upper limit of the dynamic range will be reached at approx. 6000 MIPs. For details about readout and calibration see [3].

The muon component of EAS is reconstructed from the 192×3.2 m² muon detectors of the KASCADE array which are located under an iron/lead absorber, resulting in a muon threshold of 230 MeV and suppressing

punch-through of the electromagnetic component efficiently above 40 m core distance. The muon number ($E_{kin} > 300$ MeV) of an air shower is therefore reconstructed from a relatively local measurement on the 200×200 m² field as described in [5].

2. Shower Reconstruction

For describing the lateral distribution of electrons in a hadronic induced air shower especially at large core distances ($r < 800$ m) a slightly modified NKG-function is used [4]:

$$\rho_e = N_e \cdot C(s) \cdot \left(\frac{r}{r_0}\right)^{s-\alpha} \cdot \left(1 + \frac{r}{r_0}\right)^{s-\beta}$$

with the normalization factor $C(s) = \Gamma(\beta - s) / (2\pi r_0^2 \Gamma(s - \alpha + 2) \Gamma(\alpha + \beta - 2s - 2))$, the shower size N_e and the so-called shower age s . Performing CORSIKA [7] air shower simulations, the parameters $\alpha = 1.5$, $\beta = 3.6$ and $r_0 = 40$ m were found as optimum for the radial distances relevant for the Grande array (opposite to the common parameters $\alpha = 2$ and $\beta = 4.5$ with $r_0 = 89$ m used for the KASCADE array at $r < 300$ m).

To describe the average arrival time \bar{t} and the time spread σ_t of the shower electrons a Linsley-function has been adapted to the time distributions of pure CORSIKA simulations:

$$\bar{t} = 2.43\text{ns} \cdot \left(1 + \frac{r}{30\text{m}}\right)^{1.55} \quad \text{and} \quad \sigma_t = 1.43\text{ns} \cdot \left(1 + \frac{r}{30\text{m}}\right)^{1.39}$$

The parameters were found to depend only weakly on the primary particle properties and to first order approximation the measured arrival time of the first out of N particles inside a detector is given by $\bar{t}_{1.ofN} = \bar{t} / \sqrt{N}$.

Since the functions above are coupled via the particle number and the core distance in shower disc coordinates, they are fitted simultaneously to the data in a combined negative-log-likelihood/ χ^2 minimization. For the calculation of the expected particle density in a Grande station a contribution from the previously reconstructed muon lateral distribution function ρ_μ (for functional form see [5]) is taken into account. Thus, the 7 free parameters of the global fit are the core position and the shower direction (including a time offset), as well as the electron number ($E_{kin} > 3\text{MeV}$) and shower age.

To test the reconstruction procedure and to estimate its uncertainties, air showers generated by the CORSIKA package using the interaction models QGSJET01 [8] and FLUKA2002.4[9] were used as input for a detailed GEANT3.21-based [6] simulation of the installation. In total, approx. 200000 proton and iron showers were generated using a E^{-2} spectrum in the energy range $10^{15} - 10^{18}\text{eV}$ and zenith angles $0^\circ - 18^\circ$. The output has then been analysed in the same way as for the measurement and the resulting spatial and directional resolution (68 % confidence level) is shown in Figure 1 (upper row) as function of shower size and for different primaries. In addition, there was a smaller data set from an updated simulation code including instrumental effects from electronics like photomultiplier responses and cable delay uncertainties whose results are plotted as open symbols. Above a threshold of 10^6 electrons corresponding to 100 % trigger efficiency the resolution is better than 12 m and 0.6° respectively and nearly independent from the primary particle.

The accuracy of the estimated electron and muon number is shown in the lower panel of figure 1. Here, the average difference between the reconstructed and true logarithmic shower sizes (systematic deviation) have been plotted together with the spread of this quantities (statistical uncertainty). As can be seen, the statistical uncertainty for both is around 25 % at threshold and decreases slightly with shower size whereas the systematic deviation for the electrons decreases from 0 to -10 % and thus stays always well below the statistical accuracy of the experiment. The systematic overestimation of the muon component is currently under investigation [5].

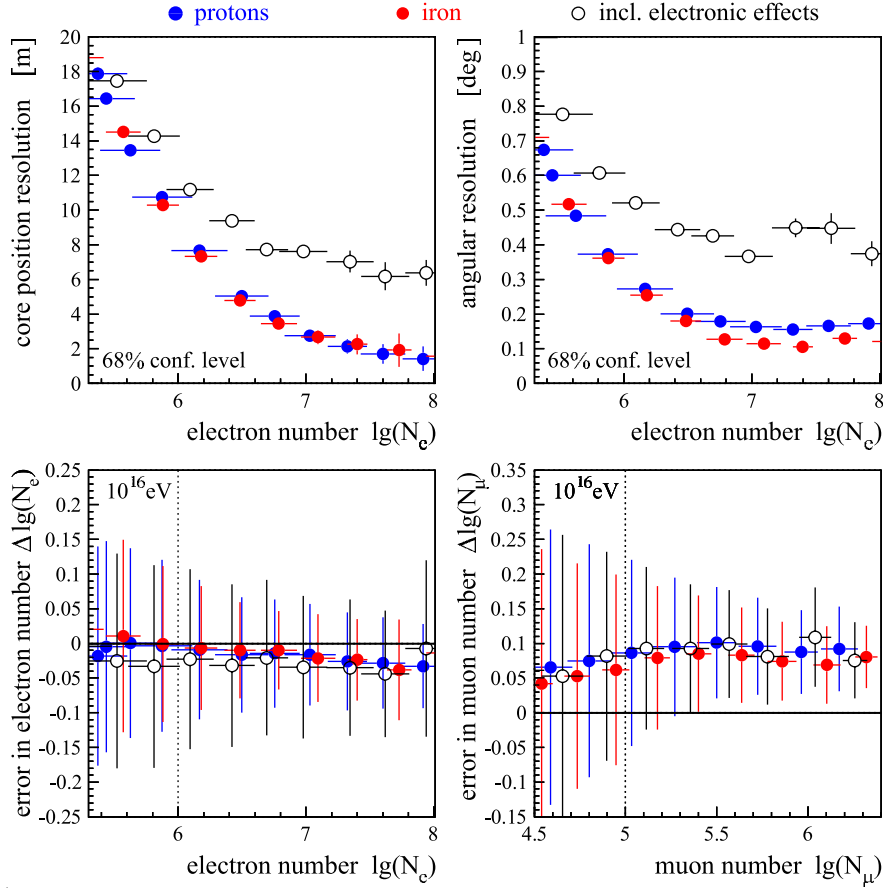


Figure 1. Reconstruction accuracy of core position (upper left) and shower direction (upper right) as function of electron number. Systematic deviation of the reconstructed electron (lower left) and muon number (lower right) as function of the true electron and muon number. The errors bars indicate the statistical error of a single reconstruction. The individual symbols correspond to a given primary energy range with isotropic zenith angles from $0^\circ - 18^\circ$ for two different primary particles (p and Fe) and a data set with less statistics (open symbols) including additional electronic effects.

3. First Results

In order to investigate the variation of the mean lateral distributions with energy, the primary energy has been roughly estimated from a linear combination of electron and muon numbers deduced from CORSIKA simulations with fixed energies and five different primaries (0° - 18°) by means of a linear regression analysis:

$$\lg(E_{est}/\text{GeV}) = 0.313 \cdot \lg N_e + 0.666 \cdot \lg N_\mu + 1.24/\cos\vartheta + 0.580$$

The result of this analysis is displayed in Fig. 2 (left) for air showers above the experimental threshold of 10^{16} eV with the fit functions $\rho_e + \rho_\mu$ shown for comparison using the average fit parameters. The average age \bar{s} of these distributions is found to increase significantly with energy ($\sigma_{\bar{s}} < 0.005$). This indicates that the composition gets heavier, i.e. more showers are starting higher in the atmosphere, with increasing energy. On the contrary, a constant composition would result in decreasing age parameters, because showers of increasing

energy would get *younger* at given atmospheric depth. This has been confirmed independently also by a KASCADE array analysis [4].

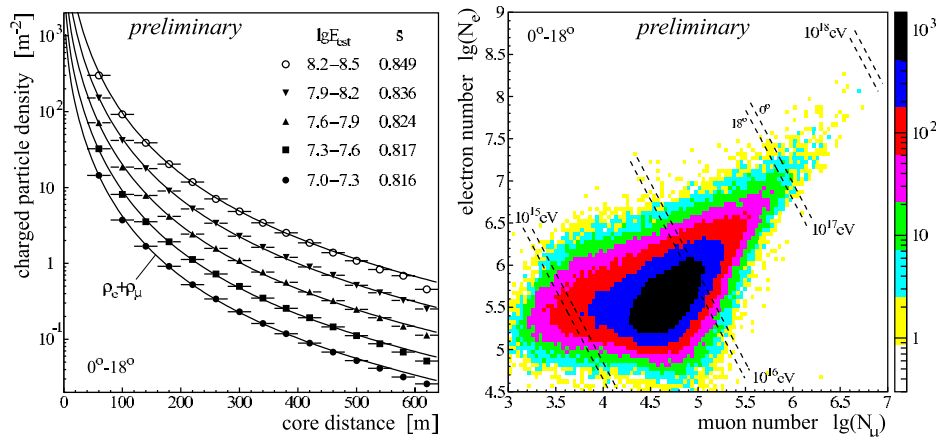


Figure 2. Measured lateral distributions of the charged particle component for 5 primary energy bins above the trigger threshold of 10^{16}eV (left). Reconstructed electron and muon number distribution of air showers measured by the KASCADE-Grande arrays (right). The dashed line pairs indicate average lines of constant energy derived from CORSIKA simulations for the extreme zenith angles.

In the last year more than 11 Mio. events triggered by the Grande array have been recorded. Fig. 2 (right) depicts the present data set in terms of the reconstructed particle numbers for zenith angles below 18° . Even though most of the triggered events are below the threshold, we have measured up to now nearly 400 events above 10^{17}eV (0° - 18°). This is about the same number of events in that energy region as have been measured by the KASCADE array in one decade. In future, these events will be the basis of a sophisticated unfolding analysis according to [10] to disentangle the mystery about the predicted *iron knee* and the elemental composition above 10^{17}eV .

Acknowledgements: The work of the presenters group is funded by the Ministry for Education and Research of the Federal Republic of Germany.

References

- [1] K.-H. Kampert et al. (KASCADE-Grande collaboration), *Nucl. Phys. B (Proc. Suppl.)* **122** (2003) 422
- [2] T. Antoni et al. (KASCADE collaboration), *Nucl. Instr. and Meth.* **A 513**, 490 (2003).
- [3] A. Chiavassa et al. (KASCADE-Grande collaboration), 2005, Proc. 29th ICRC, these proceedings.
- [4] W.D. Apel et al. (KASCADE collaboration), *Astropart. Phys.*, submitted (2005).
- [5] J. van Buren et al. (KASCADE-Grande collaboration), 2005, Proc. 29th ICRC, these proceedings.
- [6] *GEANT - Detector Desc. and Sim. Tool*, CERN Program Library Long Writeup **W5013**, CERN (1993)
- [7] D. Heck et al., Forschungszentrum Karlsruhe, Report FZKA 6019 (1998).
- [8] N.N. Kalmykov and S.S. Ostapchenko, *Phys. Atom. Nucl.* **56**, 346 (1993).
- [9] A. Fassò et al., *FLUKA: Status and Prospective of Hadronic Applications*, Proc. Monte Carlo 2000 Conf., Lisbon, Oct. 23-26, 2000, A. Kling et al., Springer (Berlin) 955 (2001).
- [10] T. Antoni et al. (KASCADE collaboration), *Astropart. Phys.*, in press (2005).

Muon Size Spectrum measured by KASCADE-Grande

J. van Buren^b, T. Antoni^a, W.D. Apel^b, F. Badea^{b,1}, K. Bekk^b, A. Bercuci^c, M. Bertaina^d, J. Blümer^{b,a}, H. Bozdog^b, I.M. Brancus^c, M. Brüggemann^e, P. Buchholz^e, A. Chiavassa^d, K. Daumiller^b, F. Di Pierro^d, P. Doll^b, R. Engel^b, J. Engler^b, F. Feßler^b, P.L. Ghia^f, H.J. Gils^b, R. Glasstetter^g, C. Grupen^e, A. Haungs^b, D. Heck^b, J.R. Hörandel^a, K.-H. Kampert^g, H.O. Klages^b, Y. Kolotaev^e, G. Maier^{b,2}, H.J. Mathes^b, H.J. Mayer^b, J. Milke^b, B. Mitrica^c, C. Morello^f, M. Müller^b, G. Navarra^d, R. Obenland^b, J. Oehlschläger^b, S. Ostapchenko^{b,3}, S. Over^e, M. Petcu^c, T. Pierog^b, S. Plewnia^b, H. Rebel^b, A. Risse^h, M. Roth^a, H. Schieler^b, J. Scholz^b, O. Sima^c, M. Stümpert^a, G. Toma^c, G.C. Trincherio^f, H. Ulrich^b, S. Valchierotti^d, W. Walkowiak^e, A. Weindl^b, J. Wochele^b, J. Zabierowski^h, S. Zagromski^b, D. Zimmermann^e

(a) Institut für Experimentelle Kernphysik, Universität Karlsruhe, 76021 Karlsruhe, Germany

(b) Institut für Kernphysik, Forschungszentrum Karlsruhe, 76021 Karlsruhe, Germany

(c) National Institute of Physics and Nuclear Engineering, 7690 Bucharest, Romania

(d) Dipartimento di Fisica Generale dell'Università, 10125 Torino, Italy

(e) Fachbereich Physik, Universität Siegen, 57068 Siegen, Germany

(f) Istituto di Fisica dello Spazio Interplanetario, INAF, 10133 Torino, Italy

(g) Fachbereich Physik, Universität Wuppertal, 42097 Wuppertal, Germany

(h) Soltan Institute for Nuclear Studies, 90950 Lodz, Poland

(1) on leave of absence from Nat. Inst. of Phys. and Nucl. Engineering, Bucharest, Romania

(2) now at University Leeds, LS2 9JT Leeds, United Kingdom

(3) on leave of absence from Moscow State University, 119899 Moscow, Russia

Presenter: H. Ulrich (Holger.Ulrich@ik.fzk.de), ger-ulrich-H-abs2-he13-poster

The reconstruction of the muonic component of extensive air showers with KASCADE-Grande is described and the quality of the reconstruction is studied with Monte Carlo simulations and compared with data from the KASCADE experiment. Furthermore, first results of mean muon lateral distributions and muon size spectra are presented.

1. Introduction

The KASCADE-Grande[1] experiment, located at the Forschungszentrum Karlsruhe, Germany, extends the existing extensive air shower experiment KASCADE[2] by an array of 37 detector stations spread over an area of 0.5 km². Its major goal is to measure the possible knee of the heavy component in the primary cosmic ray energy spectrum, expected at $\approx 10^{17}$ eV. The new array comprises 18 hexagonal trigger cells (7 stations), and 100% efficiency is reached with a 7 out of 7 coincidence condition at primary energies of $\approx 3 \times 10^{16}$ eV. With this configuration it is possible to measure and reconstruct extensive air showers of primary energies up to 10^{18} eV. Each detector station houses 10 m² of plastic scintillators, that are sensitive to the electromagnetic and muonic component above a threshold of 5 MeV, enabling the reconstruction of the number of charged particles of an extensive air shower. The field array of the KASCADE experiment with its electron and muon detectors covers an area of 200 m \times 200 m and consists of 252 stations. It provides a coverage of 490 m² for e/γ and 622 m² for muons, with an energy threshold for vertical incidence of $E_e > 5$ MeV and $E_\mu > 230$ MeV. In order to infer the energy spectra of the primary cosmic ray particles for different mass groups with unfolding

techniques using the two dimensional electron-muon size spectrum, both total particle numbers have to be known.

2. Approach and accuracy

The Grande array measures the densities and arrival times of the charged particles, from which one can reconstruct the shower core and arrival direction. The total muon number is obtained in a likelihood fit to the muon densities measured by the KASCADE muon detectors, located in the outer 192 stations of the KASCADE array. To describe the lateral distribution of the muons a function similar to the one proposed in Ref.[3] for the electron component is used:

$$\rho_\mu(r) = N_\mu \cdot f(r), \text{ with } f(r) = \frac{0.28}{r_0^2} \left(\frac{r}{r_0}\right)^{p1} \cdot \left(1 + \frac{r}{r_0}\right)^{p2} \cdot \left(1 + \left(\frac{r}{10 \cdot r_0}\right)^2\right)^{p3} \quad (1)$$

The parameters $p1$, $p2$, $p3$ were obtained to be -0.69 , -2.39 and -1.0 respectively by fitting the lateral distribution function to 10^{16} eV and 10^{17} eV proton and iron induced air showers simulated with CORSIKA[4] using the interaction model QGSJet[5]. A scaling radius of $r_0 = 320$ m is used. Due to the low measured muon densities and in order to obtain stable fit results, the curvature of the lateral muon densities is kept constant and only the muon number N_μ is estimated by $N_\mu^{est} = \sum_i n_i / \sum_i (f(r_i) \cdot A_i \cdot \cos(\theta))$. Where n_i are the number of particles measured in a core distance r_i in an area A_i and θ is the zenith angle of the air shower. Due to punch through of the electromagnetic component close to the shower core an inner radial cut of $r_i > 40$ m is applied. A fiducial area of $500 \text{ m} \times 600 \text{ m}$ is defined to reduce the effect of misreconstructed core positions at the edges of the Grande array. Requiring the core of a shower to be inside this frame results in a measurement of the muon density in a radial distance of $275 - 625$ m to the shower core for $\approx 68\%$ of the showers. Typical densities for an air shower of 10^{17} eV range from 0.1 to 1 particle per m^2 in this radial range. Further quality

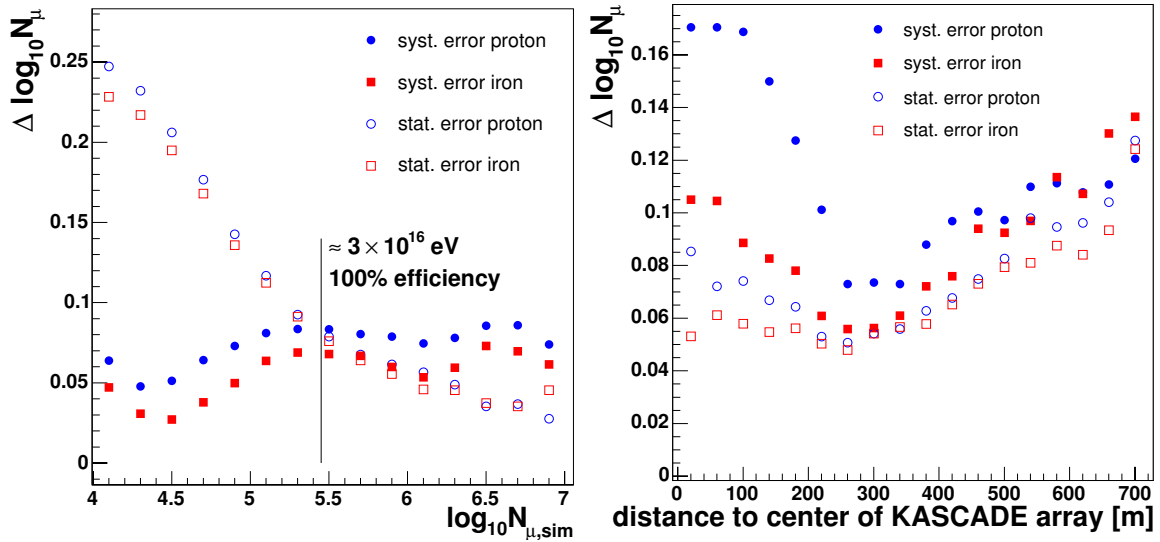


Figure 1. Uncertainties in reconstruction of total muon number depending on the muon number (left) and depending on distance to the KASCADE array (right). In the right handed figure only air showers with $\log_{10} N_\mu > 5.5$ are shown.

cuts applied include the requirement of at least 16 Grande stations in an event and a cut on the age parameter s in the electron size fit (see also [6]). The systematics and uncertainties have been studied with Monte Carlo simulations using CORSIKA and the interaction model QGSJet (2001 version). The simulations comprise 380000 air showers each for proton and iron in an energy range from 10^{15} eV to 10^{18} eV and zenith angles from 0° to 42° . The simulated events have been scattered over the Grande array and tracked through a detailed GEANT[7] based detector simulation. For muon numbers larger than $\log_{10} N_\mu \approx 5.5$, which corresponds to an energy of approximately 3×10^{16} eV the systematic error of the reconstructed total muon number is constant at around 15% (Fig. 1 left). It shows an offset between proton and iron of 0.01. The statistical error does not show a dependence on the primary particle. As expected, the statistical uncertainty decreases with increasing muon number. From around 20% at trigger threshold to approximately 8% at the upper limit of the energy range. Figure 1 right shows the dependency of the reconstruction accuracies on the distance of the core to the KASCADE array. In the important radial range of 275 – 625 m, the statistical error increases from around 10% to approximately 20%. The relatively large systematic error for small distances is due to the steepness of the lateral distribution close to the shower core and to the punch through of the e/γ component close to the core. The reconstruction systematics shown in Fig. 1 are understood and will be dealt by the correct implementation of the lateral energy conversion function for the muon detectors.

3. Muon lateral distributions

Figure 2 left shows a comparison of mean muon lateral distributions from simulations with the measured data. The showers are binned in intervals of total muon number, being a good estimator of primary energy. The points for iron and proton lie very close to each other, as the shape of the muon lateral distribution is not very sensitive to the nature of the primary particle. The lateral distribution obtained from the data agrees relatively well with the simulations. The lines shown correspond to Eq.1 where N_μ is set to the measured mean muon

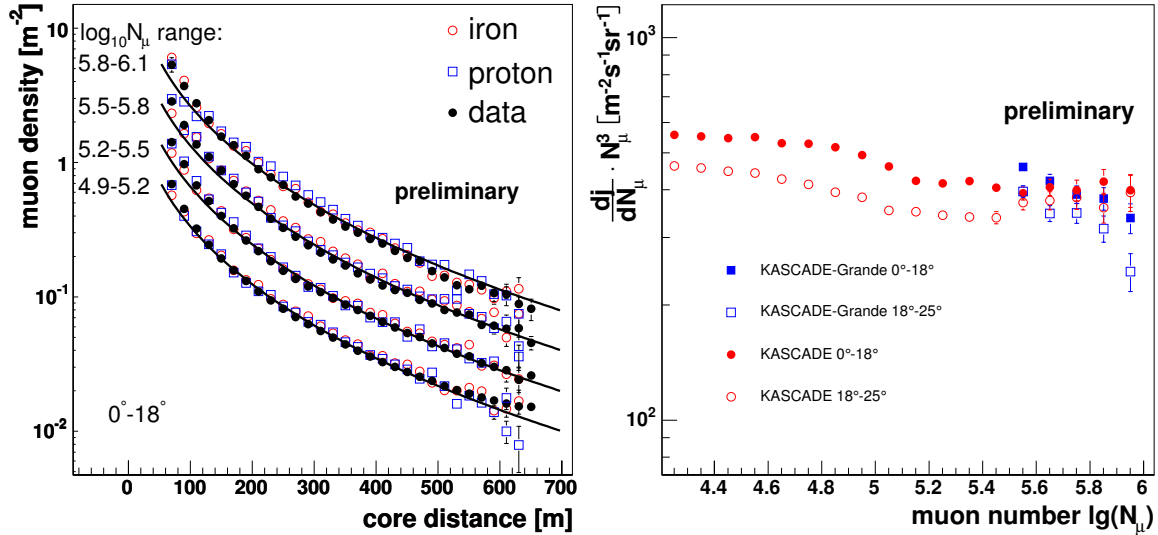


Figure 2. Left: Lateral density distributions of muons measured with KASCADE-Grande. Right: Reconstructed muon size spectrum for two zenith angle ranges

number obtained in each interval. At small radii the function has problems in describing the data, which might be due to punch through up to a range of 100 m core distance.

4. Reconstructed muon size spectrum

The shown differential muon size spectrum (Fig. 2 right) is based on a data set of 5.5×10^6 triggered events for KASCADE-Grande, taken between March 2004 and March 2005. The effective time of combined data taking of the Grande array and the KASCADE array was approximately 163 days, which is relevant for the flux determined by KASCADE-Grande. The flux for the KASCADE spectrum was obtained in approximately 1300 days of effective data taking. Both muon sizes are corrected for their systematic errors in reconstruction, derived from Monte Carlo studies. The correction applied to data from the KASCADE array in the high energy region might be too low. As one can see there is good agreement between the two measured fluxes in the overlap area in both shown zenith angle ranges. Furthermore the spectral structure shows reasonable continuation: Around a total muon number of $\log_{10} N_\mu \approx 4.8$ one sees a steepening of the spectrum for the first zenith angle range, corresponding to the knee in the light component of the energy spectrum. For the second zenith angle range it is shifted lower to $\log_{10} N_\mu \approx 4.6$. The steepening of the spectrum is followed by a flattening that corresponds to the relative increase of the heavy component. For more detailed statements on the shape of the muon size spectrum beyond $\log_{10} N_\mu \approx 6$ more data is needed.

5. Conclusion

It has been shown that it is possible to reconstruct the total muon number with only a small fraction of radial coverage and first results look promising. The number of events measured with KASCADE-Grande above 100% efficiency are comparable to the ones measured by KASCADE, despite a factor of nearly ten in exposure time. With the above described reconstruction of the muon component together with the measured number of charged particles from the Grande array, one is able to reconstruct the electron size of an air shower measured with KASCADE-Grande (see [6]). With the information of the electron and muon size together, we expect to be able to infer the mass of the primary cosmic ray particles with an sophisticated unfolding analysis[8].

References

- [1] A. Haungs *et al.* (KASCADE-Grande Collaboration), in *Proc. 28th Int. Cosmic Ray Conf., Tsukuba* **2**, 985 (2003).
- [2] T. Antoni *et al.* (KASCADE Collaboration), *Nucl. Instrum. Meth.* **A513**, 490 (2003).
- [3] A. A. Lagutin and R. I. Raikin, *Nucl. Phys. B (Proc. Suppl.)* **97**, 274 (2001).
- [4] D. Heck *et al.*, Forschungszentrum Karlsruhe, Report FZKA 6019 (1998).
- [5] N. N. Kalmykov *et al.*, *Nucl. Phys. B (Proc. Suppl.)*, **52B** 17 (1997).
- [6] R. Glasstetter *et al.*, these proceedings.
- [7] CERN Software Division, *GEANT Detector Description and Simulation Tool*, CERN Program Library Long Writeup W5013 (1993)
- [8] T. Antoni *et al.* (KASCADE Collaboration), *Astropart. Phys.* in press (2005).

Studies of different LDFs for primary energy estimation and mass discrimination of cosmic rays by the EAS lateral charged particle distribution as observed by KASCADE-Grande

H. Rebel^b, O. Sima^{c,1}, T. Antoni^a, W.D. Apel^b, F. Badea^{b,2}, K. Bekk^b, A. Bercuci^c, M. Bertaina^d, J. Blümer^{b,a}, H. Bozdog^b, I.M. Brancus^c, M. Brüggemann^e, P. Buchholz^e, A. Chiavassa^d, K. Daumiller^b, F. Di Pierro^d, P. Doll^b, R. Engel^b, J. Engler^b, F. Feßler^b, P.L. Ghia^f, H.J. Gils^b, R. Glasstetter^g, C. Grupen^e, A. Haungs^b, D. Heck^b, J.R. Hörandel^a, K.-H. Kampert^g, H.O. Klages^b, Y. Kolotaev^e, G. Maier^{b,3}, H.J. Mathes^b, H.J. Mayer^b, J. Milke^b, B. Mitrica^c, C. Morello^f, M. Müller^b, G. Navarra^d, R. Obenland^b, J. Oehlschläger^b, S. Ostapchenko^{b,4}, S. Over^e, M. Petcu^c, T. Pierog^b, S. Plewnia^b, A. Risse^h, M. Roth^a, H. Schieler^b, J. Scholz^b, M. Stümpert^a, G. Toma^c, G.C. Trincherio^f, H. Ulrich^b, S. Valchierotti^d, J. van Buren^b, W. Walkowiak^e, A. Weindl^b, J. Wochele^b, J. Zabierowski^h, S. Zagromski^b, D. Zimmermann^e

(a) Institut für Experimentelle Kernphysik, Universität Karlsruhe, 76021 Karlsruhe, Germany

(b) Institut für Kernphysik, Forschungszentrum Karlsruhe, 76021 Karlsruhe, Germany

(c) National Institute of Physics and Nuclear Engineering, 7690 Bucharest, Romania

(d) Dipartimento di Fisica Generale dell'Università, 10125 Torino, Italy

(e) Fachbereich Physik, Universität Siegen, 57068 Siegen, Germany

(f) Istituto di Fisica dello Spazio Interplanetario, INAF, 10133 Torino, Italy

(g) Fachbereich Physik, Universität Wuppertal, 42097 Wuppertal, Germany

(h) Soltan Institute for Nuclear Studies, 90950 Lodz, Poland

¹ University of Bucharest, Dpt. of Physics, Bucharest, Romania

² on leave of absence from Nat. Inst. of Phys. and Nucl. Engineering, Bucharest, Romania

³ now at University Leeds, LS2 9JT Leeds, United Kingdom

⁴ on leave of absence from Moscow State University, 119899 Moscow, Russia

Presenter: H. Rebel (rebel@ik.fzk.de), ger-rebel-H-abs1-he13-oral

On basis of simulation studies the reconstruction quality and some features of the lateral distribution of charged particles from extensive air showers (EAS) have been explored as observed with the KASCADE-Grande detector array in the primary energy range of 10^{16} eV - 10^{18} eV. Special emphasis is put on the study of observables serving for energy determination and mass discrimination of the cosmic rays primaries.

1. Introduction

The lateral distribution of various charged particles is a basic quantity of extended air showers (EAS) observed with ground arrays. In present work we explore the quality of its reconstruction for the detector layout of KASCADE-Grande [1] and study salient features of the reconstructed average distribution $S(r)$. The detection efficiency and the response of the detector have been taken into account by a dedicated reconstruction program SHOWREC [2] recently developed and designed for EAS of vertical and inclined incidence as observed with the KASCADE-Grande array. It calibrates the detector signals of the KASCADE-Grande stations in terms of charged particles densities. The reconstruction quality is studied by comparing "true" and reconstructed simulated distributions, and various parameterizations (LDFs) have been scrutinized with respect to the reproduction of $S(r)$ in the radial range of KASCADE-Grande observations (about $r \leq 700$ m). It turns out the

region of the lateral charged particles distribution around $r = 500$ m (dominated by the muon component) indicates the energy of the primary particles, nearly independent of the mass, while the region about 100- 200 m (dominated by the electron gamma component) is sensitive to the primary mass.

2. EAS simulations

A set of showers with random angles of incidence, induced by H, C and Fe primaries have been simulated with CORSIKA Monte Carlo program (version 6.023) [3], using QGSJET model for describing the high-energy hadronic interaction for various energy ranges between $(1.00 - 1.78)10^{16}$ eV up to $(5.62 \cdot 10^{17} - 1.00 \cdot 10^{18})$ eV. The results are "distorted" by the SHOWREC program taking into account the detector responses and reconstruction features, thus providing quasi-experimental observables.

3. Reconstruction of the lateral particle density distribution by the program SHOWREC

The reconstruction procedures are based on the simulation of the energy deposit per charged particle (muons and electrons) in the Grande detector stations deduced with the code GEANT [4], and evaluated as function of the distance from the shower axis by introducing a lateral energy correction function. From the reconstructed number of charged particles, found for each detector station of the Grande array the reconstructed charged particle density $S(r)$ in the plane normal to the shower axis has been deduced. The distribution and number of the original CORSIKA charged particles hitting each detector are also recorded for sake of comparison and controlling the reconstruction performance. The present study extensively compares the features of the "true" density $\rho_{ch}(r)$ with the reconstructed density $S(r)$. The charged particle distributions (either the sampled CORSIKA distributions $\rho_{ch}(r)$ or the reconstructed distribution $S(r)$) adopt an a-priori anticipated form of the lateral distribution function (LDF) used for the interpolation of the charged particle density between the detector stations.

Different parameterizations of the LDF have been scrutinized, in particular the NKG function [5], the Linsley - LDF [6], the Lagutin - LDF [7] and a description as sum of polynomials [8]. Adopting adequate values for the scaling radius R_0 , the shape parameters of these forms and the total number of charged particles (normalisation of the LDF) have been determined by a fitting procedure. Actually none of the studied LDF describes the reconstructed lateral distribution perfectly over the whole r - range. Hence average EAS observables would be best determined by fitting the average lateral distribution in restricted ranges, e.g. $\langle S^{500} \rangle$ or equivalently $\langle N_{ch}^{500-600} \rangle$ (the integrated particle number between $r = 500$ and 600 m), and $\langle S^{200} \rangle$ (or equivalently $\langle N_{ch}^{100-200} \rangle$, the integrated particle number between $r = 100$ and 200 m). However these fits provide generally minor quality when extrapolated beyond the fitting range. Such a procedure deriving relevant EAS observables from fits to the observed lateral distributions over restricted lateral ranges would not be efficiently feasible for analyses of single showers on an event by event basis. Fortunately the fitted Linsley and Lagutin LDF do reproduce the reconstructed average lateral distribution $S(r)$ over large r -ranges with sufficient accuracy increasing with the primary energy.

In addition to the question how well a particular LDF reproduces the observed $S(r)$ is the question how well a certain quantity derived from the reconstructed lateral distribution reflects the "true" value.

Fig.1 displays a comparison of the reconstructed observables S^{200} and $N_{ch}^{100-200}$, respectively. These observables show some features, particularly useful for mass discrimination.

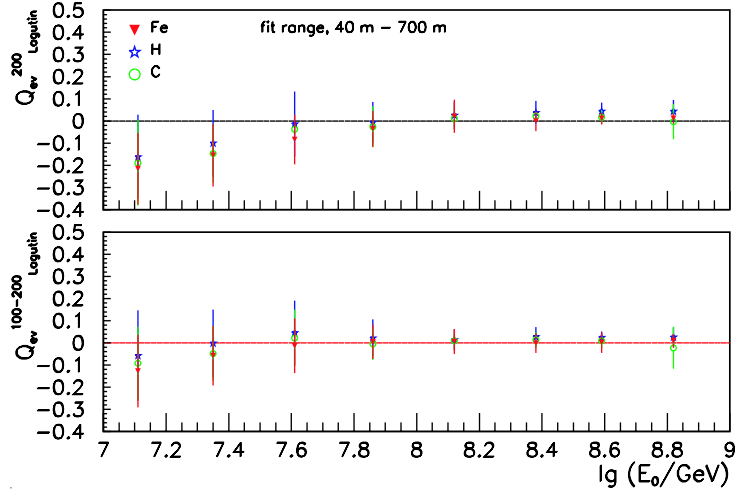


Figure 1. Energy variation of the reconstruction quality displayed by the quantity $Q(r) = (O(S_{rec}) - O(\rho_{ch}(r)))/O(\rho_{ch}(r))$ for the reconstructed observables $O = S^{200}$ and $N_{ch}^{100-200}$, respectively. The displayed quantity Q_{ev} is the average over many single showers of the sample, comparing the reconstructed observable with the "true" (i.e. undistorted CORSIKA) value.

4. Energy estimation by S^{500}

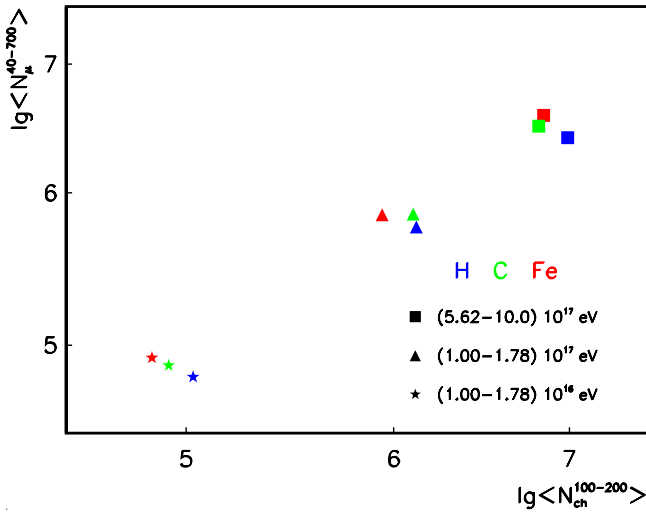


Figure 2. The $N_{ch}^{100-200} - N_{\mu}^{40-700}$ correlation of the averaged lateral distributions for various primaries and primary energy ranges.

While the KASCADE experiment is able to use a combination of the shower sizes of the electromagnetic and muon components for the energy determination, KASCADE-Grande [1] relies - in the present layout - on the observation of the charged particles, in general without discrimination between muons and electrons. This feature suggests to consider the procedure first suggested by Hillas et al. [9] to exploit the information of the lateral distribution $S(r)$ in the region of 500-600 m distance from the shower core. The results of the analysis display a linear energy dependence of the average reconstructed $\log \langle S^{500} \rangle$ for proton and iron induced EAS, exhibiting a rather weak dependence on the primary mass and a slight dependence on the angle of shower incidence. It should be noted that the reconstruction quality of S^{500} and $N_{ch}^{400-600}$, respectively gets reduced (within the error bars up to 50%) at lower primary energies. This is due to the reduced efficiency of the apparatus observing charged particles of lower energy EAS at $r \approx 500$ m. This feature, however, is included in the energy calibration of $\langle S^{500} \rangle$ and $\langle N_{ch}^{400-600} \rangle$, respectively.

5. Observables for mass discrimination

A particular aim is to explore EAS features which may carry information about mass composition in the primary energy range 10^{16} eV to 10^{18} , i.e. within the energy range of the KASCADE-Grande experiment. The shape parameter η of the Linsley LDF shows some mass discrimination power. Promising and more pronounced discrimination features of $\langle S^{200} \rangle$ get evident by well reconstructed values of $\langle S^{100/200} \rangle$ or alternatively $\langle N_{ch}^{100-200} \rangle$. The studies of the correlation distributions with various EAS observables exhibit pronounced mass discrimination features when correlating S^{200} ($N_{ch}^{100-200}$) with the muon density observed at adequate distance from the shower axis or with an adequately reconstructed muon number. In the present status we use as muon number (N_{μ}^{40-700}) a value reconstructed from the number of muons expected from the CORSIKA simulations hitting the Grande detectors (and using an adequate LDF for fitting the distribution in the range $r = 40 - 700$ m, see also ref. [10]).

6. Conclusions

1. The reconstructed averaged charged particle density in a range of distances of 500 m and 600 m from the shower core is only very weakly dependent on the primary mass and can be used as good energy identifier for EAS observed with KASCADE-Grande array.
2. Magnitude and shape of $\langle S(r) \rangle$ in the region $r \approx 200$ m show a distinct dependence of the primary mass. The $S^{100}-N_{\mu}$ correlation proves to be a powerful mass discriminator. This feature has been shown for the average lateral distributions of the charged particles and muons (reconstructed for the layout of KASCADE-Grande).
3. These results suggest the application in event-by-event analyses where the mass discrimination can be quantitatively specified by nonparametric statistical multivariate analyses providing the true - and misclassification probabilities for the mass assignments [11].

The methods worked out for the analysis of lateral distributions of charged EAS particles have been started to get applied to the analysis of real showers.

Acknowledgements

This work is supported by a grant of the Deutsche Forschungsgemeinschaft (grant: GZ436RUM).

References

- [1] A.Haungs et al. - KASCADE-Grande collaboration, Proc.28th ICRC (Tsukuba, Japan) 2 (2003) 985
- [2] O.Sima, I.M.Brancus, H.Rebel and A.Haungs, FZKA-Report 6985, Forschungszentrum Karlsruhe (2004)
- [3] D.Heck et al., FZKA-Report 6019, Forschungszentrum Karlsruhe (1998)
- [4] GEANT user's guide, CERN program library (1997)
- [5] K. Kamata and J. Nishimura, Prog. Theoret. Phys. Suppl. 6 (1958)93
- [6] J. Linsley et al., Journ. Phys. Soc. Japan 17 (1962) A-III
- [7] A. A. Lagutin and R.I.Raikin, Nucl. Phys. B (Proc.Suppl.) 97 (2001) 274
- [8] R. Glasstetter et al. - KASCADE-Grande Collaboration, Proc. 28th ICRC(Tsukuba,Japan) 2 (2003) 781
- [9] A.M. Hillas et al., Proc.12th ICRC (Hobart, Australia) 3 (1971) 1001
- [10] J. van Buren et al. - KASCADE-Grande Collaboration; Contr. 29th ICRC 2005, these proceedings
- [11] I.M. Brancus et al., Internal Report - KASCADE-Grande 2005-02, Forschungszentrum Karlsruhe; Contr.29th ICRC 2005, these proceedings

Event - by - event studies of the discriminative features of the LDF of charged EAS particles: observable correlations and non -parametric analyses of multivariate distributions

I.M. Brancus^c, T. Antoni^a, W.D. Apel^b, F. Badea^{b,1}, K. Bekk^b, A. Bercuci^c, M. Bertaina^d, J. Blümer^{b,a}, H. Bozdog^b, M. Brüggemann^e, P. Buchholz^e, A. Chiavassa^d, K. Daumiller^b, F. Di Pierro^d, P. Doll^b, R. Engel^b, J. Engler^b, F. Feßler^b, P.L. Ghia^f, H.J. Gils^b, R. Glasstetter^g, C. Grupen^e, A. Haungs^b, D. Heck^b, J.R. Hörandel^a, K.-H. Kampert^g, H.O. Klages^b, Y. Kolotaev^e, G. Maier^{b,2}, H.J. Mathes^b, H.J. Mayer^b, J. Milke^b, B. Mitrica^c, C. Morello^f, M. Müller^b, G. Navarra^d, R. Obenland^b, J. Oehlschläger^b, S. Ostapchenko^{b,3}, S. Over^e, M. Petcu^c, T. Pierog^b, S. Plewnia^b, H. Rebel^b, A. Risse^h, M. Roth^a, H. Schieler^b, J. Scholz^b, O. Sima^c, M. Stümpert^a, G. Toma^c, G.C. Trincherio^f, H. Ulrich^b, S. Valchierotti^d, J. van Buren^b, W. Walkowiak^e, A. Weindl^b, J. Wochele^b, J. Zabierowski^h, S. Zagromski^b, D. Zimmermann^e

(a) Institut für Experimentelle Kernphysik, Universität Karlsruhe, 76021 Karlsruhe, Germany

(b) Institut für Kernphysik, Forschungszentrum Karlsruhe, 76021 Karlsruhe, Germany

(c) National Institute of Physics and Nuclear Engineering, 7690 Bucharest, Romania

(d) Dipartimento di Fisica Generale dell'Università, 10125 Torino, Italy

(e) Fachbereich Physik, Universität Siegen, 57068 Siegen, Germany

(f) Istituto di Fisica dello Spazio Interplanetario, INAF, 10133 Torino, Italy

(g) Fachbereich Physik, Universität Wuppertal, 42097 Wuppertal, Germany

(h) Soltan Institute for Nuclear Studies, 90950 Lodz, Poland

¹ on leave of absence from Nat. Inst. of Phys. and Nucl. Engineering, Bucharest, Romania

² now at University Leeds, LS2 9JT Leeds, United Kingdom

³ on leave of absence from Moscow State University, 119899 Moscow, Russia

Presenter: I.M. Brancus (iliana@ifin.nipne.ro), rom-brancus-IM-abs1-he13-oral

Using the reconstruction of the charged particle density for KASCADE-Grande, based on different LDF parameterizations, extensive studies have been done to explore features for energy estimation and mass discrimination around 10^{17} eV. Taking into account the response of the Grande detectors, results from CORSIKA simulated showers for H, C, and Fe primaries in 8 energy intervals, (10^{16} eV - 10^{18} eV), give the charge particle density S^{500}/S^{600} or $N_{ch}^{400-600}$, with similar energy dependence for all primaries, indicating such observables are suitable as energy identifier. The correlations of the reconstructed particle density S^{100}/S^{200} , or $N_{ch}^{100-200}$, with a muon number N_{μ}^{40-700} present features for mass discrimination.

1. Data basis

Using the Monte Carlo program CORSIKA (version 6.023) [1], including the QGSJET [2] model for the description of high energy hadronic interactions, a set of showers of randomly distributed angles of incidence has been performed for H, C and Fe primaries in eight energy ranges: $1.0 \cdot 10^{16}$ eV to $1.0 \cdot 10^{18}$ eV, with a statistics decreasing from 300 to 20 showers.

In order to reconstruct the particle numbers corresponding to the individual KASCADE-Grande detector stations [3], the energy deposit per charged particle (muons and electrons) from CORSIKA simulated showers has been evaluated with the GEANT [4] code. Using the SHOWREC program [5], the charged particle dis-

tributions have been fitted with the Linsley LDF [6] and Lagutin LDF [7]. Fig.1. shows the distributions of integrated numbers of charged particles in the range 100 m - 200 m as obtained by a Linsley-fit to the densities in the range of 40 m to 700 m core distance.

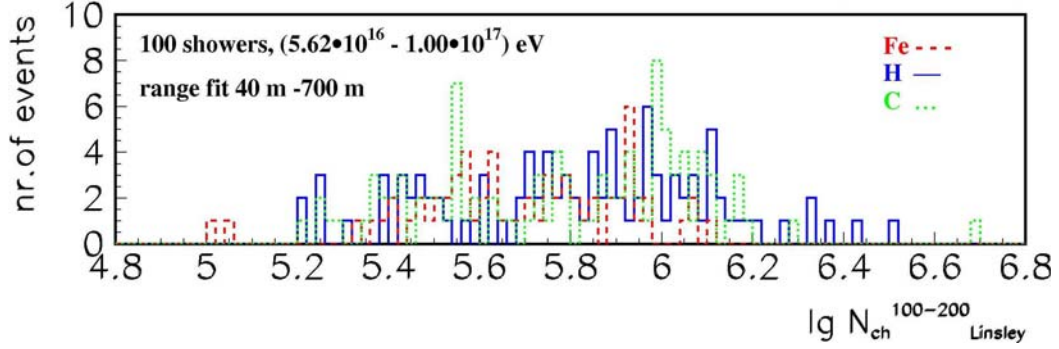


Figure 1. The distributions of $\lg N_{ch}^{100-200}$ using Linsley fit for H, C and Fe primaries with energies ($5.62 \cdot 10^{16}$ eV- $1.00 \cdot 10^{17}$ eV)

2. Energy estimation

Following previous investigations [9, 10] and based on the present studies the charged particle densities S^{500} , S^{600} as well as the integrated charged particle number $N_{ch}^{400-600}$ are suitable as energy identifier with a similar energy dependence for all primaries, see Fig.2-left. A fit with a straight line at this log-log-plot was performed for the observable $N_{ch}^{400-600}$, giving almost identical slopes for both primaries and both Linsley and Lagutin LDF descriptions.

$$\begin{aligned} \langle \lg N_H^{400-600} \rangle &= -4.96 + 1.27 \lg E_0 \\ \langle \lg N_{Fe}^{400-600} \rangle &= -4.98 + 1.27 \lg E_0 \end{aligned}$$

3. Correlations of relevance and mass discrimination

The charged particle density at lower distances, 100m - 200m, where the electron-gamma component is dominating, has features for mass discrimination. The observables S^{100} , S^{200} or $N_{ch}^{100-200}$ could play in the Grande array a similar role as the electron size N_e at the KASCADE array [11]. In the KASCADE-Grande experiment the density of muons cannot be detected in small radial ranges like for the electromagnetic component, so we have to introduce another observable of interest, N_{μ}^{40-700} , the integrated number of muons in the range of 40 m - 700 m. Our results indicate a $N_{\mu}^{40-700} - N_{ch}^{100-200}$ correlation as the possible correlation for mass discrimination in KASCADE-Grande observations, being analogue to $N_{\mu}^{tr} - N_e$ correlation for the KASCADE experiment [8].

Fig.2, the right panel, compares the $N_{\mu}^{40-700} - N_{ch}^{100-200}$ correlation for restricted energy ranges, selected energy ranges of the CORSIKA simulations.

Using non-parametric statistical analysis, the multidimensional observable distributions are studied by associating the single observed events to different classes and comparing the observed events with the model distributions (reference pattern) without using a pre-chosen parameterization. Applying this technique based on the

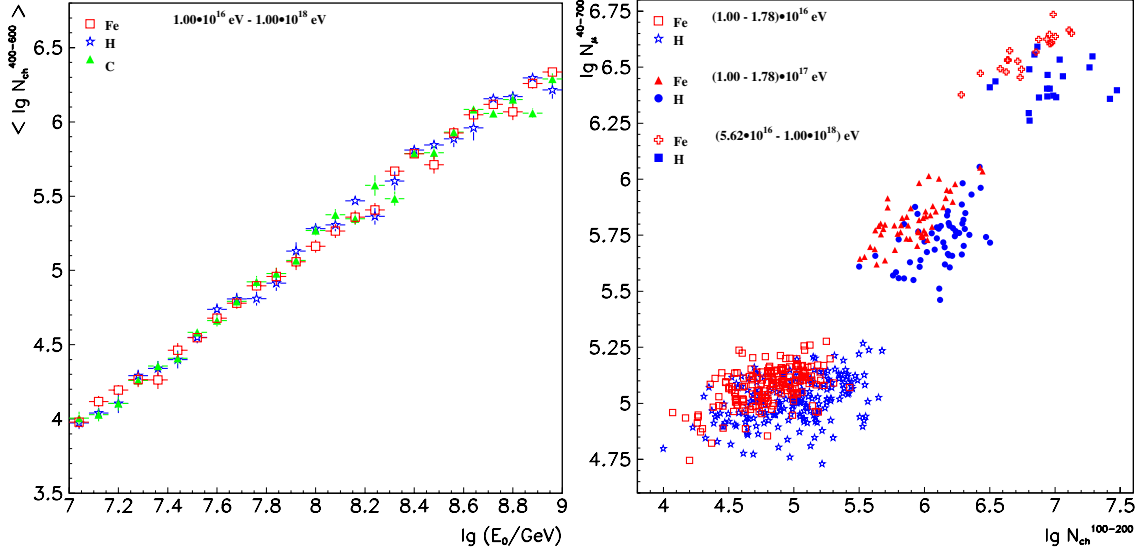


Figure 2. Left panel: The variation of average charged particle densities, $\langle \lg N_{ch}^{400-600} \rangle$ with $\lg E_0$ for H, C and Fe primaries with energies ($1.00 \cdot 10^{16} \text{ eV} - 1.00 \cdot 10^{18} \text{ eV}$). Right panel: The mean values of the $\lg N_{\mu}^{40-700} - \lg N_{ch}^{100-200}$ correlation for H, C and Fe primaries with energies ($1.00 \cdot 10^{16} \text{ eV} - 1.00 \cdot 10^{18} \text{ eV}$) for different energy ranges.

ANI code [12] (using the one-leave-out test to characterise the quality of the classification [13]), the discrimination of 3 classes of EAS primaries, H, C and Fe is represented by the degree of separation of multidimensional distributions. The procedure takes into account the EAS fluctuations and specifies the uncertainties by estimating the true classification and misclassification probabilities, based on Bayesian decision rule. Using a set of observables based on the basic $N_{\mu}^{40-700} - N_{ch}^{100-200}$ correlation, a good classification in 3 classes of primaries is obtained, being improved by adding the angle of incidence, Θ , to correct for the angular dependent attenuation of the N_{ch} parameters. Fig.3 presents the discriminative power by the classification probabilities of the $N_{\mu}^{40-700} - N_{ch}^{100-200} - \Theta$ correlation with higher incident energy.

4. Conclusions

The present studies are based on an event-by event analysis of EAS leading to the following concluding remarks:

- i). The reconstructed charged particle density in a range of distances of 500 m and 600 m could be used as good energy identifier for EAS observed with KASCADE-Grande array, indicating that the $\langle \lg N_{ch}^{400-600} \rangle$ observable can be suitable for energy estimation.
- ii). The reconstructed charged particle density at 100 m - 200 m exhibits features of mass discrimination in correlation with the number of muons, suggesting the $N_{\mu}^{40-700} - N_{ch}^{100-200}$ correlation as the relevant correlation for mass discrimination in KASCADE-Grande observations, being analogue to $N_{\mu}^{tr} - N_e$ correlation for the KASCADE experiment.
- iii). Using a non-parametric multidimensional statistical analysis with the ANI program, taking into consideration event-by-event showers, a set of three observables, $N_{\mu}^{40-700} - N_{ch}^{100-200} - \Theta$, leads for both cases, Linsley

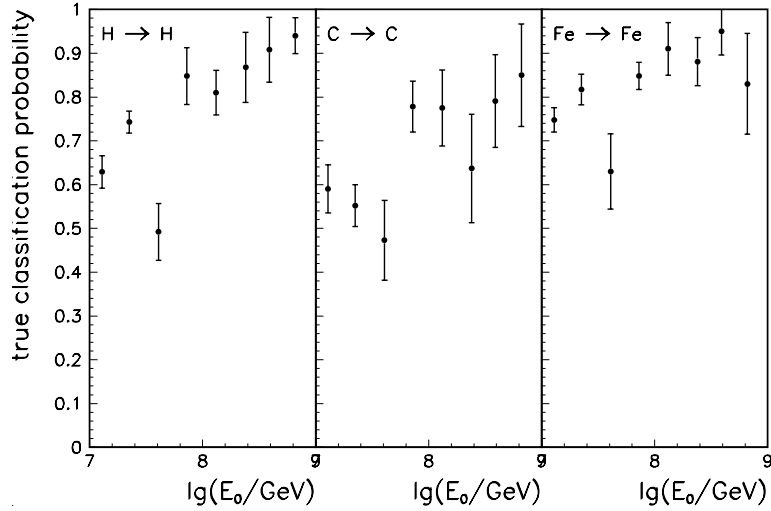


Figure 3. The energy variation of the true classification probabilities using the $\lg N_\mu^{40-700}$, $\lg N_{ch}^{100-200}$, and Θ observables as input in the non-parametric statistical analysis. The observable $N_{ch}^{100-200}$ is obtained using fits with the Linsley lateral distribution function.

and Lagutin fit, to a good classification in three classes of primaries, H, C and Fe. The studies will be continued in the future by applying the procedures described to the experimental data of KASCADE-Grande.

References

- [1] D. Heck et al., FZKA-Report 6019 Forschungszentrum Karlsruhe (1998)
- [2] N.N. Kalmykov and S.S. Ostapchenko, Phys. At. Nucl. 56 346 (1993)
- [3] A. Haungs et al., KASCADE-Grande collaboration, Proc.28th ICRC Tsukuba Japan vol.2, 985 (2003)
- [4] GEANT, Detector Description and Simulation Tool, CERN Program Library Long Writeup W5013, CERN (1993)
- [5] O. Sima et al., FZKA-Report 6985 Forschungszentrum Karlsruhe (2004)
- [6] J. Linsley et al., Journ. Phys. Soc. Japan 17 A-III (1962)
- [7] A. Lagutin et al, Nucl. Phys. B (Proc.Suppl.) 97 274 (2001)
- [8] H. Ulrich et al. - KASCADE collaboration, Proc. 29th ICRC Pune India, these proceedings
- [9] M. Hillas et al., Proc.12th ICRC Hobart Australia 3 1001 (1971)
- [10] M. Nagano et al., Astropart. Phys. 13 277 (2000)
- [11] T. Antoni et al. - KASCADE collaboration, Astropart. Phys. 14 245 (2001)
- [12] A. Chilingarian, G.Z. Zasian, Nuovo Cim. 14 355 (1991)
- [13] I. M. Brancus et al., J. Phys. G: Nucl. Part. Phys. 29 453 (2003)
- [14] I. M. Brancus et al., Astropart. Phys. 7 343 (1997)
- [15] T. Antoni et al. - KASCADE collaboration, Astropart. Phys. 18 319 (2003)

A self-triggered, high-resolution data acquisition system for the KASCADE-Grande experiment

M. Brüggemann^e, T. Antoni^a, W.D. Apel^b, F. Badea^{b,1}, K. Bekk^b, A. Bercuci^c, M. Bertaina^d, J. Blümer^{b,a}, H. Bozdog^b, I.M. Brancus^c, P. Buchholz^e, A. Chiavassa^d, K. Daumiller^b, F. Di Pierro^d, P. Doll^b, R. Engel^b, J. Engler^b, F. Feßler^b, P.L. Ghia^f, H.J. Gils^b, R. Glasstetter^g, C. Grupen^e, A. Haungs^b, D. Heck^b, J.R. Hörandel^a, K.-H. Kampert^g, H.O. Klages^b, Y. Kolotaev^e, G. Maier^{b,2}, H.J. Mathes^b, H.J. Mayer^b, J. Milke^b, B. Mitrica^c, C. Morello^f, M. Müller^b, G. Navarra^d, R. Obenland^b, J. Oehlschläger^b, S. Ostapchenko^{b,3}, S. Over^e, M. Petcu^c, T. Pierog^b, S. Plewnia^b, H. Rebel^b, A. Risse^h, M. Roth^a, H. Schieler^b, J. Scholz^b, O. Sima^c, M. Stümpert^a, G. Toma^c, G.C. Trinchero^f, H. Ulrich^b, S. Valchierotti^d, J. van Buren^b, W. Walkowiak^e, A. Weindl^b, J. Wochele^b, J. Zabierowski^h, S. Zagromski^b, D. Zimmermann^e

(a) Institut für Experimentelle Kernphysik, Universität Karlsruhe, 76021 Karlsruhe, Germany

(b) Institut für Kernphysik, Forschungszentrum Karlsruhe, 76021 Karlsruhe, Germany

(c) National Institute of Physics and Nuclear Engineering, 7690 Bucharest, Romania

(d) Dipartimento di Fisica Generale dell'Università, 10125 Torino, Italy

(e) Fachbereich Physik, Universität Siegen, 57068 Siegen, Germany

(f) Istituto di Fisica dello Spazio Interplanetario, INAF, 10133 Torino, Italy

(g) Fachbereich Physik, Universität Wuppertal, 42097 Wuppertal, Germany

(h) Soltan Institute for Nuclear Studies, 90950 Lodz, Poland

¹ on leave of absence from Nat. Inst. of Phys. and Nucl. Engineering, Bucharest, Romania

² now at University Leeds, LS2 9JT Leeds, United Kingdom

³ on leave of absence from Moscow State University, 119899 Moscow, Russia

Presenter: H. Rebel (Heinrich.Rebel@ik.fzk.de), ger-rebel-H-abs2-he15-poster

In order to achieve a measurable energy range of 10^{14} eV – 10^{18} eV for primary cosmic particles which includes the expected second knee, the detection area of the detector field array KASCADE has been extended from 0.04 km^2 to about 0.5 km^2 by an array of 37 scintillator stations, which form the Grande array. KASCADE and the Grande array take data in coincidence since December 2002 and allow a multiparameter measurement of extensive air showers up to above 10^{18} eV. The quality of the data will be improved by the usage of a new self-triggered, high-resolution data acquisition system based on signal digitization by FADCs and optical data transmission, which is unaffected by external noise.

1. Introduction

The FADC data acquisition system has two important features – it is self-triggering and dead-time free. These properties enable us to analyse air showers with higher resolution and allow to look for new time critical phenomena in the development of extensive air showers. While it is common for scintillation detectors to measure only one quantity – the overall energy deposited by cosmic particles passing the detector – the FADC system will provide additional time information by sampling the photomultiplier pulses. The complete signal shape can be analyzed later in full detail using offline reconstruction algorithms. Example applications are to resolve the internal structure of the shower disc based on the analysis of the signal variation with time and an improvement of the signal to noise ratio by noise reduction via digital filters.

2. The FADC system

The KASCADE-Grande FADC data acquisition system is a modular system comprising three custom made electronic parts. Digitizer boards, which sample the analog input signals from photomultipliers, form the first part of the system. Those boards are being installed in each detector station. The second part of the FADC system consists of receiver boards, which receive the digitized data transmitted by the digitizer boards of up to eight detector stations via an optical link. PCI interfaces connected to the receiver boards assure a fast data transmission rate to a PC farm and form the third part of the FADC system.

Digitizer board. The concept of signal treatment by the digitizer board is depicted in figure 1. On each board four FADCs per analog input channel running at 62.5 MHz with a 12-bit resolution are operated in interleaved mode with a displacement of 4 ns to reach an effective sampling frequency of 250 MHz. The FADCs are digitizing the signals permanently, while the data transmission is triggered by a comparator logic, which fires as soon as the input signal exceeds a programmable threshold. In case of a threshold transition, the digitizer board produces a data packet comprising a $1 \mu\text{s}$ long snapshots of the two input signals, timestamp information received from the experiment as well as the identification number of the detector station and transmits this data via an optical link to a receiver board. This process runs for each detector independent of other detectors which means that each detector runs self-triggered. For long signals, additional $1 \mu\text{s}$ sampling periods can be appended without gap to avoid dead-time.

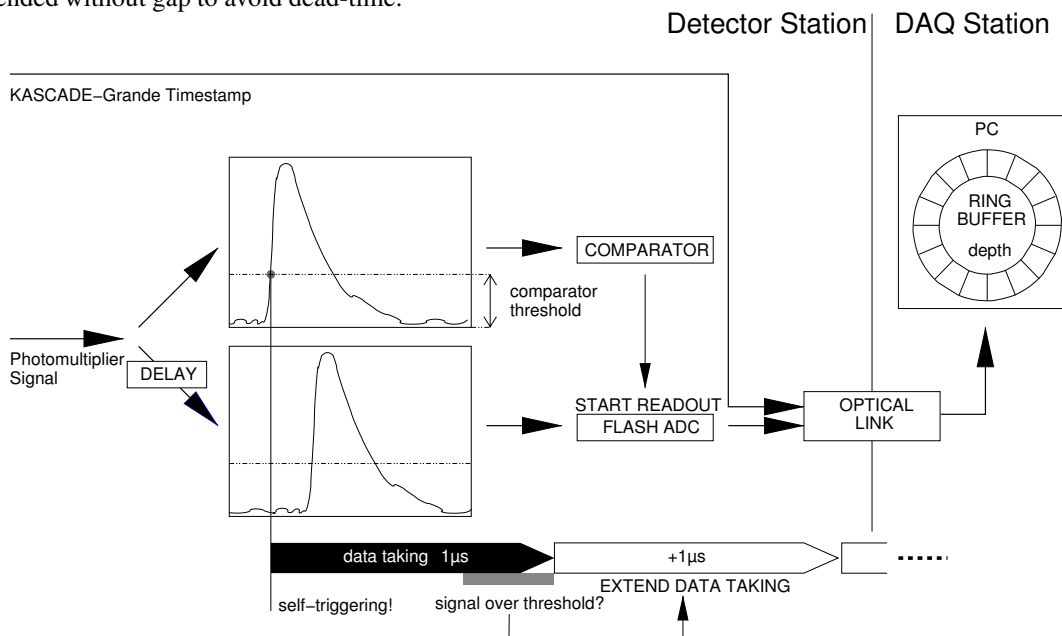


Figure 1. Concept of the FADC-based data acquisition system on the transmission side

Receiver board. The receiver board is a 9U VME board equipped with 8 optical links, which receive data packets from up to 8 digitizer boards. It derandomizes the data from the detector stations by the use of one FIFO per input channel, which can hold up to 16 data packets. The optical signals are converted into electrical signals and the data packets are then multiplexed to one common output buffer. Finally, the data is handed over to a PCI interface via a 32-bit wide LVDS link. The VME bus is used to configure the receiver board and allows hardware based debugging.

PCI-Interface. The PCI interface is the last stage of the FADC system. It consists of a commercial PCI prototyping board and a custom made piggy-back card and serves as the connection between the custom made electronics and a PC farm. It receives data from the receiver board and provides a fast data transfer rate into the memories of farm PCs via direct memory access (DMA). While the size of one data packet amounts to 1 KB, the rate of data packets to be transferred into the PC memories is given by the rate of uncorrelated particles passing the detector stations. The data acquisition system currently taking data measures a rate of 2.5 kHz for those particles. Taking this as a reference rate, each detector station provides a data rate of 2.5 MB/s. With 8 stations connected to a receiver board, the PCI interface has to provide an average transfer rate of at least 20 MB/s. Test measurements have shown that a maximum transfer rate of 85 MB/s can be reached.

Event building and data storage. All data packets transmitted by the digitizer boards are kept in the memory of the 5 farm PCs for approximately 40 s. A master PC looks for coincidences in the timestamp values of the data packets it receives from the farm PCs. Only those data packets are written to the mass storage which lie with a timestamp within a programmable time window around the coincidence. This reduces the amount of data to be stored permanently to approximately 100 kB/s. The path of the detector data after transmission by the digitizer boards onwards is shown in figure 2.

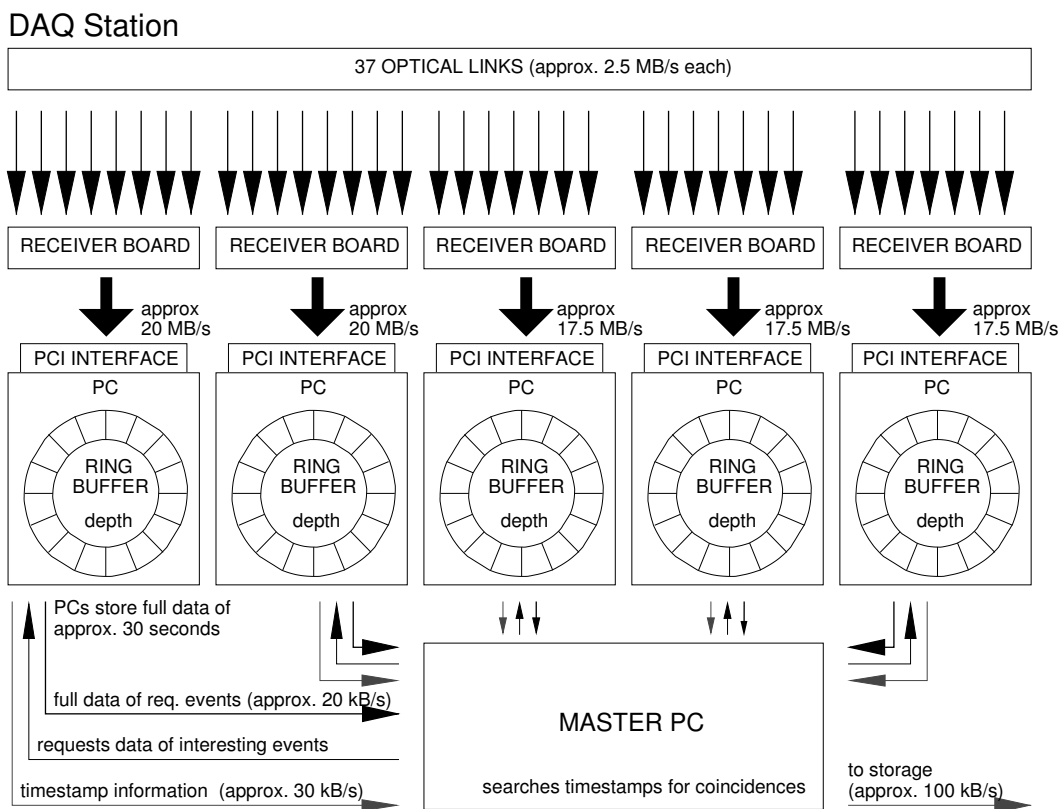


Figure 2. Data collection and event building on the receiving side

First data. After the installation of the first digitizer boards, the system has been tested by taking calibration spectra by measuring uncorrelated muons. Since the integral of the digitized signal shape is a measure for

the energy deposit in the detector, the integrals of these single particle events have been accumulated in the calibration spectrum depicted in figure 3. The upper part of the figure also shows a typical photomultiplier pulse shape of an uncorrelated particle recorded by the FADC system. To avoid that noise dominates the values of the integrals, the integration was constrained to the peak region indicated by the vertical dashed lines in the upper plot. The resulting calibration spectrum in the lower part of the figure was fitted with a parametrization

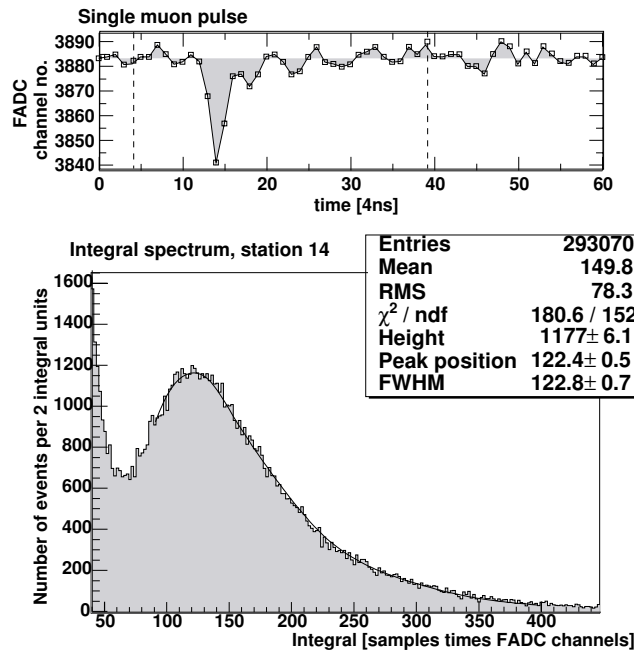


Figure 3. *Top:* Pulse shape of a single particle traversing the detector recorded by the FADC system. The limits of the constrained integration are indicated. *Bottom:* Calibration spectrum for station 14 resulting from constrained integration of single particle pulses.

of a simulated single muon spectrum, which is shown as smooth line. The peak position of the parametrization gives in integral units the most probable energy deposit of single muons passing the detector.

3. Status and Outlook

The FADC system is completely installed and currently being commissioned. As soon as the system is in full operation we look forward to take at least two years of high-quality data with the FADC system.

References

- [1] Antoni, T. et al. - KASCADE-Grande collaboration, 2003 *Nucl. Instrum. Meth.* **A513** 490-510
- [2] Haungs, A. et al. - KASCADE-Grande collaboration, 2003 *Proc. of 28th ICRC, Tsukuba, Japan* 985
- [3] Navarra, G. et al. - KASCADE-Grande collaboration, 2004 *Nucl. Instr. Meth.* **A518** 207
- [4] Walkowiak, W. et al. - KASCADE-Grande collaboration, *to be published in Trans. Nuc. Sci.*, (IEEE Nuclear Science Symposium 2004, Rome)

Hadrons in a calorimeter measured in air showers and at an accelerator

S. Plewnia^b, T. Antoni^a, W.D. Apel^b, F. Badea^{b,1}, K. Bekk^b, A. Bercuci^c, M. Bertaina^d, J. Blümer^{b,a}, H. Bozdog^b, I.M. Brancus^c, M. Brüggemann^e, P. Buchholz^e, A. Chiavassa^d, K. Daumiller^b, F. Di Pierro^d, P. Doll^b, R. Engel^b, J. Engler^b, F. Feßler^b, P.L. Ghia^f, H.J. Gils^b, R. Glasstetter^g, C. Grupen^e, A. Haungs^b, D. Heck^b, J.R. Hörandel^a, K.-H. Kampert^g, H.O. Klages^b, Y. Kolotaev^e, G. Maier^{b,2}, H.J. Mathes^b, H.J. Mayer^b, J. Milke^b, B. Mitrica^c, C. Morello^f, M. Müller^b, G. Navarra^d, R. Obenland^b, J. Oehlschläger^b, S. Ostapchenko^{b,3}, S. Over^e, M. Petcu^c, T. Pierog^b, H. Rebel^b, A. Risse^h, M. Roth^a, H. Schieler^b, J. Scholz^b, O. Sima^c, M. Stümpert^a, G. Toma^c, G.C. Trinchero^f, H. Ulrich^b, S. Valchierotti^d, J. van Buren^b, W. Walkowiak^e, A. Weindl^b, J. Wochele^b, J. Zabierowski^h, S. Zagromski^b, D. Zimmermann^e

(a) Institut für Experimentelle Kernphysik, Universität Karlsruhe, 76021 Karlsruhe, Germany

(b) Institut für Kernphysik, Forschungszentrum Karlsruhe, 76021 Karlsruhe, Germany

(c) National Institute of Physics and Nuclear Engineering, 7690 Bucharest, Romania

(d) Dipartimento di Fisica Generale dell'Università, 10125 Torino, Italy

(e) Fachbereich Physik, Universität Siegen, 57068 Siegen, Germany

(f) Istituto di Fisica dello Spazio Interplanetario, INAF, 10133 Torino, Italy

(g) Fachbereich Physik, Universität Wuppertal, 42097 Wuppertal, Germany

(h) Soltan Institute for Nuclear Studies, 90950 Lodz, Poland

¹ on leave of absence from Nat. Inst. of Phys. and Nucl. Engineering, Bucharest, Romania

² now at University Leeds, LS2 9JT Leeds, United Kingdom

³ on leave of absence from Moscow State University, 119899 Moscow, Russia

Presenter: H. Rebel (rebel@ik.fzk.de), ger-rebel-H-abs3-hel11-poster

Properties of hadronic cascades in a calorimeter are studied for two detectors, one exposed to hadrons up to 350 GeV at the CERN SPS accelerator, the second one, the hadron calorimeter of the KASCADE-Grande experiment registers cosmic-ray induced hadrons. The data obtained are compared to results of Monte Carlo simulations using the GEANT/FLUKA code.

1. Introduction

To measure properties of high-energy cosmic rays and to study the development of extensive air showers in the atmosphere the multi detector set-up KASCADE-Grande [1, 2] measures simultaneously the electromagnetic, muonic, and hadronic shower components. In particular, hadrons are measured by an iron sampling calorimeter [3] with the lateral dimensions $16 \times 20 \text{ m}^2$. It consists of 9 layers of liquid ionization chambers and a layer of plastic scintillation counters to provide fast trigger signals interspaced between a 4000 t iron absorber. A lead filter above the absorber serves to suppress the electromagnetic component of air showers. In total, 11 000 liquid ionization chambers are installed. Each chamber has the dimensions $50 \times 50 \times 1 \text{ cm}^3$ and contains four independent electronic channels. A feed-back preamplifier is mounted directly on the chamber in order to reduce noise pick-up. The detectors are filled with the room-temperature liquids tetramethylsilane (TMS, $\text{Si}(\text{CH}_3)_4$) or tetramethylpentane (TMP, C_9H_{20}).

With this detector the hadronic shower component is investigated in detail. Basis for these investigations is a precise energy calibration of the detector in a three step procedure [3]. First, an electronic calibration. Second, the conversion from the charge yield to deposited energy is derived from the signal of incident muons.

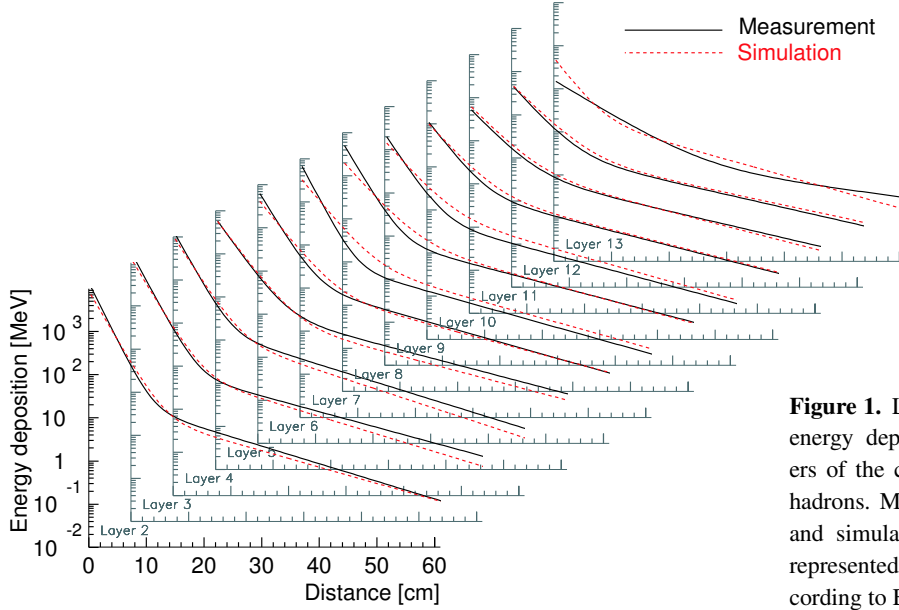


Figure 1. Lateral distribution of the energy deposition in different layers of the calorimeter for 300 GeV hadrons. Measurements (solid lines) and simulations (dashed lines) are represented by parameterizations according to Eq. (1).

Finally, the conversion from energy deposition to incident hadron energy is based on simulations of the detector response with the GEANT code [4] using FLUKA [5] to describe hadronic interactions.

For a direct verification of the calibration chain a test calorimeter with a set-up similar to the KASCADE calorimeter has been exposed to hadrons (pions and protons) up to 350 GeV at the CERN SPS accelerator [6]. It had the lateral dimensions $1 \times 1 \text{ m}^2$ and consisted of 15 layers of liquid ionization chambers. The first two were separated by a 5 cm lead filter, all subsequent layers by a 10 cm iron absorber, each. In the following some results of this calibration measurements are presented and the data are compared to air shower measurements with the KASCADE calorimeter.

2. Results

The lateral distribution of the energy in an hadronic cascade seems to consist of two components, a strongly collimated component at distances closer than 20 cm to the cascade axis and a more weakly attenuated component at larger distances, see [3]. Simulations show that the latter (flat component) consists of low-energy neutrons. In this work, two exponential functions are used to describe the energy density ρ_E as function of distance r to the center of the cascade

$$\rho_E(r) = C_1 \exp(-r/r_1) + C_2 \exp(-r/r_2). \quad (1)$$

A parameterization of measured data with this function is shown in Fig. 1 for different layers in the calorimeter for 300 GeV hadrons. The two components can easily be distinguished. As can be recognized from the figure, the energy distribution falls steeply as function of distance. Within the central 15 cm the energy density decreases by about three orders of magnitudes. Hence, for a fit of Eq. (1) to the data the integral over Eq. (1) has been calculated within the boundaries of each electronic channel ($25 \times 25 \text{ cm}^2$), the resulting functions are shown in the figure for measured and simulated data. The measurements show that the parameters r_1 and r_2 , the widths of the cascade, within the energy of the two components falls off by a factor of $1/e$, are almost independent of the energy of the incident particle. For the inner component r_1 increases approximately linearly

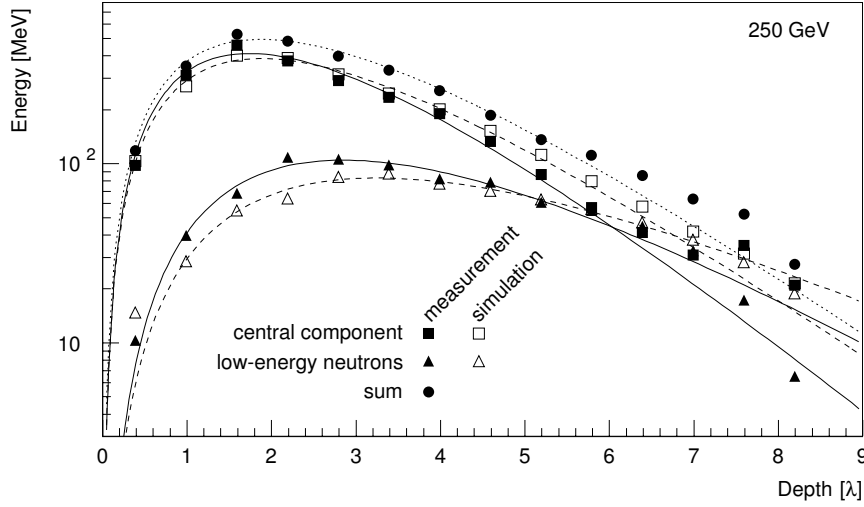


Figure 2. Longitudinal profile of the energy deposition for 250 GeV hadrons. The contributions of the central and the low-energy neutron components are shown separately. The accelerator data are compared to simulations using GEANT/FLUKA. The lines indicate fits to the data points according to Eq. (2).

as function of depth in the detector from 1.5 cm at a depth of $0.4 \lambda_i$ to about 2.5 cm at $7 \lambda_i$. A similar behavior is obtained for the outer (low-energy neutron) component, the values for r_2 increase from about 9 cm at $0.4 \lambda_i$ to almost 14 cm at $7 \lambda_i$. Overall, the simulated energy deposition agrees well with the measured data within the statistical uncertainties.

Integration of the curves in Fig. 1 gives the energy deposition in each layer. The longitudinal profiles of the energy deposition for the two components are shown in Fig. 2 for hadrons with an energy of 250 GeV. The longitudinal behavior is approximated by the function

$$E_{dep}(t) = A \cdot t^\mu \cdot \exp(t/\lambda_0), \quad (2)$$

where t is the depth in the absorber, λ_0 the attenuation length at large depths, μ characterizes the grow of the particle multiplicity in the cascade, and A is a normalization constant.

The inner component reaches its maximum at a depth of $1/(\mu\lambda_0) \approx 1.5 \lambda_i$. The low-energy neutrons penetrate deeper into the absorber and reach their cascade maximum at about $2.5 \lambda_i$. The exponential attenuation at large depths is for the low energy neutrons significantly weaker as compared to the central component. Due to this effect, the low energy neutron component, which is suppressed by about a factor of five in the region of the cascade maximum, equalizes with the central component at large depths (typically around $\sim 6 \lambda_i$). Also depicted are results from simulations using the GEANT/FLUKA codes. For the central component, the simulations follow the measurements up to about the maximum of the cascade and the exponential attenuation is less pronounced in the simulations. For the low-energy neutron component the simulated showers penetrate slightly deeper into the absorber and, in addition, the attenuation at large depths is weaker than for the measured cascades. The total energy deposition, obtained as sum of the two components, is shown in the figure as well.

An important check of the calibration procedure is the comparison of the data acquired at the accelerator compared to hadrons measured in air showers. A subset of hadrons has been selected from cosmic-ray induced events, namely unaccompanied or single hadrons. These are debris of small showers interacting at high altitudes. Most particles have been absorbed in the atmosphere and only one hadron has been reconstructed in the calorimeter. These hadrons should behave like artificially accelerated hadrons, but much higher energies are reached. For example, the most energetic single hadron detected so far at KASCADE-Grande has an energy of 67 TeV. The energy spectrum of these hadrons follows a power law [7]. Narrow intervals $\Delta \lg(E/\text{GeV}) = 0.1$ have been selected for a comparison with accelerator data at fixed energies.

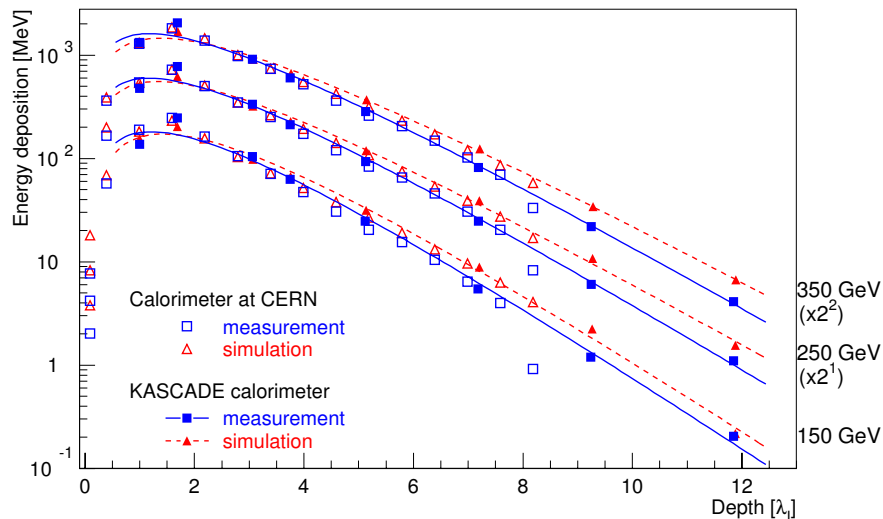


Figure 3. Longitudinal energy deposition in a calorimeter for hadrons with energies from 150 to 350 GeV. Measurements at an accelerator are compared to air shower data.

For these hadrons the longitudinal profiles of the energy deposition are compared to the results from the accelerator measurements in Fig. 3 for three different hadron energies. The different sampling structures of the two calorimeters can be noticed, the test calorimeter had a homogeneous sampling, while the absorber thickness increases as function of depth for the KASCADE calorimeter. The cascade development of the artificially accelerated and the cosmic-ray induced hadrons agrees very well. An important result, since this verifies the calibration chain applied for the air shower measurements.

The results of a GEANT/FLUKA detector simulation for both event classes are depicted in the figure as well. The two simulation sets agree well with each other. Nevertheless, a comparison to the measurements exhibits a difference at large depths. The attenuation of the simulated cascades beyond the maximum is weaker as compared to the measurements, a behavior already observed for the individual components in Fig. 2. For both, measurements and simulations, the position of the cascade maximum increases as function of energy by about $0.67 \lambda_i/\text{decade}$, but the maximum is shifted deeper into the absorber by about $0.1 \lambda_i$ for the simulations.

In **summary**, the accelerator measurements proof the validity of the calibration chain for the KASCADE-Grande hadron calorimeter and deficiencies in simulations of the cascades, as pointed out earlier [3], have been confirmed.

References

- [1] T. Antoni *et al.* (KASCADE Collaboration), *Nucl. Instr. & Meth. A* **513**, 490 (2003).
- [2] G. Navarra *et al.* (KASCADE-Grande Collaboration), *Nucl. Instr. & Meth. A* **518**, 207 (2004).
- [3] J. Engler *et al.*, *Nucl. Instr. & Meth. A* **427**, 528 (1999).
- [4] Geant 3.21 detector description and simulation tool, CERN Program Library Long Writeup W5013, CERN (1993).
- [5] P.A. Aarnio *et al.*, Fluka user's guide, Technical Report TIS-RP-190, CERN (1990).
- [6] S. Plewnia *et al.*, *Calorimetry in Particle Physics*, C. Cecchi, P. Cenci, P. Lubrano, M. Pepe (eds.), World Scientific (2005), p. 199.
- [7] T. Antoni *et al.* (KASCADE Collaboration), *Astrophys. J.* **612**, 914 (2004).

Investigation of Hadronic Interaction Models with the KASCADE-Grande Hadron Calorimeter

J. Milke^a, T. Antoni^b, W.D. Apel^a, F. Badea^{a,1}, K. Bekk^a, A. Bercuci^c, M. Bertaini^d, J. Blümer^{a,b}, H. Bozdog^a, I.M. Brancus^c, M. Brüggemann^e, P. Buchholz^e, A. Chiavassa^d, K. Daumiller^a, F. Di Pierro^d, P. Doll^a, R. Engel^a, J. Engler^a, F. Feßler^a, P.L. Ghia^f, H.J. Gils^a, R. Glasstetter^g, C. Grupen^e, A. Haungs^a, D. Heck^a, J.R. Hörandel^b, K.-H. Kampert^g, H.O. Klages^a, Y. Kolotaev^e, G. Maier^{a,2}, H.J. Mathes^a, H.J. Mayer^a, B. Mitrica^c, C. Morello^f, M. Müller^a, G. Navarra^d, R. Obenland^a, J. Oehlschläger^a, S. Ostapchenko^{a,3}, S. Over^e, M. Petcu^c, T. Pierog^a, S. Plewnia^a, H. Rebel^a, A. Risse^h, M. Roth^b, H. Schieler^a, J. Scholz^a, O. Sima^c, M. Stümpert^b, G. Toma^c, G.C. Trincherio^f, H. Ulrich^a, S. Valchierotti^d, J. van Buren^a, W. Walkowiak^e, A. Weindl^a, J. Wochele^a, J. Zabierowski^h, S. Zagromski^a, D. Zimmermann^e

(a) Institut für Kernphysik, Forschungszentrum Karlsruhe, 76021 Karlsruhe, Germany

(b) Institut für Experimentelle Kernphysik, Universität Karlsruhe, 76021 Karlsruhe, Germany

(c) National Institute of Physics and Nuclear Engineering, 7690 Bucharest, Romania

(d) Dipartimento di Fisica Generale dell'Università, 10125 Torino, Italy

(e) Fachbereich Physik, Universität Siegen, 57068 Siegen, Germany

(f) Istituto di Fisica dello Spazio Interplanetario, INAF, 10133 Torino, Italy

(g) Fachbereich Physik, Universität Wuppertal, 42097 Wuppertal, Germany

(h) Soltan Institute for Nuclear Studies, 90950 Lodz, Poland

(1) on leave of absence from Nat. Inst. of Phys. and Nucl. Engineering, Bucharest, Romania

(2) now at University Leeds, LS2 9JT Leeds, United Kingdom

(3) on leave of absence from Moscow State University, 119899 Moscow, Russia

Presenter: H. Ulrich (holger.ulrich@ik.fzk.de), ger-milke-J-abs1-he12-oral

The influence of hadronic interaction models on the simulation of extensive air showers has been studied using the correlation between the hadronic, electromagnetic, and muonic components of air showers measured with KASCADE. Both, high-energy (DPMJET, QGSJET, SIBYLL) and low-energy (GHEISHA, FLUKA) interaction models have been investigated.

1. Introduction

The interpretation of measurements of extensive air showers is usually based on the comparison with simulations of the shower development. Therefore, it is mandatory to check the reliability of the air shower simulations. This can be done by investigating the correlations between the hadronic, electromagnetic, and muonic components. The major uncertainty of the shower simulations is the description of the hadronic interactions. In the simulation program CORSIKA [1] different models are used for high-energy ($E_{\text{lab}} \gtrsim 100 \text{ GeV}$) and low-energy ($E_{\text{lab}} \lesssim 100 \text{ GeV}$) interactions. The high-energy model controls especially the first few interactions of an air shower and, therefore, the overall shower development. On the other side, most of the particles detected at ground level are produced in low-energy interactions.

In the energy range covered in this analysis ($5 \cdot 10^{14}$ – $5 \cdot 10^{16}$ eV) the composition of cosmic rays is not well known. Hence, in a first step proton and iron primary particles are taken as extreme assumptions. It is then checked, if the measurements are bracketed by this hypothesis. Another possibility is to assume in the

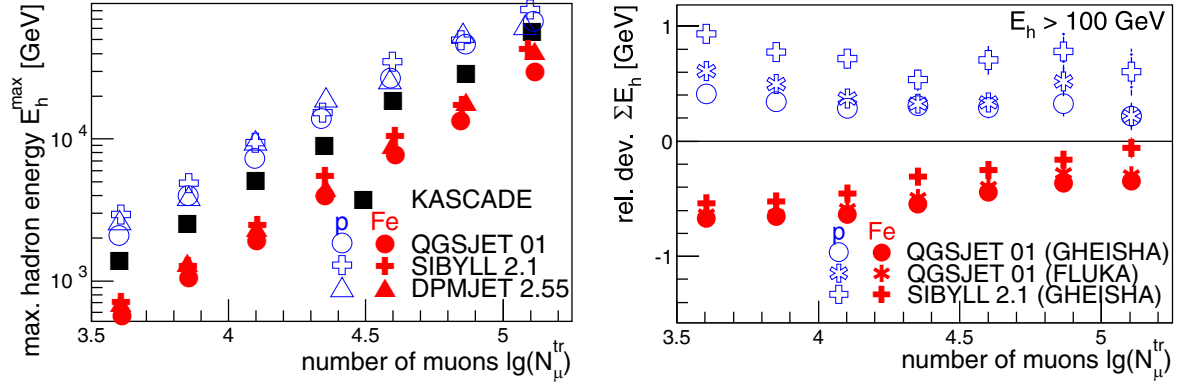


Figure 1. On the left hand side the correlations between the most energetic hadron E_h^{\max} and the number of muons N_μ^{tr} for 3 high-energy models are plotted (GHEISHA for low energies). The right panel shows the correlation between the hadronic energy sum ΣE_h and N_μ^{tr} for QGSJET combined with FLUKA and GHEISHA, as well as SIBYLL with GHEISHA. To make the small differences better visible, the relative deviations between simulation and measurement are plotted.

simulation a mass composition derived from the two-dimensional N_e - N_μ^{tr} -spectrum [2] and to examine, if the simulations are able to reproduce the hadronic observables.

2. Measurement and simulation

The air shower data analysed have been recorded by the multi detector setup KASCADE [3]. A $200 \times 200 \text{ m}^2$ array of 252 detector stations, equipped with scintillation counters, measures the electromagnetic and muonic parts of extensive air showers. They are used to determine the position and direction of the showers as well as the number of electrons (N_e) and muons (N_μ^{tr} , distance range 40–200 m). In the center of the detector array an iron sampling calorimeter (area $16 \times 20 \text{ m}^2$) detects hadrons. The calorimeter is equipped with 11 000 warm-liquid ionization chambers in nine layers [4]. Due to the fine segmentation ($25 \times 25 \text{ cm}^2$) energy, position, and angle of incidence can be measured for individual hadrons ($E_h > 50 \text{ GeV}$).

The air shower simulations have been performed using the program CORSIKA. For the description of the high-energy hadronic interactions the models DPMJET 2.55 [5], QGSJET 01 [6], and SIBYLL 2.1 [7] have been applied. GHEISHA ($E_{\text{lab}} \leq 80 \text{ GeV}$) [8] (with correction patches [9] which improve energy and momentum conservation) and FLUKA ($E_{\text{lab}} \leq 200 \text{ GeV}$) [10] have been used to check the influence of the low-energy model. The detector response has been determined by a detector simulation program based on GEANT 3 [11].

3. Results

3.1 Test with proton and iron as extrem assumption for the primary masses

In earlier investigations [12, 13, 14] it was found, that some of the hadronic interaction models failed to describe all aspects of the shower development simultaneously. For example, NEXUS 2 [15] could not describe the correlation between hadrons and electrons, while DPMJET 2.5 overestimated the number of hadrons and electrons in dependence of the number of muons. In the meantime new versions of the interaction models are available. The differences in the model predictions have become smaller and within the range given by proton and iron as primary particles the models DPMJET 2.55, QGSJET 01, and SIBYLL 2.1 are to a large

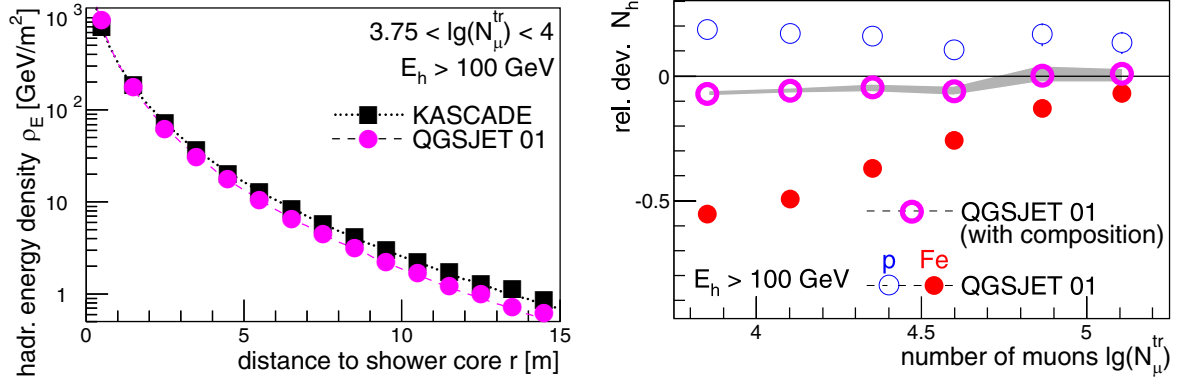


Figure 2. For the simulation using QGSJET/GHEISHA a mass composition has been assumed (see text). Shown are hadron lateral distributions (left hand side) and the correlation between hadron number N_h and muon number N_μ^{tr} (right hand side). The shaded band indicates the error caused by the statistical uncertainty of the assumed mass composition.

extent compatible with the measurements of the hadronic component and its correlation with electromagnetic and muonic particles. As example, on the left hand side of figure 1 the correlation between the most energetic hadron E_h^{max} and the number of muons N_μ^{tr} is shown.

The influence of the low-energy interaction model is demonstrated on the right hand side of figure 1. Shown are simulations using QGSJET as high-energy model and FLUKA and GHEISHA for low energies. The difference is caused by different number of muons predicted by the model combinations. Since FLUKA predicts fewer muons than GHEISHA, a higher primary energy is needed for the same muon number interval. Therefore, the hadronic energy sum is increased. Due to the energy threshold for the reconstructed hadrons of 100 GeV the hadronic component itself is not influenced by the low-energy model. In addition, results for a SIBYLL/GHEISHA simulation are plotted. It can be seen that the difference between the high-energy models is still larger than between different low-energy codes.

3.2 Assuming a composition in the simulations

For a more detailed test of the interaction models one has to assume a mass composition in the simulation to compare a single simulation curve with the measured distribution. This can be done consistently by taking a mass composition derived from other observables using the same combination of low-energy and high-energy models. In the following, compositions determined by an unfolding procedure of the two-dimensional $\lg N_e$ - $\lg N_\mu^{\text{tr}}$ spectrum [2] are used to check, if the models can describe the hadronic observables.

Results for the simulation using QGSJET/GHEISHA are shown in figure 2. On the left hand side an example for a lateral distribution of the hadrons is plotted. The model prediction is steeper than the measured distribution. The correlation between hadron number and muon number is plotted on the right hand side. For muon numbers $\lg N_\mu^{\text{tr}} < 4.7$ the simulation is rather below the measurement. This is compatible with a consistency check for the unfolding of the $\lg N_e$ - $\lg N_\mu^{\text{tr}}$ spectrum, which shows that QGSJET cannot describe the electron-muon data in this range consistently, while for larger muon numbers (respectively primary energies) the description becomes better. The situation for SIBYLL/GHEISHA is opposite. While for smaller primary energies the hadronic observables as well as the electron-muon data are reproduced rather well, there are discrepancies at larger muon numbers. The left panel of figure 3 shows a good agreement for measured and simulated hadron energy spectra. The correlation between the numbers of hadrons and muons (right hand side

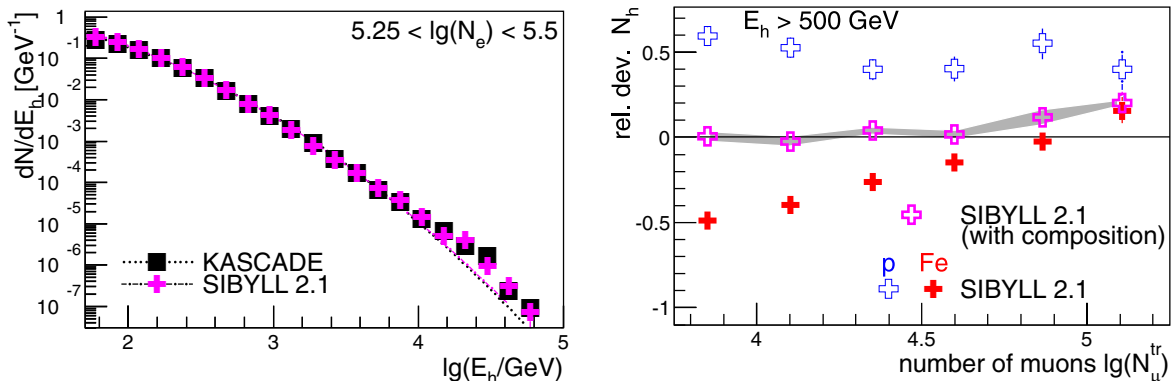


Figure 3. The left figure shows a hadron energy spectrum, the electron number interval corresponds to a primary energy around 3 PeV. On the right hand side the correlation of the number of hadrons above 500 GeV and the muon number N_{μ}^{tr} assuming a mass composition for the SIBYLL/GHEISHA simulation is plotted.

of figure 3) is well described by the model for small muon numbers, whereas with increasing muon number differences between simulation and measurement arise.

4. Conclusion

Although the differences between different high-energy hadronic interaction models have become smaller during the last years, there are still discrepancies, which influence the interpretation of extensive air shower measurements significantly. Also an influence of the low-energy model used is found, even though smaller than in case of the high-energy models. All models investigated so far are able to describe some aspects of the shower development, but for other shower correlations or in some energy ranges deficiencies are found.

References

- [1] D. Heck et al., Report **FZKA 6019** (1998), Forschungszentrum Karlsruhe.
- [2] T. Antoni et al. (KASCADE collaboration), *Astroparticle Physics* (in press), astro-ph/0505413.
- [3] T. Antoni et al. (KASCADE collaboration), *Nucl. Instr. Meth. A* **513** (2003) 490.
- [4] J. Engler et al., *Nucl. Instr. Meth. A* **427** (1999) 528.
- [5] J. Ranft, *Phys. Rev. D* **51** (1995) 64.
- [6] N.N. Kalmykov and S.S. Ostapchenko, *Phys. Atom. Nucl.* **56** (1993) 346.
- [7] R. Engel et al., *Proc. 26th ICRC, Salt Lake City* **1** (1999) 415.
- [8] H. Fesefeldt, Report **PITHA-85/02** (1985), RWTH Aachen.
- [9] R.E. Cassell and G. Bower (SLAC), private communication to D. Heck (2002).
- [10] A. Fassò et al., *FLUKA: Status and Prospective of Hadronic Applications*, Proc. Monte Carlo 2000 Conf., Lisbon, A. Kling et al. eds., Springer (Berlin) 955 (2001).
- [11] GEANT, Detector Description and Simulation Tool, CERN Program Library Long Writeup W5013, CERN (1993).
- [12] T. Antoni et al. (KASCADE collaboration), *J. Phys. G* **25** (1999) 2161.
- [13] T. Antoni et al. (KASCADE collaboration), *J. Phys. G* **27** (2001) 1785.
- [14] J. Milke et al. (KASCADE collaboration), *Nucl. Phys. B (Proc. Suppl.)* **122** (2003) 388; J. Milke et al. (KASCADE collaboration), *Proc. 27th Int. Cosmic Ray Conf., Hamburg* **1** (2001) 241.
- [15] H.J. Drescher et al., *Phys. Rep.* **350** (2001) 93.

The influence of properties of individual hadronic interactions on the development of extensive air showers

J.R. Hörandel^a, T. Antoni^a, W.D. Apel^b, F. Badea^{b,1}, K. Bekk^b, A. Bercuci^c, M. Bertaina^d, J. Blümer^{b,a}, H. Bozdog^b, I.M. Brancus^c, M. Brüggemann^e, P. Buchholz^e, A. Chiavassa^d, K. Daumiller^b, F. Di Pierro^d, P. Doll^b, R. Engel^b, J. Engler^b, F. Feßler^b, P.L. Ghia^f, H.J. Gils^b, R. Glasstetter^g, C. Grupen^e, A. Haungs^b, D. Heck^b, K.-H. Kampert^g, H.O. Klages^b, Y. Kolotaev^e, G. Maier^{b,2}, H.J. Mathes^b, H.J. Mayer^b, J. Milke^b, B. Mitrica^c, C. Morello^f, M. Müller^b, G. Navarra^d, R. Obenland^b, J. Oehlschläger^b, S. Ostapchenko^{b,3}, S. Over^e, M. Petcu^c, T. Pierog^b, S. Plewnia^b, H. Rebel^b, A. Risse^b, M. Roth^a, H. Schieler^b, J. Scholz^b, O. Sima^c, M. Stümpert^a, G. Toma^c, G.C. Trinchero^f, H. Ulrich^b, S. Valchierotti^d, J. van Buren^b, W. Walkowiak^e, A. Weindl^b, J. Wochele^b, J. Zabierowski^b, S. Zagromski^b, D. Zimmermann^e

(a) *Institut für Experimentelle Kernphysik, Universität Karlsruhe, 76021 Karlsruhe, Germany*

(b) *Institut für Kernphysik, Forschungszentrum Karlsruhe, 76021 Karlsruhe, Germany*

(c) *National Institute of Physics and Nuclear Engineering, 7690 Bucharest, Romania*

(d) *Dipartimento di Fisica Generale dell'Università, 10125 Torino, Italy*

(e) *Fachbereich Physik, Universität Siegen, 57068 Siegen, Germany*

(f) *Istituto di Fisica dello Spazio Interplanetario, INAF, 10133 Torino, Italy*

(g) *Fachbereich Physik, Universität Wuppertal, 42097 Wuppertal, Germany*

(h) *Soltan Institute for Nuclear Studies, 90950 Lodz, Poland*

(1) *on leave of absence from Nat. Inst. of Phys. and Nucl. Engineering, Bucharest, Romania*

(2) *now at University Leeds, LS2 9JT Leeds, United Kingdom*

(3) *on leave of absence from Moscow State University, 119899 Moscow, Russia*

Presenter: J.R. Hörandel (hoerandel@ik.fzk.de), ger-hoerandel-J-abs2-he12-oral

To study the effects of uncertainties in the description of individual hadronic interactions on the development of extensive air showers, simulations have been carried out with the CORSIKA program, using the interaction models QGSJET and FLUKA. Within the QGSJET code, inelastic cross sections and the inelasticity of hadronic interactions have been altered within the uncertainties given by accelerator measurements. The influence of these variations on shower observables is discussed. The predictions are compared to measurements of the electromagnetic, muonic, and hadronic shower components with the KASCADE-Grande experiment.

1. Introduction

The uncertainties in the simulation of extensive air showers in the atmosphere are dominated by the limited understanding of high-energy hadronic interactions. To evaluate the effect of uncertainties in the description of individual interactions on the development of air showers, the inelastic proton-proton cross section and the elasticity of interactions have been varied within the error bounds given by accelerator measurements [1]. For the studies parameters in the hadronic interaction model QGSJET 01 [2] have been modified.

The inelastic proton-proton cross section has been lowered from 57 mbarn to 51 mbarn at 10^6 GeV. In the model a change of the proton-proton cross section influences all other hadronic cross sections as well. For example, the proton-air cross section is changed from 385 mbarn to 364 mbarn at 10^6 GeV. The lower values are in good agreement with recent measurements from the HiRes experiment [3, 4]. The variation of QGSJET 01 is labeled model 3 in the following. Another parameter to describe the interactions is the elasticity, i.e. the ratio

of energy carried away by the most energetic secondary particle. For the modification with the reduced cross section (model 3) also the elasticity has been increased by about 10% – 15%, this variation is referred to as model 3a.

The influence of this changes on the integral multiplicity of high-energy muons and the average depth of the shower maximum have been described earlier [4]. In the present article the influence of the modifications on the electromagnetic, muonic, and hadronic shower components as measured by the KASCADE-Grande experiment are investigated.

Objective of the KASCADE-Grande experiment is the investigation of the origin of cosmic-rays in the energy range from several 10^{13} eV to 10^{18} eV [5, 6]. The three main components of air showers are detected simultaneously: The electromagnetic component is detected with a $200 \times 200 \text{ m}^2$ and a $700 \times 700 \text{ m}^2$ scintillator array. The energy, as well as point and angle of incidence for hadrons with energies $E_h > 50 \text{ GeV}$ are measured in a sampling calorimeter. Muons are registered with different thresholds in lead shielded detectors in the scintillator array ($E_\mu > 230 \text{ MeV}$), as well as in the calorimeter with a layer of scintillators ($E_\mu > 490 \text{ MeV}$) and below it with three layers of position sensitive detectors ($E_\mu > 2.4 \text{ GeV}$). In addition, high-energy muons are measured by an underground muon tracking detector equipped with limited streamer tubes ($E_\mu > 0.8 \text{ GeV}$).

To evaluate the impact of the modified parameters on the air shower development the simulation tool CORSIKA [7] is used. The electromagnetic component is modeled with the EGS4 code [8]. Hadronic interactions above 200 GeV are described with QGSJET 01 and with FLUKA [9] at lower energies. All particles reaching ground level are considered in a detector simulation program based on GEANT 3 [10].

2. Results

A lower cross section implies a longer mean free path for the hadrons in the atmosphere and thus a reduction of the number of interactions. A larger elasticity means that more energy is transferred to the leading particle. Both changes applied result in showers which penetrate deeper into the atmosphere. For example, the average depth of the shower maximum for protons at 100 PeV is shifted by 24 g/cm^2 due to the lower cross section and by 10 g/cm^2 due to the higher elasticity [1].

The shift of the shower maximum also affects the number of particles registered at ground level. Since the maximum moves closer to the observation level one expects an increase of the number of particles. However, reducing the number of interactions due to a lower cross section also reduces the possibility to produce secondary particles and an increase of the elasticity implies at the same time that less energy is available for multi-particle production. This means that we are faced with two competing processes influencing the number of particles observed.

The simulations reveal that an increase of the elasticity enhances the particle numbers for all species observed (electrons, muons, and hadrons). An increase is registered for both, primary protons and iron nuclei. This means the effect of deeper penetrating cascades seems to dominate. As an example, the increase of the number of muons when increasing the elasticity is illustrated in Fig. 1. Shown are the relative changes in the number of muons for model 3a relative to model 3 ($\delta N_\mu = (N_\mu^{3a} - N_\mu^3)/N_\mu^3$) for primary protons and iron induced showers as function of primary energy.

The increase of the number of muons N_μ as function of primary energy E_0 has been estimated using a Heitler model to be $N_\mu = (E_0/\xi_c^\pi)^\beta$, where $\xi_c^\pi \approx 20 \text{ GeV}$ is the critical energy for pions at which the probability for an interaction and decay are about equal [11]. The exponent β depends on the elasticity of the interaction as $\beta \approx 1 - 0.14(1 - \kappa)$. Using the energy dependence of κ for the two modifications of QGSJET [1] and introducing an energy dependent β , an increase of the number of muons as function of energy is expected as

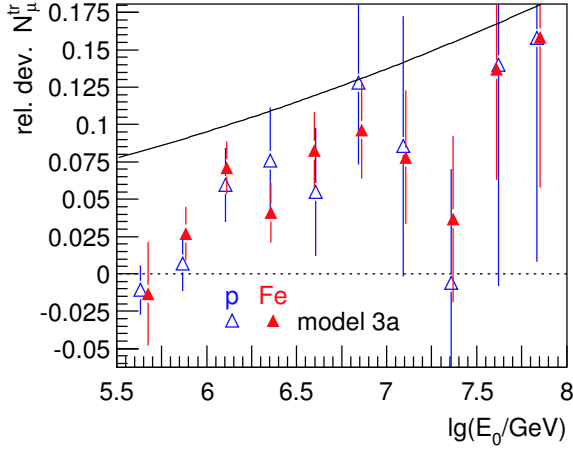


Figure 1. Relative deviation of the number of muons in model 3a relative to model 3, i.e. the change of the number of muons related to an increase of the elasticity as function of primary energy. The line indicates an estimate according to a simple Heitler model.

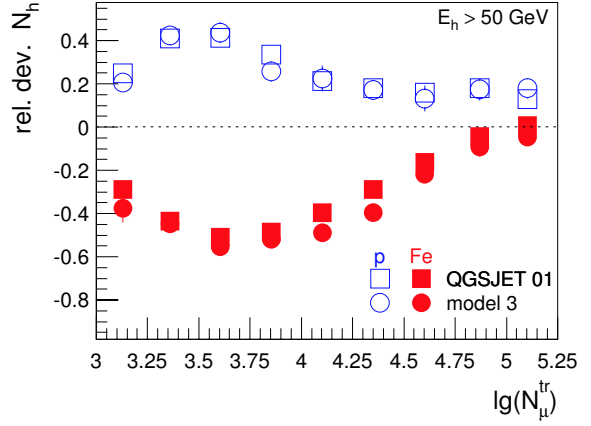


Figure 2. Relative deviation of the number of hadrons as predicted from the measured values as function of the number of muons. Predictions for primary protons and iron nuclei are shown for the original QGSJET and a variation with lower cross sections.

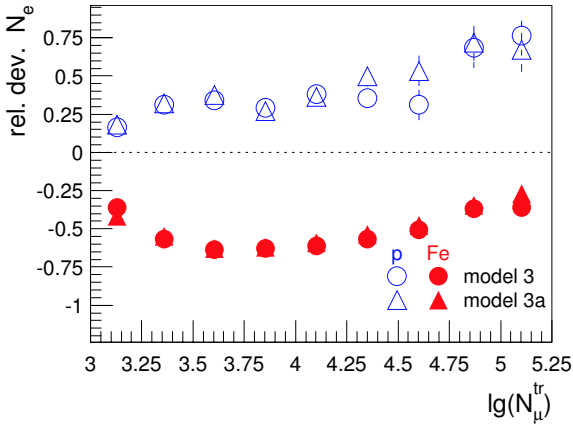


Figure 3. Relative deviation of the predicted number of electrons from the values measured by KASCADE as function of the number of muons. Shown are results for primary protons and iron nuclei for modification of QGSJET with lower inelastic cross sections (model 3) and increased elasticity (model 3a).

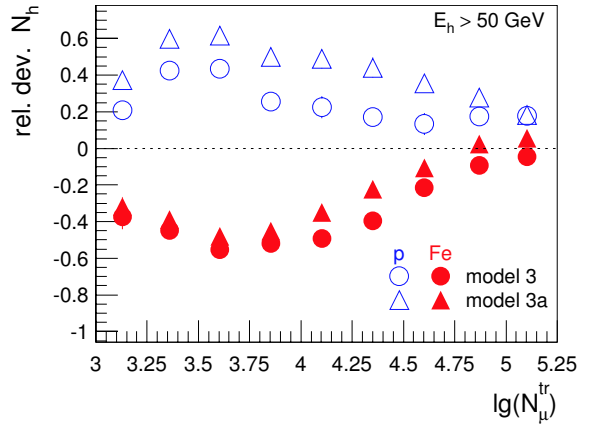


Figure 4. Relative deviation of the predicted number of hadrons from the values measured by KASCADE as function of the number of muons. Shown are results for primary protons and iron nuclei for modifications of QGSJET with lower inelastic cross sections (model 3) and increased elasticity (model 3a).

indicated by the line in Fig. 1. The general trend of the simple estimate is reflected by the detailed simulations, but the absolute values are about 5% larger for the simple estimate as compared to the full simulation.

In addition to the number of muons, also the number of electrons is increased in a similar way. This means that the data points are shifted in the N_e-N_μ plane parallel to the energy axis (i.e. along a diagonal) [12].

Consequently, there is no observable change when these quantities are reconstructed in an experiment. Fig. 3 shows the relative deviations of the predictions for proton and iron induced showers from the data measured with KASCADE-Grande as function of the number of muons. The two models shown differ in the elasticity of the hadronic interactions, but can not be distinguished in this observable. On the other hand, investigating the number of hadrons exhibits a clear difference in the order of 20% for primary protons. This is illustrated in Fig. 4, where the relative deviations of the predicted number of hadrons for two primary species from the measured data are shown. The change in the number of hadrons scales about linearly with the elasticity increase as has been seen in additional simulations assuming different values for the elasticity.

Turning to the alterations of the cross section the situation with the competing processes mentioned above becomes more complex. Reducing the cross section enhances the number of muons with energies above 230 GeV for both primary species, protons and iron nuclei. On the other hand, looking at the number of electrons and hadrons, their number increases for primary protons and decreases for iron nuclei. This behavior influences the correlation between the observed number of hadrons and the number of muons. The relative deviation of the number of hadrons predicted for two primary species from the measured values is depicted in Fig. 2 as function of the number of muons. Calculations with the original QGSJET code are compared to model 3. Due to the behavior of the individual shower components, as just described, the influence of the lower cross section is rather small for primary protons. On the other hand there is a clear and measurable difference in the order of $\sim 10\%$ for iron induced showers.

3. Conclusion

The effect of lower cross sections and higher elasticities for individual hadronic interactions on the air shower development has been investigated. It has been demonstrated that such variations yield significant differences in observable quantities, like the number of secondary particles at ground level. For a complete picture correlations between all shower components have to be analyzed. In particular, it is not sufficient to measure the correlation between the electromagnetic and muonic shower components only. Most directly the influence of properties of individual hadronic interactions can be measured investigating the hadronic air shower component and the average depth of the shower maximum.

References

- [1] J.R. Hörandel, *J. Phys. G: Nucl. Part. Phys.* **29**, 2439 (2002).
- [2] N.N. Kalmykov et al., *Nucl. Phys. B (Proc. Suppl.)* **52B**, 17 (1997).
- [3] K. Belov et al., *Nucl. Phys. B (Proc. Suppl.)* (Proc. 13th ISVHECRI) in press (2005).
- [4] J.R. Hörandel, *Nucl. Phys. B (Proc. Suppl.)* (Proc. 13th ISVHECRI) in press (2005).
- [5] T. Antoni et al. (KASCADE Collaboration), *Nucl. Instr. & Meth. A* **513**, 490 (2003).
- [6] G. Navarra et al. (KASCADE-Grande Collaboration), *Nucl. Instr. & Meth. A* **518**, 207 (2004).
- [7] D. Heck et al., Report FZKA 6019, Forschungszentrum Karlsruhe (1998).
- [8] W. Nelson et al., Report SLAC 265, Stanford Linear Accelerator Center (1985).
- [9] A. Fassò et al., *FLUKA: Status and Prospective of Hadronic Applications*, p. 955, Proc. Monte Carlo 2000 Conf., Lisbon, A. Kling, F. Barao, M. Nakagawa, P. Vaz eds., Springer (Berlin) (2001).
- [10] Geant 3.21 detector description and simulation tool, CERN Program Library Long Writeup W5013, CERN (1993).
- [11] J. Matthews, *Astropart. Phys.* **22**, 387 (2005).
- [12] J.R. Hörandel et al. (KASCADE-Grande Collaboration), *Nucl. Phys. B (Proc. Suppl.)* (Proc. 13th ISVHECRI) in press (2005).

Muon Density Measurements with KASCADE-Grande

A. Haungs^b, T. Antoni^a, W.D. Apel^b, F. Badea^{b,1}, K. Bekk^b, A. Bercuci^c, M. Bertaina^d, J. Blümer^{b,a}, H. Bozdog^b, I.M. Brancus^c, M. Brüggemann^e, P. Buchholz^e, A. Chiavassa^d, K. Daumiller^b, F. Di Pierro^d, P. Doll^b, R. Engel^b, J. Engler^b, F. Feßler^b, P.L. Ghia^f, H.J. Gils^b, R. Glasstetter^g, C. Grupen^e, D. Heck^b, J.R. Hörandel^a, K.-H. Kampert^g, H.O. Klages^b, Y. Kolotaev^e, G. Maier^{b,2}, H.J. Mathes^b, H.J. Mayer^b, J. Milke^b, B. Mitrica^c, C. Morello^f, M. Müller^b, G. Navarra^d, R. Obenland^b, J. Oehlschläger^b, S. Ostapchenko^{b,3}, S. Over^e, M. Petcu^c, T. Pierog^b, S. Plewnia^b, H. Rebel^b, A. Risse^h, M. Roth^a, H. Schieler^b, J. Scholz^b, O. Sima^c, M. Stümpert^a, G. Toma^c, G.C. Trincherio^f, H. Ulrich^b, S. Valchierotti^d, J. van Buren^b, W. Walkowiak^e, A. Weindl^b, J. Wochele^b, J. Zabierowski^h, S. Zagromski^b, D. Zimmermann^e

(a) Institut für Experimentelle Kernphysik, Universität Karlsruhe, 76021 Karlsruhe, Germany

(b) Institut für Kernphysik, Forschungszentrum Karlsruhe, 76021 Karlsruhe, Germany

(c) National Institute of Physics and Nuclear Engineering, 7690 Bucharest, Romania

(d) Dipartimento di Fisica Generale dell'Università, 10125 Torino, Italy

(e) Fachbereich Physik, Universität Siegen, 57068 Siegen, Germany

(f) Istituto di Fisica dello Spazio Interplanetario, INAF, 10133 Torino

(g) Fachbereich Physik, Universität Wuppertal, 42097 Wuppertal, Germany

(h) Soltan Institute for Nuclear Studies, 90950 Lodz, Poland

¹ on leave of absence from Nat. Inst. of Phys. and Nucl. Engineering, Bucharest, Romania

² now at University Leeds, LS2 9JT Leeds, United Kingdom

³ on leave of absence from Moscow State University, 119899 Moscow, Russia

Presenter: A. Haungs (haungs@ik.fzk.de), ger-haungs-A-abs1-he13-oral

KASCADE-Grande is a multi detector setup for the investigation of extensive air showers in the primary energy range of the knee including energies around the so-called second knee. Besides total number of electrons and muons the experiment measures local muon densities of air showers for different muon energy thresholds between 230 MeV and 2.4 GeV. These densities are reconstructed for showers in the primary energy range up to 1 EeV and in radial distances up to 700 m. Expectations of detailed Monte Carlo shower simulations based on various hadronic interaction models in the frame of the CORSIKA code are compared to the data and their validity is discussed. This allows a comprehensive test of the simulation procedures of the muon energy spectrum in the Monte Carlo codes.

1. Introduction

The validity of hadronic interaction models used as generators of Monte Carlo simulations is an important subject in context of EAS analyses. A co-operation between present and future accelerator experiments and the cosmic ray investigations is aspired for tests, but also by means of cosmic ray measurements there appear possibilities to probe the validity of the models [1]. In the present contribution we endeavor to analyze local muon densities in air showers in the primary energy range $10^{14} - 10^{18}$ eV for three different muon energy thresholds. Therewith, the consistency of the simulations with respect to the muon energy spectrum and systematic features of different Monte Carlo models can be revealed.

Analyzing KASCADE [2] data, local muon densities were used to reconstruct the primary energy spectrum of cosmic rays in the energy range of 1 to 10 PeV [3]. A systematic inconsistency was found by using two different

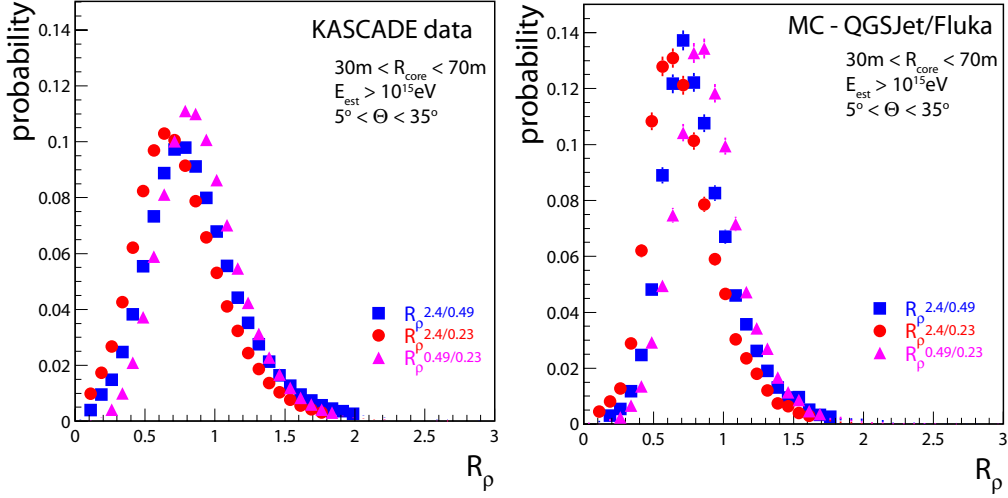


Figure 1. Examples of distributions of the ratio parameters R_ρ of local muon densities measured by KASCADE (left) and predictions by QGSJet/Fluka simulations.

muon thresholds for transforming the measured local muon density spectrum to the primary energy spectrum with help of Monte Carlo simulation procedures. To proceed a more direct comparison between measured and simulated data in respect to the muon energy spectrum, the ratio R_ρ of these local muon densities estimated on an event-by-event basis was used [4]. It was found, that there is a general disagreement between the predicted muon density ratio by different hadronic interaction models and the measurements.

With the extension of KASCADE to KASCADE-Grande [5] this kind of analysis can be continued and applied on data of higher primary energies and for larger core distances. This seems to be very important as simulations have shown, that at large distances from the shower core the muon generation is dominated by the low-energy hadronic interactions, whereas at small distances high-energy interactions are responsible [6]. This gives a handle to check the validity of high-energy and low-energy interaction models embedded in the CORSIKA [7] simulation program separately. Additionally, at KASCADE-Grande energies, systematic validity checks of the models are even more important, as no accelerator data will exist in next decades at energies above 100 PeV, but the models will be used for interpretations of the data of giant air-shower experiments.

2. Reconstruction of local muon density ratios

The local muon density of the EAS is measured for three muon energy thresholds by separate detector set-ups of KASCADE. Two of them are installed at the central detector which is placed in the geometrical center of the KASCADE detector array. A setup of 32 large multiwire proportional chambers (MWPC) is installed in the basement of the building and enables the estimation of the muon density $\rho_\mu^{2.40\text{GeV}}$ for each single EAS. The total absorber corresponds to a threshold for muons of 2.4 GeV kinetic energy. The second muon detection system is a layer of 456 plastic scintillation detectors in the third gap of the central detector, called trigger plane. Here the muon density $\rho_\mu^{0.49\text{GeV}}$ is estimated for muons with a threshold of 490 MeV for vertical incidence. The third local muon density is reconstructed with help of the KASCADE array data. 196 detector stations contain shielded plastic scintillators which are used to reconstruct the total muon number of the EAS by fitting the lateral distributions. For the present analyses this LDF is used to estimate the densities of muons at the

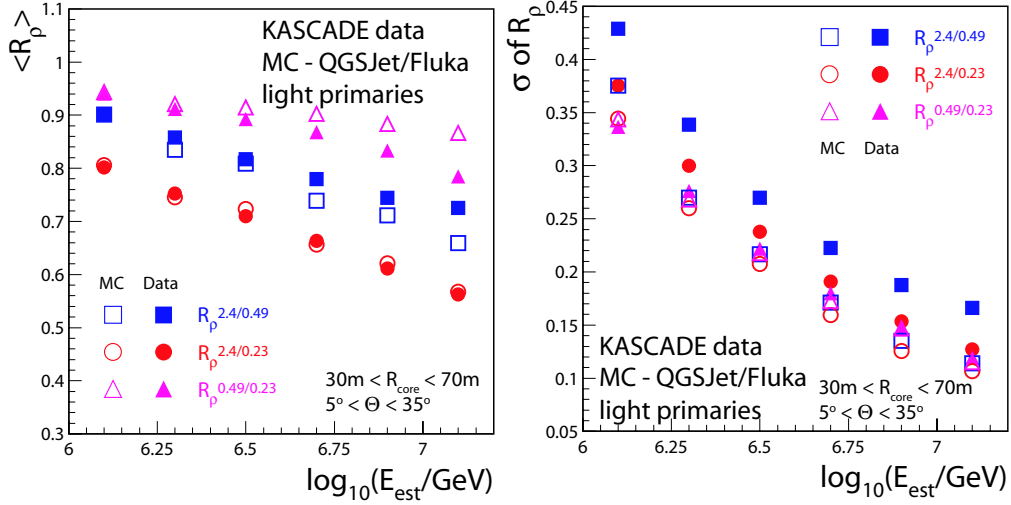


Figure 2. Mean and width of the muon density ratio distributions R_ρ vs. primary energy for measurements and simulations using QGSJet/Fluka.

place of the central detector ($\rho_\mu^{0.23\text{GeV}}$). Global shower parameters like core position, arrival direction, and primary energy are reconstructed with help of the KASCADE-Grande detector arrays. The primary energy is roughly estimated by a combination of reconstructed shower size determined by data of the KASCADE or the Grande array and the shower muon number determined by the KASCADE array muon detectors optimized by detailed shower simulations. The total sample of measured EAS is further divided in “electron-rich” and “electron-poor” showers performed by a cut along the ratio $\lg(N_\mu)/\lg(N_e)$, i.e. observables estimated by the arrays data only.

The ratios $R_p^{2.4/0.49} = \rho_\mu^{2.40\text{GeV}}/\rho_\mu^{0.49\text{GeV}}$, $R_p^{2.4/0.23} = \rho_\mu^{2.40\text{GeV}}/\rho_\mu^{0.23\text{GeV}}$, and $R_p^{0.49/0.23} = \rho_\mu^{0.49\text{GeV}}/\rho_\mu^{0.23\text{GeV}}$ are the relevant parameters for the present analyses. Due to the already available large data set measured by the original KASCADE experiment first the analyses will be concentrated to showers in the core distance of 30 – 70 m (inside KASCADE, but not disturbed by punch-through or trigger effects at the central detector), requiring primary energy above 10^{15} eV. But, the same analyses will be performed also for showers where the global parameters are estimated with help of the Grande array. Grande measures in coincidence with KASCADE since end of the year 2003. Fig. 1, left shows as example the measured distributions of the R_ρ parameters for the whole selected data set from KASCADE events.

3. Comparisons with simulations

A large set of CORSIKA simulations [7] have been performed using different interaction models, e.g. QGSJET (vers. of 1998 [8]) or SIBYLL (vers.2.1 [9]), for the high-energy interactions and GHEISHA [10] and Fluka [11] for low-energy interactions. Observation level, Earth’s magnetic field, and the particle thresholds are chosen in accordance with the experimental situation of KASCADE-Grande as well as the simulation of the detector responses. The simulations are performed for the zenith angular range $0^\circ - 42^\circ$ and for five primary masses: protons, helium, oxygen, silicon, and iron nuclei. The right part of Fig. 1 shows the predictions in the muon density ratios in the case of QGSJet/Fluka simulations, again with cuts applied for the case

of the KASCADE selection for a direct comparison with the measurements. Differences for various primaries (electron-rich EAS as predominantly induced by light ions and electron-poor EAS as predominantly induced by heavy ions) are found to be small compared to the width of the distributions. Beside the influence of the unknown composition of the primary cosmic rays, further possible uncertainties in the R_ρ parameters, like the unknown slope of the primary energy spectrum or effects of detector inefficiencies were investigated. Whereas varying the slopes of the simulations from -2.3 to -3.3 show no influence on the final distributions of the muon density ratios, efficiency effects of the detectors do so. The efficiencies are calculated for the individual detector components for each run using the shower data. Despite the fact, that the data are corrected for these effects, a remaining uncertainty of 5% in the R_ρ parameters have to be assumed regarding the following considerations.

Fig. 2 shows the dependence of the mean and fluctuations (width of distributions) of the three considered density ratios on the primary energy for data and predictions by the model combination QGSJET/Fluka analyzed by same procedures. The general behavior of decreasing mean and fluctuation with increasing energy is reproduced by the simulations, but a clear deviation on the mean values and on the amount of fluctuations is visible. QGSJET/Fluka are in agreement with the data for low energies and for the full energy range in the ratio $R_\rho^{2.4/0.23}$, which is not the case for other model combinations. For the other two ratio parameters $R_\rho^{2.4/0.49}$, $R_\rho^{0.49/0.23}$ and, especially for the amount on predicted fluctuations there is a general deviation from the data. Other interaction model combinations (e.g. Sibyll/GHEISHA) show a similar behavior, but the disagreement is smallest for the Fluka model.

At KASCADE-Grande [5] similar measurements can be performed for EAS of primary energies at least up to 10^{17} eV. The muon detection at the KASCADE central detector will then be possible for core distances of 50 – 550m with reasonable muon statistics. This test of the validity of the muon component will be of high relevance for the shower simulation procedures at ultra-high energies.

4. Acknowledgments

This work is partly supported by the DAAD-PPP grant (DAAD-PPP 323 Polen) and by a grant from Committee for Scientific Research (KBN) for 2004-2006.

References

- [1] A. Haungs et al. - KASCADE Collaboration, Nucl.Phys.B (Proc.Suppl.) (2005), in press, preprint astro-ph/0412610
- [2] T. Antoni et al. - KASCADE Collaboration, Nucl. Instr. Meth. A 513 (2003) 490
- [3] T. Antoni et al. - KASCADE Collaboration, Astropart.Phys. 16 (2002) 373
- [4] A. Haungs et al. - KASCADE-Grande Collaboration, Proc.28th ICRC (Tsukuba, Japan) 1 (2003) 37
- [5] A. Haungs et al. - KASCADE-Grande collaboration, Proc.28th ICRC (Tsukuba, Japan) 2 (2003) 985
- [6] J. Zabierowski et al.-KASCADE-Grande collaboration, Proc.29th ICRC (Pune, India), these proceedings
- [7] D. Heck et al., FZKA 6019, Forschungszentrum Karlsruhe 1998
- [8] N.N. Kalmykov and S.S. Ostapchenko, Yad. Fiz. 56 (1993) 105
- [9] R. Engel, Proc.26th ICRC (Salt Lake City, US) 1 (1999) 415
- [10] H. Fesefeldt, PITHA-85/02, RWTH Aachen 1985
- [11] A. Fassò et al., proc. Monte Carlo 2000 Conf., Lisbon, eds. A.Kling, F.Barao, M.Nakagawa, P.Vaz, Springer (Berlin) 955 (2001)

Analysis of Muon Production Heights using KASCADE parameters

R. Obenland^b, T. Antoni^a, W.D. Apel^b, F. Badea^{b,1}, K. Bekk^b, A. Bercuci^c, M. Bertaina^d, J. Blümer^{b,a}, H. Bozdog^b, I.M. Brancus^c, M. Brüggemann^e, P. Buchholz^e, A. Chiavassa^d, K. Daumiller^b, F. Di Pierro^d, P. Doll^b, R. Engel^b, J. Engler^b, F. Feßler^b, P.L. Ghia^f, H.J. Gils^b, R. Glasstetter^g, C. Grupen^e, A. Haungs^b, D. Heck^b, J.R. Hörandel^a, K.-H. Kampert^g, H.O. Klages^b, Y. Kolotaev^e, G. Maier^{b,2}, H.J. Mathes^b, H.J. Mayer^b, J. Milke^b, B. Mitrica^c, C. Morello^f, M. Müller^b, G. Navarra^d, J. Oehlschläger^b, S. Ostapchenko^{b,3}, S. Over^e, M. Petcu^c, T. Pierog^b, S. Plewnia^b, H. Rebel^b, A. Risse^h, M. Roth^a, H. Schieler^b, J. Scholz^b, O. Sima^c, M. Stümpert^a, G. Toma^c, G.C. Trincherio^f, H. Ulrich^b, S. Valchierotti^d, J. van Buren^b, W. Walkowiak^e, A. Weindl^b, J. Wochele^b, J. Zabierowski^h, S. Zagromski^b, D. Zimmermann^e

(a) Institut für Experimentelle Kernphysik, Universität Karlsruhe, 76021 Karlsruhe, Germany

(b) Institut für Kernphysik, Forschungszentrum Karlsruhe, 76021 Karlsruhe, Germany

(c) National Institute of Physics and Nuclear Engineering, 7690 Bucharest, Romania

(d) Dipartimento di Fisica Generale dell'Università, 10125 Torino, Italy

(e) Fachbereich Physik, Universität Siegen, 57068 Siegen, Germany

(f) Istituto di Fisica dello Spazio Interplanetario, INAF, 10133 Torino, Italy

(g) Fachbereich Physik, Universität Wuppertal, 42097 Wuppertal, Germany

(h) Soltan Institute for Nuclear Studies, 90950 Lodz, Poland

¹ on leave of absence from Nat. Inst. of Phys. and Nucl. Engineering, Bucharest, Romania

² now at University Leeds, LS2 9JT Leeds, United Kingdom

³ on leave of absence from Moscow State University, 119899 Moscow, Russia

Presenter: J. Zabierowski (janzab@zpk.u.lodz.pl), pol-zabierowski-J-abs2-he12-poster

The Muon Tracking Detector (MTD; $E_{\mu}^{th}=0.8$ GeV, $128m^2$) [1] of the KASCADE-Grande experiment [2] enables the analysis of the longitudinal shower development by means of the Muon Production Height (MPH). The analysis employs radial and tangential angles of the muon track with respect to the shower direction and in addition the distance of the muon hit to the shower core. Dividing the air shower data into heavy and light primary enriched samples, by means of $\lg(N_{\mu}^0)/\lg(N_e^0)$ ratio, a clear sensitivity of the MTD parameters to the mass of the primary particle has been observed.

1. Efficiency and Data Selection

To describe the orientation of muon tracks with respect to the shower axis, radial and tangential angles are used [3]. Both angles are studied with respect to $\lg(N_{\mu}^{tr})$ which corresponds to the total number of muons that are within 40-200m of the KASCADE array and which represents [4] an approximate energy estimator of the primary cosmic ray particles. In the present analysis a consistency check between the array data and the MTD data is performed.

The simulated detection efficiencies for the KASCADE array for proton and iron primaries is shown in the left part of Fig.1 as solid symbols. Also included in Fig.1 is the efficiency of having at least one muon track in the MTD (> 40m from shower core, open symbols). Iron showers which are richer in muons are having a larger probability already at the threshold of the KASCADE array but proton showers are not fully measured even above $\lg(N_e) > 4.8$ (arrow) where usually the KASCADE array analysis starts.

The right side of Fig.1 shows the mean $\lg(N_{\mu}^0)/\lg(N_e^0)$ ratio which turned out [4] to be a good mass discrim-

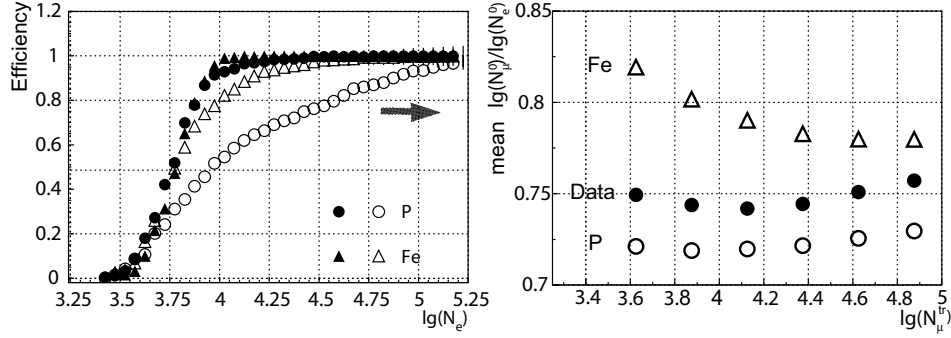


Figure 1. Simulated efficiencies of the KASCADE array (full symbols) and the MTD (open symbols) (left panel). Simulated $\lg(N_\mu^0)/\lg(N_e^0)$ ratios compared to data (right panel).

ination parameter. The $\lg(N_\mu^0)$, $\lg(N_e^0)$ numbers are the shower angle (Θ_s) and attenuation lengths (λ_e , λ_μ) corrected [5] original $\lg(N_\mu^{tr})$, $\lg(N_e)$ numbers. Such presentation was employed in the past [4] to deduce the relative weights of light and heavy cosmic ray primaries. In Fig.1 (right panel) iron (Fe) exhibits strongest dependence on shower energy, because of strong dependence of electron longitudinal shower development. The simulations involved in Fig.1 are based on the CORSIKA [6] program version 6.156 with QGSJet01. Selecting the shower data ($\Theta_s < 30^\circ$) according to the $\lg(N_\mu^0)/\lg(N_e^0)$ ratio being larger (electron poor) or smaller (electron rich) than 0.74, heavy or light cosmic ray primaries are chosen, respectively. Choosing e.g. a ratio of 0.75 would provide a larger fraction of light primaries.

2. Mean Radial Angles and Muon Production Heights

Mean radial angles have been calculated between $0^\circ - 6^\circ$ and derived as function of $\lg(N_\mu^{tr})$ in different distance bins with respect to the shower core. In Fig.2 we concentrate on distance values between the muon hit and the shower core from 80-120m. The mean radial angles exhibit a clear dependence on the shower energy and on light and heavy enriched shower samples. This observation provides an interesting aspect with respect to even larger shower energies and core distances in the upcoming KASCADE-Grande data analysis. Extending the distance range helps in getting more abundantly larger radial angles and, therefore, testing lower muon pseudorapidities [7]. The band around the light or heavy data points corresponds to a variation of the ratio cut from 0.73 (large $\langle \rho \rangle$) to 0.75 (small $\langle \rho \rangle$). Selecting in future analysis different muon multiplicities in the MTD may help to improve the discrimination between light and heavy primaries.

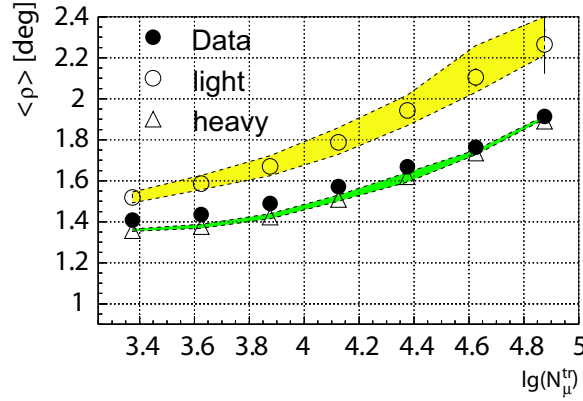


Figure 2. Mean radial angles $\langle \rho \rangle$ and their dependence on $\lg(N_\mu^{tr})$ for 80-120m core distance. Note bias of full 'Data' towards heavy primaries.

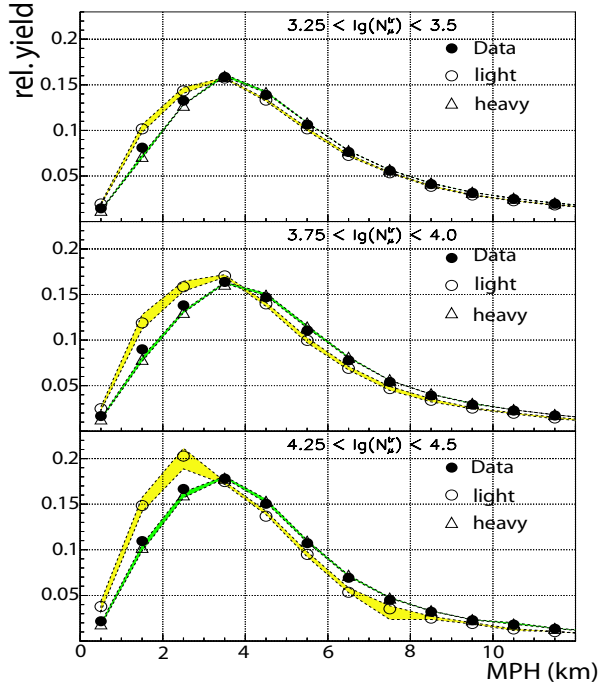


Figure 3. Muon production height distributions for full data together with light and heavy data subsamples.

In Fig.3 MPH distributions along the shower axis are shown for 80-120m muon distance range to the shower core. With increasing primary energy $\lg(N_\mu^{tr})$ comparatively more muons stem from lower production heights.

We observe from Fig.1 (left) for $\lg(N_e) > 4.8$ due to the comparatively reduced efficiency for proton showers, that the full data lie closer to the heavy enriched part of the data. Therefore, our data exhibit an over-representation of heavy showers. Application of an efficiency correction may move the data for small $\lg(N_\mu^{tr})$ towards the light enriched data and hence providing a more pronounced trend towards heavy primaries with increasing shower energy. This correction will be investigated in an ongoing analysis.

The MPH is calculated by triangulation employing the radial angles and the distance of the muon hit to the shower core. Applying a tangential angle cut by excluding the tails above 0.7° one enriches data sample with higher energy muons. Again, light and heavy data subsamples were created, in a similar way as for $\langle \rho \rangle$, based on a $\lg(N_\mu^0)/\lg(N_e^0)$ ratio boundary value 0.74.

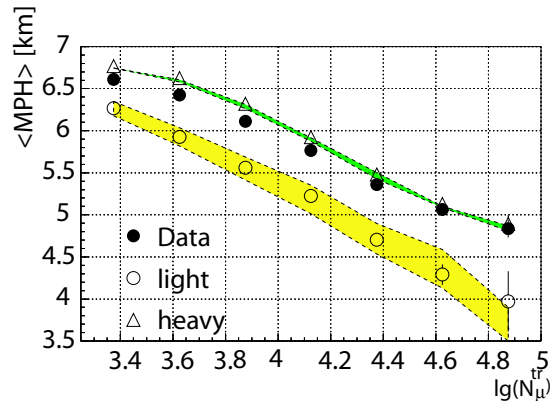


Figure 4. Mean muon production heights $\langle MPH \rangle$ and their dependence on $lg(N_{\mu}^{tr})$ for 80-120m core distance. Note bias of full 'Data' towards heavy primaries.

Selecting in future analysis different muon multiplicities in the MTD may provide more detailed information on longitudinal shower development. In Fig.4 the mean MPH values (calculated between 0-15km) a clear distinction between light and heavy enriched data samples is observed which is of similar size as known from simulations. The bias towards heavier composition at lower primary energies, resulting from the efficiency discussed above, is also present here. Having this in mind one can notice the clear trend towards heavier composition with increasing primary energy also in this analysis. Moving to larger distances in KASCADE-Grande, as shown in [7], will improve the accuracy of MPH analysis.

3. Conclusion

The mean radial angle and mean MPH analysed with the experimental data alone show the trend towards heavier primary composition with the increase of the energy in the “knee” region of the primary spectrum. Extending the analysis to KASCADE-Grande showers and to even larger shower energies enables the continuation of this type of analysis with respect to an expected change above a conjectured iron knee.

4. Acknowledgements

The support by DAAD-PPP grant (DAAD 323-bis PPP Polen) and by grant from Committee for Scientific Research (KBN) for 2004-2006 is kindly acknowledged by Polish group.

1. Doll P. et al. Nucl. Instr. Meth. **A488**(2002)517
2. Badea F. et al., Nucl.Phys.B(Proc.Suppl.)136(2004)384
3. Büttner C. et al., Proc. 28th ICRC, Tsukuba, 33, 2003
4. Weber J.H. et al. Proc. 25th ICRC, Durban, Vol. 6, p. 153, 1997
5. Antoni T. et al. Astroparticle Phys. 19 (2003) 703
6. Heck D. et al. FZKA 6019, Forschungszentrum Karlsruhe (1998)
7. Zabierowski J. et al. Proc. 29th ICRC, Pune, these proceedings

Muon Tracking In KASCADE-Grande: CORSIKA Simulation Study

J. Zabierowski^a, T. Antoni^b, W.D. Apel^c, F. Badea^{c,1}, K. Bekk^c, A. Bercuci^d, M. Bertaina^e, J. Blümer^{c,b}, H. Bozdog^c, I.M. Brancus^d, M. Brüggemann^f, P. Buchholz^f, A. Chiavassa^e, K. Daumiller^c, F. Di Pierro^e, P. Doll^c, R. Engel^c, J. Engler^c, F. Feßler^c, P.L. Ghia^g, H.J. Gils^c, R. Glasstetter^h, C. Grupen^f, A. Haungs^c, D. Heck^c, J.R. Hörandel^b, K.-H. Kampert^h, H.O. Klages^c, Y. Kolotaev^f, G. Maier^{c,2}, H.J. Mathes^c, H.J. Mayer^c, J. Milke^c, B. Mitrica^d, C. Morello^g, M. Müller^c, G. Navarra^e, R. Obenland^c, J. Oehlschläger^c, S. Ostapchenko^{c,3}, S. Over^f, M. Petcu^d, T. Pierog^c, S. Plewnia^c, H. Rebel^c, A. Risse^a, M. Roth^b, H. Schieler^c, J. Scholz^c, O. Sima^d, M. Stümpert^b, G. Toma^d, G.C. Trinchero^g, H. Ulrich^c, S. Valchierotti^e, J. van Buren^c, W. Walkowiak^f, A. Weindl^c, J. Wochele^c, S. Zagromski^c, D. Zimmermann^f

(a) *Soltan Institute for Nuclear Studies, 90950 Lodz, Poland*

(b) *Institut für Experimentelle Kernphysik, Universität Karlsruhe, 76021 Karlsruhe, Germany*

(c) *Institut für Kernphysik, Forschungszentrum Karlsruhe, 76021 Karlsruhe, Germany*

(d) *National Institute of Physics and Nuclear Engineering, 7690 Bucharest, Romania*

(e) *Dipartimento di Fisica Generale dell'Università, 10125 Torino, Italy*

(f) *Fachbereich Physik, Universität Siegen, 57068 Siegen, Germany*

(g) *Istituto di Fisica dello Spazio Interplanetario, INAF, 10133 Torino, Italy*

(h) *Fachbereich Physik, Universität Wuppertal, 42097 Wuppertal, Germany*

¹ *on leave of absence from Nat. Inst. of Phys. and Nucl. Engineering, Bucharest, Romania*

² *now at University Leeds, LS2 9JT Leeds, United Kingdom*

³ *on leave of absence from Moscow State University, 119899 Moscow, Russia*

Presenter: J. Zabierowski (janzab@zpk.u.lodz.pl), pol-zabierowski-J-abs1-he13-poster

The use of Muon Tracking Detector of KASCADE EAS experiment in the KASCADE-Grande setup is analyzed. By means of Monte Carlo simulations done with modified CORSIKA code benefits and new possibilities are shown when tracking muons arriving up to 700 m from the shower core comparing to 160 m maximum distance available in KASCADE.

1. Introduction

The Muon Tracking Detector (MTD; $E_{\mu}^{th}=0.8$ GeV, area= $128m^2$) [1] in KASCADE-Grande EAS experiment [2] allows precise measurement of muon directions in air showers. This information has been used to investigate mean muon production heights (primary mass sensitive parameter) [3] as well as muon pseudorapidities and momenta [4]. The latter, being highly correlated with pseudorapidities and momenta of parent hadrons, are very good probe of high-energy hadronic interactions and thus serve as a tool to test and improve existing hadronic interaction models. In the KASCADE-Grande experimental setup muons arriving up to 700 m from the shower core can be tracked, comparing to 160 m maximum distance available in KASCADE. The experiment layout is shown in Fig. 1 where the distance relations can be seen. The CORSIKA [5] Monte Carlo simulations with the QGSJET and GHEISHA hadronic interaction models were used to show how the increase in this distance influences the measured distributions of various quantities characterizing muons. A special version of CORSIKA code has been used, which allowed to get not only information on muons at the detection level but also on their “mother” and “grandmother” hadrons. For the analysis large statistics of muons was simulated ($\approx 1.8 \times 10^7$) for proton and iron primaries with $10^{16}eV$ primary energy. With this Monte Carlo

data muon pseudorapidity and muon production heights distributions were analysed. Only muons with energy above 1 GeV (MTD threshold) were considered.

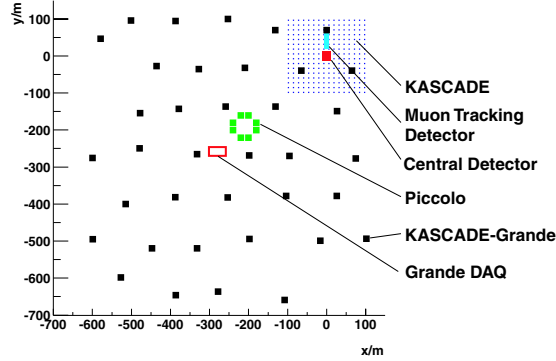


Figure 1. Layout of KASCADE-Grande experiment. Note the location of Muon Tracking Detector.

2. Muon pseudorapidity distributions in EAS - investigation of hadronic interactions

Using angular information about muon directions with respect to the direction of the shower it is possible to calculate the pseudorapidity of registered muons in the shower coordinates, where the vertical axis coincides with the axis of the shower [6]. Investigation of pseudorapidity distribution of EAS muons on ground is of interest because its shape nearly exactly follows the shape of pseudorapidity of their parent hadrons (Fig. 2 - left panel). One gets this way an inside look into VHE hadronic interaction in the forward kinematical region.

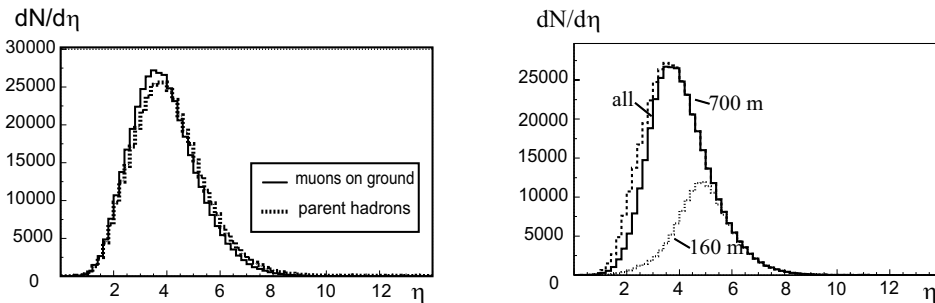


Figure 2. Pseudorapidity distributions for EAS muons. Comparison with the pseudorapidity of parent hadrons (left) and influence of the collecting distance to the core (right).

The right panel of Fig. 2 shows the influence of the experimental conditions, namely distance from the shower core at which one can track muons, on the shape of pseudorapidity distribution. It is seen that in KASCADE-Grande conditions (tracking up to 700 m) one obtains nearly true pseudorapidity distribution of all muons created in a shower which survived to the observation level. In KASCADE, where tracking is possible maximum to 160 m, the obtained distribution contains only a small fraction of all muons, where muons below $\eta = 4$ are nearly absent. As seen from Fig. 3 only in KASCADE-Grande one collects 90% of muons having parent hadrons of energy > 80 GeV and 75% of those with parent hadron energy < 80 GeV. So, high- and low-energy interaction model tests with muon pseudorapidity are possible rather only there.

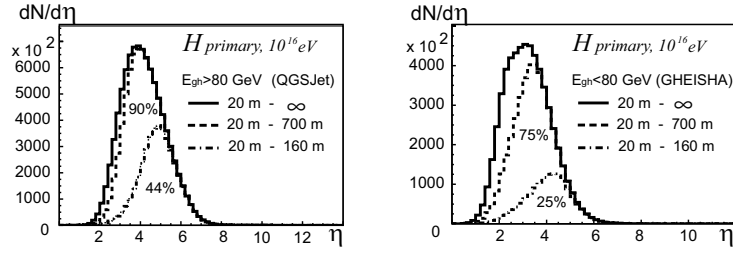


Figure 3. Distributions of muon pseudorapidities for different collecting distances for two ranges of grandmother hadron energies: $E_{gh} > 80$ GeV (left) and $E_{gh} < 80$ GeV (right)

3. Muon production heights

Muon production height distribution is showing sensitivity to the primary mass, as seen in Fig. 4. Muons from iron showers are generated higher than from proton ones. This feature allows to use a mean production height of muons as a mass sensitive parameter. Fig. 4 shows also, that the shape of the distribution for distance 20 -160 m (KASCADE case) has no pronounced peak. Comparing mean values is then prone to large systematic errors. Measuring muons up to larger distances, e.g. 20 - 700 m, one gets the distributions being close to the distribution for all muons in a shower. Dividing the full numbers of tracked muons into two groups, depending on their grandmother hadron energy, one finds also the possibility to disentangle between low- (GHEISHA) and high- (QGSJet) energy interaction models. As it is shown in Fig. 5, with the small collection distance muons created by hadrons of energy < 80 GeV (below this energy GHEISHA model is used in simulations) are nearly absent. Therefore, any discrepancy between data and simulations one can assign mostly to the high energy model. With the distance 20 - 700 m data contains large fraction of muons from both, low- and high-energy hadron regions. Therefore, low-energy interaction models can also be tested.

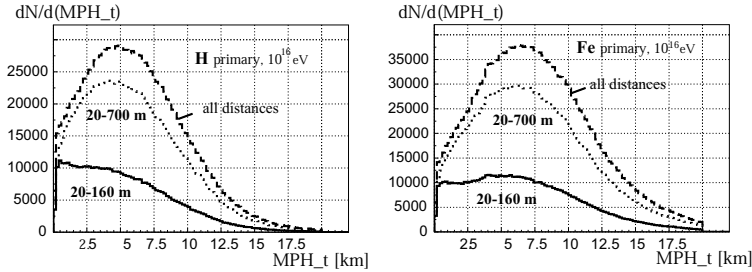


Figure 4. Distributions of true (MPH_t) muon production heights for different collecting distances for two primary particles: protons and iron nuclei.

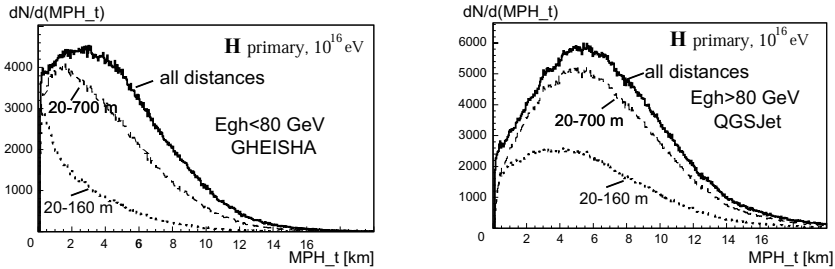


Figure 5. Distribution of true (MPH_t) muon production heights for two groups of grandmother hadron energies and three ranges of collecting distances.

Such separate tests of low- and high-energy hadronic interaction models are really of interest. In Fig. 6 the distribution of grandmother hadrons of muons which can be registered in the MTD as a function of their energy is shown for three collecting distances.

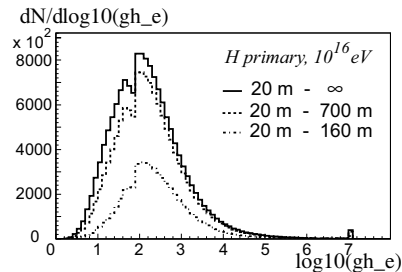


Figure 6. Distribution of “grandmother” hadron energies for muons reaching the MTD. Note the break at 80 GeV, where the interaction models change.

The break at 80 GeV, where the change of the interaction model takes place is clearly seen. It is more pronounced in KASCADE setup and indicates that number of muons produced according to both models do not match at the boundary energy.

4. Conclusions

It has been shown, that in KASCADE-Grande much larger part of longitudinal development of muon component in a shower is probed. Therefore, the composition study and model tests with the mean muon production heights and muon pseudorapidity distributions will give much more reliable results. In addition, tests of low-energy interaction models become now possible.

5. Acknowledgements

The support by DAAD-PPP grant (DAAD 323-bis PPP Polen) and by grant from Committee for Scientific Research (KBN) for 2004-2006 is kindly acknowledged by Polish group.

References

- [1] Doll P. et al. Nucl. Instr. Meth. A488 (2002) 517.
- [2] Badea F. et al., Nucl.Phys.B (Proc.Suppl.), 136 (2004) 384.
- [3] Büttner C. et al., Proc. 28th ICRC 2003, Tsukuba, Japan, 33.
- [4] Zabierowski J. et al., Proc. 28th ICRC 2003, Tsukuba, Japan, 29.
- [5] Heck D. et al. FZKA 6019, Forschungszentrum Karlsruhe (1998)
- [6] Zabierowski J. et al., Nucl Phys.B (Proc.Suppl.), 122 (2003) 275.

Approach to elemental energy spectra of cosmic rays by correlation curves method

I. Lebedev^{b,1}, T. Antoni^a, W.D. Apel^b, F. Badea^{b,2}, K. Bekk^b, A. Bercuci^c, J. Blümer^{b,a}, E. Boos¹, H. Bozdog^b, I.M. Brancus^c, A. Chilingarian^d, K. Daumiller^b, P. Doll^b, R. Engel^b, J. Engler^b, F. Feßler^b, H.J. Gils^b, R. Glasstetter^{a,2}, A. Haungs^b, D. Heck^b, J.R. Hörandel^a, K.-H. Kampert^{a,b,3}, H.O. Klages^b, G. Maier^{b,4}, H.J. Mathes^b, H.J. Mayer^b, J. Milke^b, M. Müller^b, R. Obenland^b, J. Oehlschläger^b, S. Ostapchenko^{b,5}, M. Petcu^c, H. Rebel^b, A. Risse^e, M. Risse^b, M. Roth^a, G. Schatz^b, H. Schieler^b, J. Scholz^b, T. Thouw^b, H. Ulrich^b, J. van Buren^b, A. Vardanyan^d, A. Weindl^b, J. Wochele^b, J. Zabierowski^e, S. Zagromski^b

(a) *Institut für Experimentelle Kernphysik, Universität Karlsruhe, 76021 Karlsruhe, Germany*

(b) *Institut für Kernphysik, Forschungszentrum Karlsruhe, 76021 Karlsruhe, Germany*

(c) *National Institute of Physics and Nuclear Engineering, 7690 Bucharest, Romania*

(d) *Cosmic Ray Division, Yerevan Physics Institute, Yerevan 36, Armenia*

(e) *Soltan Institute for Nuclear Studies, 90950 Lodz, Poland*

¹ *home address: Institute of Physics and Technology, 480082 Almaty, Kazakhstan*

² *on leave of absence from Nat. Inst. of Phys. and Nucl. Engineering, Bucharest, Romania*

³ *now at Fachbereich Physik, Universität Wuppertal, 42097 Wuppertal, Germany*

⁴ *now at University Leeds, LS2 9JT Leeds, United Kingdom*

⁵ *on leave of absence from Moscow State University, 119899 Moscow, Russia*

Presenter: A. Haungs (haungs@ik.fzk.de), kaz-lebedevI-abs1-he12

Using correlation information of different observables in extensive air shower experiments allows to reduce the influence on intrinsic fluctuations at the shower development for the reconstruction of energy and mass of the primary cosmic rays. The basic idea is that all showers which are produced by the same initial parameters (energy, mass) have (at least after the shower maximum) similar developments. The method is discussed by applying it to measured KASCADE array data, i.e. by investigating the correlation of the electron and muon numbers of the EAS. The correlation curves are obtained by fitting detailed Monte Carlo simulations including detector response based on different hadronic interaction models. Systematic uncertainties of the reconstruction method are discussed in detail. The resulting energy spectra for individual mass groups of the cosmic rays will be compared for different ranges in zenith angle, for different interaction models and with the results of the KASCADE unfolding procedures [1].

1. Introduction

The observation of the change of the power law slope (the so-called knee [2]) of the all-particle cosmic ray (CR) spectrum at an energy of $\sim 3 \cdot 10^{15}$ eV has induced considerable interest and experimental activities. Nevertheless, despite of about 50 years of extensive air shower (EAS) measurements, the origin of the knee phenomenon has not yet been convincingly explained [3]. Many of the hypotheses explaining the knee, predict a detailed shape of the primary cosmic ray spectrum around the knee, but with specific variations of the elemental composition. Thus the experimental access to attack the knee problem is to perform detailed and accurate measurements and sophisticated reconstruction methods of the energy spectra of individual cosmic ray elements or elemental groups, at least.

In this studies we present a method to reconstruct the energy spectra of CR elemental groups by an investigation

of the correlation of the electron, N_e , and muon, N_μ , numbers in the EAS. The method and some preliminary results are discussed by applying it to measured KASCADE array data.

The KASCADE experiment [4] located at the site of the Forschungszentrum Karlsruhe, Germany, measure various observables of extensive air showers with primary energy between 10^{14} and 10^{17} eV. It consists of three major detector components: the field array, the muon tracking detector and the central detector complex. The field array extends over an area of 40.000 m^2 and consists of 252 detector stations for the detection of the electron and the muon component of the EAS.

The simulation of the EAS development have been performed using the QGSJET [5] and SIBYLL [6] hadronic interaction models embedded in the CORSIKA program set (ver. 6.15)[7]. Low energy hadronic interactions are treated by the FLUKA model [8]. In the case of QGSJET about 2 millions of EAS in the energy interval of 10^{14} eV to 10^{18} eV for each of 5 primaries (p, He, C, Si, Fe) have been simulated. The energy distribution follows a power law with a slope index of -2. The zenith angles are distributed in the range $[0^\circ - 42^\circ]$. Same characteristics are valid for the SIBYLL case, but with lower statistics. In order to take into account the installation response a detailed GEANT [9] simulation of the KASCADE detectors are performed. The shower observables are reconstructed by the standard KASCADE reconstruction software.

2. Method

The sensitivity of most of the EAS methods to reconstruct the mass of primary cosmic ray particles is rather weak due to huge fluctuations of the shower development in the atmosphere. The reconstruction gets even more difficult at the analysis of EAS with different zenith angles, θ , because the overburden varies with $\cos(\theta)$ representing different column densities for different zenith angles.

An approach to this problem can be found by the correlation analysis of few observables measured at the same shower events. In Fig.1-left all showers of the same mass and energy in a wide interval of zenith angles are shown overlayed on the full distribution of all simulated showers. They are concentrated around specific $\log(N_e)$ vs. $dN_{e\mu}$ correlation curves, where $dN_{e\mu} = \log(N_e) - \log(N_\mu)$. Therefore, the large absolute fluctuations in $\log(N_e)$ can be transformed to smaller fluctuations (in relation to the correlation curves also shown in the figure). Additionally, in this approach the energy reconstruction using these curves seems to be independent on the zenith angle due to the fact that showers with large and small θ are placed around the same curves.

For mass reconstruction it was found that the $dN_{e\mu}$ vs. N_μ correlation curves are convenient, as all showers of the same mass and zenith angle in a wide interval of primary energy ($10^{15} - 10^{18}$ eV) are placed around these specific correlation curves. In Fig.1-right it is seen that these curves differ for proton and iron showers significantly.

Hence the applied procedure of energy and mass reconstruction is following: By use of the Monte Carlo (MC) data, in narrow bins of zenith angles for each of the 5 primaries the $dN_{e\mu}$ vs. N_μ -distribution is fitted by a polynomial function with θ and A as free parameters. This yields to a function $dN_{e\mu}(N_\mu, A, \theta)$. The mass of a single shower is then determined from the function by varying A and minimizing the difference between the measured $dN_{e\mu}$ and the function $dN_{e\mu}(N_\mu, A, \theta)$ with fixed (measured) θ and N_μ .

For the energy reconstruction the MC data at different fixed energies and masses are used. Here, the $\log(N_e)$ vs. $dN_{e\mu}$ - distributions are fitted with a polynomial function taking E_0 and A as free parameters, i.e. this yields to a function $\log N_e(dN_{e\mu}, E_0, A)$. The primary energy is then determined from the function by varying E_0 and minimizing the difference between the measured $\log(N_e)$ and the function $\log N_e(dN_{e\mu}, E_0, A)$ with fixed (measured) $dN_{e\mu}$ and (beforehand reconstructed) mass A .

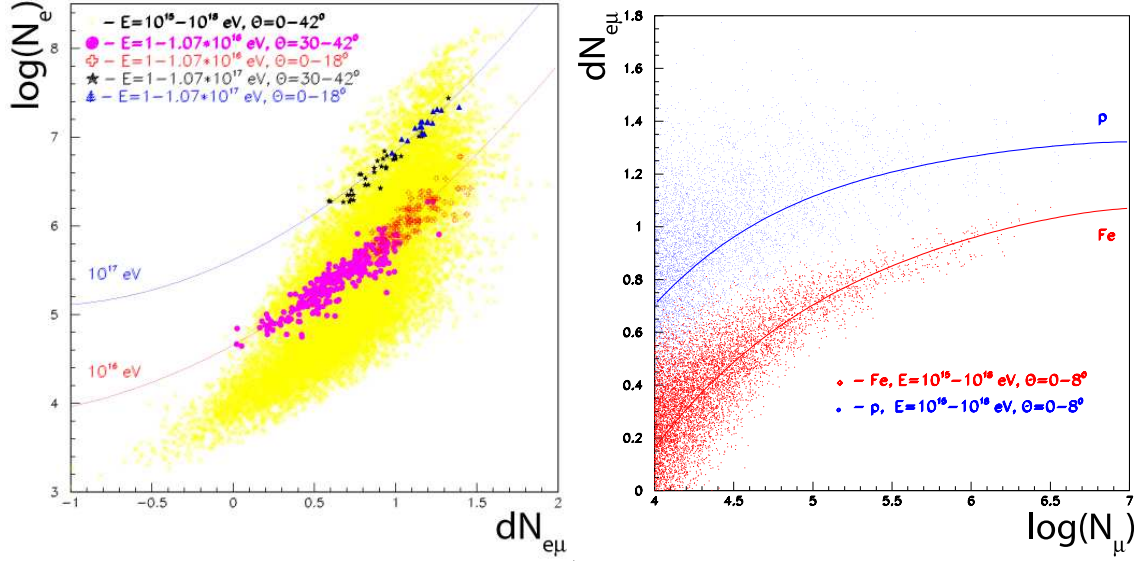


Figure 1. Left: $\log(N_e)$ vs. $dN_{e\mu}$ -distribution for proton EAS, simulated by QGSJET including the KASCADE detector response, and correlation curves as used for the energy reconstruction. Right: $dN_{e\mu}$ vs. $\log(N_\mu)$ dependences for iron and proton showers and correlation curves as used for mass reconstruction.

3. Results

Systematic uncertainties of the method were estimated by applying the described method to artificial elemental spectra obtained by different weightings in slopes and abundances of the Monte Carlo data sets. Resulting energy spectra are then compared to the input-spectra. As example for this procedure Fig. 2 shows input and outgoing spectra for five mass groups. By such investigations it could be shown that the statistical uncertainties of the energy reconstruction is $\sim 15\%$. Systematic uncertainties (inside on hadronic interaction model) are around 2%, only. Uncertainties in the mass classification could be obtained for example concerning the primary Irons as $\sim 27\%$ for Fe-Si classification (Iron misinterpreted as Silicon), $\sim 7\%$ for Fe-C classification, $< 2\%$ for Fe-He classification, and $< 1\%$ for Fe-p classification. Thus, systematical uncertainties of the reconstructed spectra depend mainly on the primary mass composition. These mis-classification probabilities and the systematic uncertainties of the energy estimation necessitates a correction to reconstruct the individual mass spectra, whose procedure is presently in work.

Similar results are obtained using SYBILL generated showers as input spectra. Investigating with same procedures different zenith angular ranges no differences were found in the obtained accuracy, i.e. the reconstruction method is working as expected.

For the application of the method to data a "good run" selection of KASCADE is used. In these runs all clusters and all detectors are present and working and are well calibrated. In total the used sample sums up to about 993 days measuring time. This is the same sample as used in ref. [1], the unfolding analysis of the two-dimensional shower size spectrum.

As preliminary result it was found that the obtained energy spectra (especially for the relative abundances of the different mass groups) depend on the hadronic interaction model used for estimating the correlation curves. Spectra calculated with correlation curves method on the basis of the SIBYLL model lead to differences in the

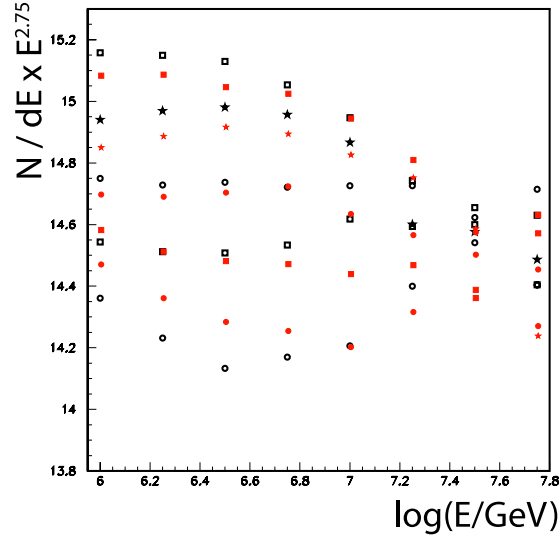


Figure 2. Comparison of simulated elemental mass spectra (p,He,C,Si,Fe from top to down) before (input spectra, open symbols) and after (output spectra, closed symbols) the application of the correlation curve method.

spectra compared to the QGSJET result as it predicts values of N_μ and N_e significantly different for the same primaries.

Nevertheless, the main peculiarities of the reconstructed spectra by SIBYLL and QGSJET models (like the knee in the total and in the light mass groups spectra as well as) as well as the general tendencies of differences between the results of the two models (like the heavier composition in case of SIBYLL) are similar to the results of the unfolding procedures [1].

In addition, due to the much faster procedures in the described method, we could compare resulting spectra of different zenith angle ranges. Indeed, there are differences in the group spectra, but not in the total spectrum if the full sample is divided in subsamples of different zenith angle ranges. If this is also due to inconsistencies in (both) interaction models is still under investigation.

Acknowledgments: The support of the Deutsche Forschungsgemeinschaft (DFG grant GZ 436 KAS 17/1/04) is gratefully acknowledged.

References

- [1] Ulrich H. et al. - KASCADE collaboration, Proc. 29th ICRC, Pune (2005), these proceedings
- [2] Kulikov G.V., Khristiansen, Soviet Physics JETP 35 (1959) 441.
- [3] Haungs A., Rebel H., Roth M., Rep Prog. Phys. 66 (2003) 1145.
- [4] Antoni T. et al. - KASCADE collaboration, Nucl. Inst. Meth. A 513 (2003) 490.
- [5] Kalmykov N.N., Ostapchenko S.S., Phys. At. Nucl. 56 (1993) 346.
- [6] Engel J. et al., Phys.Rev D50 (1994) 5013
- [7] Heck D. et al., FZKA-Report 6019, Forschungszentrum Karlsruhe, 1998.
- [8] Fassò A. et al., proc. Monte Carlo 2000, Lisbon, eds. A.Kling et al., Springer (Berlin) 955 (2001)
- [9] CERN, GEANT: CERN Program Library Long Writeups, 1993

LOPES30: A digital antenna array for measuring high-energy cosmic ray air showers

S. Nehls^a, W.D. Apel^a, F. Badea^a, L. Bühren^b, K. Bekk^a, A. Bercuci^c, M. Bertaina^d, P.L. Biermann^e, J. Blümer^{a,f}, H. Bozdog^a, I.M. Brancus^c, S. Buitink^g, M. Brüggemann^h, P. Buchholz^h, H. Butcher^b, A. Chiavassa^d, K. Daumiller^a, A.G. de Bruyn^b, C.M. de Vos^b, F. Di Pierro^d, P. Doll^a, R. Engel^a, H. Falcke^{b,e,i,g}, H. Gemmekeⁱ, P.L. Ghia^j, R. Glasstetter^k, C. Grupen^h, A. Haungs^a, D. Heck^a, J.R. Hörandel^f, A. Horneffer^{e,g}, T. Huege^{a,e}, K.-H. Kampert^k, G.W. Kant^b, U. Klein^l, Y. Kolotaev^h, Y. Koopman^b, O. Krömerⁱ, J. Kuijpers^g, S. Lafebvre^g, G. Maier^a, H.J. Mathes^a, H.J. Mayer^a, J. Milke^a, B. Mitrica^c, C. Morello^j, G. Navarra^d, A. Nigl^g, R. Obenland^a, J. Oehlschläger^a, S. Ostapchenko^a, S. Over^h, H.J. Pepping^b, M. Petcu^c, J. Petrovic^g, T. Pierog^a, S. Plewnia^a, H. Rebel^a, A. Risse^m, M. Roth^f, H. Schieler^a, G. Schoonderbeek^b, O. Sima^c, M. Stümpert^f, G. Toma^c, G.C. Trinchero^j, H. Ulrich^a, S. Valchierotti^d, J. van Buren^a, W. van Capellen^b, W. Walkowiak^h, A. Weindl^a, S. Wijnholds^b, J. Wochele^a, J. Zabierowski^m, J.A. Zensus^e, D. Zimmermann^h

(a) Institut für Kernphysik, Forschungszentrum Karlsruhe, 76021 Karlsruhe, Germany

(b) ASTRON, 7990 AA Dwingeloo, The Netherlands

(c) National Institute of Physics and Nuclear Engineering, 7690 Bucharest, Romania

(d) Dipartimento di Fisica Generale dell'Università, 10125 Torino, Italy

(e) Max-Planck-Institut für Radioastronomie, 53010 Bonn, Germany

(f) Institut für Experimentelle Kernphysik, Universität Karlsruhe, 76021 Karlsruhe, Germany

(g) Department of Astrophysics, Radboud University Nijmegen, 6525 ED Nijmegen, The Netherlands

(h) Fachbereich Physik, Universität Siegen, 57068 Siegen, Germany

(i) Inst. Prozessdatenverarbeitung und Elektronik, Forschungszentrum Karlsruhe, 76021 Karlsruhe, Germany

(j) Istituto di Fisica dello Spazio Interplanetario, INAF, 10133 Torino, Italy

(k) Fachbereich Physik, Universität Wuppertal, 42097 Wuppertal, Germany

(l) Radioastronomisches Institut der Universität Bonn, 53020 Bonn, Germany

(m) Soltan Institute for Nuclear Studies, 90950 Lodz, Poland

Presenter: A. Haungs (andreas.haungs@ik.fzk.de), ger-haungs-A-abs2-he15-poster

LOPES, a digital radio antenna array is designed to measure radio emission in extensive air showers (EAS) generated by high-energy cosmic rays. LOPES30 is the extension of an array of 10 antennas, LOPES10, to now 30 inverted V-shaped dipole antennas measuring in the frequency range between 40 and 80 MHz. LOPES operates in coincidence with the KASCADE-Grande air shower experiment, which provides trigger information and well-calibrated parameters of the air-shower properties on a single EAS basis in the energy range from 10 PeV to 1 EeV. The extension of the new antenna field with a maximum baseline of ~ 270 m will allow to measure the lateral distribution of the radio signal as well as the absolute field strengths and will significantly improve the pointing accuracy compared to LOPES10.

1. Introduction

Due to their stochastic production processes cosmic ray air showers are a complicated phenomenon. Therefore as many observables as possible are needed to reconstruct the shower parameters correctly. There are different approaches to achieve this experimentally. One can detect the particles produced in many interactions forming

a cascade of particles on the ground. A more direct way to study EAS is the detection of fluorescence light produced during the shower development. This allows a time resolved investigation of the shower but with the limitation of measurements only in dark, clear, and, moonless nights. There is additionally a third method to investigate high-energy EAS: The detection of radio emission generated by electron positron pairs deflected in the Earth's magnetic field. These radio emission of the EAS particles superimposes to a short coherent radio pulse easily detectable on the ground. The LOPES experiment [1] is measuring this radio emission from EAS.

2. EAS and radio emission

High-energy particles, cosmic rays, arriving at the Earth atmosphere undergo a first interaction with the nitrogen or oxygen nuclei in the upper layers. From this first and the following interactions a cascade of secondary particles arises. The air shower consists of different types of particles, for example hadrons and leptons. The electromagnetic component interacts also with the nuclei of the air by photo pair production and bremsstrahlung. Within these processes relativistic photons, electrons, and positrons are produced were the charged particles are deflected in the Earth's magnetic field. They will emit synchrotron radiation strongly beamed in the forward direction with an opening angle $\propto 1/\gamma$, with the Lorentz factor $\gamma = 1/\sqrt{1 - \beta^2}$. Theoretical studies of this so called geosynchrotron mechanism were published by Huege & Falcke [3]. From all emitting electrons and positrons a beamed coherent short radio pulse is generated. This pulse contains information about the electromagnetic component of the EAS integrated over the whole shower development.

Some properties of radio emission from EAS were obtained by earlier experiments and summarized in a review by Allan (1971) [5]. For a given energy E_p of the primary particle, an angle α to the geomagnetic field, zenith angle θ , and distance R to the shower center an approximate formula for the received voltage ϵ_ν per unit bandwidth can be written as:

$$\epsilon_\nu = 20 \left(\frac{E_p}{10^{17} eV} \right) \sin(\alpha) \cos(\theta) \exp \left(\frac{-R}{R_0(\nu, \theta)} \right) \left[\frac{\mu V}{mMHz} \right] \quad (1)$$

with a parameter R_0 around 110 m at a frequency ν of 55 MHz. Compared with recent theoretical studies [4] it could be shown that this formula is in the right order of magnitude and describes the observed dependencies rather well. Now experiments like LOPES have to verify the radio emission in EAS by detecting the amplitude of the radio pulse in dependence of the shower parameters.

3. LOPES30 hardware

The hardware design of LOPES is based on the concept of the "Low frequency array" - LOFAR which will be an astrophysical research project in the frequency range 10 - 200 MHz. For this radio telescope, a large array of 100 stations with 100 omnidirectional dipole antennas, each is planned to be installed in the Netherlands and partially in Germany. In LOFAR and LOPES the entire data stream can be stored for a certain period of time and therefore transient phenomena like EAS will be detectable.

Using the antenna design from LOFAR, LOPES was built at the site of KASCADE-Grande at the research center Karlsruhe, Germany. It is measuring in the frequency range 40 - 80 MHz, avoiding the short-wave and the strong FM-band. Within this range there are only a few radio transmitters with small bandwidth allowing a relatively good RF suppression. In the first stage of LOPES, ten antennas were running over nearly one year. Since early 2005 LOPES is extended to 30 antennas, fully in data acquisition since March. Analysis results based on LOPES10 data are subject of further contributions at this conference [2, 6].

The inverted V-shaped dipole antenna with an opening angle of 82.5° is connected to a low noise amplifier

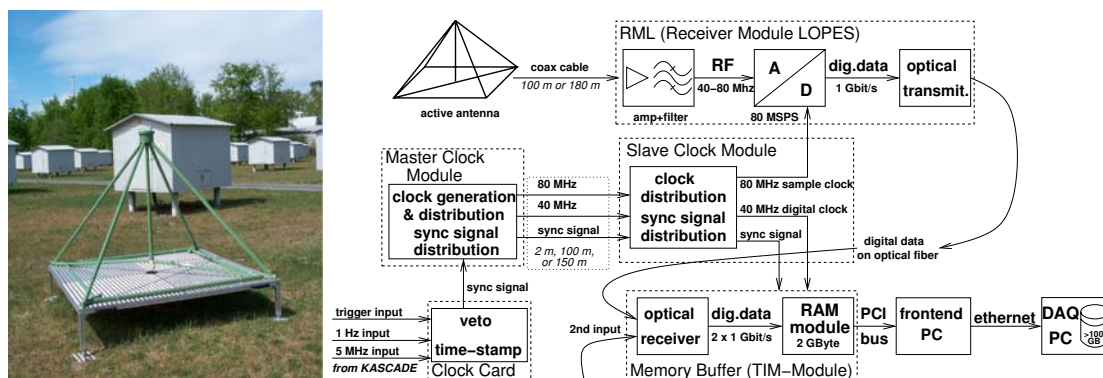


Figure 1. Antenna and scheme of LOPES30. Incoming radio pulses from EAS are transmitted over 100 m to 180 m coax cable to the Receiver Module (RML). Over an optical fiber the digitized signals are sent to a memory buffer. Receiving triggers from KASCADE-Grande a master clock module distributes the synchronization signal to slave clock modules.

mounted on top of a pyramidal antenna frame (see Fig.1, left). All antennas are equipped with dipoles in east-west direction, measuring the east-west polarization of the radio emission. The received voltage is again amplified after transmitting the signals from the field antenna to an electronic cluster dedicated to ten antennas. The radio signal is filtered in a sophisticated bandpass filter and afterwards digitized with 12-bit ADCs. The necessary dynamic range to detect weak pulses while not saturating the ADC with radio interference is achieved with these 12-bit ADCs. They are working with 80 MHz, allowing 2nd Nyquist sampling of the signal and resulting in a 12.5 ns time resolution. The 30 antennas are divided into three clusters having the same sampling clock for the ADCs. The sample clock is generated by a master clock module and is then distributed over slave clock modules to all A/D-boards (see Fig.1, right). This allows to combine data from all antennas as a phased array and thus enhances the sensitivity. After the digitization the signal is converted into an optical signal transferred via fiber optics to a memory module and stored in a front-end PC. From the KASCADE-Grande experiment LOPES30 receives a trigger if a majority condition 10 out of 16 clusters of the KASCADE array detecting an EAS is fulfilled, which requires ≈ 10 PeV primary energy. Under this trigger condition 800 μsec of data from the memory buffer of all antennas are saved on a central DAQ-PC.

4. Status of LOPES30

With LOPES10 the “proof of principal” in detecting radio signals was achieved by comparing relative field strengths in the antenna array [7]. The analysis was done without a precise absolute calibration. For a detailed comparison with theoretical predictions of the expected electric field strengths and polarization of radio emission in EAS an absolute calibration of the LOPES30 antenna system is essential. Therefore a conversion factor for received electric field strengths from EAS and measured voltage amplitudes of the antenna system is determined. In a first step the electronic part is calibrated, including receiver module (RML), optical transmission, and TIM-module (see Fig.1) resulting in a frequency dependent amplification factor. In a second step the whole system will be calibrated, which will be done with a biconical shaped reference radio source mounted on a wooden frame or a stationary balloon. The analysis of the absolute calibration is in progress and will give us a calibrated antenna system to compare theoretical predictions with received voltages of the radio field strength in EAS.

The LOPES30 system is currently triggered by the KASCADE array giving an upper limit in energy of 80 PeV

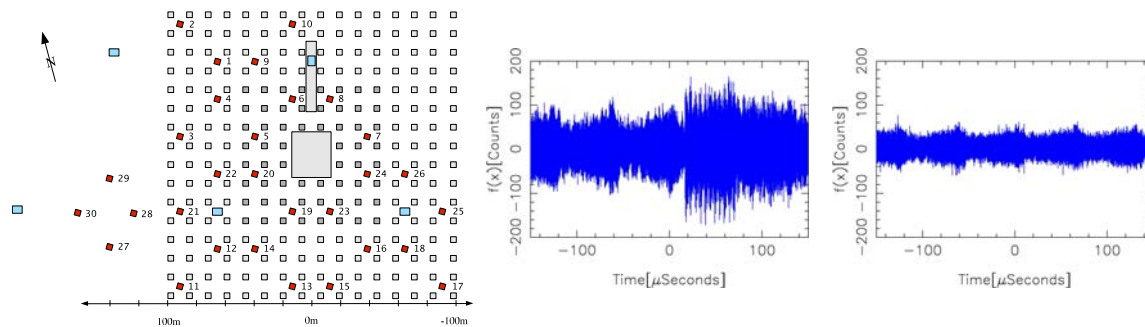


Figure 2. Left: LOPES30 antenna positions (numbered squares) at the KASCADE-Grande experiment. The latter forms a quadratic grid with a central detector and a muon detector. 5 Grande stations are represented by rectangles. Center and right: Voltage amplitude received in antenna 20 (mid.) and antenna 27 (right) during one event trigger.

for detecting EAS. By including the KASCADE-Grande trigger this limit is extended to energies of ≈ 1 EeV. The antenna layout of LOPES30 is depicted in Fig. 2, left. During a shower detection there are RF interferences generated in the detector huts surrounding an antenna. The RF interference correlates with deposited energy in the huts making it more difficult to distinguish the radio signal from induced noise. Four antennas (27 to 30) are placed outside of the KASCADE array. They were installed to investigate the noise during radio wave detection. For these four antennas on the field the RF interference from the huts is negligible, see an example in Fig. 2. The center and right picture shows the signal of a triggered single event in a time window of $300 \mu\text{sec}$ for antenna 20 (inside the KASCADE array) and antenna 27 (outside the array). A further noise reduction will decrease the detection limit of LOPES30 allowing to investigate threshold effects of the detection and the lateral distribution of the radio emission. Having a maximum baseline of ~ 270 m a lateral distribution of the radio signal on single event basis can be seen and comparisons with theoretical predictions will be done. The extension to 30 antennas significantly improves the pointing accuracy compared to LOPES10. This can be used as additional information for the KASCADE-Grande reconstruction of the EAS.

5. Outlook

The LOPES antenna system as a LOFAR prototype showed the possibility to measure radio emission from EAS. With a calibrated system we will be able to verify theoretical predictions about the field strength of radio emission in EAS. Measuring both polarizations of the radio emission will directly verify the geosynchrotron effect as the dominant emission process in EAS.

References

- [1] Haungs, A. et al. - LOPES coll., Proc. 22nd Texas Symp., 2004, eConf C041213, 2413
- [2] Horneffer, A. et al. - LOPES coll., Proc. 29th ICRC Pune, 2005, these proceedings
- [3] Huege, T. and Falcke, H., A&A, 2003, 412, 19
- [4] Huege, T. and Falcke, H., A&A, 2005, 430, 779
- [5] Allan, H. R., Prog. in Elem. part. and Cos. Ray Phys., 1971, 10, 171
- [6] Badea, A. F. et al. - LOPES coll., Proc. 29th ICRC Pune, 2005, these proceedings
- [7] Falcke, H. et al. - LOPES coll., Nature, 2005, 435, 313

Detection of radio pulses from extensive air showers

A. Horneffer^{a,b}, W.D. Apel^c, F. Badea^c, L. Bühren^d, K. Bekk^c, A. Bercuci^e, M. Bertainaf^f, P.L. Biermann^b, J. Blümer^{c,g}, H. Bozdog^c, I.M. Brancus^e, S. Buitink^a, M. Brüggemann^h, P. Buchholz^h, H. Butcher^d, A. Chiavassa^f, K. Daumiller^c, A.G. de Bruyn^d, C.M. de Vos^d, F. Di Pierro^f, P. Doll^c, R. Engel^c, H. Falcke^{a,b,d}, H. Gemmekeⁱ, P.L. Ghia^j, R. Glasstetter^k, C. Grupen^h, A. Haungs^c, D. Heck^c, J.R. Hörandel^g, T. Huege^{b,c}, K.-H. Kampert^k, G.W. Kant^d, U. Klein^l, Y. Kolotaev^h, Y. Koopman^d, O. Krömerⁱ, J. Kuijpers^a, S. Lafebrea^a, G. Maier^c, H.J. Mathes^c, H.J. Mayer^c, J. Milke^c, B. Mitrica^e, C. Morello^j, G. Navarra^f, S. Nehls^c, A. Nigl^a, R. Obenland^c, J. Oehlschläger^c, S. Ostapchenko^c, S. Over^h, H.J. Pepping^d, M. Petcu^e, J. Petrovic^a, T. Pierog^c, S. Plewnia^c, H. Rebel^c, A. Risse^m, M. Roth^g, H. Schieler^c, G. Schoonderbeek^d, O. Sima^e, M. Stümpert^g, G. Toma^e, G.C. Trinchero^j, H. Ulrich^c, S. Valchierotti^f, J. van Buren^c, W. van Capellen^d, W. Walkowiak^h, A. Weindl^c, S. Wijnholds^d, J. Wochele^c, J. Zabierowski^m, J.A. Zensus^b, D. Zimmermann^h

(a) Department of Astrophysics, Radboud University Nijmegen, 6525 ED Nijmegen, The Netherlands

(b) Max-Planck-Institut für Radioastronomie, 53010 Bonn, Germany

(c) Institut für Kernphysik, Forschungszentrum Karlsruhe, 76021 Karlsruhe, Germany

(d) ASTRON, 7990 AA Dwingeloo, The Netherlands

(e) National Institute of Physics and Nuclear Engineering, 7690 Bucharest, Romania

(f) Dipartimento di Fisica Generale dell'Università, 10125 Torino, Italy

(g) Institut für Experimentelle Kernphysik, Universität Karlsruhe, 76021 Karlsruhe, Germany

(h) Fachbereich Physik, Universität Siegen, 57068 Siegen, Germany

(i) Inst. Prozessdatenverarbeitung und Elektronik, Forschungszentrum Karlsruhe, 76021 Karlsruhe, Germany

(j) Istituto di Fisica dello Spazio Interplanetario, INAF, 10133 Torino, Italy

(k) Fachbereich Physik, Universität Wuppertal, 42097 Wuppertal, Germany

(l) Radioastronomisches Institut der Universität Bonn, 53121 Bonn, Germany

(m) Soltan Institute for Nuclear Studies, 90950 Lodz, Poland

Presenter: Andreas Horneffer (A.Horneffer@astro.ru.nl), ger-horneffer-A-abs1-he13-oral

LOPES is a LOFAR Prototype Station aimed to measure radio pulses from air showers. LOFAR is a new digital radio interferometer, that is being built in The Netherlands. Working in the frequency range of 10-210 MHz LOFAR is well suited to measure the radio emission of air showers. LOPES is set up at the site of the KASCADE-Grande air shower array. It samples the radio signal in the band of 40-80 MHz with high bandwidth ADCs and stores the whole waveform information in digital form. This allows us to suppress the radio interference at this site with digital filtering and beam forming. Thus LOPES is able to continuously measure radio pulses from air showers. The data taken with the first phase of LOPES from January to September 2004 has been analysed in conjunction with air shower parameters from the KASCADE array. Clear correlations between the radio pulse height and the shower size and the angle to the geomagnetic field have been found. The data supports the theory that the emission is coherent synchrotron radiation in the geomagnetic field.

1. Introduction

A standard method to observe cosmic rays is to measure the secondary particles of an air shower with an array of particle detectors on the ground. Very useful information for the determination of primary particle energy

and type can be obtained by observing the air shower as it evolves. So far this is only done by observing optical emission like fluorescence light. This requires clear, dark nights and limits the duty cycle to ca. 10%.

Measuring radio emission from air showers can be an alternative method for such observations, providing a much better efficiency. Radio emission from cosmic ray air showers were discovered for the first time by Jelly [5] at 44 MHz. The results were soon verified and in the late 1960's emission from 2 MHz up to 520 MHz were found. In the following years these activities ceased due to difficulty with radio interference, uncertainty about the interpretation of the results, and the success of other methods. The known radio properties of extensive air showers were summarised in a review by Allan [1]. The main result of this review can be summarised by an approximate formula for the received voltage per unit bandwidth:

$$\epsilon_\nu = 20 \left(\frac{E_p}{10^{17} \text{eV}} \right) \sin \alpha \cos \theta \exp \left(\frac{-R}{R_0(\nu, \theta)} \right) \left[\frac{\mu\text{V}}{\text{m MHz}} \right] \quad (1)$$

Here E_p is the primary particle energy, α is the angle to the geomagnetic field, θ is the zenith angle, R is the distance to the shower axis, R_0 is around 110 m at 55 MHz, and ν is the observing frequency.

Recent theoretical studies, modelling the radio emission from air showers as coherent synchrotron radiation in the earth's magnetic field, have been able to reproduce the existing data to a good degree (see [4]).

2. LOFAR and LOPES

LOFAR is a new attempt to revitalise astrophysical research at 10-210 MHz with the means of modern information technology. LOPES is a “LOFAR Prototype Station” tailored for the detection of air showers. The basic idea is to build an array of simple, quasi-omnidirectional dipole antennas in which the received waves are digitised and sent to a central computer. A new feature of this design is the possibility to store the entire data stream for a certain period of time. If one detects a transient phenomenon like an air shower one can then retrospectively form a beam in the desired direction. A related experiment, with a similar technology, uses part of the Nançay decametric array [6].

LOPES is set up at the site of KASCADE-Grande [7]. The data from a well tested air shower experiment not only allows us to calibrate the radio data with other air shower parameters. It also provides us with starting points for the air shower reconstruction. LOPES operates in the frequency range of 40 to 80 MHz and does direct sampling of the radio signal. Its short dipole antennas are currently set up to measure the east-west polarised component of the signal. After each trigger 0.82 ms worth of raw data are read out of the memory buffer and stored on hard disk.

3. Processing of Radio Data

The first step of the analysis is to Fourier transform the data into frequency space. Here, narrow-band interference shows as spikes in the spectrum and can be flagged. Then a beam is formed into the direction of the air shower, as given by KASCADE-Grande. For this the data for each antenna has to be shifted in time. Short time pulses that are not correlated with the air shower can then be identified by their different arrival times in the antennas. The left panel of Figure 1 shows the electric field of all antennas after filtering and time shifting for an example event. At $-1.8 \mu\text{s}$ a coherent pulse from the direction of the air shower can be seen (all the lines lie on top of each other). The region of $-1.75 \mu\text{s}$ to $-1.4 \mu\text{s}$ is filled by the noise from the particle detectors. When the data from all antennas is combined in the beamforming process, the coherent pulse is enhanced and the noise is reduced, as shown in the middle panel of Figure 1. (A more detailed description of LOPES and the LOPES data processing can be found in [3].)

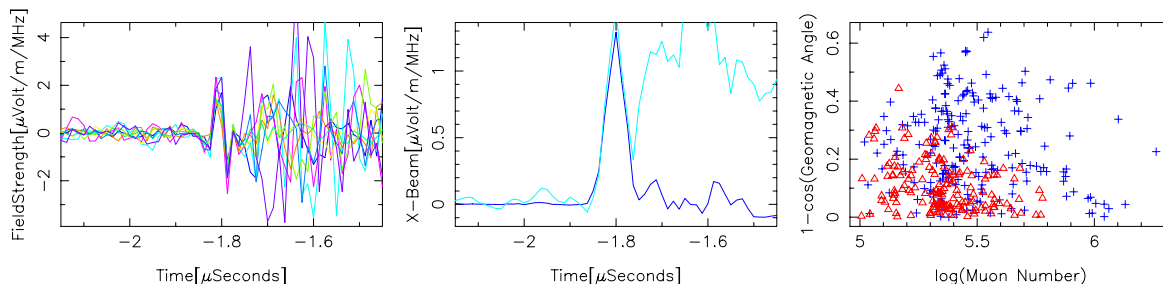


Figure 1. Left: The electric field of the LOPES antennas (in different colours) after filtering of narrow band interference and time shifting. The short pulse at $-1.8 \mu\text{s}$ is coherent (all the lines lie on top of each other), while the later pulses (noise from the particle detectors) are not. Middle: The same data after beamforming (dark blue) and as comparison the power averaged data (light blue). Right: Good events in which a coherent pulse from the air shower was detected (crosses), and bad events that were selected but in which no pulse from the air shower was detected (triangles). The fraction of good to bad events rises with muon number and angle to the geomagnetic field.

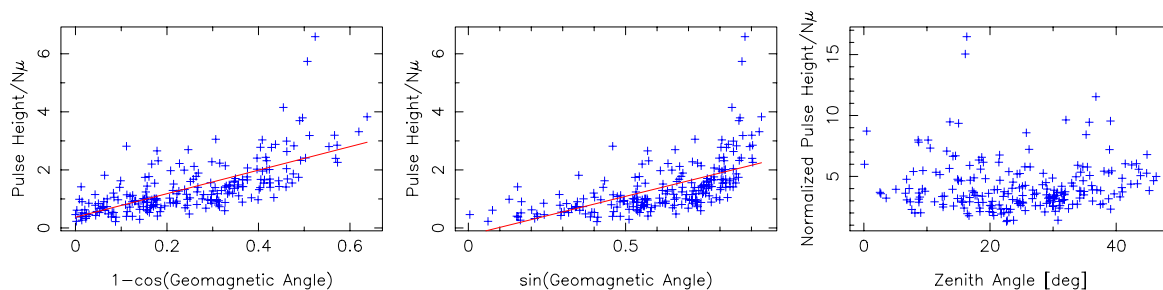


Figure 2. Left: Height of the radio pulse, divided by the muon number, against the cosine of the geomagnetic angle. Middle: Pulse height against the sine of the geomagnetic angle. Both relations (sine and cosine) can be approximated by a linear dependence, although the cosine gives a better fit. Right: Radio pulse height scaled with the results of the fit in the left panel. After taking out the effect of the geomagnetic angle, no further dependence on the zenith angle can be seen.

4. Results

From January to September 2004 LOPES collected ca. 630 thousand events. For this analysis we selected the largest events in which: a) the KASCADE array processor did not fail, b) the distance of the shower core to the array centre was less than 91 m, and c) the electron number was greater than 5×10^6 or the truncated muon number was greater than 2×10^5 . This selected 412 events, in 228 of which events we found a coherent pulse from the air shower and which are therefore called “good” events. In the remaining “bad” events the pulse from the air shower is too small so that it is hidden in the noise.

The height of the radio pulses correlates with several air shower parameters: It rises with shower size (i.e. with the electron number or the muon number), it rises with increasing angle to the geomagnetic field and it falls with increasing distance of the shower axis to the antennas. This explains the rise of the fraction of good to bad events with muon number and geomagnetic angle, seen in the right panel of Figure 1.

As the dependence on the shower size is most pronounced, in a first step we normalised the pulse height by dividing by the truncated muon number. The left and middle panel of Figure 2 show the dependence of the thus normalised pulse height on the cosine and sine of the geomagnetic angle. Both relations show an approximately linear dependence, although the cosine gives a somewhat better fit. This difference in the quality of the fit is

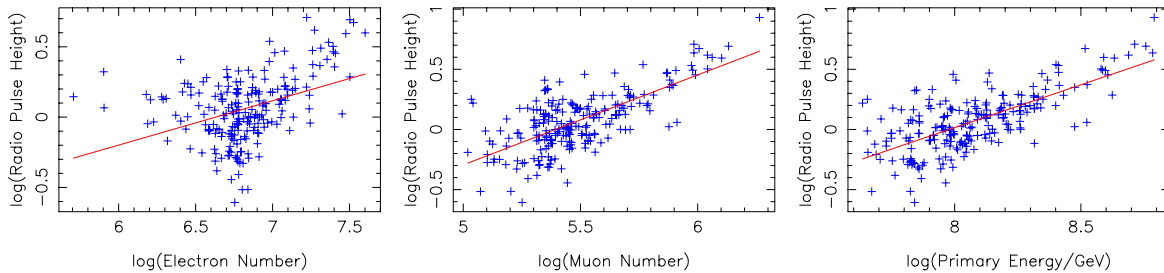


Figure 3. Normalised radio pulse height after scaling by the fit to the geomagnetic angle and distance to the shower axis. Plotted against the electron number (left), muon number (middle) and primary particle energy (right).

present in all (sub)selections of the data. In the right panel of Figure 2 we additionally normalised the pulse height with the values of the fit in the left panel, by multiplying with the fraction of the fit results at 90° to those at the angle of the air shower. After taking out the effect of the angle to the geomagnetic field, no further dependence on the zenith angle can be seen. The same is true for the azimuthal angle.

In Figure 3 the pulse height was scaled with the results of the fit to the geomagnetic angle and the results of a fit to the distance of the antennas to the shower axis. The difference between the left and the middle panel shows that the radio pulse height is better correlated with the muon number than with the electron number. This is expected as at the KASCADE Grande experiment the muon number is a better tracer of the total number of particles during the shower evolution than the electron number. Combining electron and muon number to a value for the primary particle energy does not improve the correlation compared to the muon number alone. The slope of the linear fit to the $\log(\text{pulse height})$ vs. $\log(\text{primary energy})$ plot is close to one. That means that the field strength indeed rises linearly with primary energy and thus the received power rises quadratically.

5. Conclusions

LOPES is able to reliably measure radio emission from air showers, and already took enough data for a first science analysis. Compared to the Allan-formula two discrepancies have been found: One is the better correlation of the pulse height with the cosine of the geomagnetic angle, compared to the sine. The other is that no dependence on the zenith angle has been found after the effect of the geomagnetic angle has been removed.

This analysis confirms the results given in [2]. With a wider selection including lower energy events and larger distances to the shower axis the detection efficiency drops as expected and more scatter is introduced. But it gives the same basic trends, i.e. 100% detection efficiency for large events, strong dependence on the geomagnetic angle and nearly linear raise of the pulse height with energy.

References

- [1] H.R. Allan, Prog. in Elem. part. and Cos. Ray Phys., Vol. 10, 171 (1971)
- [2] H. Falcke et al., Nature 435, 313 (2005)
- [3] A.Horneffer et al., Proc. SPIE 5500-21, (2004)
- [4] T. Huege & H. Falcke, A&A. Vol. 430, 779-798, (2005)
- [5] J.V. Jelly et al., Nature 205, 327 (1965)
- [6] O. Ravel et al., Nuclear Instr. & Methods in Physics A 518, 213-215 (2004)
- [7] H. Schieler et al., Proc. SPIE 4858-5, (2002)

First determination of the reconstruction resolution of an EAS radio detector

A.F. Badea^a, W.D. Apel^a, L. Bähren^b, K. Bekk^a, A. Bercuci^c, M. Bertaina^d, P.L. Biermann^e, J. Blümer^{a,f}, H. Bozdog^a, I.M. Brancus^c, S. Buitink^g, M. Brüggemann^h, P. Buchholz^h, H. Butcher^b, A. Chiavassa^d, K. Daumiller^a, A.G. de Bruyn^b, C.M. de Vos^b, F. Di Pierro^d, P. Doll^a, R. Engel^a, H. Falcke^{b,e,g}, H. Gemmekeⁱ, P.L. Ghia^j, R. Glasstetter^k, C. Grupen^h, A. Haungs^a, D. Heck^a, J.R. Hörandel^f, A. Horneffer^{e,g}, T. Huege^{a,e}, K.-H. Kampert^k, G.W. Kant^b, U. Klein^l, Y. Kolotaev^h, Y. Koopman^b, O. Krömerⁱ, J. Kuijpers^g, S. Lafebre^g, G. Maier^a, H.J. Mathes^a, H.J. Mayer^a, J. Milke^a, B. Mitrica^c, C. Morello^j, G. Navarra^d, S. Nehls^a, A. Nigl^g, R. Obenland^a, J. Oehlschläger^a, S. Ostapchenko^a, S. Over^h, H.J. Pepping^b, M. Petcu^c, J. Petrovic^g, T. Pierog^a, S. Plewnia^a, H. Rebel^a, A. Risse^m, M. Roth^f, H. Schieler^a, G. Schoonderbeek^b, O. Sima^c, M. Stümpert^f, G. Toma^c, G.C. Trinchero^j, H. Ulrich^a, S. Valchierotti^d, J. van Buren^a, W. van Capellen^b, W. Walkowiak^h, A. Weindl^a, S. Wijnholds^b, J. Wochele^a, J. Zabierowski^m, J.A. Zensus^e, D. Zimmermann^h

(a) Institut für Kernphysik, Forschungszentrum Karlsruhe, 76021 Karlsruhe, Germany

(b) ASTRON, 7990 AA Dwingeloo, The Netherlands

(c) National Institute of Physics and Nuclear Engineering, 7690 Bucharest, Romania

(d) Dipartimento di Fisica Generale dell'Università, 10125 Torino, Italy

(e) Max-Planck-Institut für Radioastronomie, 53121 Bonn, Germany

(f) Institut für Experimentelle Kernphysik, Universität Karlsruhe, 76021 Karlsruhe, Germany

(g) Department of Astrophysics, Radboud University Nijmegen, 6525 ED Nijmegen, The Netherlands

(h) Fachbereich Physik, Universität Siegen, 57068 Siegen, Germany

(i) Inst. Prozessdatenverarbeitung und Elektronik, Forschungszentrum Karlsruhe, 76021 Karlsruhe, Germany

(j) Istituto di Fisica dello Spazio Interplanetario, INAF, 10133 Torino, Italy

(k) Fachbereich Physik, Universität Wuppertal, 42097 Wuppertal, Germany

(l) Radioastronomisches Institut der Universität Bonn, 53121 Bonn, Germany

(m) Soltan Institute for Nuclear Studies, 90950 Lodz, Poland

Presenter: A.F. Badea (Florin.Badea@ik.fzk.de), ger-badea-AF-abs1-he13-poster

LOPES [1] is set-up at the location of the KASCADE-Grande extensive air shower experiment in Karlsruhe, Germany and is a "LOfar PrototypE Station" aimed to measure radio pulses from Extensive Air Showers (EAS). The time shifting procedure of the pulses measured by the LOPES antennas in order to reveal the coherent radio signals induced by the shower in the Earth's atmosphere is based on the values provided by the KASCADE-Grande [2] reconstruction of shower axis direction and shower core position. It has been found that small variations of the shower position and direction reconstructed by KASCADE-Grande translate into large variations of the estimated radio pulse amplitude. On the other hand, by maximizing the radio coherence the estimate of the shower axis direction and shower core position can be improved.

1. Introduction

The KASCADE [3] experiment (see sketch in Fig. 1a) measures showers in a primary energy range from 100 TeV to 80 PeV and provides multi-parameter measurements on a large number of observables concerning

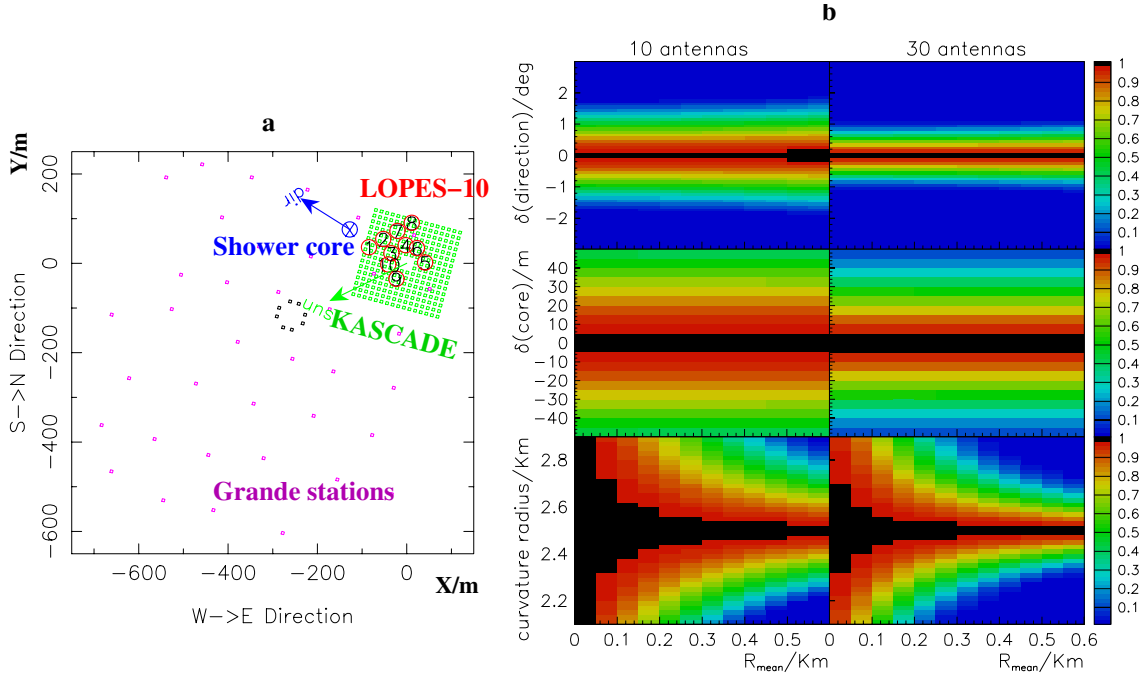


Figure 1. a) sketch of KASCADE-Grande and LOPES-10; b) sensitivity of the (cross correlation) CC-beam estimator to the shower direction, shower core position and curvature radius of the radio front for LOPES-10 and LOPES-30 configurations.

electrons, muons at 4 energy thresholds, and hadrons. The main detector components of KASCADE are Field Array, Central Detector and Muon Tracking Detector. The Field Array consists of 252 stations grouped in 16 clusters, for measuring the electromagnetic and muonic shower component. At present, LOPES operates 30 dipole radio antennas (LOPES-30) positioned inside or nearby KASCADE. In Fig. 1a only the 10 antennas of LOPES-10 are depicted. The radio data is collected when a trigger is received from KASCADE. The logical condition for trigger is at least 10 out of the 16 clusters of the Field Array to be fired. This translates to primary energies above 10^{16} eV; such showers are detected at a rate of 2 per minute. The antennas operate in the frequency range of 40-80 MHz. KASCADE-Grande is the extension of the multi-detector setup KASCADE to cover a primary cosmic ray energy range from 100 TeV to 1 EeV. The enlarged EAS experiment provides comprehensive observations of cosmic rays in the energy region around the knee. Grande is an array of $700 \times 700 \text{ m}^2$ equipped with 37 plastic scintillator stations sensitive to measure energy deposits and arrival times of air shower particles. The Grande reconstruction accuracy of shower core position and direction is in the order of 4 m (13 m) and 0.18° (0.32°) with 68% (95%) confidence level for simulated proton and iron showers at 100 PeV primary energy and 22° zenith angle [4].

2. Beamforming and coherence of the radio signal; efficiencies

A crucial element of the detection method is the digital beamforming which allows to place a narrow antenna beam in the direction of the cosmic ray event. This is possible because the phase information of the radio waves is preserved by the digital receiver and the cosmic ray produces a coherent pulse. This method is also very effective in suppressing interference from the particle detectors which radiate incoherently. Fig. 1b, based on analytical calculations for a point source radiating with 60 MHz, placed at 2.5 km along shower axis, gives

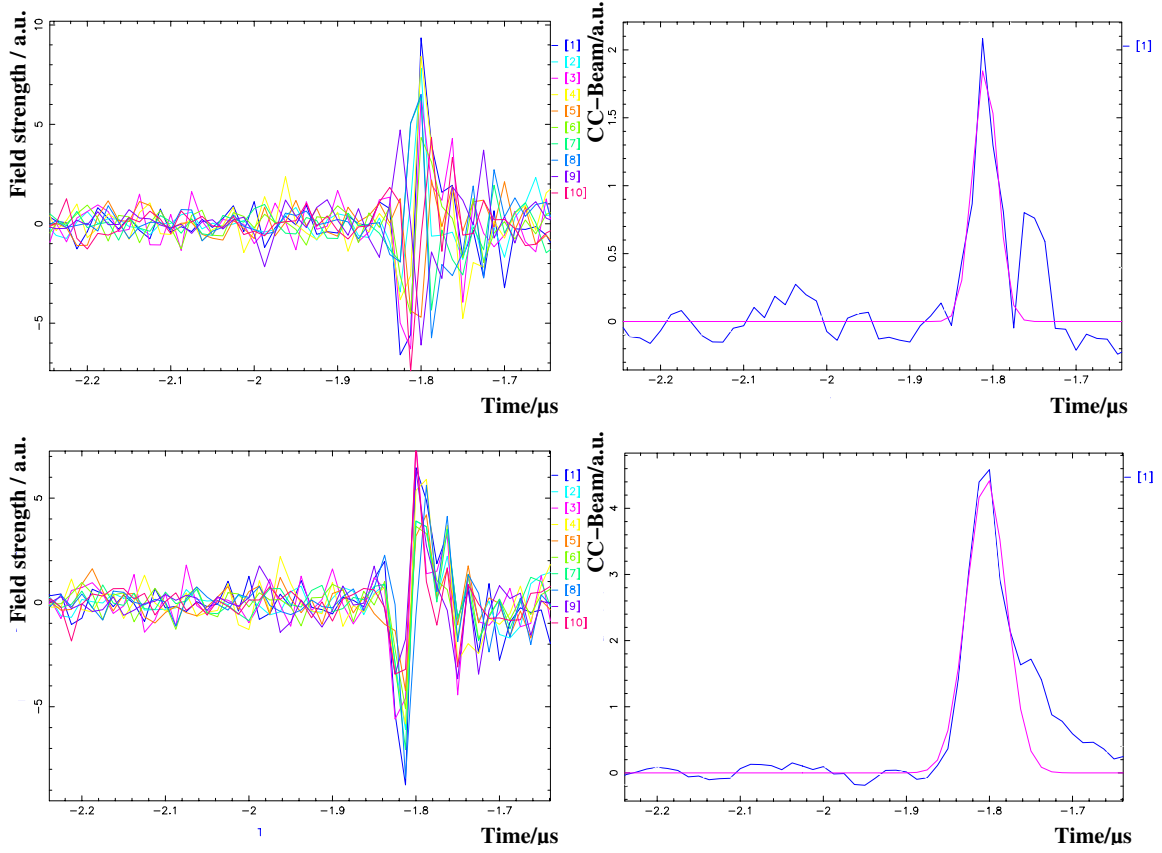
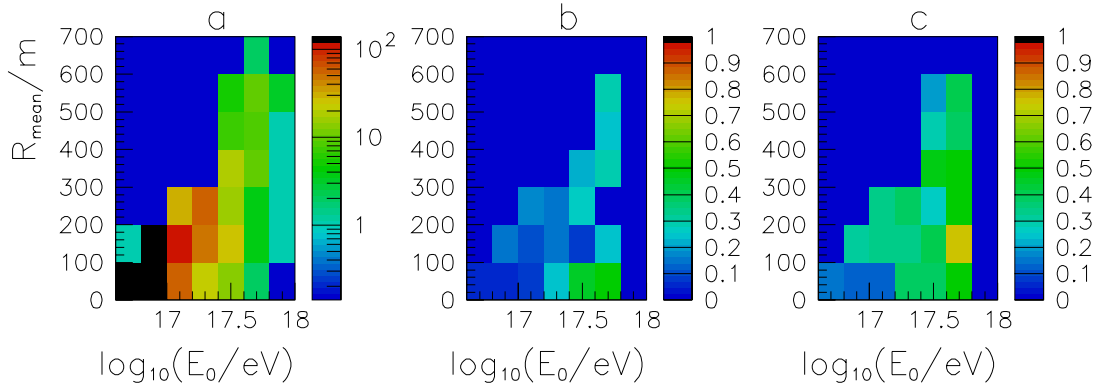


Figure 2. Radio signals in the 10 antennas and the CC-beam coherence estimator after beamforming (upper panels) and after *optimised* beamforming (lower panels).

an impression of the sensitivity of the (cross correlation) CC-beam estimator to the shower direction, shower core position and curvature radius of the radio front for LOPES-10 and LOPES-30 configurations. The z-axis is normalised to the value of the CC-beam estimator in case of the "perfect" coherence i.e. no "errors" in the guessed position of the radio pointsource ($\delta(\text{direction})=0$, $\delta(\text{core})=0$, curvature=2.5 km). The procedure of time shifting of the radio signals in the antennas is relatively safe when based on the values provided by Field Array reconstruction for shower core and shower axis (SCA); due to the high granularity of KASCADE stations the accuracy in reconstructing SCA is high enough to obtain a good coherence of the radio signals. Of course, this is valid for shower cores inside Field Array and for not too energetic showers which may lead to saturation of the detection. Grande reconstruction of SCA is required for shower cores outside the Field Array. The Grande stations, 10 m² of plastic scintillator detectors each, are spaced at $\simeq 130$ m and cannot assure a SCA accuracy comparable with Field Array. So, an optimised beamforming, searching for maximum coherence by varying the SCA around the value provided by the Grande reconstruction is required. Fig. 2 shows the result of such an optimised beamforming compared with a normal beamforming for a single event. This radio event corresponds to the shower displayed in Fig. 1a; the arrow points towards the incoming shower direction. An increase of 200% may be seen in the CC-beam estimator after the optimised beamforming. Table 1 contains the values composing SCA (azimuthal angle ϕ , zenith angle θ , X_{core} and Y_{core}) reconstructed by Grande and the corresponding values obtained after maximizing the radio coherence for this event; small shifts in SCA assure an almost perfect coherence of the radio signal (lower left panel in Fig. 2). The maximization of the

Table 1. SCA values from Grande reconstruction and after maximized radio coherence for an example event.

SCA values	Grande reconstruction	maximized radio coherence
ϕ	302.2°	299.3°
θ	41.0°	39.9°
X_{core}/m	-142.8	-139.2
Y_{core}/m	40.3	51.6

**Figure 3.** a) distribution of the candidate events on primary energy and distance to the shower axis; b) efficiency of the radio detection for an usual beamforming; c) preliminary efficiency of the radio detection for an optimised beamforming (only performed for half of the sample, yet).

radio coherence (optimised beamforming) plays a key role in establishing the right correlations [5] between the intensity of the radio signal and the other EAS parameters. Fig. 3b shows the efficiency of detecting radio signals for the EAS events in Fig. 3a (for selection conditions see [5]) using normal beamforming procedure based on the values provided by Grande reconstruction of SCA. After an optimised beamforming the efficiency is as displayed in Fig. 1c. The efficiency will be even higher because the optimised beamforming has been applied only for half of the candidate events, yet.

3. Conclusions

The coherence of the radio signal is very sensitive to the shower axis and shower core positions. On one hand, very small fluctuations in the shower observables reconstructed by Grande translate into large fluctuations on the estimated radio pulse amplitude. On the other hand, by maximizing the radio coherence, very precise estimations of SCA can be performed.

References

- [1] H. Falcke et al. - LOPES collab., Nature 435, 313 (2005).
- [2] G. Navarra et al. - KASCADE-Grande collab., Nucl. Instr. & Meth. A 518, 207 (2004).
- [3] T. Antoni et al. - KASCADE collab., Nucl. Instr. & Meth. A 513, 429 (2003).
- [4] R. Glasstetter et al. - KASCADE-Grande collab., Proc. of 28th ICRC, Tsukuba, Japan, 781 (2003).
- [5] A.F. Badea et al. – LOPES collab., Remote event analyses of LOPES-10, these proceedings.

Remote event analyses of LOPES-10

A.F. Badea^a, W.D. Apel^a, L. Bähren^b, K. Bekk^a, A. Bercuci^c, M. Bertaina^d, P.L. Biermann^e, J. Blümer^{a,f}, H. Bozdog^a, I.M. Brancus^c, S. Buitink^g, M. Brüggemann^h, P. Buchholz^h, H. Butcher^b, A. Chiavassa^d, K. Daumiller^a, A.G. de Bruyn^b, C.M. de Vos^b, F. Di Pierro^d, P. Doll^a, R. Engel^a, H. Falcke^{b,e,g}, H. Gemmekeⁱ, P.L. Ghia^j, R. Glasstetter^k, C. Grupen^h, A. Haungs^a, D. Heck^a, J.R. Hörandel^f, A. Horneffer^{e,g}, T. Huege^{a,e}, K.-H. Kampert^k, G.W. Kant^b, U. Klein^l, Y. Kolotaev^h, Y. Koopman^b, O. Krömerⁱ, J. Kuijpers^g, S. Lafebre^g, G. Maier^a, H.J. Mathes^a, H.J. Mayer^a, J. Milke^a, B. Mitrica^c, C. Morello^j, G. Navarra^d, S. Nehls^a, A. Nigl^g, R. Obenland^a, J. Oehlschläger^a, S. Ostapchenko^a, S. Over^h, H.J. Pepping^b, M. Petcu^c, J. Petrovic^g, T. Pierog^a, S. Plewnia^a, H. Rebel^a, A. Risse^m, M. Roth^f, H. Schieler^a, G. Schoonderbeek^b, O. Sima^c, M. Stümpert^f, G. Toma^c, G.C. Trinchero^j, H. Ulrich^a, S. Valchierotti^d, J. van Buren^a, W. van Capellen^b, W. Walkowiak^h, A. Weindl^a, S. Wijnholds^b, J. Wochele^a, J. Zabierowski^m, J.A. Zensus^e, D. Zimmermann^h

(a) Institut für Kernphysik, Forschungszentrum Karlsruhe, 76021 Karlsruhe, Germany

(b) ASTRON, 7990 AA Dwingeloo, The Netherlands

(c) National Institute of Physics and Nuclear Engineering, 7690 Bucharest, Romania

(d) Dipartimento di Fisica Generale dell'Università, 10125 Torino, Italy

(e) Max-Planck-Institut für Radioastronomie, 53121 Bonn, Germany

(f) Institut für Experimentelle Kernphysik, Universität Karlsruhe, 76021 Karlsruhe, Germany

(g) Department of Astrophysics, Radboud University Nijmegen, 6525 ED Nijmegen, The Netherlands

(h) Fachbereich Physik, Universität Siegen, 57068 Siegen, Germany

(i) Inst. Prozessdatenverarbeitung und Elektronik, Forschungszentrum Karlsruhe, 76021 Karlsruhe, Germany

(j) Istituto di Fisica dello Spazio Interplanetario, INAF, 10133 Torino, Italy

(k) Fachbereich Physik, Universität Wuppertal, 42097 Wuppertal, Germany

(l) Radioastronomisches Institut der Universität Bonn, 53010 Bonn, Germany

(m) Soltan Institute for Nuclear Studies, 90950 Lodz, Poland

Presenter: A.F. Badea (Florin.Badea@ik.fzk.de), ger-badea-AF-abs2-he13-oral

LOFAR (**LO**w **F**requency **AR**ray) [1] will be a new digital interferometer and is an attempt to revitalize astrophysical research by measuring radio wave emission at 10–240 MHz. A "LOfar PrototypE Station" (LOPES) has been built at the KASCADE-Grande experiment in order to test the LOFAR technology and to demonstrate its capability for radio measurements of Extensive Air Showers (EAS). Here we report the analysis performed by correlating the radio signals measured by LOPES-10 with EAS events reconstructed by KASCADE-Grande with remote cores included. Results will be discussed in particular concerning the correlation of the radio pulse amplitude with the primary cosmic ray energy and with the lateral distance from the shower axis.

1. Introduction

KASCADE-Grande [2] is the extension of the multi-detector setup KASCADE [3] and allows a full coverage of the energy range around the so-called "knee" of the primary cosmic ray spectrum ($10^{14} - 10^{18}$ eV). At present, LOPES operates 30 dipole radio antennas in coincidence with KASCADE; for this analysis only the 10 antennas forming LOPES-10 (see Fig. 2, left panel) are relevant. The 37 stations of the Grande extension

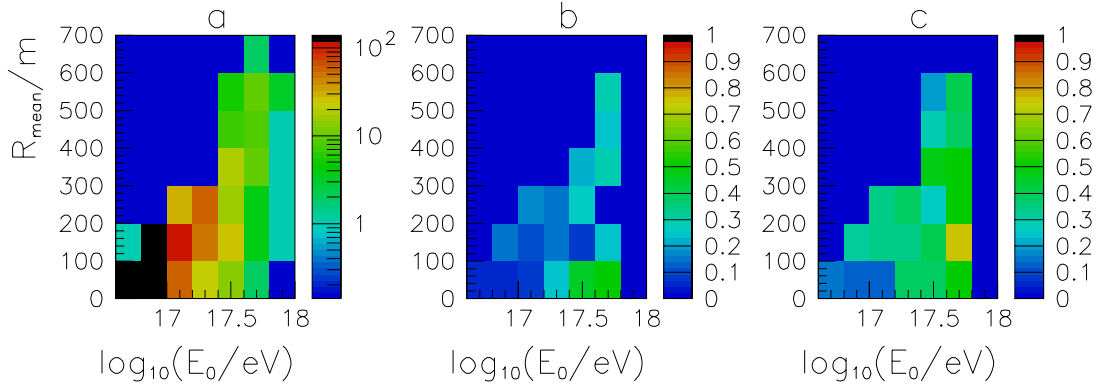


Figure 1. a) distribution of the candidate events on primary energy and distance to the shower axis; b) efficiency of the radio detection after beamforming; c) preliminary efficiency of the radio detection for an optimised beamforming (only performed for half of the sample, yet).

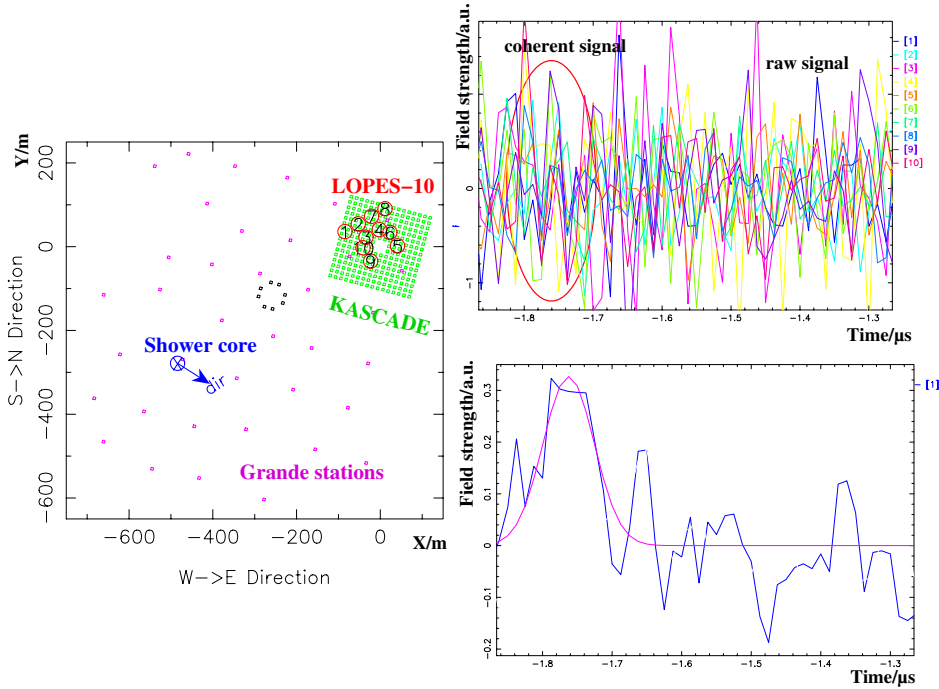


Figure 2. Remote event: mean distance to the shower axis $R_{mean} = 556.0$ m, zenith angle $\theta = 27.2^\circ$, angle to the geomagnetic field $\alpha = 24.3^\circ$, primary energy $E_0 = 10^{17.7}$ eV, curvature radius 2250 m (details in text).

of the KASCADE experiment covering approx. 0.5 km^2 are taking data in coincidence with KASCADE and LOPES and enable to reconstruct showers with primary energies up to 10^{18} eV and with distances between shower core and the LOPES-10 antennas up to 700 m. Due to the extremely low flux of the primary cosmic rays of ultrahigh energies, larger detectors with high acceptance and duty cycle are required. Besides the contribution of KASCADE-Grande to the astrophysics of high-energy cosmic rays, it is also the testbed [4] for the development and calibration of new air-shower detection techniques like the measurement of EAS radio

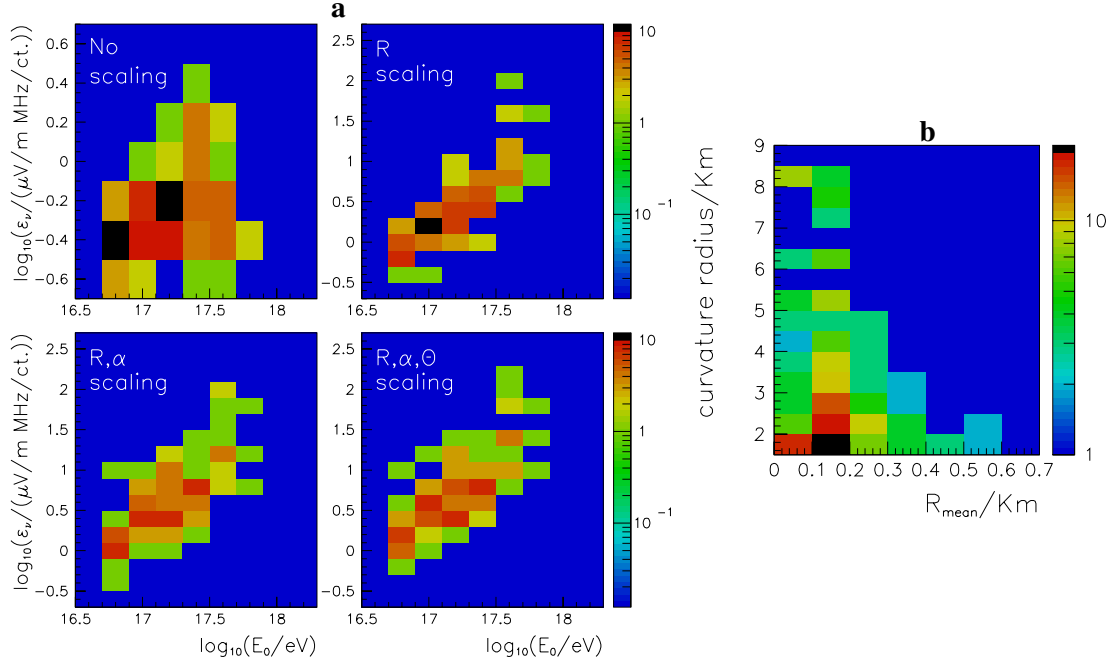


Figure 3. a) correlations of the primary energy and radio signals; b) correlation of the distance to the shower axis and curvature radius of the radio signal.

emission. Radio emission produced by EAS in the Earth's atmosphere is unaffected by attenuation, has a high duty cycle, is calorimetric and is very sensitive to the direction of the incoming primary cosmic ray [5].

2. Allan's formula; selection of events

It is believed that the pulse amplitude per unit bandwidth (ϵ_ν) of the radio signal induced by an EAS is described by the Allan's formula [6]:

$$\epsilon_\nu = 20 \cdot \left(\frac{E}{10^{17} \text{ eV}} \right) \cdot \sin \alpha \cdot \cos \theta \cdot \exp \left(-\frac{R}{R_0(\nu, \theta)} \right) \left[\frac{\mu\text{V}}{\text{m} \cdot \text{MHz}} \right] \quad (1)$$

with E – primary energy, α – angle to the geomagnetic field, θ – zenith angle, R – distance to the shower axis and the scaling radius $R_0 = 110$ m at 55 MHz; the exponential radial factor may play a significant role for remote showers. Due to the significant background encountered at the KASCADE-Grande site inside Forschungszentrum Karlsruhe, present LOPES procedures to analyse radio signals are semi-automatic and, at the end, a final check, by eye, event-by-event, is required. So, it looked reasonable to consider a radius dependent cut on the primary energy in order to reduce the number of (most probable) useless events. It has been considered a primary energy cut described by:

$$\lg \left(\frac{E}{\text{eV}} \right) > \lg \left(\frac{E_0}{\text{eV}} \right) + 0.4343 \cdot \frac{R}{R_0} \quad \text{OR} \quad \lg \left(\frac{E}{\text{eV}} \right) > 17.5 \quad (2)$$

with $E_0 = 10^{16.5}$ eV and $R_0 = 160$ m i.e. weaker than Allan's scaling with radius. Due to the lack of absolute calibration of the radio signal, the threshold primary energy E_0 has been chosen based on the results

from ref. [5] and data reduction considerations. Following additional cuts have been considered: period of joint acquisition LOPES + Grande Array + Field Array during 5 months at the beginning of 2004; a Field Array trigger, 10 clusters out of 16, as a necessary condition to have LOPES data; EAS zenith angle reconstructed by Grande Array below 50° ; a geometrical cut on the Grande Array reconstructed shower core position: $(X_C/m, Y_C/m) \in (-550, 0) \times (-600, 50)$. After all cuts, 862 candidate events have been obtained, as shown in Fig. 1a.

3. Efficiency of the radio detection; remote radio events; correlations

Fig. 1b shows the efficiency of the detection of radio signals in EAS using beamforming procedures based on the values provided by Grande reconstruction of the shower core and shower axis (SCA). The coherence of the 10 radio signals measured by LOPES-10 antennas is very sensitive to SCA [7]. After an optimised beamforming, searching for maximum coherence by varying the SCA inside the Grande reconstruction uncertainties, the efficiency is displayed by Fig. 1c. The efficiency is even higher because the optimised beamforming has been applied only for half of the candidate events, yet. Fig. 2 shows an example of a remote event with a clear radio signal. The arrow in the left panel points towards the incoming shower direction. The mean distance from the antennas to the shower axis is more than 550 m. After the time shifting procedure of the signals in the 10 antennas a clear coherence may be seen in the upper-right panel with the corresponding peak in the (cross correlation) CC-beam estimator of the coherence (down-right panel). In Fig. 3a all events from Fig. 1c, with good coherent radio signals, have been considered. No correlation between primary energy and the radio pulse amplitude can be seen in the upper-left panel; this is a normal behaviour due to the large surface of the Grande Array. By scaling the pulse amplitude according to the exponential radius factor of Allan's formula a clear correlation is seen, displayed in the upper right panel. By scaling subsequently with the sine of the angle to the geomagnetic field (down-left panel) and the cosine of the zenith angle, correlation in the down right panel has been obtained, which is comparable with the upper one but more symmetrical. Fig. 3b is a plot of the curvature radius of the radio front as function of the mean distance from the antennas to the shower axis. It appears an anticorrelation of the curvature radius with increasing distance to the shower axis.

4. Conclusions

LOPES-10 is able to detect radio signals induced by remote Extensive Air Showers even at distances from the shower axis of more than 500 m, for primary energies above $10^{17.7}$ eV. Allan's formula seems to be verified at least on the radius correlation. Curvature radius of the radio front decreases with increasing distance to the shower axis.

References

- [1] <http://www.lofar.org/>
- [2] G. Navarra et al. - KASCADE-Grande collab., Nucl. Instr. & Meth. A 518, 207 (2004).
- [3] T. Antoni et al. - KASCADE collab., Nucl. Instr. & Meth. A 513, 429 (2003).
- [4] A.F. Badea et al. - LOPES collab., Proceedings of CRIS2004, Nucl. Phys. Proc. Suppl. 136B, 384 (2004).
- [5] H. Falcke et al. - LOPES collab., Nature 435, 313 (2005).
- [6] H.R. Allan, Prog. in Element. Part. and Cos. Ray Phys., Vol. 10, 171 (1971).
- [7] A.F. Badea et al. - LOPES collab., First determination of the reconstruction resolution of an EAS radio detector, these proceedings.

Radio emission of highly inclined cosmic ray air showers measured with LOPES

J. Petrovic^g, W.D. Apel^a, F. Badea^a, L. Bühren^b, K. Bekk^a, A. Bercuci^c, M. Bertaina^d, P.L. Biermann^e, J. Blümer^{a,f}, H. Bozdog^a, I.M. Brancus^c, S. Buitink^g, M. Brüggemann^h, P. Buchholz^h, H. Butcher^b, A. Chiavassa^d, K. Daumiller^a, A.G. de Bruyn^b, C.M. de Vos^b, F. Di Pierro^d, P. Doll^a, R. Engel^a, H. Falcke^{b,e,g}, H. Gemmekeⁱ, P.L. Ghia^j, R. Glasstetter^k, C. Gruppen^h, A. Haungs^a, D. Heck^a, J.R. Hörandel^l, A. Horneffer^{e,g}, T. Huege^{a,e}, K.-H. Kampert^k, G.W. Kant^b, U. Klein^l, Y. Kolotaev^h, Y. Koopman^b, O. Krömerⁱ, J. Kuijpers^g, S. Lafebre^g, G. Maier^a, H.J. Mathes^a, H.J. Mayer^a, J. Milke^a, B. Mitrica^c, C. Morello^j, G. Navarra^d, S. Nehls^a, A. Nigl^g, R. Obenland^a, J. Oehlschläger^a, S. Ostapchenko^a, S. Over^h, H.J. Pepping^b, M. Petcu^c, T. Pierog^a, S. Plewnia^a, H. Rebel^a, A. Risse^m, M. Roth^f, H. Schieler^a, G. Schoonderbeek^b, O. Sima^c, M. Stümpert^f, G. Toma^c, G.C. Trinchero^j, H. Ulrich^a, S. Valchierotti^d, J. van Buren^a, W. van Capellen^b, W. Walkowiak^h, A. Weindl^a, S. Wijnholds^b, J. Wochele^a, J. Zabierowski^m, J.A. Zensus^e, D. Zimmermann^h

(a) Institut für Kernphysik, Forschungszentrum Karlsruhe, 76021 Karlsruhe, Germany

(b) ASTRON, 7990 AA Dwingeloo, The Netherlands

(c) National Institute of Physics and Nuclear Engineering, 7690 Bucharest, Romania

(d) Dipartimento di Fisica Generale dell'Università, 10125 Torino, Italy

(e) Max-Planck-Institut für Radioastronomie, 53010 Bonn, Germany

(f) Institut für Experimentelle Kernphysik, Universität Karlsruhe, 76021 Karlsruhe, Germany

(g) Department of Astrophysics, Radboud University Nijmegen, 6525 ED Nijmegen, The Netherlands

(h) Fachbereich Physik, Universität Siegen, 57068 Siegen, Germany

(i) Inst. Prozessdatenverarbeitung und Elektronik, Forschungszentrum Karlsruhe, 76021 Karlsruhe, Germany

(j) Istituto di Fisica dello Spazio Interplanetario, INAF, 10133 Torino, Italy

(k) Fachbereich Physik, Universität Wuppertal, 42097 Wuppertal, Germany

(l) Radioastronomisches Institut der Universität Bonn, 53121 Bonn, Germany

(m) Soltan Institute for Nuclear Studies, 90950 Lodz, Poland

Presenter: S. Buitink (sbuitink@astro.ru.nl)

LOPES (LOFAR Prototype Station) is an array of dipole antennas used for detection of radio emission from air showers. It is co-located and triggered by the KASCADE (Karlsruhe Shower Core and Array Detector) experiment, which also provides informations about air shower properties. Even though neither LOPES nor KASCADE are completely optimized for the detection of highly inclined events, a significant number of showers with zenith angle larger than 50° have been detected in the radio domain, and many with very high field strengths. Investigation of inclined showers can give deeper insight into the nature of primary particles that initiate showers and also into the possibility that some of detected showers are triggered by neutrinos. In this paper, we show the example of such an event and present some of the characteristics of highly inclined showers detected by LOPES.

1. Introduction

When a cosmic ray interacts with particles in the Earth atmosphere, it produces a shower of elementary particles propagating towards the grounds with almost the speed of light. The first suggestion that these air showers can produce radio emission was given by Askaryan [1] based on a charge-excess mechanism. Recently, Falcke&Gorham [2] proposed that the mechanism for radio emission of air showers is coherent geosynchrotron radiation. Secondary electrons and positrons produced in the particle cascade are deflected in the Earth magnetic field and this produces dipole radiation that is relativistically beamed in the forward direction. The shower front emitting the radiation has a thickness which is comparable to a wavelength for radio emission below 100MHz (around few meters). The emission is coherent which amplifies the signal.

Radio emission of cosmic ray air showers has been detected by LOPES (LOFAR Prototype Station) [3], a phased array of dipole antennas co-located with the KASCADE (Karlsruhe Shower Core and Array Detector) experiment which provides coincidence triggers for LOPES and well-calibrated informations about air-shower properties, like electron number N_e , reconstructed muon number N_μ , azimuth and zenith angle of the event. The LOPES experiment and data reduction are described in detail by Horneffer et al. [4].

Highly inclined showers are expected to be very well detectable in the radio domain [5],[6]. However, we have to mention that neither LOPES nor KASCADE are optimized for large zenith angles. For example, KASCADE reconstruction of electron and muon number can be not accurate especially in cases when the shower core of specific event falls out of the KASCADE array.

Inclined cosmic ray air showers are specific, since they travel trough few times longer distances in the Earth atmosphere compared to vertical showers, and due to this most of the electromagnetic (particle) component of those showers has been absorbed. So, inclined showers that start high in the atmosphere (initiated by protons, iron nuclei or gamma-photons) will have large electron deficiency on the ground level compared to vertical showers. On the other hand, neutrino induced showers may be generated at any distance from the ground [7] so they could clearly be distinguished from those whose primary particle initiated the shower high in the atmosphere by the number of electrons that reach the ground level.

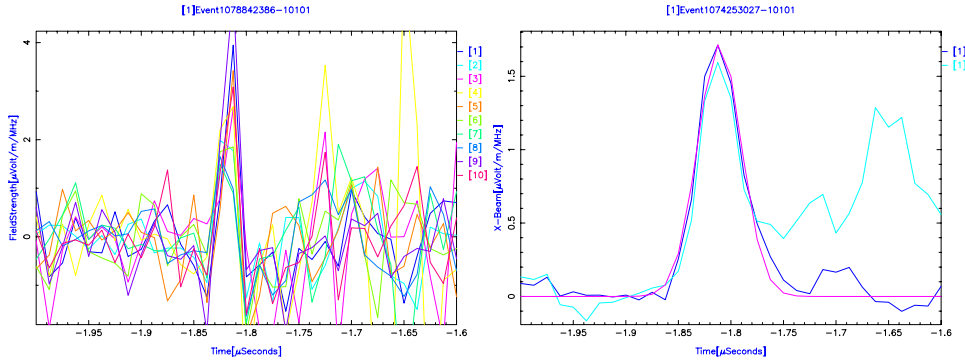


Figure 1. Left: Electric field as a function of time for 10 LOPES antennas for an event detected in March 2004 with zenith angle 53.3° and azimuth 54.7° . The angle between the shower core and the Earth magnetic field is 69.8° . $N_e=1.5 \cdot 10^6$, $N_\mu=1.0 \cdot 10^6$, reconstructed by KASCADE. Right: Radio emission as a function of time after beam forming for the same event. Dark blue line represents X-beam, light blue line the total power and pink line the Gaussian fit for X-beam.

2. Discussion

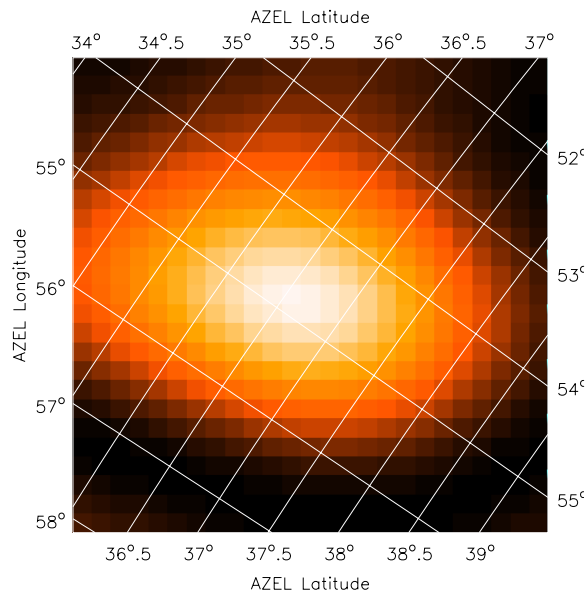


Figure 2. Radio map of the cosmic ray shower with zenith angle 53.3° detected in March 2004. Azimuth (AZEL longitude) and elevation (AZEL latitude) of the event are given on the axes.

We made a selection of inclined events from data taken during year 2004 (also detected by the KASCADE array where the reconstructed shower cores were less than 100m away from the array center). We found 2017 events with zenith angle larger than 50° . Then we introduced an additional condition: $N_\mu > 10^5$. In this way we narrowed the selection to 51 event and more than 40% of those are detected in the radio domain, many with very large field strengths, even though a threshold on muon number is lower than the one used for bright events in [3]. However, as we already mentioned, KASCADE is not optimized for large zenith angles, so the reconstruction of the electron and muon number failed for half of the detected events. This leaves us with 10 events with strong radio signal and reliable shower properties reconstructed by KASCADE.

As an example, we show here one of those events, detected in March 2004 with zenith angle 53.3° and azimuth 54.7° with roughly the same number of electrons and muons $N_e, N_\mu \approx 1.5 \cdot 10^6$ (reconstructed by KASCADE). The angle between the shower axis and the Earth magnetic field (geomagnetic angle) is 69.8° .

In Figure 1 (left) we show the electric field as a function of time for each antenna. The field is coherent at $-1.825\mu\text{s}$ which is the arrival time of the shower. The incoherent noise after is radio emission from photomultipliers and in this case is very weak. Figure 1 (right) shows the radio emission as a function of time after X(excess)-beam forming. This beam is formed in the following way. First squared signals of all antennas are summed which gives the total power. Then signals of all two antenna combinations are multiplied and summed which gives the CC(cross correlation)-beam. Finally, CC-beam is multiplied with the ratio between CC-beam and total power. In this way a suppression of incoherent noise is achieved.

Figure 2 is a radio map of the example event. The air shower is the brightest point in the sky for several tens of nanoseconds. The resolution of the map is $\sim 2^\circ$ in azimuth and elevation towards the zenith.

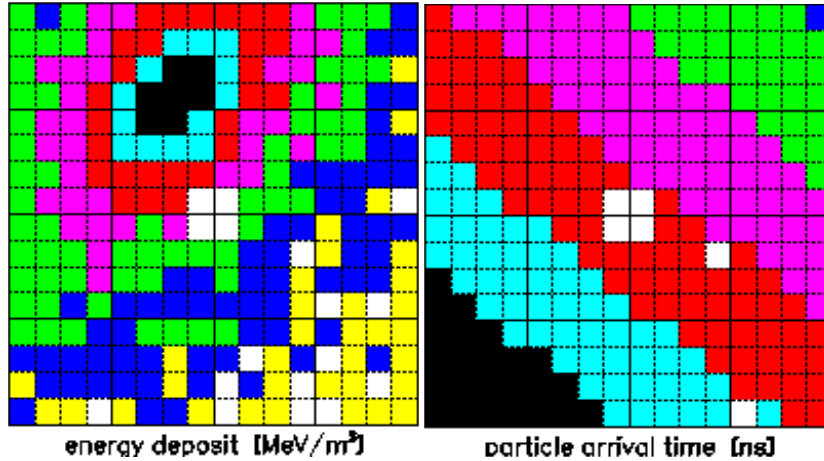


Figure 3. Left: Energy deposit of the cosmic ray shower with zenith angle 53.5° detected in March 2004 for e/γ KASCADE detectors. Dark blue color shows energy deposit of $100\text{MeV}/\text{m}^2$, red color $1000\text{MeV}/\text{m}^2$. Maximum energy deposit for this event is $\sim 4500\text{MeV}/\text{m}^2$. Right: Particle arrival time for the same event. Dark blue color represents $\sim 300\text{ns}$, red $\sim 800\text{ns}$.

Figure 3 gives the energy deposit of the chosen cosmic ray shower over the KASCADE array with e/γ detectors (left panel) and particle arrival time (right panel). We can see that the shower core falls within the KASCADE array and that the maximum energy is deposited in the north-western part, within the LOPES array. We can notice elliptical shapes of isolines of energy deposit, which is typical for inclined events.

3. Conclusions

Even though neither LOPES nor KASCADE are completely optimized for the detection of highly inclined events, we find that in a selection of events with zenith angle larger than 50° and $N_\mu > 10^5$ (51 event) around 40% of all events is detected in the radio domain, and some of them with very high field strengths, like the example we have presented in this paper. The most inclined cosmic ray air shower that we detected with LOPES has a zenith angle of almost 70° .

After checking the reconstruction of N_e and N_μ different correlations can be considered, for example between radio pulse height and muon number, electron number or geomagnetic angle. This will also give more insight into the nature of primary particles that initiate showers and the possibility that some of detected showers might have been triggered by neutrinos.

References

- [1] Askaryan, G. A., Soviet Phys. JETP 14, 441-443 (1962)
- [2] Falcke, H., Gorham, P.W., Astropart. Phys. 19,477-494 (2003)
- [3] Falcke, H. et al., Nature, 435,7040, 313-316 (2005)
- [4] Horneffer, A. et al., Proceedings of the SPIE 5500, 129-138 (2004)
- [5] Huege, T., Falcke, H., Astropart. Phys. (in press), astro-ph/0501580 (2005)
- [6] Gousset, T., Ravel, O., Roy, C., Astropart. Phys. 22, 103-107 (2004)
- [7] Capelle, K. S., Cronin, J. W., Parente, G., Zas, E., Astropart. Phys. 8, 321-328.

Electric field influence on the radio emission of air showers

S. Buitink^g, W.D. Apel^a, F. Badea^a, L. Bühren^b, K. Bekk^a, A. Bercuci^c, M. Bertaina^d, P.L. Biermann^e, J. Blümer^{a,f}, H. Bozdog^a, I.M. Brancus^c, M. Brüggemann^h, P. Buchholz^h, H. Butcher^b, A. Chiavassa^d, K. Daumiller^a, A.G. de Bruyn^b, C.M. de Vos^b, F. Di Pierro^d, P. Doll^a, R. Engel^a, H. Falcke^{b,e,g}, H. Gemmekeⁱ, P.L. Ghia^j, R. Glasstetter^k, C. Grupen^h, A. Haungs^a, D. Heck^a, J.R. Hörandel^f, A. Horneffer^{e,g}, T. Huege^{a,e}, K.-H. Kampert^k, G.W. Kant^b, U. Klein^l, Y. Kolotaev^h, Y. Koopman^b, O. Krömerⁱ, J. Kuijpers^g, S. Lafebre^g, G. Maier^a, H.J. Mathes^a, H.J. Mayer^a, J. Milke^a, B. Mitrica^c, C. Morello^j, G. Navarra^d, S. Nehls^a, A. Nigl^g, R. Obenland^a, J. Oehlschläger^a, S. Ostapchenko^a, S. Over^h, H.J. Pepping^b, M. Petcu^c, J. Petrovic^g, T. Pierog^a, S. Plewnia^a, H. Rebel^a, A. Risse^m, M. Roth^f, H. Schieler^a, G. Schoonderbeek^b, O. Sima^c, M. Stümpert^f, G. Toma^c, G.C. Trinchero^j, H. Ulrich^a, S. Valchierotti^d, J. van Buren^a, W. van Capellen^b, W. Walkowiak^h, A. Weindl^a, S. Wijnholds^b, J. Wochele^a, J. Zabierowski^m, J.A. Zensus^e, D. Zimmermann^h

(a) Institut für Kernphysik, Forschungszentrum Karlsruhe, 76021 Karlsruhe, Germany

(b) ASTRON, 7990 AA Dwingeloo, The Netherlands

(c) National Institute of Physics and Nuclear Engineering, 7690 Bucharest, Romania

(d) Dipartimento di Fisica Generale dell'Università, 10125 Torino, Italy

(e) Max-Planck-Institut für Radioastronomie, 53010 Bonn, Germany

(f) Institut für Experimentelle Kernphysik, Universität Karlsruhe, 76021 Karlsruhe, Germany

(g) Department of Astrophysics, Radboud University Nijmegen, 6525 ED Nijmegen, The Netherlands

(h) Fachbereich Physik, Universität Siegen, 57068 Siegen, Germany

(i) Inst. Prozessdatenverarbeitung und Elektronik, Forschungszentrum Karlsruhe, 76021 Karlsruhe, Germany

(j) Istituto di Fisica dello Spazio Interplanetario, CNR, 10133 Torino, Italy

(k) Fachbereich Physik, Universität Wuppertal, 42097 Wuppertal, Germany

(l) Radioastronomisches Institut der Universität Bonn, 53121 Bonn, Germany

(m) Soltan Institute for Nuclear Studies, 90950 Lodz, Poland

Presenter: S. Buitink (s.buitink@astro.ru.nl), net-buitink-SJ-abs1-he13-oral

The radio emission of extensive air showers can be understood as coherent geosynchrotron emission of electrons and positrons travelling through the earth's magnetic field. Here we investigate if atmospheric electric fields can play a significant role in the emission process. For fair weather conditions ($E \approx 100\text{Vm}^{-1}$) this effect can only slightly change the emission intensity. We show that these changes depend on the direction to the observer. In thunderclouds, however, electric fields reach much higher magnitudes that enhance the emission strongly. We investigate LOPES data that was recorded during thunderstorms and compare it with fair weather data. We find that air showers that take place during thunderstorms emit more radio emission than fair weather air showers with similar characteristics.

1. Introduction

The secondary electrons and positrons of an extensive air shower produce coherent radio emission in the atmosphere. It was shown by Falcke et al.[1] that the intensity of the radio emission is strongly correlated with the angle of the shower direction with the geomagnetic field, proving that the emission is of geosynchrotron

nature. We investigate if the electric field in the atmosphere can play a significant role in the emission mechanism. We consider two types of electric fields: the fair weather field, which is always around 100 Vm^{-1} at ground level, rapidly decreasing with altitude, and the fields in and around thunderclouds. The largest electric field magnitude typically measured at the base of a thundercloud is $10 - 50 \text{ kVm}^{-1}$ and $70 - 200 \text{ kVm}^{-1}$ inside the thundercloud. At ground level the field strength is typically $1 - 10 \text{ kVm}^{-1}$ during thunderstorm conditions (all values taken from [2]). Under fair weather conditions the electric field can affect the radio emission due to the electric force acceleration. This is described in section 2. Under influence of the large fields inside thunderclouds this effect increases, but also other effects can play a role. Electrons that are created by ionization can runaway and start breakdown avalanches [3], also contributing to the radio emission. In section 3 we investigate the data recorded by the LOPES experiment during thunderstorms and compare it to fair weather data.

2. Electric field effect on radio emission

As the electrons and positrons are curved in the geomagnetic field they emit synchrotron radiation. The intensity of the emission is determined by the acceleration of the particles. A force applied perpendicular to the direction of motion produces a total radiated power which is a factor γ^2 larger than the same force parallel to the direction of motion. The Lorentz force is always perpendicular to the particles' direction, but the electric force can have any angle with respect to the trajectory. Figure 1 shows the trajectories of an electron-positron pair that is created in a vertical shower. The electric field is directed downwards and the magnetic field out of the paper. As the particles curve in the magnetic field, the radius of curvature of the positrons increases, while that of the electrons decreases. In the first part of the trajectories the electric force is parallel to the direction of

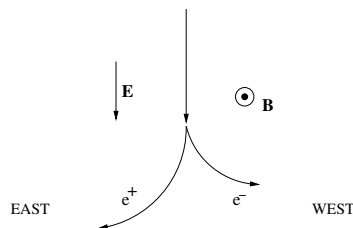


Figure 1. The electrons and positrons make curved trajectories in the magnetic field. Under influence of a downward directed electric field, the positron (electron) radius of curvature will increase (decrease). The asymmetry in the trajectories will be reflected in the radio emission.

motion and will not significantly change the emitted power unless the field strength is very high. The emission from this part reaches observers on the north-south axis. Here the electric field effect will be minimal. The further the electrons curve to the west, the higher the fraction of the electric force that acts perpendicular to the direction of motion becomes. The electric force is in the same direction as the Lorentz force, so the acceleration will increase. Observers in the west will therefore see an increase in radio emission. To the east the electric force acts opposite to the Lorentz force and a decrease in radio emission is to be expected. The magnitude of the increase or decrease in radio emission can be estimated by comparing the electric force to the Lorentz force. For a vertical shower under fair weather conditions at the site of the LOPES experiment the electric force is below 3% of the Lorentz force. For highly inclined showers the electric force will have a larger component

perpendicular to the direction of motion and its effect will be larger. In thunderstorm electric fields the electric force can even become larger than the Lorentz force.

3. Evaluation of thunderstorm data

From the LOPES event database we selected a set of 2214 events that took place during thunderstorm conditions. These conditions were identified by looking at lightning maps from a weather station and LOPES detections of lightning strikes, which can be recognized because they produce a saturated signal over the whole frequency range (43-73 MHz). In this way we found 25 hours of useful data divided over 7 separate thunderstorms.

A combined signal of all LOPES antennas was reconstructed by temporal shifting of the pulses in accordance with the arrival direction in the KASCADE air-shower data [4]. The coherence is further optimized by varying the radius of curvature of the shower front. In the dataset we found 6 bright radio pulses. For all these events (A-F) we made a selection of twin events, i.e. events that are associated with a shower with similar electron and muon number (within 10%) but occurred under fair weather conditions. The bright events in these twin groups were compared to the thunderstorm events. The plots of Figure 2 show the normalized radio peak height for all bright events in the 6 twin groups. The thunderstorm event is indicated with a red circle. To normalize, the radio intensity is divided by the muon number and corrected for the geomagnetic angle. For the latter an empirical result from [1] was used: the radio emission peak height is proportional to $(1 - \cos \alpha)$, where α is the angle of the shower direction with the geomagnetic field. In all groups, the thunderstorm event has the highest normalized radio intensity. For some (B,C,D) the intensity of the thunderstorm event is more than three times as large as the fair weather events. To check if our procedure was not biased by selection effects we repeated

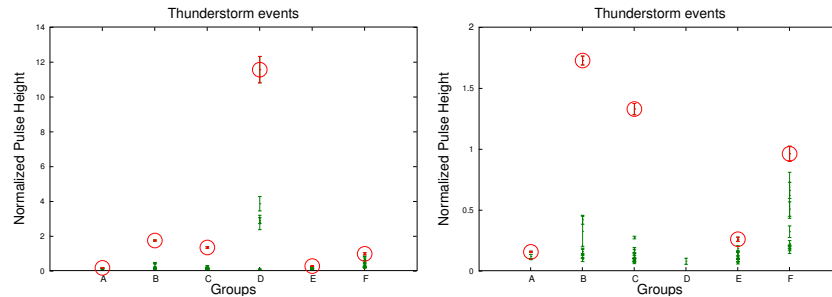


Figure 2. Normalized radio pulse height for 6 groups of twin events. The thunderstorm events are indicated with red circles. Their fair weather twin events are plotted in green. The right plot zooms in on the lower part of the left plot.

the whole procedure with a new data set of 2150 events that were recorded during 25 hours of fair weather. In this set, 3 bright events were found. These events and their twin group (G-I) are plotted in Figure 3. In none of the cases the preselected event is the largest of its group.

4. Conclusions and discussion

Figure 2 shows that for all the 6 bright thunderstorm events that we found, the radio emission is stronger than that of showers with similar electron and muon number. In three cases (B,C,D) this difference is of a factor > 3 . In Figure 3 this behaviour is not seen, which proves that it is not a selection effect. The mean distance

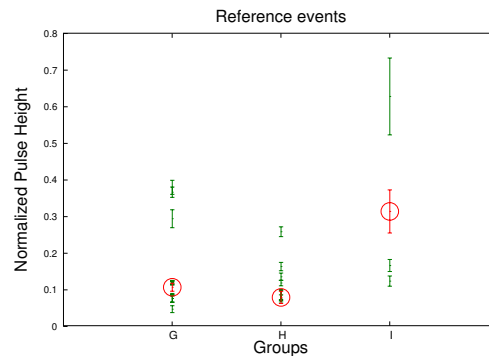


Figure 3. Same as Figure 2 for 3 groups of twin events. The events indicated with red circles are the original events. None of the events are thunderstorm events.

between the shower core and the antennas is not the same for each event and has a small effect on the measured intensity, which is not corrected for in our analysis.

The enhancement of the radio emission strongly depends on the direction of the electric field. Since electric fields inside thunderclouds can have either positive or negative polarity and are sometimes even horizontally directed, the effect on the air shower electrons/positrons can be different from storm to storm. It is therefore not surprising that some cases show larger radio enhancement than other cases. Our result clearly shows that thunderstorm data should be handled separately from other events. Better statistics can be achieved by evaluating more thunderstorms and improving the detection method for thunderstorm activity. This could be done with a trigger from the radio data or an electric field mill that measures the electric field at ground level.

5. Outlook

We will improve the Monte Carlo code presented in [5] with routines to calculate radio emission of air showers in an electric field. With the code, we will investigate the effect of the fair weather electric field on the radio emission and look for east-west asymmetries in the results. A good understanding of the geometry and size of this effect will improve the accuracy of an air shower energy estimate based on radio emission. Also, we will simulate the effect of strong local magnetic fields as they occur inside thunderclouds. At the same time more thunderstorms will be investigated to gain better statistics and find geometrical asymmetries.

The interaction of air showers and thunderstorms can lead to interesting phenomena. Runaway ionization electrons created by an air shower can cause local field amplification which might produce narrow radio pulses or trigger lightning strikes [3]. The unique possibility of the LOPES experiment to distinguish air shower radio pulses from radio pulses of a different nature, allows us to investigate such theories.

References

- [1] H. Falcke et al., *Nature* 435, 313-316 (2005).
- [2] D. MacGorman and W. Rust, *The electrical nature of storms* (Oxford University Press, New York, 1998)
- [3] A. V. Gurevich et al., *Physics Letters A* 301, 320-326 (2002)
- [4] A. Horneffer et al., *Proc. SPIE* 550-21 (2004)
- [5] T. Huege and H. Falcke, *A&A* 430, 779-798 (2005)

A Cosmic Ray Trigger for LOFAR

S. Lafebre^a, A. Nigl^a, W.D. Apel^b, F. Badea^b, L. Bähren^c, K. Bekk^b, A. Bercuci^d, M. Bertaina^e, P.L. Biermann^f, J. Blümer^{b,g}, H. Bozdog^b, I.M. Brancus^d, S. Buitink^a, M. Brüggemann^h, P. Buchholz^h, H. Butcher^c, A. Chiavassa^e, K. Daumiller^b, A.G. de Bruyn^c, C.M. de Vos^c, F. Di Piero^e, P. Doll^b, R. Engel^b, H. Falcke^{a,c,f}, H. Gemmekeⁱ, P.L. Ghia^j, R. Glasstetter^k, C. Grupen^h, A. Haungs^b, D. Heck^b, J.R. Hörandel^g, A. Horneffer^{a,f}, T. Huege^{b,f}, K.-H. Kampert^k, G.W. Kant^c, U. Klein^l, Y. Kolotaev^h, Y. Koopman^c, O. Krömerⁱ, J. Kuijpers^a, G. Maier^b, H.J. Mathes^b, H.J. Mayer^b, J. Milke^b, B. Mitrica^d, C. Morello^j, G. Navarra^e, S. Nehls^b, R. Obenland^b, J. Oehlschläger^b, S. Ostapchenko^b, S. Over^h, H.J. Pepping^c, M. Petcu^d, J. Petrovic^a, T. Pierog^b, S. Plewnia^b, H. Rebel^b, A. Risse^m, M. Roth^g, H. Schieler^b, G. Schoonderbeek^c, O. Sima^d, M. Stümpert^g, G. Toma^d, G.C. Trinchero^j, H. Ulrich^b, S. Valchierotti^e, J. van Buren^b, W. van Capellen^e, W. Walkowiak^h, A. Weindl^b, S. Wijnholds^c, J. Wochele^b, J. Zabierowski^m, J.A. Zensus^f, D. Zimmermann^h

(a) Dept. of Astrophysics, IMAPP, Radboud University, 6525 ED Nijmegen, The Netherlands

(b) Institut für Kernphysik, Forschungszentrum Karlsruhe, 76021 Karlsruhe, Germany

(c) ASTRON, 7990 AA Dwingeloo, The Netherlands

(d) National Institute of Physics and Nuclear Engineering, 7690 Bucharest, Romania

(e) Dipartimento di Fisica Generale dell'Università, 10125 Torino, Italy

(f) Max-Planck-Institut für Radioastronomie, 53121 Bonn, Germany

(g) Institut für Experimentelle Kernphysik, Universität Karlsruhe, 76021 Karlsruhe, Germany

(h) Fachbereich Physik, Universität Siegen, 57068 Siegen, Germany

(i) Inst. Prozessdatenverarbeitung und Elektronik, Forschungszentrum Karlsruhe, 76021 Karlsruhe, Germany

(j) Istituto di Fisica dello Spazio Interplanetario, INAF, 10133 Torino, Italy

(k) Fachbereich Physik, Universität Wuppertal, 42097 Wuppertal, Germany

(l) Radioastronomisches Institut der Universität Bonn, 53010 Bonn, Germany

(m) Soltan Institute for Nuclear Studies, 90950 Lodz, Poland

Presenter: Andreas Nigl (a.nigl@astro.ru.nl), net-nigl-abs2-he15-poster

We present the development and first results of an independent cosmic ray trigger for the multiple dipole antenna radiotelescope LOFAR (LOw Frequency ARray). LOPES (LOfar PrototypE Station), at the KASCADE (KARlsruhe Shower Core and Array DETector) site in Germany, has been initiated as a test case for LOFAR, and designed to detect air showers through their coherent radiation pulses upon external triggers by particle detectors. To fully exploit the capabilities in detecting CRS with the final LOFAR telescope, however, an independent, radio-only trigger is needed. We are searching for pulse coincidences in the antenna digital data stream. The limiting factor for applying real-time detection is the capacity of digital processing of the $8 \cdot 10^7$ samples per second per antenna. Here, we discuss constraints on basic criteria for the detection, like number of antennas, pulse height, pulse width, direction, distance of shower maximum and polarisation. We also present the first results of the application of such a trigger, and discuss optimization of the different parameters.

1. Introduction

A Dutch consortium, headed by ASTRON (The Netherlands Foundation for Research in Astronomy), is building a new radio telescope which is based on an array consisting of simple dipole antennas (see Figure 1a) with bandwidths of 30 to 80 MHz and 120 to 240 MHz. This telescope is called LOFAR (Low Frequency ARray), and will consist of a core of a few square kilometers (3 200 antennas), and 61 outer stations with a diameter of 100–200 m (100 detectors) each, spread out over an area 150 km in diameter in total (see Figure 1b). The total bandwidth from 30 to 240 MHz is covered by two different antenna types. The *low frequency antennas* are tuned to 30 to 80 MHz, the *high frequency antennas* to 120 to 240 MHz.

Of the five key projects, four propose to observe specific astronomical objects, and one addresses the study of Ultra High Energy Cosmic Rays (UHECR). In this latter project, we aim to detect air showers through radiosynchrotron radiation. The charged particles in the shower (mainly electrons and positrons) are deflected in the Earth's magnetic field and emit coherent geosynchrotron radiation [1, 2].

Currently, three test stations for LOFAR exist, two of which are optimized for cosmic ray air shower measurements in the radio regime from 40 to 80 MHz. LOPES [3], the LOfar PrototypE Station consists of 30 dipoles. For simultaneous data acquisition of particles and radio emission, LOPES is triggered by the KARlsruhe Shower Core and Array DETector (KASCADE), situated at the Forschungszentrum Karlsruhe in Germany [4]. Since the beginning of 2004 we have recorded more than a million triggered events, more than a thousand of which are detected in radio. The second prototype is called LORUN (LOfar @ Radboud University Nijmegen) consisting of four crossed dipole antennas on top of the university building. LORUN is triggered by two particle detectors of the Nijmegen Area High School Array (NAHSA). The use of this prototype station lies mainly in the fields of outreach and education. The third test station is ITS (Initial Test Station), but currently no cosmic ray research has been carried out with this instrument.

From confirmed detections of cosmic ray air showers with LOPES [5], we have learned about basic properties of the antenna response to the radio signal. Based on this experience, we are developing a method to trigger the antennas without using particle detectors. In this way, all kinds of transient events in the radio data can be studied, and detecting air showers is not limited to the field of view and sensitivity of an external particle detector.

In this article we explain the self-trigger method and discuss its application for the LOFAR project.

2. Method

For the detection of Cosmic Rays (CR) with LOFAR dipole antennas, we develop an algorithm to find short pulses in the digitized data. The LOFAR design suggests to divide the trigger into three hardware levels:

In the first step, the signal will be monitored on a per-antenna level. A dedicated transient buffer board, consisting of Field Programmable Gate Arrays (FPGAs), performs real-time data analysis according to the algorithm

$$|x(t)| > \mu_n(t - t_1) + k\sigma_n(t - t_1), \quad (1)$$

where $x(t)$ is the received signal, and $\mu_n(t - t_1)$ is the time averaged signal, running over a time interval t_n (containing n samples) ending at time $t - t_1$. This is done to avoid 'contamination' of the average. $\sigma_n(t - t_1)$ is the standard deviation over the same sample block, and k is the threshold factor for the standard deviation. When the condition is fulfilled and the signal is above an overall power level, the station core processor is notified.

At station level, the core processor monitors the antenna messages. A station trigger is generated, when the



Figure 1. **A:** A prototype LOFAR antenna. The dipoles run down the black PVC tubes. **B:** LOFAR layout showing the core and logarithmically spaced remote stations on five spiral arms in the border region of the Netherlands and Germany.

number of antenna messages exceeds a decision limit n_a within a certain time window t_2 , e.g. the light travel time between the antennas. When the decision for a trigger is made, the relevant part of the data buffer for all antennas in the station is downloaded and sent to the LOFAR core processor (~ 25 MB for 1 ms of data per antenna). Since the data production is not continuous the data transfer can be performed without disturbing the data acquisition of other observations.

Finally, at full LOFAR level, the obtained event is roughly analyzed to obtain estimates for shower properties like direction of arrival, lateral particle distribution, and primary energy. If the event is found to be a ‘random’ occurrence it is deleted, else it is transferred to the data center at the Radboud University Nijmegen, where further offline analysis is performed. We estimate to receive up to a few GB of data per day.

3. Parameter optimization

The above trigger introduces a handful parameters to adjust. First of all, we have to rely on absolute gain calibration of a single antenna element to set a minimum absolute signal height for the peak search algorithm. This level also sets a lower limit on the minimum cosmic ray energy that can be detected at single antenna level. Since no absolute calibration is available yet for LOPES or LOFAR, we will not discuss this parameter here.

To test dependencies on the other parameters, a collection of bright events was used, which is a subset of the selection by A. Horneffer [3]. Steps 1 and 2 of the trigger algorithm were run over 156 event files, using various combinations of parameters. Because the exact time of the occurrence of a cosmic ray pulse is known, the returned triggers could be marked ‘correct’ or ‘incorrect’.

Changing n_a between 4 and 7 (out of 8 available dipole signals) does not influence the amount of correct detections much. Changing the value for t_2 also hardly has an effect on the trigger quality; a value of $0.63 \mu\text{s}$, slightly larger than the light travel time through the detector, does the trick quite well, and this value has been used throughout.

The block size t_n and threshold value k are probably the most important selector for the type of event one wants to trigger on: larger block sizes will trigger broader events, higher threshold values will produce less

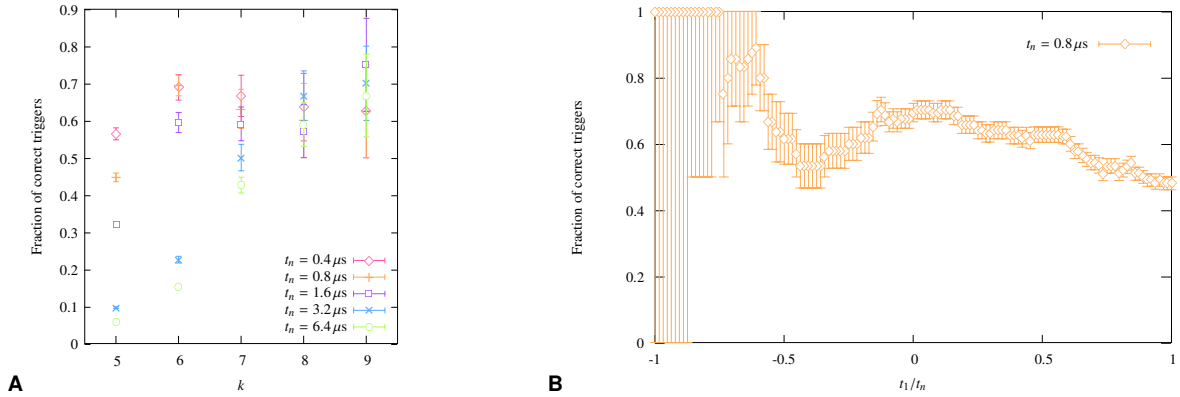


Figure 2. A: Trigger performance for the discussed trigger algorithm for various values of k and t_n . In this plot, $t_1 = 0$, $t_2 = 63 \mu\text{s}$, and $n_a = 5$. The error bars are a measure for the absolute number of detected events: the longer the error bars, the smaller the number of events. **B:** Trigger performance for the discussed trigger algorithm for various values of t_1 . In this plot, $t_n = 0.8 \mu\text{s}$, $k = 6.0$, $t_2 = 63 \mu\text{s}$, and $n_a = 5$. t_1 is expressed in units of t_n .

triggers in general. In Figure 2a, we tested the performance of our algorithm for certain values of k and t_n . This performance ratio, given on the vertical axis, is the fraction of correctly delivered triggers over the total amount of triggers. The error bars also provide some information on the total amount of triggers given: the longer the bars, the lower the number of triggers. Therefore, good data points lie in the top of the diagram and have a small error bar. From the diagram, it is clear that the performance ratio greatly varies with the parameters, and one can say that a combination of $k = 6$, $t_n = 0.8 \mu\text{s}$ gives best results.

The time shift t_1 also turns out to be an important marker. For $t_n = 0.8 \mu\text{s}$, $k = 6$, and $n_a = 5$, Figure 2b gives the trigger performance for various values of t_1 between t_n (corresponding to a trigger at the beginning of the sampled average) and $-t_n$ (a trigger t_n after the last sample of the average). A value of $t_1 = 0$, putting the trigger at the end of the sampled average, gives best results.

4. Conclusions

For the brightest events ($E > 10^{17}$ eV), the proposed trigger seems to work reasonably well. One has to keep in mind, of course, that the data set over which it was tested is not extensive, and that the final setup will be different from the one currently in use. For example, in the final LOFAR setup there will be a lot less radio noise than in LOPES. Further testing on more (LOPES) data will hopefully provide more insight. But only after the first dipoles of LOFAR itself will have been set up, we will know whether our results prove to be valid.

References

- [1] H. Falcke, P. W. Gorham; *Astropart. Phys.* 19, 477–494 (2003).
- [2] T. Huege, H. Falcke; *A&A* 430, 779–798 (2005).
- [3] A. Horneffer et al.; *Proc. SPIE* 5500, 129–138 (2004).
- [4] T. Antoni et al.; *Nucl. Instr. Meth.* A513, 490 (2003).
- [5] H. Falcke et al.; *Nature Phys. Lett.* 435, 313–316 (2005).
- [6] P. Marciniwski; PhD Thesis, Uppsala University (2001)

Fluctuations in the EAS radio signal derived with improved Monte Carlo simulations based on CORSIKA

T. Huege^{a,e}, W.D. Apel^a, F. Badea^a, L. Bühren^b, K. Bekk^a, A. Bercuci^c, M. Bertaina^d, P.L. Biermann^e, J. Blümer^{a,f}, H. Bozdog^a, I.M. Brancus^c, S. Buitink^g, M. Brüggemann^h, P. Buchholz^h, H. Butcher^b, A. Chiavassa^d, K. Daumiller^a, A.G. de Bruyn^b, C.M. de Vos^b, F. Di Pierro^d, P. Doll^a, R. Engel^a, H. Falcke^{b,e,g}, H. Gemmekeⁱ, P.L. Ghia^j, R. Glasstetter^k, C. Grupen^h, A. Haungs^a, D. Heck^a, J.R. Hörandel^f, A. Horneffer^{e,g}, K.-H. Kampert^k, G.W. Kant^b, U. Klein^l, Y. Kolotaev^h, Y. Koopman^b, O. Krömerⁱ, J. Kuijpers^g, S. Lafebre^g, G. Maier^a, H.J. Mathes^a, H.J. Mayer^a, J. Milke^a, B. Mitrica^c, C. Morello^j, G. Navarra^d, S. Nehls^a, A. Nigl^g, R. Obenland^a, J. Oehlschläger^a, S. Ostapchenko^a, S. Over^h, H.J. Pepping^b, M. Petcu^c, J. Petrovic^g, T. Pierog^a, S. Plewnia^a, H. Rebel^a, A. Risse^m, M. Roth^f, H. Schieler^a, G. Schoonderbeek^b, O. Sima^c, M. Stümpert^f, G. Toma^c, G.C. Trinchero^j, H. Ulrich^a, S. Valchierotti^d, J. van Buren^a, W. van Capellen^b, W. Walkowiak^h, A. Weindl^a, S. Wijnholds^b, J. Wochele^a, J. Zabierowski^m, J.A. Zensus^e, D. Zimmermann^h

(a) Institut für Kernphysik, Forschungszentrum Karlsruhe, 76021 Karlsruhe, Germany

(b) ASTRON, 7990 AA Dwingeloo, The Netherlands

(c) National Institute of Physics and Nuclear Engineering, 7690 Bucharest, Romania

(d) Dipartimento di Fisica Generale dell'Università, 10125 Torino, Italy

(e) Max-Planck-Institut für Radioastronomie, 53010 Bonn, Germany

(f) Institut für Experimentelle Kernphysik, Universität Karlsruhe, 76021 Karlsruhe, Germany

(g) Department of Astrophysics, Radboud University Nijmegen, 6525 ED Nijmegen, The Netherlands

(h) Fachbereich Physik, Universität Siegen, 57068 Siegen, Germany

(i) Inst. Prozessdatenverarbeitung und Elektronik, Forschungszentrum Karlsruhe, 76021 Karlsruhe, Germany

(j) Istituto di Fisica dello Spazio Interplanetario, INAF, 10133 Torino, Italy

(k) Fachbereich Physik, Universität Wuppertal, 42097 Wuppertal, Germany

(l) Radioastronomisches Institut der Universität Bonn, 53121 Bonn, Germany

(m) Soltan Institute for Nuclear Studies, 90950 Lodz, Poland

Presenter: T. Huege (tim.huege@ik.fzk.de), ger-huege-T-abs1-he14-oral

Cosmic ray air showers are known to emit pulsed radio emission which can be understood as coherent geosynchrotron radiation arising from the deflection of electron-positron pairs in the earth's magnetic field. Here, we present simulations carried out with an improved version of our Monte Carlo code for the calculation of geosynchrotron radiation. Replacing the formerly analytically parametrised longitudinal air shower development with CORSIKA-generated longitudinal profiles, we study the radio flux variations arising from inherent fluctuations between individual air showers. Additionally, we quantify the dependence of the radio emission on the nature of the primary particle by comparing the emission generated by proton- and iron-induced showers. This is only the first step in the incorporation of a more realistic air shower model into our Monte Carlo code. The inclusion of highly realistic CORSIKA-based particle energy, momentum and spatial distributions together with an analytical treatment of ionisation losses will soon allow simulations of the radio emission with unprecedented detail. This is especially important to assess the emission strengths at large radial distances, needed for event-to-event comparisons of the radio signals measured by LOPES in conjunction with KASCADE-Grande and for considerations regarding large arrays of radio antennas intended to measure the radio emission from ultra-high energy cosmic rays, as with LOFAR or in the Pierre Auger Observatory.

1. Introduction

As part of LOPES [1], a digital radio interferometer working in conjunction with the KASCADE-Grande experiment, we have developed a model of the emission mechanism responsible for the radio pulses produced by extensive air showers. Describing the emission as coherent geosynchrotron radiation arising from the deflection of electron-positron pairs in the earth’s magnetic field, we have performed analytical calculations [2] followed by detailed Monte Carlo simulations [3], which were then used to derive important dependences of the radio emission on specific air shower parameters [4]. For the first time, our simulations have employed a realistic model of the air shower producing the radio emission. Important air shower properties such as the longitudinal (“arrival time”) and lateral particle distributions in the shower pancake, the particle energy and track length distributions and the overall longitudinal evolution of the shower were taken into account via “standard” analytical parametrisations such as NKG functions (lateral distributions) and Greisen parametrisations (longitudinal evolution). While a number of important results have already been obtained with this model [4], the next step in improving the simulations is to substitute the underlying air shower model by a more realistic one based on histogrammed distributions derived from CORSIKA [5] simulations.

Here, we present a first result derived with these improved simulations, namely the influence of the air showers’ realistically simulated longitudinal profiles. These realistic CORSIKA-generated profiles allow us to evaluate shower-to-shower fluctuations in the radio emission as well as the influence of the nature of the primary particle on the radio signal.

2. Discussion

To assess the relative fluctuations in the radio signal between individual air showers, we have simulated 10 very weakly thinned proton induced air showers and 10 very weakly thinned iron induced air showers with a primary particle energy of 10^{16} eV and vertical incidence. The geomagnetic field was adopted the same as in [4], namely 70° inclined with a strength of 0.5 Gauss, which approximately corresponds to the geomagnetic field configuration in Central Europe. CORSIKA was used with the GHEISHA2002 model [6] for low-energy hadronic interactions and the QGSJET01 model [7] for high-energy hadronic interactions. The relatively low primary particle energy was chosen to minimise the computation time in this early stage of analysis. We will reconsider the effects for higher energies at a later time in conjunction with a much broader analysis of the improvements achieved with the adoption of the other CORSIKA-based particle distributions.

For the proton and iron showers each, the 10 simulations were averaged to obtain an “average air shower” with which one can then compare the individual showers. For this purpose, the individual showers were reviewed by eye and the cases with longitudinal profiles differing most from the average profile were selected. Simulations of the associated radio signal were then performed with our Monte Carlo code. Only the longitudinal profile of the shower development was taken from the CORSIKA simulations. All other air shower properties (energy distributions, spatial particle distributions, ...) were retained using the analytical distributions employed in [4]. This procedure allows a simple first estimate of the importance of the fluctuations in the shower development. For comparison, we also calculated the radio emission from a fully parametrised shower, retaining a Greisen parametrisation for the longitudinal development.

The left panel of figure 1 shows a comparison of the longitudinal profiles taken into account for the analysis of the proton induced showers. In particular, the analytical Greisen parametrisation used so far in the code is very similar to the profile of the averaged proton shower. It does, however, overestimate the number of particles generated by $\sim 15\%$, as it describes a purely electromagnetic shower of the given energy without significant “losses” to a muonic component. The three selected individual shower profiles represent cases of a shower

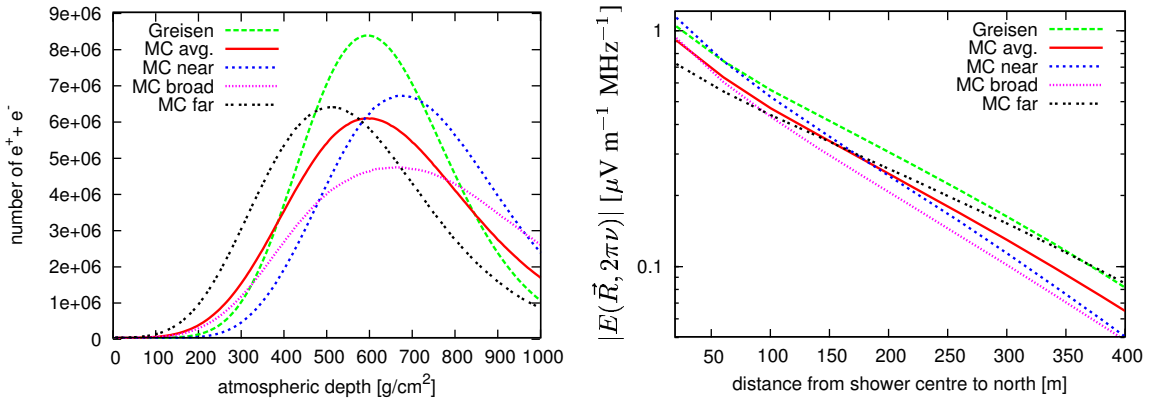


Figure 1. Left: Longitudinal development profiles of vertical CORSIKA-simulated 10^{16} eV proton-induced air showers in comparison with an averaged profile derived from CORSIKA and a Greisen-parametrised profile. Right: Simulated radial dependence of the 10 MHz radio signal as calculated using the longitudinal profiles displayed on the left.

developing to its maximum far away from the ground, a shower developing to its maximum close to the ground, and a shower having a generally much broader maximum. The right panel of figure 1 shows the 10 MHz radio signal obtained from these longitudinal shower profiles. Due to the overestimation of the number of particles in the Greisen parametrisation, the emission is about $\sim 15\%$ higher for the fully parametrised shower. Apart from this constant enhancement factor, the radial profile of the radio emission is very similar to that of the averaged proton shower, which indeed has a very similar longitudinal evolution. The individual showers, in comparison, show significant deviations from the radial profile generated by the average shower. While the overall emission level (directly related to the number of electrons and positrons) stays similar, the slope of the radial emission profile changes. The shower with the maximum close to the ground has a steeper slope, the one with the maximum far away from the ground has a flatter slope. This dependence of the radio emission on the depth of the shower maximum was already shown in [4]. The shower with the broader maximum has slightly lower radio emission over the radial distances considered here. This arises from the lower total number of electrons and positrons sampled in the atmosphere’s ~ 1000 $g\ cm^{-2}$ over the ground, after which the profile is “truncated”. Overall, the deviations in the field strengths are of the order $\sim 30\%$.

For the iron-induced showers, the fluctuations in the longitudinal shower development are much smaller, as expected from the simplified “superposition model” interpreting an iron-induced shower as a superposition (and thus averaging) of 56 nucleon-induced showers. Correspondingly, the deviations of the radio signal between the “average shower” and the individual showers are much smaller. This is shown in figure 2 in comparison with the fluctuations for the proton-induced showers. As the iron-induced showers grow to their maxima at larger distances from the observer than the proton induced showers, the radial profiles of their radio emission are somewhat flatter. Additionally, the emission amplitudes are slightly lower. This is due to the fact that for iron-induced showers, the fraction of energy going into the muonic shower component is higher (and thus the fraction going into the electromagnetic component lower) than in proton-induced showers.

3. Conclusions

Using CORSIKA-generated air shower development profiles, we have analysed the influence of shower-to-shower fluctuations on the associated radio signal. While vertical 10^{16} eV showers induced by proton primaries show fluctuations of the order 30%, the fluctuations for iron-induced showers with the same parameters are

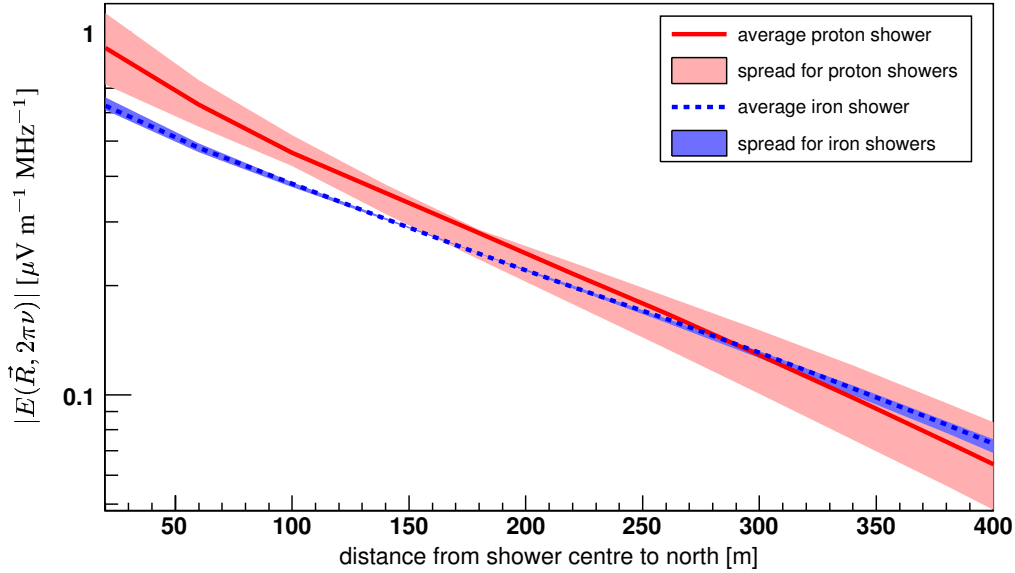


Figure 2. Radial dependence of the 10 MHz radio emission from vertical 10^{16} eV air showers induced by protons and iron nuclei, respectively, comparing the emission from an averaged shower with that from individual showers.

negligible. Two characteristics of the shower profiles have a direct impact on the radio emission: the distance of the shower maximum from the observer on the ground, directly influencing the slope of the radial dependence, and the total number of electrons and positrons integrated over the shower evolution, directly determining the absolute strength of the emission. Differences in the radio emission of individual showers and also differences in the emission from showers induced by different primaries can be related directly to these two effects.

The analysis we performed constitutes a first step towards composition studies of cosmic rays with radio techniques. However, it was carried out with only limited statistics at relatively low energies, and only for vertical air showers. A more complete analysis at higher energies and various zenith angles will be performed soon in conjunction with a detailed analysis of the effects introduced by substituting other analytical parametrisations such as those describing energy and pitch-angle distributions by more realistic CORSIKA-derived data. It is, however, clear that the influence of differences in the longitudinal shower profiles on the radio emission will still mainly be related to the spatial distance of the shower maximum to the ground and the total number of electrons and positrons integrated over the shower evolution.

References

- [1] H. Falcke et al. - LOPES collaboration, *Nature* 435, 313-316 (2005).
- [2] T. Huege and H. Falcke, *Astronomy Astroph.* 412, 19-34 (2003).
- [3] T. Huege and H. Falcke, *Astronomy Astroph.* 430, 779-798 (2005).
- [4] T. Huege and H. Falcke, *Astropart. Phys.* in press (2005), astro-ph/0505180.
- [5] D. Heck et al., *Forschungszentrum Karlsruhe Report FZKA 6019* (1998).
- [6] H. Fesefeldt, *RWTH Aachen Report PITHA-85/02* (1985).
- [7] N.N. Kalmykov, S.S. Ostapchenko and A.I. Pavlov, *Nucl. Phys. B (Proc. Suppl.)* 52B, 17 (1997).

Simulations and parametrisation of radio emission from cosmic ray air showers

T. Huege^{a,b} and H. Falcke^{b,c,d}

(a) *Institut für Kernphysik, Forschungszentrum Karlsruhe, 76021 Karlsruhe, Germany*

(b) *Max-Planck-Institut für Radioastronomie, 53010 Bonn, Germany*

(c) *Department of Astrophysics, Radboud University Nijmegen, 6525 ED Nijmegen, The Netherlands*

(d) *ASTRON, 7990 AA Dwingeloo, The Netherlands*

Presenter: T. Huege (tim.huege@ik.fzk.de), ger-huege-T-abs2-he13-poster

Cosmic ray air showers are known to emit pulsed radio emission at frequencies around a few tens of MHz. Accompanying the experimental efforts of the LOPES project, situated at the KASCADE-Grande site of the Forschungszentrum Karlsruhe, we have modeled the underlying emission mechanism in the scheme of coherent geosynchrotron radiation from electron-positron pairs deflected in the earth's magnetic field. As a follow-up to our earlier analytical calculations, we have developed a Monte Carlo simulation based on analytic parametrisations of air shower properties, including longitudinal and lateral particle distributions, particle energy and track-length distributions, and the longitudinal shower development as a whole. Here we present detailed simulation results. Important findings are the absence of significant asymmetries in the total field strength emission pattern in spite of the asymmetry introduced by the geomagnetic field, the polarisation characteristics of the geosynchrotron emission, allowing an unambiguous test of the geomagnetic emission mechanism, and the dependence of the radio emission on important shower parameters such as the shower zenith angle, the primary particle energy and the depth of the shower maximum. As a particularly useful result, these dependences have been summarized in a simple parametrisation formula, providing a solid basis for the interpretation of experimental data gathered with current and future experiments.

1. Introduction

Radio emission from extensive air showers (EAS) has been known to exist since its initial discovery in the 1960ies. Today's digital signal processing capabilities led to the idea of using digital radio interferometers such as LOFAR for its observation [1]. These considerations sparked the LOPES project situated at the KASCADE-Grande site of the Forschungszentrum Karlsruhe in Germany, with the intention to develop a prototype for the measurement of radio emission from EAS based on LOFAR hardware. In the meantime, LOPES has successfully delivered proof-of-principle results confirming a geomagnetic origin of the emission [2]. In conjunction with the plans for an experimental design, a new approach for the interpretation of the emission mechanism was proposed [1]. In this approach, the emission is interpreted as coherent geosynchrotron radiation arising from the deflection of the air shower cascade's secondary electron-positron pairs in the earth's magnetic field. Following this concept, we have carried out analytical calculations [3], followed by detailed Monte Carlo simulations [4] of the radio emission from cosmic ray air showers. The Monte Carlo simulations are based on an air shower model describing important shower properties such as the longitudinal and lateral particle distributions, the particle energy and track-length distributions and the overall longitudinal development of the air shower cascade with realistic, widely-used parametrisation formulas such as NKG-functions and Greisen-parametrisations, reaching a hitherto unprecedented level of detail in the simulations. Having verified the consistency of the analytical and Monte Carlo simulations, we now present a number of important results for the radio emission's dependence on specific air shower properties derived with this Monte Carlo model. A more complete discussion of these results can be found in [5].

2. Discussion

To illustrate general radio emission properties, it is useful to first have a look at a very simple configuration, a vertical 10^{17} eV air shower. The magnetic field throughout this work is adopted as the one present in Central Europe, i.e., 70° inclined with a strength of 0.5 Gauss. Two very important characteristics of the radio emission from EAS are its spatial emission pattern and its frequency spectrum on the ground, shown in figure 1. The total field strength emission pattern depicted in the left panel is remarkably circular. This is by no means self-evident, because the deflection of electrons and positrons is always directed in the east-west direction, making the emission of geosynchrotron radiation itself a highly asymmetrical process. The weakness of the asymmetry in the total field strength emission pattern is mainly due to the superior number of short particle tracks, which are much more numerous than long particle tracks that would lead to significant asymmetries.

The right panel of figure 1 shows the frequency spectra emitted by the vertical air shower as observed at various distances from the shower centre to the north. It is clear that the spectra cut off quickly to high frequencies, and measurements should thus concentrate on low frequencies if allowed by the noise background. The spectral cutoff is caused by the loss of coherence once the wavelength of the emission becomes comparable to or smaller than the thickness of the air shower disk. The effect becomes more dramatic when one goes to higher distances due to projection effects enlarging the apparent thickness of the disk. At high frequencies, especially far away from the shower centre, one enters the incoherent regime and the Monte Carlo simulations show an unphysical seeming, rapidly alternating series of interference minima and maxima. These are an artifact of the total homogeneity of the particle distributions in the simulated showers. To make statements about the emission levels in the incoherent regime (which could well be of measurable strength), one therefore needs a better air shower model, as is currently being implemented in the Monte Carlo code [6] using particle distributions derived from CORSIKA [7] simulations.

The picture changes when one looks at an inclined air shower. Figure 2 shows again the total field strength emission pattern and the frequency spectra, but now for the radio emission from a 10^{17} eV air shower with 45° zenith angle coming from the south. Comparing the emission pattern with that of figure 1, one immediately notices a strong projection effect, elongating the pattern along the shower axis. Apart from this intuitive projection effect, the pattern also generally gets broader, even in the direction perpendicular to the shower axis. This is a consequence of the shower maximum's much larger spatial distance to the observer for an inclined shower as compared with a vertical shower. (The same effect arises when varying the depth of shower maximum for a fixed air shower geometry [5].) Their much broader emission pattern thus makes inclined showers a specifically suitable target for observations of the radio emission from EAS, see also [8] and [9]. Comparing the frequency spectra of the inclined shower (right panel of figure 2) with those of the vertical shower (right panel of figure 1) demonstrates a similar effect. For the inclined air shower, the emission stays coherent up to much higher distances from the shower centre, again allowing much easier detection of inclined showers compared with vertical showers.

A more quantitative view of the air shower inclination's effects on the emission pattern is given in the left panel of figure 3. It shows the 10 MHz electric field strength as a function of radial distance to the north of the shower centre (i.e., cuts through the emission pattern along the shower axis). While the effect is only minimal up to $\sim 15\text{--}20^\circ$, the pattern becomes much more elongated and broader at zenith angles greater than $\sim 30^\circ$.

Another very important result of the simulations are the polarisation characteristics of the emission. While the total field strength emission pattern only exhibits a very subtle dependence on the magnetic field direction, separate measurements of the north-south and east-west polarisation components should show a significant dependence on the shower azimuth angle relative to the magnetic field. The simulations predict that the emission is predominantly linearly polarised. The right panel of figure 3 shows a blow-up of the total field strength emission pattern of the 45° inclined air shower. Overlaid are indicators denoting the ratio of east-west to north-

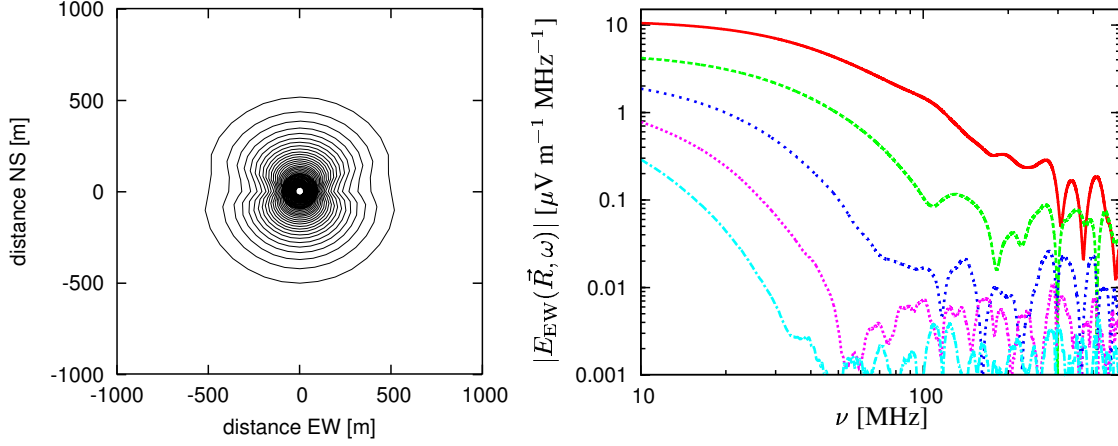


Figure 1. 10 MHz radio emission from a vertical 10^{17} eV air shower. Left: Total field strength emission pattern. Right: Frequency spectra at (from top to bottom) 20 m, 140 m, 260 m, 380 m and 500 m north of the shower centre.

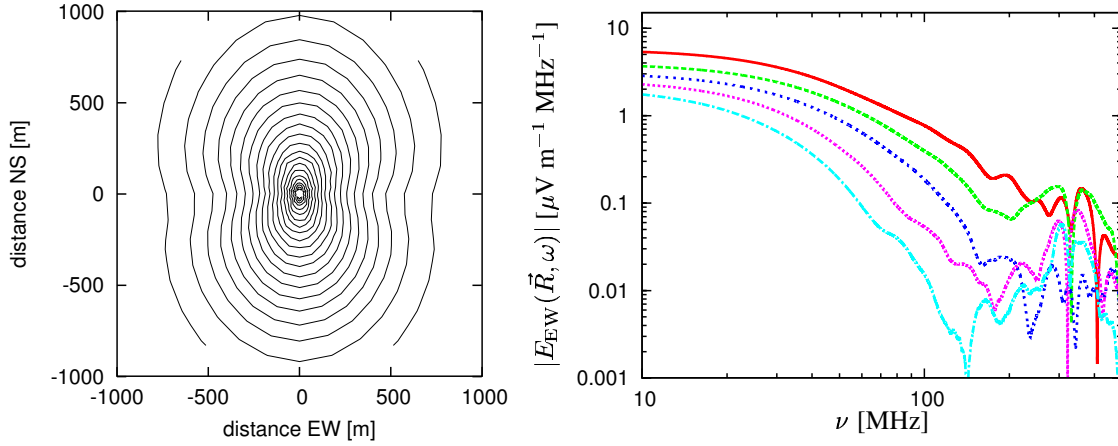


Figure 2. 10 MHz radio emission from a 45° inclined 10^{17} eV air shower. Left: Total field strength emission pattern. Right: Frequency spectra at (from top to bottom) 20 m, 140 m, 260 m, 380 m and 500 m north of the shower centre.

south polarisation. (Horizontal indicators denote pure east-west polarisation, vertical ones pure north-south polarisation.) The figure demonstrates that close to the shower centre, the emission is predominantly polarised in the direction perpendicular to the magnetic field and shower axis, which was also a result of the analytic calculations [3] and historical works investigating a geomagnetic emission mechanism. For other possible radio emission mechanisms such as Askaryan-type Čerenkov radiation which plays a dominant role in dense media, the expected polarisation characteristics are different. Linear polarisation measurements, as are possible with LOPES, can thus verify the geomagnetic origin of the emission in a very direct way.

The simulations also confirm the expected linear scaling of the electric field amplitudes with the primary particle energy, as long as one observes in the coherent regime, where the emission from all individual particles adds up coherently and thus scales linearly with particle number. Some deviations from the linear scaling arise through the additional effect that higher energy showers on average penetrate deeper into the atmosphere than lower energy ones. The overall effect is demonstrated again in [5].

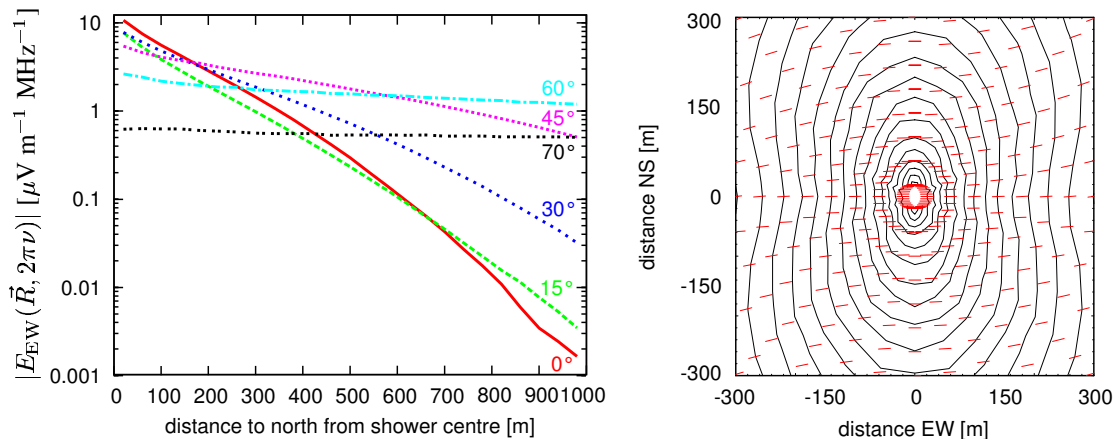


Figure 3. Left: Radial dependence of the 10 MHz electric field strength emitted by 10^{17} eV air showers with various zenith angles (coming from the south). Right: Zoomed in total field strength emission pattern of a 10^{17} eV air shower with 45° zenith angle overplotted with indicators denoting the ratio of east-west to north-south linear polarisation.

To give a summary of the aforementioned and additional dependences of the radio emission on the underlying air shower parameters, we have derived a simple, analytical parametrisation formula reproducing the Monte Carlo results with good accuracy [5]. This parametrisation has been implemented as a web-based online-calculator that can be a useful tool for estimates of the radio emission.

3. Conclusions

We have established important characteristics of the radio emission from EAS and their dependence on the properties of the underlying air showers. Among the most important results we demonstrate that inclined air showers pose a particularly interesting target for radio observations due to their larger emission pattern and better coherence up to high frequencies. We demonstrate that linear polarisation measurements can be used to directly verify the geomagnetic origin of the emission. A simple parametrisation formula summarises our results in a particularly useful way. Our Monte Carlo code is currently being equipped with a CORSIKA-based air shower model, allowing further improvements in the modelling quality.

References

- [1] H. Falcke and P. Gorham, *Astropart. Phys.* 19, 477-494 (2003).
- [2] H. Falcke et al. - LOPES collaboration, *Nature* 435, 313-316 (2005).
- [3] T. Huege and H. Falcke, *Astronomy Astroph.* 412, 19-34 (2003).
- [4] T. Huege and H. Falcke, *Astronomy Astroph.* 430, 779-798 (2005).
- [5] T. Huege and H. Falcke, *Astropart. Phys.* in press (2005), astro-ph/0505180.
- [6] T. Huege et al. - LOPES collaboration, these proceedings (2005).
- [7] D. Heck et al., *Forschungszentrum Karlsruhe Report FZKA 6019* (1998).
- [8] J. Petrovic et al. - LOPES collaboration, these proceedings (2005).
- [9] T. Gousset, O. Ravel and C. Roy, *Astropart. Phys.* 22, 103-107 (2004).

Simulation Cherenkov and Synchrotron Radio Emission in EAS

R. Engel^a, N.N. Kalmykov^b, A.A. Konstantinov^b.

(a) Forschungszentrum Karlsruhe, Institut fuer Kernphysik, Postfach 3640, D-76021 Karlsruhe, Germany

(b) Skobeltsyn Institute of Nuclear Physics, Moscow State University, Leninskie Gory 1, 119992, Moscow, Russia

Presenter: R. Engel (Ralph.Engel@ik.fzk.de), ger-engel-R-abs3-he11-poster

Cherenkov and geosynchrotron radiation are considered as two fundamental mechanisms of the radio emission generated by extensive air showers (EAS). The code EGSnrc is used for Monte-Carlo simulations of the individual shower development. Calculations of the radial dependence and frequency spectrum of the emitted radiation are performed for the LOPES experiment frequency range.

1. Introduction

Coherent radio emission generated by extensive air showers was theoretically predicted by Askaryan in 1961 [1] and experimentally discovered by Jelly et al. in 1965 at a frequency of 44 MHz [2]. Over a period of time this phenomenon has been considered as an interesting alternative to traditional methods of detection of high-energy cosmic rays with energy greater than 10^{17} eV. In the 1960th and 1970th the experimental and theoretical efforts in this direction had no actual success [3]. Modern experiments, such as CODALEMA [4] and LOPES [5], aimed at EAS radio emission studies use modern, improved instruments and thus can hope for the final success. But there are still many questions concerning the quantitative radio emission theory.

Several mechanisms of radio emission generation in air have been identified after the pioneering work of Askaryan where the coherent Cherenkov radiation of the charge-excess was put forward [1]. This radiation is very strong for showers developing in dense media [6]. In the case of EAS there is also an alternative radiation due to the acceleration of charged shower particles in the Earth's magnetic field. It is called geosynchrotron mechanism and has been recently investigated in detail [7]. However we still have no sufficiently clear understanding what interrelation exists between these two essential mechanisms. So, one needs to perform accurate radio emission calculations for these mechanisms within the framework of a unified approach. In our work we present a model in which Cherenkov and geosynchrotron radiation are combined. In a sense, our work is complementary to [7] where only the geosynchrotron radiation was considered.

2. Calculations

To calculate the radio emission of air showers an EGSnrc-based [8] program code has been developed. For reproduction of the Earth's atmosphere we have taken 200 strata of air, with density and optical properties varying from stratum to stratum according to the atmospheric profile. The declination and strength of the Earth's magnetic field [9] correspond to those for Karlsruhe, where the LOPES experiment is being performed. Radio emission characteristics (radial dependence, frequency spectrum, polarization and some others) are calculated taking into account contributions from each charged particle.

There are two different radiation mechanisms adopted in the model and the separation of them is realized as follows. If a charged particle is moving in the magnetic field characterized by the field strength \mathbf{B} and the

refractive index is equal to n , we may present the electric field E as the sum of two parts with the following properties

$$E = E_{(1)} + E_{(2)},$$

where $E_{(1)} \rightarrow \mathbf{0}$, when $B \rightarrow \mathbf{0}$, and $E_{(2)} \rightarrow \mathbf{0}$, when $n \rightarrow 1$. We accept that $E_{(1)}$ is the electric field due to the Earth's magnetic field (*geosynchrotron radiation*) and $E_{(2)}$ is the electric field due to medium (air) properties (*Cherenkov radiation*).

3. Simulation results

Vertical showers were simulated for primary photons with the energies 1 and 10 TeV and for energy thresholds of 100 keV and 1 MeV. The primary particle is injected at 30 km above the ground level. The lateral distributions of radio emission were calculated simultaneously at several frequencies: 10, 30 and 100 MHz. In total 50 ground-level observation points were uniformly distributed over a straight line from the shower axis to the direction of the geographic north in the range of distances up to 500 m.

The mean longitudinal profile of showers with 1 TeV primary photon energy and 1 MeV threshold energy is presented on Figure 1. Such showers have the negative charge excess (ϵ) of about 20% in the maximum. It should be stressed that electrons and positrons emit Cherenkov radiation if their energy exceeds the Cherenkov threshold (that is equal to 21 MeV at sea level) and thus only $\approx 1/3$ of the above-mentioned excess particles give a contribution to the observed electric field. This is in contrast to the situation in ice where, due to a rather large refractive index, almost all excess particles emit Cherenkov radiation.

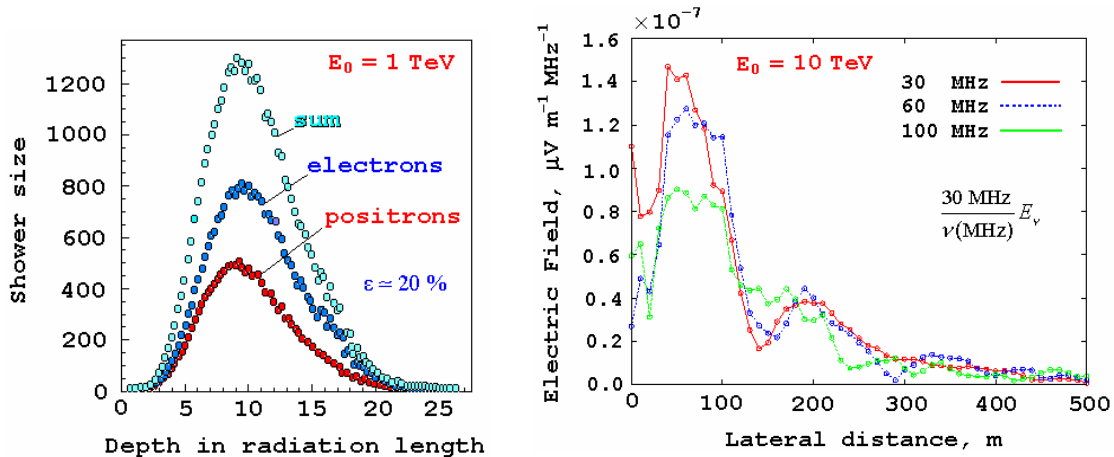


Figure 1. Number of shower particles as a function of depth ($E_{\text{thr}} = 1$ MeV, averaged over 20 showers).

Figure 2. Lateral distribution of Cherenkov radio emission at different frequencies ($E_{\text{thr}} = 100$ keV, 5 showers).

Figure 2 shows the lateral distribution of the electric field produced by Cherenkov radiation of shower particles. The primary energy is 10 TeV and the electric field is normalized at the frequency 10 MHz. We associate this radiation with Askaryan's mechanism (radiation of the negative charge excess). This idea was confirmed by direct calculations: when the excess is zero then we have a decrease of the field by two to three orders of magnitude (depending on the considered frequency). It is also interesting to note that the Cherenkov radiation demonstrates a diffraction pattern.

The full pattern of the radio emission lateral distribution is shown in Figure 3 for 10 TeV-showers. Plotted are the Cherenkov, geosynchrotron and total (the sum of Cherenkov and geosynchrotron contributions) radio emission at 30 and 100 MHz. We see that there exists practically full domination of the geosynchrotron radiation in the low frequency part of the radio emission spectrum at all distances. But it is not so for higher frequencies and especially at the main Cherenkov peak.

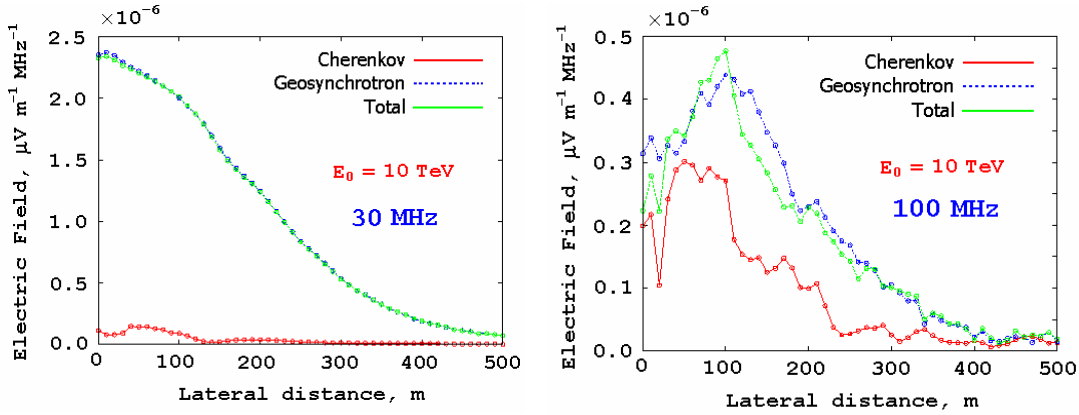


Figure 3. Lateral distribution of geosynchrotron, Cherenkov and total radio emission at different frequencies ($E_{\text{thr}} = 100$ keV, averaged over 5 showers).

It seems that we can interpret this behavior as due to the difference in spectral properties of the two types of radiation. This is confirmed by Figure 4 where the spectral distribution of the radio emission at 100 and 300 m from the shower axis of 1 TeV-showers are shown. We see (picture for 100 m) that the coherent regime for the Cherenkov emission is maintained up to higher frequencies than in the case of the geosynchrotron emission. It seems that the main reason of this situation is that the effective dimension of the radiation region is smaller for the Cherenkov emission than for the geosynchrotron emission due to the large Cherenkov threshold energy. The situation is similar at larger distances from shower axis (results are given at 300 m).

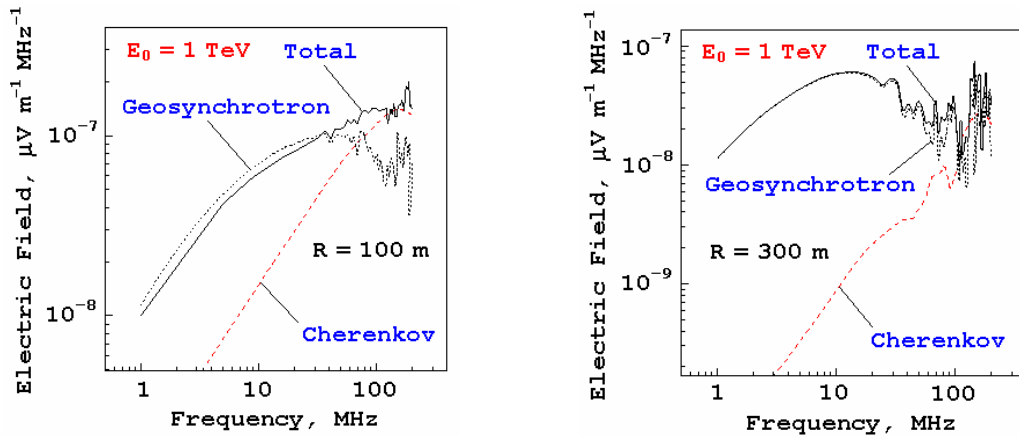


Figure 4. Spectral distribution of geosynchrotron, Cherenkov and total radio emission at different distances from shower axis ($E_{\text{thr}} = 1$ MeV, averaged over 5 showers).

4. Conclusions

Realistic air shower and radio signal simulations for primary energies 1÷10 TeV have been performed. The calculations show that there is no full domination of one of the two radiation mechanisms in the Earth's atmosphere. It seems that an appropriate radio emission theory needs to take into account the Cherenkov radiation as well as the geosynchrotron mechanism.

The contribution of the Cherenkov radiation to the total field is not identical at different distances from shower axis. At small distances, including the main peak, the role of the Cherenkov component grows with the increase of the observation frequency due to violation of the coherence condition for the geosynchrotron radio emission whereas it is conserved for the Cherenkov radiation. We also observe the same situation at larger distances from shower axis. However the flow of the geosynchrotron radio emission falls with distance more slowly than for the Cherenkov emission and thus the amplitude of the Cherenkov radiation at these distances is much smaller.

The amplitude of the geosynchrotron mechanism essentially depends on the configuration of the system "shower axis - magnetic field" and there is a need to simulate showers with different arrival directions relative to the local magnetic field. In parallel one certainly needs to push up the primary energy and statistics of the simulations to attain better understanding of radiation processes in air.

5. Acknowledgements

We thank T. Huege for useful discussions on the simulation of geosynchrotron radio emission.

References

- [1] G.A. Askaryan, Soviet Phys. JETP 41, 616 (1961).
G.A. Askaryan, Soviet Phys. JETP 48, 988 (1965).
- [2] J.V. Jelley *et al.*, Nature 205, 237 (1965).
- [3] S.N. Vernov *et al.*, in Proceedings of the 11-th International Cosmic Ray Conference, Budapest (1969).
H.R. Allan, Prog. in Element. part. and Cos. Ray Phys. 10, 171 (1971).
- [4] O. Ravel *et al.*, CODALEMA Collab., Nucl. Instrum. Meth. A 518, 213, astro-ph/0409039 (2004).
- [5] A. Horneffer *et al.*, LOPES Collab., Proc. SPIE 5500-21, astro-ph/0409641 (2004).
H. Falcke *et al.*, LOPES Collab., Nature 435, 313 (2005).
- [6] D. Saltzberg *et al.*, Phys. Rev. Lett. 86, 2802 (2001).
E. Zas *et al.*, Phys. Rev. D45, 1 (1992).
S. Razzaque *et al.*, astro-ph/0112505 (2002).
- [7] T. Huege and H. Falcke, astro-ph/0309622 (2003).
T. Huege and H. Falcke, Astron. and Astroph., 430, 779 (2005).
T. Huege and H. Falcke, astro-ph/0501580 (2005).
- [8] <http://www.irs.inms.nrc.ca/inms/irs/EGSnrc/EGSnrc.html> .
- [9] National Geophysical Data Center, Boulder (CO), USA: <http://www.ngdc.noaa.gov>.

Hadronic Interactions in QGSJET-II: Physics and Results

S. Ostapchenko^{ab} and D. Heck^a

(a) Forschungszentrum Karlsruhe, Institut für Kernphysik, 76021 Karlsruhe, Germany

(b) D.V. Skobeltsyn Institute of Nuclear Physics, Moscow State University, 119992 Moscow, Russia

Presenter: S. Ostapchenko (serguei@ik.fzk.de), ger-ostapchenko-S-abs1-he14-oral

A new hadronic interaction model QGSJET-II is presented. The key feature of the model is the treatment of non-linear interaction effects described by enhanced Pomeron diagrams, which are re-summed to all orders. This allows us to employ realistic parton momentum distribution functions, measured in deep inelastic scattering experiments, while being consistent with hadronic cross section measurements. On the other hand, the model tuning to the data of fixed target experiments has been significantly improved compared to original QGSJET. The model predictions for extensive air shower (EAS) characteristics are analyzed, in particular, concerning the energy dependence of shower maximum position and of EAS electron and muon numbers.

1. Introduction

During the last decade a significant progress has been observed in experimental studies of high energy cosmic rays (CR) by means of extensive air shower (EAS) techniques. To a large extent this was due to a new strategy of data analysis, most consequently put forward by the KASCADE experiment [1], which devoted significant efforts to achieve a proper understanding of their measurements, based on extensive simulation studies of both nuclear-electro-magnetic cascading process in the atmosphere and of particle interactions in the ground detectors. Thus, contemporary EAS experiments greatly resemble their accelerator counterparts: actively using simulation tools, in particular the CORSIKA program [2], with different particle interaction models employed, they significantly enhance the accuracy of data analysis, which allows to obtain impressive results. On the other hand, studying correlations of various shower characteristics allows one to discriminate between available interaction models and to increase the quality of the simulation procedures.

An important part of the latter are so-called hadronic interaction models. Being calibrated at comparatively low energies, mainly with the data of fixed target experiments, they have to extrapolate corresponding knowledge over many energy decades, thus relying heavily on the underlying theoretical approach. For practical applications the most powerful one proved to be the Gribov-Regge scheme [3], which treats high energy hadron-hadron (hadron-nucleus, nucleus-nucleus) collisions as multiple scattering processes; elementary re-scatterings correspond to microscopic parton cascades and are described phenomenologically as Pomeron exchanges.

Among a number of hadronic Monte Carlo (MC) generators, developed in this framework, the QGSJET model [4] has been widely used in the field by a large number of experimental collaborations. This MC generator is essentially based on the physics picture of the Quark-Gluon String model [5]. The latter supplements the general Gribov-Regge treatment with a specific hadronization model: each elementary particle production process is assumed to give rise to creation and fragmentation of two strings, with the corresponding parameters being expressed via intercepts of secondary Regge trajectories. In turn, the basic innovation of the QGSJET model has been an explicit treatment of perturbative parton evolution in an elementary re-scattering process. Thus, a general Pomeron is represented there by a sum of the "soft" Pomeron contribution, corresponding to a pure non-perturbative (low p_t) parton cascade, and of the "semi-hard Pomeron", composed of a piece of QCD ladder sandwiched between two soft Pomerons [4], – for a cascade which at least partly develops in the high p_t region. The mentioned semi-hard contribution dominates hadronic interactions in the very high energy limit. Consequently, the approach allows to relate high energy asymptotics of hadronic scattering amplitudes to the perturbative QCD evolution and thus to enhance the predictive power of the model.

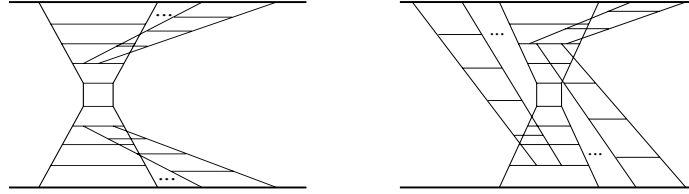


Figure 1. Examples of diagrams which give rise to non-linear parton effects.

However, an essential drawback of the whole scheme is that individual re-scattering processes are assumed to proceed independently, with any non-linear interaction effects being completely neglected. This approximation is invalid in the limit of very high energies and small impact parameters of the interaction, where one inevitably encounters high parton density effects: individual parton cascades start to overlap and to interact with each other. Due to the lack of such mechanisms present Gribov-Regge models can be considered as rather effective ones; there is no possibility to employ realistic parton momentum distribution functions (PDFs), measured at the HERA collider, without being in contradiction with observed energy behavior of total proton-proton cross section and of the multiplicity of secondary particles produced. In particular, the original QGSJET model is based on rather "flat" (pre-HERA) PDFs.

2. Hadronic interactions in the QGSJET-II model

To obtain a reliable description of hadronic interactions at very high energies, one necessarily has to account for non-linear interaction effects, which appear to be of extreme importance at sufficiently high parton densities. At microscopic level, this amounts to consider contributions of diagrams of Fig. 1, corresponding to mutual interaction of individual parton cascades, the latter being treated as merging of parton ladders [6]. In the Gribov-Regge scheme such parton cascades are described by Pomeron contributions whereas multi-ladder vertices correspond to Pomeron-Pomeron interactions [7]. Using a phenomenological parameterization for the latter one can re-sum all significant contributions of that kind and to develop a self-consistent MC generation procedure for hadronic and nuclear collisions [8]. As a result, the approach allows to resolve the inconsistency between the realistic PDFs and the observed hadronic cross sections, as shown in Fig. 2.

In addition to this main development, model calibration to the data of fixed target experiments has been significantly improved, in particular, concerning secondary particle multiplicity, see Fig. 3.

Though parton densities of QGSJET-II model increase much faster in the small Feynman x limit than in

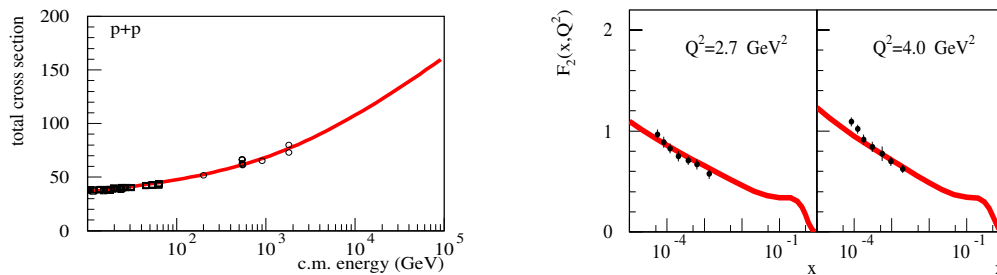


Figure 2. Total pp cross section (left) and proton structure function F_2 (right) as calculated in the QGSJET-II model compared to experimental data [9, 10].

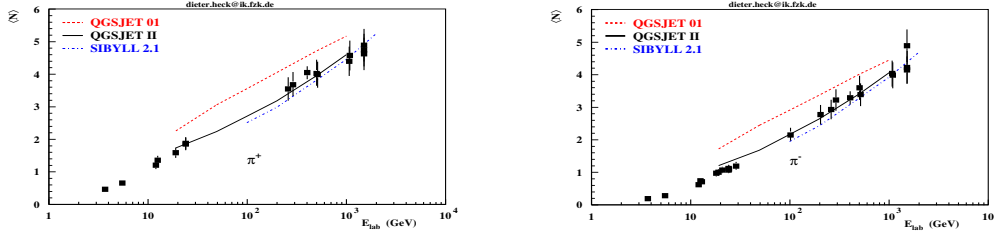


Figure 3. Multiplicity of positive (left) and negative (right) pions in proton-proton collisions as calculated with the QGSJET-II, QGSJET, and SIBYLL models.

original QGSJET, being now fixed by the measured structure function $F_2(x, Q^2)$, the corresponding effect is essentially compensated by the non-linear screening corrections in what concerns proton-proton cross sections and secondary particle multiplicity. Similarly, the proton-air cross section of the QGSJET-II model is very similar to old QGSJET results. The corresponding energy increase is significantly slower than, for example, in the SIBYLL model [11], where non-linear effects are introduced via an energy-dependent p_t -cutoff for semi-hard processes and thus are neglected for non-perturbative (low p_t) processes.

On the other hand, the influence of non-linear effects on particle production in hadron-nucleus and nucleus-nucleus collisions is much stronger compared to the hadron-hadron case, the corresponding corrections increasing with projectile and target mass numbers. In particular, the model appears to be in agreement with the data of the RHIC collider on the multiplicity of secondary hadrons produced in central nucleus-nucleus collisions, as shown in Fig. 4. In turn, for hadron-air collisions the inelasticity and multiplicity are significantly reduced compared to QGSJET results, being in a wide energy range even lower than in the SIBYLL model, see Fig. 5.

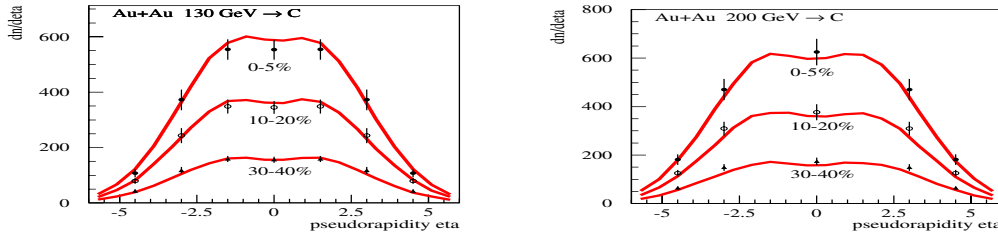


Figure 4. Multiplicity of charged particles in $Au-Au$ collisions of 130 AGeV (left) and 200 AGeV (right) c.m. energies for different event "centrality" selections (indicated in the Figure as the percentage of all minimum bias events) as calculated in the QGSJET-II model compared to the data of BRAHMS collaboration [12].

3. Impact on extensive air shower characteristics

The discussed reduction of secondary particle production in hadron-nucleus and nucleus-nucleus interactions makes a strong impact on the calculated EAS characteristics. The position of the shower maximum X_{\max} is systematically shifted deeper in the atmosphere compared to original QGSJET, as seen in Fig. 6(left). The calculated electron number at sea level, being strongly correlated with X_{\max} , is significantly enhanced – correspondingly by about 20% and 30% for vertical proton- and iron-initiated showers of energy 10^{15} eV; at the energy 10^{19} eV this reduces to 10% effect compared to QGSJET results. On the other hand, one obtains a sizable reduction of EAS muon number, as shown in Fig. 6(right), with the difference between the QGSJET-II and SIBYLL models being only about 10% at highest CR energies.

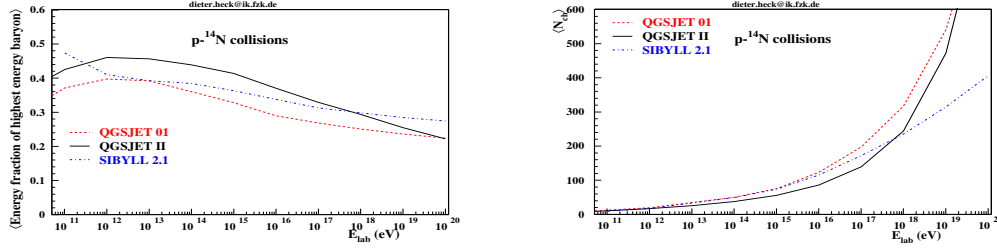


Figure 5. Elasticity and multiplicity in $p - {}^{14}\text{N}$ collisions as calculated with QGSJET-II, QGSJET, and SIBYLL.

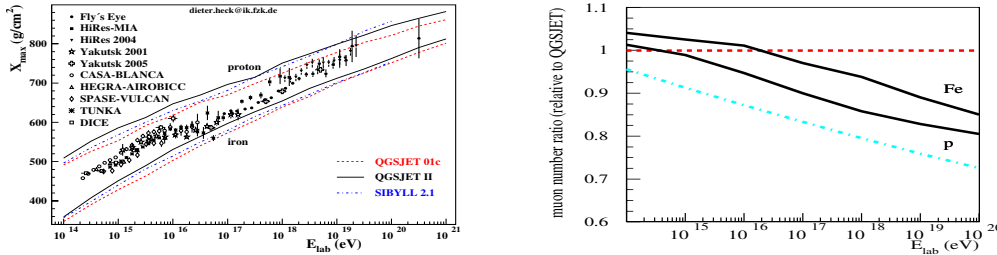


Figure 6. Left: position of the shower maximum for proton- and iron-induced EAS, as calculated with QGSJET-II, QGSJET, and SIBYLL, compared to cosmic ray data [13]. Right: ratio of EAS muon number ($E_\mu > 1$ GeV) as calculated with QGSJET-II (for p - and Fe -induced EAS) and SIBYLL (for p -induced EAS) with respect to QGSJET results.

In conclusion, the main feature of QGSJET-II is a microscopic treatment of non-linear interaction effects. This allows us to obtain a consistent description of hadronic cross sections and parton momentum distributions and to account for non-linear screening effects in individual hadronic and nuclear collisions. The discussed developments provide a more solid ground for model extrapolation towards highest CR energies.

References

- [1] T. Antoni et al., Nucl. Instr. & Meth. A 513, 490 (2003).
- [2] D. Heck et al., "CORSIKA: A Monte Carlo code to simulate extensive air showers", FZKA 6019, Forschungszentrum Karlsruhe, 1998.
- [3] V. N. Gribov, Sov. Phys. JETP 26, 414 (1968); 29, 483 (1969).
- [4] N. N. Kalmykov, S. S. Ostapchenko, and A. I. Pavlov, Bull. Russ. Acad. Sci. Phys. 58, 1966 (1994); Nucl. Phys. Proc. Suppl. 52B, 17 (1997).
- [5] A. B. Kaidalov and K. A. Ter-Martirosyan, Sov. J. Nucl. Phys. 39, 979 (1984).
- [6] L. Gribov, E. Levin, and M. Ryskin, Phys. Rep. 100, 1 (1983).
- [7] O. Kancheli, JETP Lett. 18, 465 (1973).
A. B. Kaidalov, L. A. Ponomarev, and K. A. Ter-Martirosyan, Sov. J. Nucl. Phys. 44, 468 (1986).
- [8] S. Ostapchenko, To appear in Nucl. Phys. Proc. Suppl. B (2005), hep-ph/0412332; hep-ph/0501093.
- [9] C. Caso et al., Eur. Phys. J. C 3, 1 (1998).
- [10] S. Chekanov et al., ZEUS Collaboration, Nucl. Phys. B 713, 3 (2005).
- [11] R. Engel et al., 26th ICRC, Salt Lake City (1999) 1, 415.
- [12] I. G. Bearden et al., BRAHMS Collaboration, Phys. Lett. B 523, 227 (2001); Phys. Rev. Lett. 88, 202301 (2002).
- [13] R. Engel and H. Klages, C. R. Physique 5, 505 (2004).

Extensive Air Shower Simulation Program CONEX: Matching Monte Carlo and Numerical Methods

M. Alekseeva^a, T. Bergmann^b, V. Chernatkin^c, R. Engel^b, D. Heck^b,
N. Kalmykov^a, S. Ostapchenko^{ba}, T. Pierog^b, K. Werner^c

(a) *D.V. Skobeltsyn Institute of Nuclear Physics, Moscow State University, 119992 Moscow, Russia*

(b) *Forschungszentrum Karlsruhe, Institut für Kernphysik, 76021 Karlsruhe, Germany*

(c) *SUBATECH, Université de Nantes – IN2P3/CNRS – Ecole des Mines, Nantes, France*

Presenter: S. Ostapchenko (serguei@ik.fzk.de), ger-ostapchenko-S-abs2-he14-poster

We discuss the structure of new extensive air shower simulation code CONEX and demonstrate the advantages of the hybrid air shower calculation scheme employed. The latter combines an explicit Monte Carlo simulation of the most energetic part of the particle cascade in the atmosphere with a numerical treatment of secondary sub-cascades of smaller energies, using a system of corresponding integro-differential equations. Special attention is paid to the accuracy and the efficiency of the method. The results of the calculations, e.g., shower size profile, number of muons, particle energy spectra, are compared to the ones obtained using the traditional Monte Carlo approach, and to calculations with the CORSIKA program. Finally, we discuss possible applications of the code and the prospects for its further development.

1. Introduction

In contemporary high energy cosmic ray (CR) experiments Monte Carlo (MC) simulations of extensive air shower (EAS) development constitute an important part of data analysis procedures. Corresponding simulation tools, like the CORSIKA [1] and ARES [2] programs, are applied to establish relations between the measured EAS characteristics and the properties of primary CR particles. However, at very high energies, such calculations are very time-consuming and therefore have to be optimized. A popular method is to replace the full MC treatment of EAS development by some weighted sampling procedures, e.g., to apply the "thinning" method [3]. A promising alternative is to employ so-called hybrid procedures, which combine a direct MC simulation of the most energetic part of the air shower, for particle energies exceeding some energy threshold E_{thr} (typically chosen to be a factor 100 smaller than the energy of the primary particle), with numerical description of particle sub-cascades of smaller energies, based on the solution of corresponding nuclear-electro-magnetic cascade equations. Such a method allows one to reduce drastically the EAS calculation time, while having the same or in some cases even superior precision compared to standard methods.

Here we discuss a new EAS simulation program of that kind – CONEX [4]. The MC treatment of high energy ($E > E_{thr}$) hadronic and electro-magnetic (e/m) cascading processes in CONEX is very similar to its implementation in CORSIKA program: one follows the propagation, interactions, and decays (when relevant) of different hadrons, electrons (positrons), photons, and muons. There, hadronic interactions are treated optionally with the NEXUS [5], QGSJET [6], or SIBYLL [7] models (at low energies the GHEISHA program [8] can be employed as well), whereas the e/m part is handled by means of the EGS4 code [9], supplemented by an account for the Landau-Pomeranchuk-Migdal effect and for the photo-production process. All particles falling below the chosen energy threshold are stored to form the initial condition (so-called source term) for the cascade equations. Finally, further development of the complete nuclear-e/m cascade at sub-threshold energies is obtained by solving a system of integro-differential equations for the process, with the initial condition defined by the *multi-particle* source term, the latter having been formed as the result of the above-threshold cascade, i.e. *individually* for each shower. More detailed description of the corresponding procedures is given elsewhere [4] (see also [10, 11]).

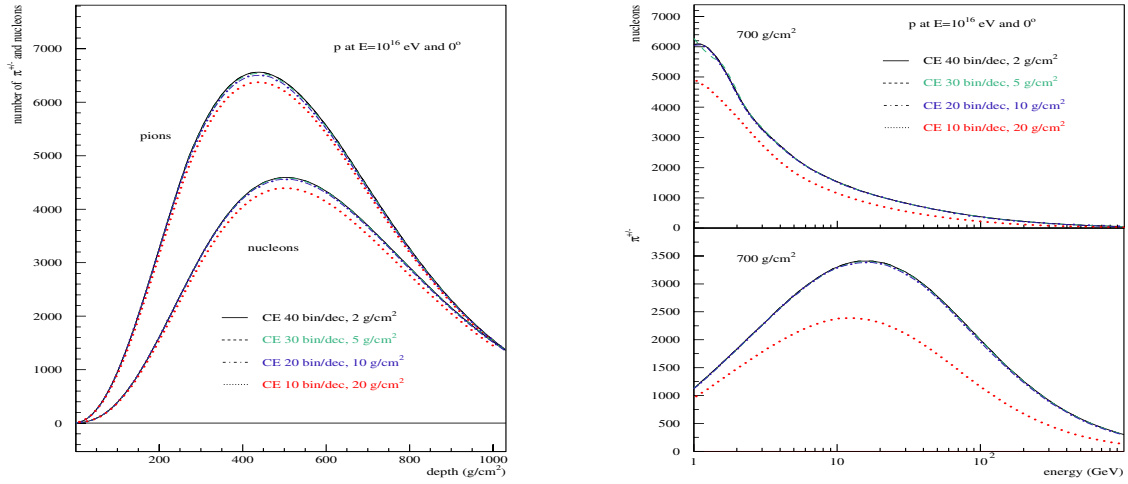


Figure 1. Longitudinal profiles (left) and energy spectra at 700 g/cm^2 (right) of nucleons and charged pions for proton-initiated vertical EAS of energy 10^{16} eV as calculated for different binning options using the numerical procedure (CE) with the QGSJET model.

2. Air shower characteristics

To illustrate the stability of our numerical procedure, we plot in Fig. 1 longitudinal profiles and energy spectra at 700 g/cm^2 of nucleons and charged pions for proton-initiated vertical EAS of energy 10^{16} eV for different binning options. Hadronic interactions have been treated using the QGSJET model. We choose correspondingly for the number of bins per energy decade and for the depth bin width (in g/cm^2) the following values: 40 and 2, 30 and 5, 20 and 10, 10 and 20. As seen from the Figure, we obtain nearly identical results in all cases, with the exception of the last, rather crude binning.

In general, the numerical procedure for the solution of e/m cascade equations is characterized by even better stability and allows to employ a more crude binning. Nevertheless, our default choice (to be applied for the calculations below) is rather conservative one, corresponding to 20 bins per energy decade and to 10 g/cm^2 step size in slant depth for both hadronic and e/m numerical procedures. In hybrid mode, the cutoff between the MC and the numerical part is set to $E_{\text{thr}} = 10^{-2} E_0$, E_0 being the primary energy. Furthermore, for comparison with CORSIKA in the following we apply GHEISHA and QGSJET for hadronic interactions below and above 80 MeV correspondingly. The typical computing time for proton-induced EAS of energy 10^{19} eV is one minute per shower using QGSJET or SIBYLL as high energy hadronic models.

In Fig. 2 we compare longitudinal profiles and energy spectra at 700 and 1000 g/cm^2 of charged pions and muons of energies above 1 GeV for proton-initiated vertical EAS of energy 10^{18} eV as calculated using the MC, numerical, and hybrid procedures, and with the CORSIKA program. Evidently, we obtain a very good agreement between the different methods.

In Fig. 3 we perform a similar comparison for longitudinal profiles and energy spectra at 700 g/cm^2 of electrons (positrons) and photons of energies above 1 MeV for proton-initiated vertical EAS of energy 10^{18} eV . Again, the results obtained with different methods agree well with each other.

Finally, we may test whether the employed hybrid scheme describes correctly EAS fluctuations. In Fig. 4(left) we plot the distribution for the deviation of the shower maximum position from its average value, $X_{\text{max}} -$

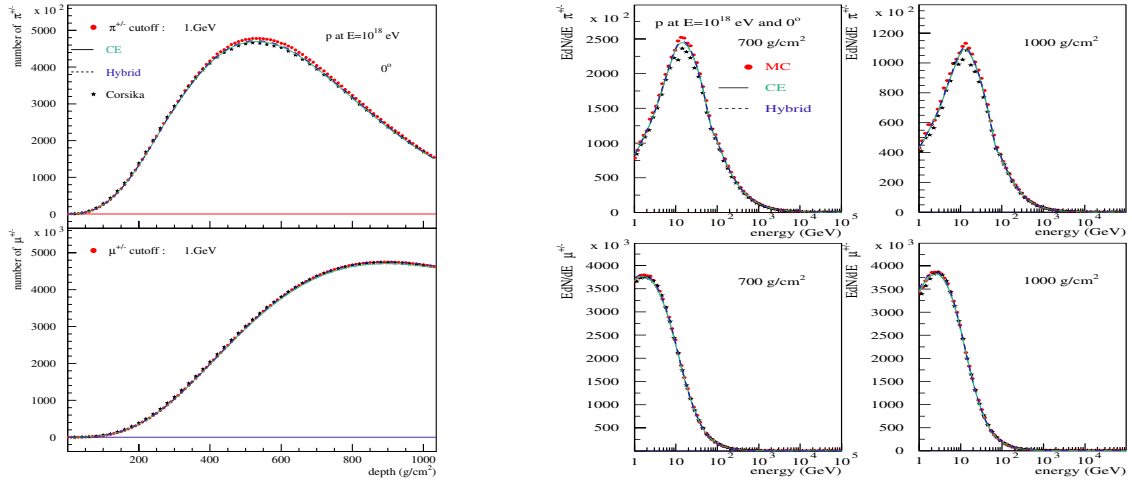


Figure 2. Longitudinal profiles (left) and energy spectra at 700 and 1000 g/cm² (right) of charged pions and muons of energies above 1 GeV for proton-initiated vertical EAS of energy 10¹⁸ eV as calculated using the MC (points), numerical (full line), and hybrid (dashed line) procedures in comparison to CORSIKA results (stars). The GHEISHA and QGSJET hadronic interaction models have been used below and above 80 MeV correspondingly.

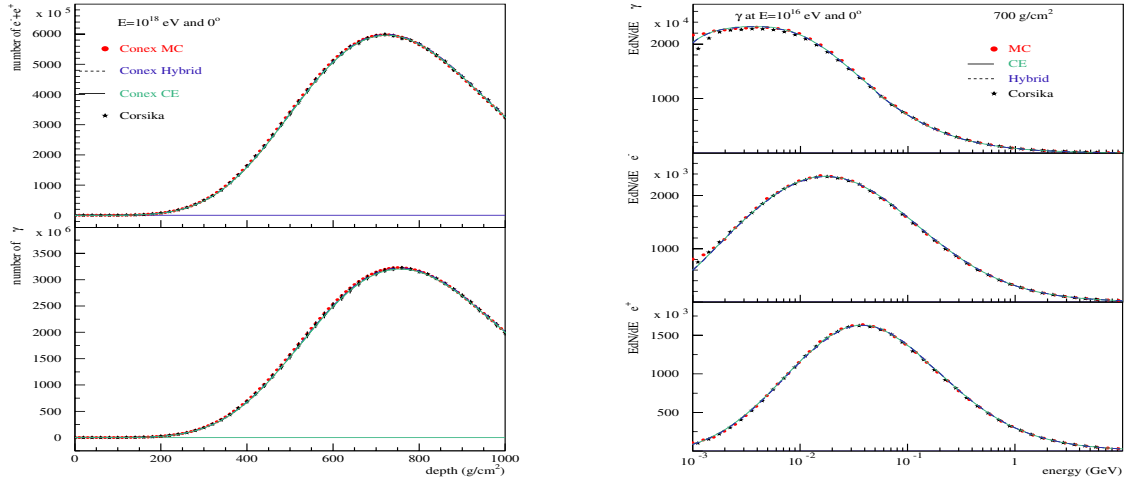


Figure 3. Longitudinal profiles of e^\pm and γ of energies above 1 MeV (left) and energy spectra of photons, electrons, and positrons at 700 g/cm² (right) for proton-initiated vertical EAS of energy 10¹⁸ eV as calculated using the MC (points), numerical (full line), and hybrid (dashed line) procedures in comparison to CORSIKA results (stars).

$\langle X_{\max} \rangle$, as calculated with the CONEX and CORSIKA programs. One observes an excellent agreement between the two results. In Fig. 4(right) we investigate the sensitivity of the obtained X_{\max} fluctuations to the choice of the threshold between the MC and numerical treatment. It is easy to see that these fluctuations are in general well described even for a rather high threshold value, $E_{\text{thr}} \simeq E_0$, being essentially defined by the propagation and interaction of the primary particle.

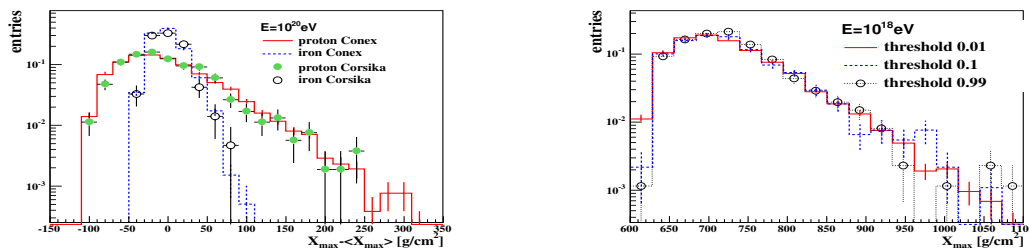


Figure 4. Left: fluctuations of the depth of shower maximum around the mean value (X_{\max}) for proton- and iron-initiated EAS of energy 10^{20} eV as calculated with the CONEX program (histograms) in comparison to CORSIKA results (points). Right: distribution of the depth of shower maximum for proton-initiated EAS of energy 10^{18} eV as calculated with the CONEX program for different thresholds between the MC and numerical parts.

3. Conclusions

We have demonstrated that the developed hybrid EAS simulation program CONEX allows us to achieve the same accuracy in describing basic shower characteristics and their fluctuations as the standard MC codes, e.g., CORSIKA code, while allowing to reduce considerably the calculation time. The results obtained with different methods, i.e. using MC, numerical, and hybrid procedures agree well with each other. While the present version of CONEX is restricted to one-dimensional (longitudinal) EAS description, further work is in progress to extend the scheme to the full three-dimensional EAS treatment [12]. On the other hand, already now the program is perfectly suitable for certain practical applications, in particular, in connection to high energy cosmic ray studies with fluorescence detectors, allowing reliable calculations of both charged particle energy spectra at various depths in the atmosphere, and of longitudinal profiles of particle energy deposits, as discussed in more detail in [13]. This gives the possibility to perform fast and accurate calculations of fluorescence and Cherenkov light production in air showers, without any need for parameterizations of shower profiles.

References

- [1] D. Heck et al., FZKA 6019, Forschungszentrum Karlsruhe, 1998.
- [2] S.J. Sciutto, astro-ph/9911331.
- [3] A.M. Hillas, Nucl. Phys. Proc. Suppl. 52B, 29 (1997).
- [4] T. Pierog et al., Nucl. Phys. Proc. Suppl. B (2005), to be published; astro-ph/0411260. N.N. Kalmykov et al., in preparation.
- [5] H.J. Drescher et al., Phys. Rep. 350, 93 (2001).
- [6] N. N. Kalmykov, S. S. Ostapchenko, and A. I. Pavlov, Bull. Russ. Acad. Sci. Phys. 58, 1966 (1994); Nucl. Phys. Proc. Suppl. 52B, 17 (1997).
- [7] R. Engel et al., 26th ICRC, Salt Lake City (1999) 1, 415.
- [8] H. Fesefeldt, Preprint PITHA 82/02, Aachen (1985).
- [9] W.R. Nelson et al., Preprint SLAC-265 (1985).
- [10] G. Bossard et al., Phys. Rev. D 63, 054030 (2001).
- [11] H.J. Drescher and G. Farrar, Phys. Rev. D 67, 116001 (2003).
- [12] K. Werner et al., AIP Conf. Proc. 739, 385 (2005).
- [13] T. Pierog et al., these proceedings (ger-engel-R-abs2-he14-oral).

Dependence of the longitudinal shower profile on the characteristics of hadronic multiparticle production

T. Pierog^a, M. Alekseeva^b, T. Bergmann^a, V. Chernatkin^c, R. Engel^a, D. Heck^a,
N.N. Kalmykov^b, S. Ostapchenko^a, M. Unger^a, and K. Werner^c

(a) Forschungszentrum Karlsruhe, Postfach 3640, D-76021 Karlsruhe, Germany

(b) Skobeltsyn Institute of Nuclear Physics, Moscow State University, Leninskie Gory 1, 119992, Moscow, Russia

(c) SUBATECH, Universite de Nantes, EMN, IN2P2/CNRS, Nantes, France

Presenter: R. Engel (Ralph.Engel@ik.fzk.de), ger-engel-R-abs2-he14-oral

The new hybrid simulation code CONEX is used to study longitudinal shower profiles and their dependence on the applied hadronic interaction model. In addition to the mean depth of shower maximum, we also investigate the model dependence of different estimators for the total shower energy. The large differences of model extrapolations to ultra-high energy are significantly reduced if the calorimetric energy of shower and energy deposit at shower maximum are considered.

1. Introduction

At shower energies above 10^{17} eV, the longitudinal shower profile can be determined from measurements of the fluorescence light signal produced in the atmosphere. The number of produced fluorescence photons is expected to be directly proportional to the ionization energy deposit of the shower particles. Therefore, the fluorescence technique allows not only the determination of the depth of shower maximum but also the direct measurement of the calorimetric energy of an air shower – the energy that is transferred to em. particles and finally converted to ionization energy. Traditionally, assuming a mean energy deposit per particle, measured fluorescence light profiles are converted to shower size curves that are then compared with theoretical predictions. However, it is much more natural to calculate and compare energy deposit profiles as they are first of all directly related to the number fluorescence photons and secondly do not depend on the simulation thresholds [1].

In this paper we use the hybrid cascade code CONEX [2] to simulate realistic energy deposit profiles of a large number of showers (about 1000 showers per energy value) to compare the predictions of different hadronic interaction models.

2. Shower depth of maximum

The mean depth of maximum of a hadron-induced shower is closely related to the description of high-energy hadron production. In Fig. 1 we compare the predictions obtained with CONEX for neXus 3.97 [3], QGSJET 01 [4], and Sibyll 2.1 [5]. GHEISHA 2002 [6] is used as low-energy model for interactions below 80 GeV lab. energy. All three high-energy interaction models differ significantly in their predictions. For example, in the case of Sibyll and QGSJET there are two counter-acting effects that nearly cancel each other. The cross section of Sibyll is much larger than that of QGSJET, leading to a higher first interaction point. At the same time the larger elasticity of Sibyll causes a shift the shower development deeper into the atmosphere. In the case of neXus and QGSJET the differences arise due mainly to the different secondary particle distributions. The cross section of neXus and QGSJET are very similar, however, neXus predicts more high-energy secondary pions.

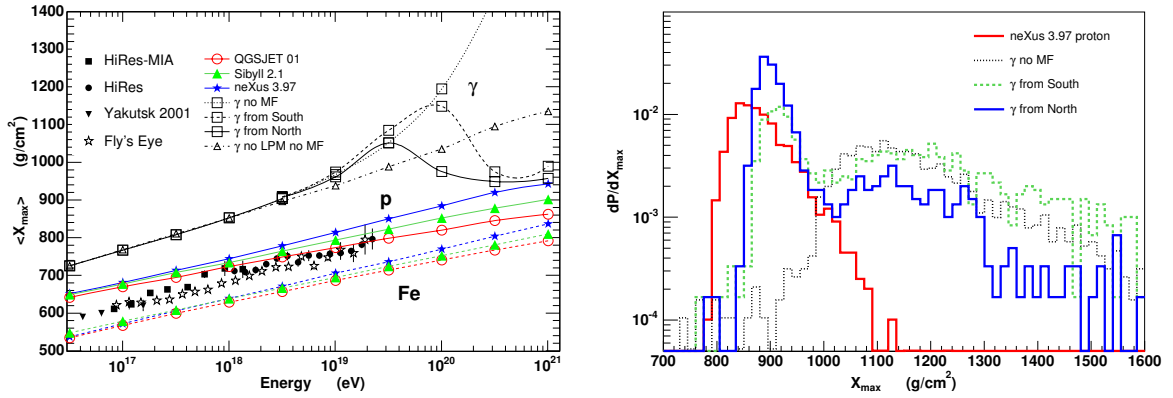


Figure 1. Left: mean depth of shower maximum of hadronic showers for three different interaction models. Also shown are photon-induced showers for different directions to the local geomagnetic field (MF). The references to the experimental data are given in [7]. Right: comparison of the distribution of the depth of maximum of photon- and proton-induced showers at 10^{20} eV.

The mean depth of maximum of photon-induced showers is strongly influenced by the Landau-Pomeranchuk-Migdal (LPM) effect and depends on the relative direction of the shower axis to the geomag. field. At high energy, photons can produce an em. shower already well above the atmosphere by interacting with the Earth’s magnetic field. In Fig. 1 this is illustrated by showing the predictions for photon showers of 60° at the southern Auger detector coming from the north (weak mag. field effect) and from the south (strong mag. field effect). For reference, also calculations without mag. field and without both LPM effect and mag. field are shown.

As many exotic models for ultra-high energy cosmic rays predict a large fraction of photons at high energy, it is interesting to compare the X_{\max} distributions of protons and photons. In Fig. 1 (right) these distributions are shown at 10^{20} eV. A significant fraction of photon showers (those that either pre-shower in the geomag. field or have a high-energy hadronic interaction in the early shower development) cannot be distinguished from proton showers on the basis of X_{\max} only.

3. Primary energy estimation

The calorimetric energy of a shower, E_{cal} , is defined as the depth-integral of the ionization energy deposit profile. Integrating numerically the simulated profiles and accounting for muons and hadrons at large depth [8], we calculate the calorimetric energy of showers for a “perfect” measurement. In Fig. 2 (left) the correction factor $f = E_{\text{tot}}/E_{\text{cal}}$ is shown with which the calorimetric energy has to be multiplied to obtain the primary particle energy. The black lines are the mean conversion factors averaged over the predictions of all three models considered here and averaged over proton and iron primaries. The ratio of the total to calorimetric energy is directly related to the number of consecutive hadronic interactions (number of generations) that pions undergo before they decay. In each of these interactions about $1/3$ of the secondary particles are neutral pions that transfer all of their energy to the electromagnetic shower component. Since the typical energy at which pions decay is about $100 - 200$ GeV, the number of generations increases with increasing primary energy. As the number of generations also influences the number of muons produced in a shower, there is a close relation between the number of muons and the calorimetric energy. Both the factor f and the predicted number of muons in high energy showers are bigger for QGSJET than Sibyll.

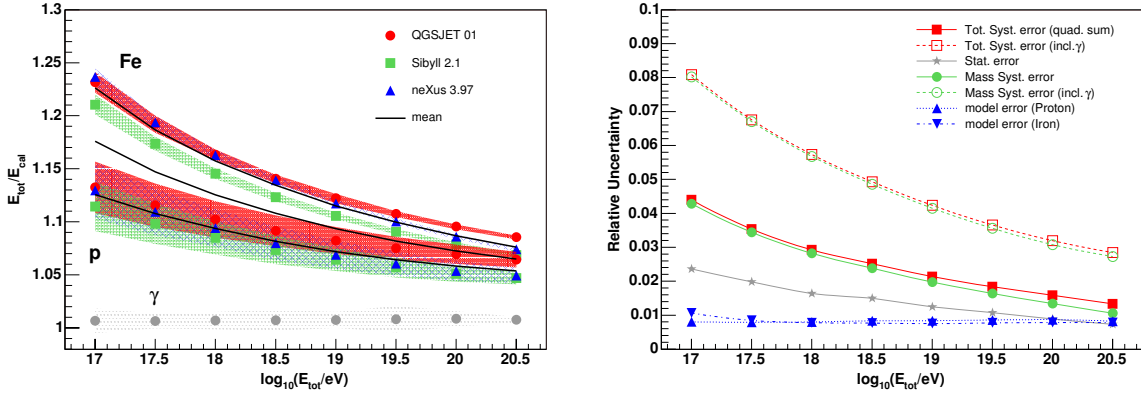


Figure 2. Left: mean value and RMS of the ratio of primary particle energy to calorimetric energy, shown for different models and primary particles. Right: relative uncertainty in energy reconstruction implied by the use of a conversion factor between the calorimetric and total energies that is averaged over models and primary particle types.

The uncertainty in reconstruction of the primary energy, assuming perfect calorimetric energy determination, is shown in Fig. 2 (right). We distinguish here between the statistical error due to shower-to-shower fluctuations and the systematic error due to differences implied by not knowing the cosmic ray composition and by different assumptions on hadronic interactions. The blue curves (triangles) show the systematic uncertainty one would have due to different interaction models if the composition were either only proton or only iron. The grey curve (stars) shows the statistical shower-to-shower uncertainty in total energy reconstruction, again assuming that the primary particle type is known. The green curve (filled circles) shows the systematic uncertainty if the composition is hadronic (in the range between proton and iron) but not known. It is calculated by applying the mean conversion factor f shown as the second black line in the l.h.s. figure. The red curve (filled squares) shows the total systematic error: the uncertainty due to the model dependence for a fixed composition is added quadratically to the uncertainty due to the unknown composition. If one considers the case of having a significant fraction of photons as primary particles, the curves with open symbols have to be used to estimate the uncertainties. They represent the composition-related and total systematic uncertainties if the conversion factor is calculated as average over proton, iron, and photon primaries.

The shower size at maximum is also well correlated with the primary energy and can be used as energy estimator. Motivated by the primary observable of fluorescence technique experiments, we show in Fig. 3 the factor by which the energy deposit at shower maximum has to be scaled to obtain the primary shower energy. Compared to the calorimetric energy, the energy deposit at shower maximum is subject to larger shower-to-shower fluctuations. On the other hand, the predictions are less model- and composition dependent over a wide energy range. In particular at about $10^{19.5}$ eV the conversion from the energy deposit to total energy is nearly independent of the primary particle type, including photons, and the assumed interaction model. Note the different behaviour of photon-induced showers due to the smaller muon number and the interplay between the LPM effect and mag. pre-showering.

The uncertainty in reconstruction of the total energy, again assuming perfect determination of the energy deposit at shower maximum, is shown in Fig. 3 (right). The labelling of the different curves is analogous to Fig. 2. The systematic uncertainty is very small at about $10^{19.5}$ eV.

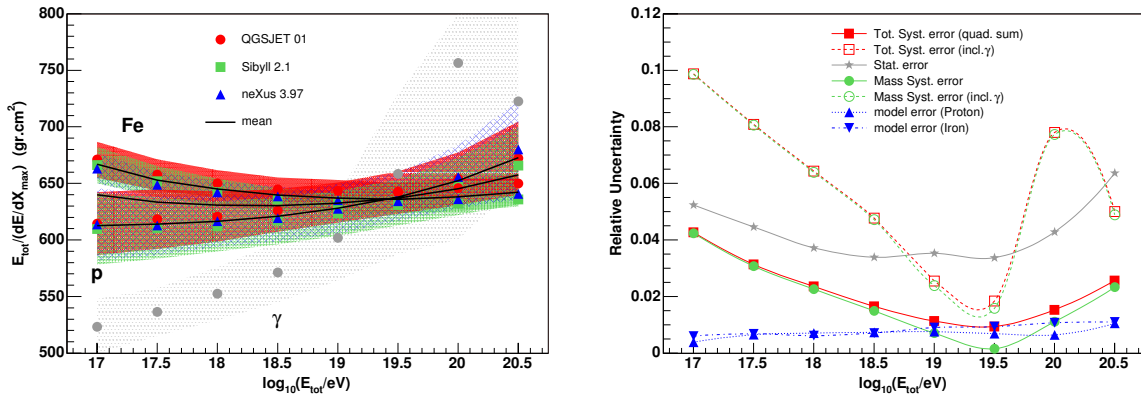


Figure 3. Left: mean ratio of total shower energy to the energy deposit at shower maximum. The shaded bands show the RMS of the shower-to-shower fluctuations. The black lines are the mean conversion factors averaged over the three models considered here and averaged over proton and iron primaries. Right: relative uncertainty in energy reconstruction implied by the use of energy deposit at shower maximum and a conversion factor that is averaged over models and primary particle types.

4. Conclusions and outlook

Differences in the extrapolation of the characteristics of had. interactions to ultra-high energy lead to a significant spread in the predictions of the mean depth of shower maximum. In contrast, the variation of the predictions on energy estimators such as the calorimetric energy and the energy deposit at shower maximum is relatively small. The total energy reconstruction uncertainty, assuming a perfect shower measurement, is dominated by the unknown primary composition. Using the calorimetric energy one obtains an uncertainty that is smaller than 4% for hadronic primaries in the energy range of relevance to current fluorescence detector experiments. The energy deposit at shower maximum can also be applied as independent energy estimator. Though being characterized by larger statistical fluctuations, it gives an almost model- and composition-independent measure of the primary energy at about 10^{19} eV.

References

- [1] M. Risse and D. Heck, *Astropart. Phys.* 20 (2004) 661.
- [2] M. Alekseeva et al., these proceedings, ger-ostapchenko-S-abs2-he14-poster; T. Pierog et al., *astro-ph/0411260*.
- [3] H.J. Drescher, M. Hladik, S. Ostapchenko, T. Pierog, and K. Werner, *Phys. Rep.* 350 (2001) 93 and *hep-ph/0007198*.
- [4] N.N. Kalmykov, S. Ostapchenko, and A.I. Pavlov, *Nucl. Phys. B (Proc. Suppl.)* 52B (1997) 17 and *Phys. At. Nucl.* 56 (1993) (3) 346.
- [5] R. Engel, T. K. Gaisser, P. Lipari, and T. Stanev, *Proc. of 26th ICRC (Salt Lake City) vol. 1*, p. 415, 1999; R. S. Fletcher, T. K. Gaisser, P. Lipari, and T. Stanev, *Phys. Rev. D* 50 (1994) 5710.
- [6] H. Fesefeldt, Report PITHA-85/02, RWTH Aachen, 1985.
- [7] R. Engel and H. Klages, *C. R. Physique* 5 (2004) 505.
- [8] H.M.J. Barbosa, F. Catalani, J.A. Chinellato, and C. Dobrigkeit, *Astropart. Phys.* 22 (2004) 159.

Hadronic multiparticle production in extensive air showers and accelerator experiments

C. Meurer^a, J. Blümer^b, R. Engel^a, A. Haungs^a, M. Roth^b

(a) Forschungszentrum Karlsruhe GmbH, Postfach 3640, D-76021 Karlsruhe, Germany

(b) Universität Karlsruhe (TH), Postfach 6980, D-76128 Karlsruhe, Germany

Presenter: M. Roth (Markus.Roth@ik.fzk.de), ger-roth-M-abs1-he21-oral

Using CORSIKA for simulating extensive air showers, we study the relation between the shower characteristics and features of hadronic multiparticle production at low energies. We report about investigations of typical energies and phase space regions of secondary particles which are important for muon production in extensive air showers. Possibilities to measure relevant quantities of hadron production in existing and planned accelerator experiments are discussed.

1. Introduction

One of the most promising approaches to determine the energy spectrum and composition of the cosmic rays with energies above 10^{15} eV is the measurement of the number of electrons and muons produced in extensive air showers (EAS). However the results of such a shower analysis are strongly dependent on the hadronic interaction models used for simulating reference showers [1]. Therefore it is important to study in detail the role of hadronic interactions and in particular the energy and secondary particle phase space regions that are most important for the observed characteristics of EAS.

The electromagnetic component of a shower is well determined by the depth of maximum and the energy of the shower. Due to the electromagnetic cascade, having a short radiation length of ~ 36 g/cm², any information on the initial distribution of photons produced in π^0 decays is lost. Therefore the electromagnetic shower component depends on the primary particle type only through the depth of shower maximum. In contrast, the muon component is very sensitive to the characteristics of hadronic interactions. Once the hadronic shower particles have reached an energy at which charged pions and kaons decay, they produce muons which decouple from the shower cascade. The muons propagate to the detector with small energy loss and deflection and hence carry information on hadronic interactions in EAS. Due to the competition between interaction and decay, most of the muons are decay products of mesons that are produced in low-energy interactions. Therefore it is not surprising that muons in EAS are particularly sensitive to hadronic multiparticle production at low energy [2]. Recent model studies show that even at ultra-high shower energies the predictions on the lateral distribution of shower particles depend strongly on the applied low-energy interaction model [3].

2. Muon production in extensive air showers

Motivated by the measurement conditions of the KASCADE array [4], we consider showers with a primary energy of 10^{15} eV and apply a muon detection threshold of 250 MeV. Using a modified version of the simulation package CORSIKA [5] we have simulated two samples of 1500 vertical and inclined (60°) proton and 500 iron induced showers. Below 80 GeV the low-energy hadronic interaction model GHEISHA 2002 [6] and above 80 GeV the high-energy model QGSJET 01 [7] are applied. In the following only vertical proton showers are discussed. The results are very similar for iron induced showers and also for zenith angles up to 60°.

In Fig. 1 the energy distribution of muons at detector level (1030 g/cm^2) is shown for several lateral distance ranges. The maximum of this distribution shifts to lower energies for larger lateral distances. Most likely four to five consecutive hadronic interactions (number of generations) take place before a hadron decays into a muon, see Fig. 2. Here and in the following we consider only those muons that reach the ground level with an energy above the detection threshold. The number of generations show no significant dependence on the lateral distance. To study the hadronic *ancestors* of muons in EAS, we introduce the terms *grandmother* and *mother particle* for each observed muon. The grandmother particle is the hadron inducing the *last* hadronic interaction that finally leads to a meson (mother particle) which decays into the corresponding muon. Most of the grandmother and mother particles are pions, but also about 20% of the grandmother particles are nucleons and a few are kaons. Details of the composition of mother and grandmother particles are given in Tab. 1.

Table 1. Particle types of mother and grandmother particles in a vertical proton induced shower at 10^{15} eV .

	mother	grandmother
pions	89.2%	72.3%
kaons	10.5%	6.5%
nucleons	-	20.9%

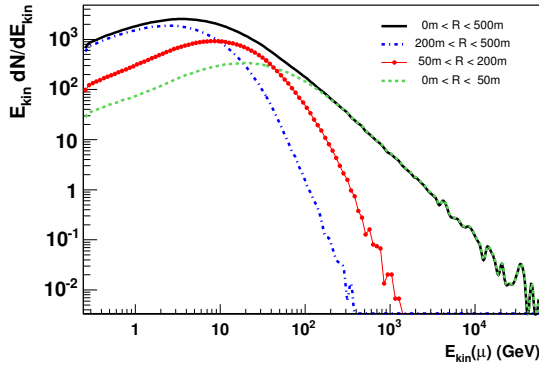


Figure 1. Simulated energy distribution of muons for different lateral distances.

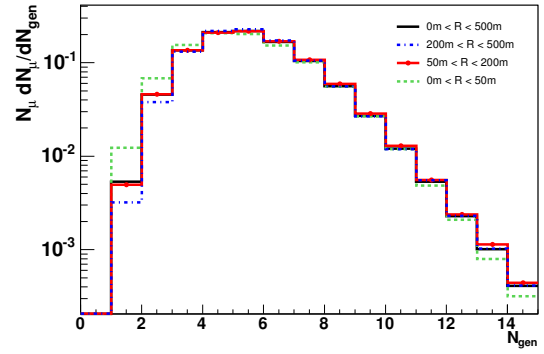


Figure 2. Averaged number of generations before producing a muon visible at ground level (shown for various lateral distances).

3. Energy and phase space regions

The energy spectra of different grandmother particles are shown in Fig. 3 (left). They cover a large energy range up to the primary energy with a maximum at about 100 GeV . The peak at 10^6 GeV in the nucleon energy spectrum shows that also a fraction of muons stems from decays of mesons produced in the first interaction in a shower. Furthermore, the step at 80 GeV clearly indicates a mismatch between the predictions of the low-energy model GHEISHA and the high-energy model QGSJET. In Fig. 3 (right) the grandmother particle energy spectrum is shown for different ranges of lateral muon distance. The maximum shifts with larger lateral distance to lower energies. Comparing the *last* interaction in EAS with collisions studied at accelerators, one has to keep in mind that the grandmother particle corresponds to the beam particle and the mother particle is equivalent to a secondary particle produced in e.g. a minimum bias p-N interaction. The most probable energy of the grandmother particle is within the range of beam energies of fixed target experiments e.g. at the SPS accelerator at CERN.

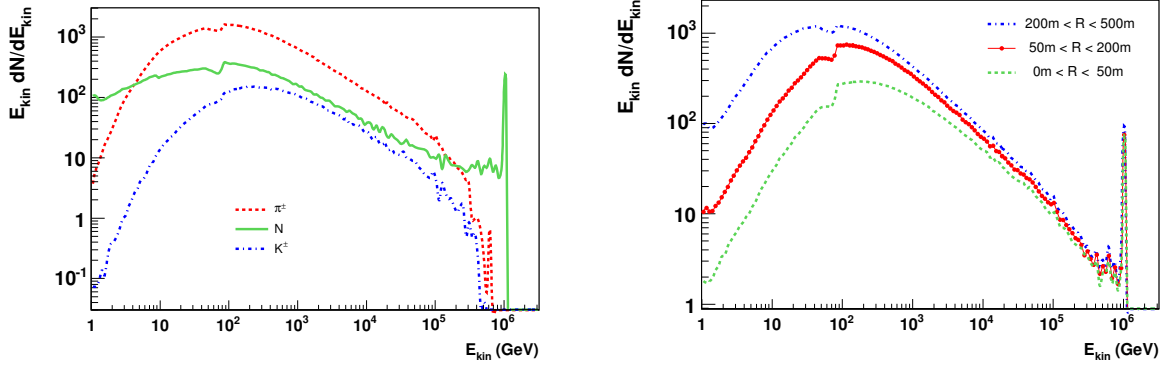


Figure 3. Energy distribution of grandmother particles. Left: different grandmother particle types; lateral distance range of muons at ground level: 0-500 m. Right: different lateral distances; all particle types are summed up.

The further study of the relevant phase space of the mother particles is done for two different grandmother energy ranges and lateral distance ranges of muons at ground level, see Tab. 2. The lateral distance ranges are chosen to resemble typical lateral distances measured at KASCADE and KASCADE-Grande, respectively. In Fig. 4 the rapidity spectra of mother particles (left: pions, right: kaons) are compared to the spectra of secondary particles of proton-carbon collisions and proton-air collisions simulated with QGSJET labeled as *fixed target*. The spectra of mother particles in air showers are scaled to fit the falling tail of the fixed-energy collision spectra. No significant differences are found comparing the rapidity distributions of secondary particles in proton-carbon and proton-air collisions. As a consequence of the different selection criteria, the forward hemisphere in the mother rapidity spectra is clearly favoured compared to the spectra of secondaries in minimum bias collisions.

Table 2. For the analysis used energy and lateral distance ranges.

energy range	average energy	lateral distance range
80-400 GeV	160 GeV	50-200 m
30-60 GeV	40 GeV	200-600 m

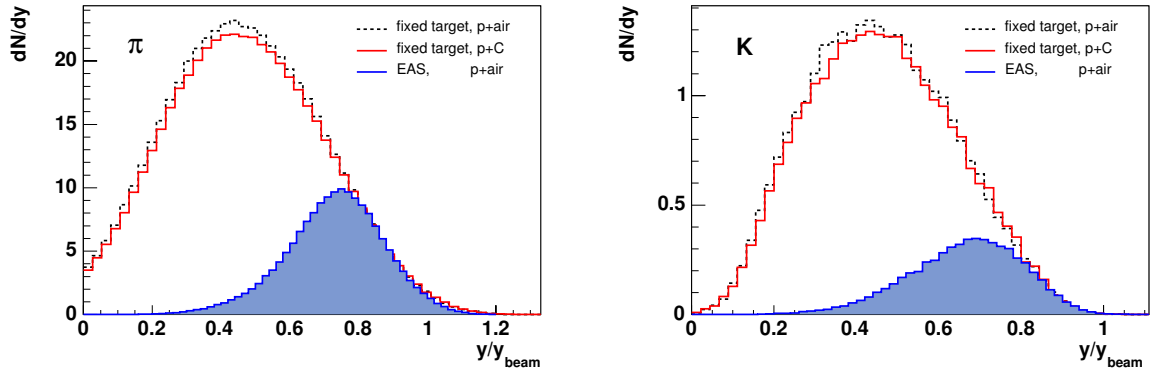


Figure 4. Rapidity distributions of mother particles (filled curves) compared with rapidity distributions of secondary particles in simulated single p+C (solid line) and simulated p+air (dashed line) collisions. Left: pions. Right: kaons. The energy range of the grandmother particle is limited to 80-400 GeV and the lateral distance of the muons to 50-200 m to match experimentally accessible regions. The fixed target collision simulation is done at 160 GeV, corresponding approximately to the mean grandmother energy. The rapidity is normalized to the rapidity of the beam and grandmother particles, respectively.

4. Conclusions and outlook

Due to the interplay between decay and interaction of pions and kaons, low energy hadronic interactions are very important for muon production in extensive air showers. With increasing lateral distance the mean energy of these interactions, which are mainly initiated by pions and nucleons, decreases. The phase space regions of relevance to EAS are shown in Fig. 5 and summarized in Tab. 3. The most important interaction energies and phase space regions fall in the range accessible to fixed target experiments with large acceptance detectors such as HARP, NA49, and MIPP (see also [8] and Refs. therein). Therefore fixed target measurements could be used to improve low energy interaction models that can be independently cross-checked by muon measurements in EAS.

Table 3. Phase space regions of hadronic interactions relevant for muon production in EAS.

average energy (GeV)	y/y_{beam}	p_{\perp} (GeV/c)
160	0.3 - 1.1	0.0 - 0.7
40	0.3 - 1.1	0.0 - 1.0

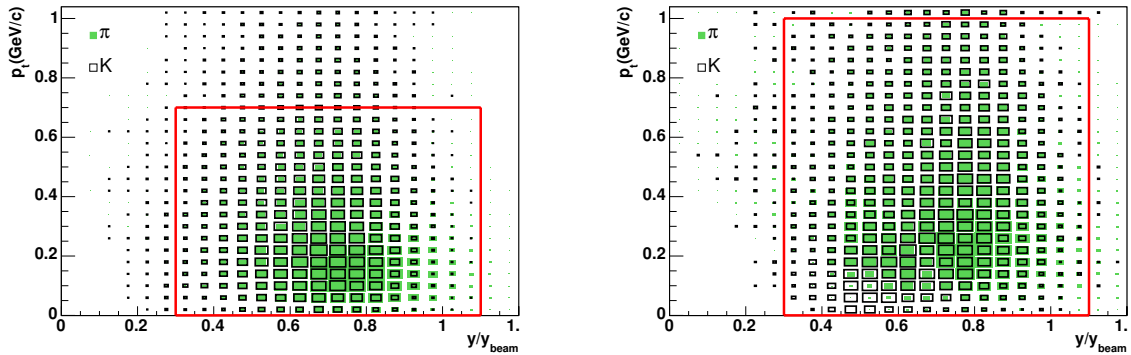


Figure 5. Phase space of mother particles. Left: grandmother energy range: 80-400 GeV. Right: 30-60 GeV. The filled symbols show the distribution for pions, the open symbols for kaons. The large box (red) indicates the most interesting phase space region which includes more than 90% of this particles.

Acknowledgements: The authors thank Dieter Heck for many fruitful discussions and help with modifying CORSIKA to include the muon ancestor information.

References

- [1] T. Antoni et al. (KASCADE Collab.) *Astropart. Phys.* in press, astro-ph/0505413.
- [2] R. Engel, T.K. Gaisser, and T. Stanev, *Proc. of ISMD*, Providence, Rhode Island, August 9-13, 1999, World Scientific (2000), p. 457; H.J. Drescher and G. Farrar, *Astropart. Phys.* 19 (2003) 235.
- [3] H.J. Drescher, M. Bleicher, S. Soff, H. Stöcker, *Astropart. Phys.* 21, 87-94 (2004); D. Heck et al., *Proc. of 28th ICRC*, Tsukuba, Japan, (2003) p. 279.
- [4] T. Antoni et al. (KASCADE Collab.) *Nucl. Instr. Meth. A* 513 (2003) 490
- [5] D. Heck, J. Knapp, J. Capdevielle, G. Schatz and T. Thouw, FZKA 6019, Forschungszentrum Karlsruhe, 1998.
- [6] H. Fesefeldt, Report PITHA-85/02, RWTH Aachen, 1985.
- [7] N.N. Kalmykov, S. Ostapchenko, and A.I. Pavlov, *Nucl. Phys. B (Proc. Suppl.)* 52B (1997) 17.
- [8] G. Barr and R. Engel, *Proc. of 13th ISVHECRI*, Pylos, Greece, (2004) submitted to *Nucl. Phys. B*, astro-ph/0504356.

Monte Carlo simulations and semianalytical parameterisations of the atmospheric muon flux controlled by muon charge ratio measurements performed with WILLI detector

I.M. Brancus^a, B. Mitrica^a, A. Bercuci^a, G. Toma^a, J. Wentz^b, H. Rebel^b, M.Duma

(a) IFIN-HH, RO-76900 Bucharest, POB MG-6, Romania

(b) Forschungszentrum Karlsruhe, POB 3640, 76021 Karlsruhe, Germany

Presenter: I.M. Brancus (iliana@muon1.nipne.ro), rom-brancus-IM-abs2-he12-poster

The atmospheric muon flux have been simulated using the CORSIKA code for two different geographical positions (Bucharest: 44 deg N, 26 deg E and Hiroshima:34 deg N, 132 deg E). The simulations have been done for different angles of incidence between 0 deg and 70 deg. The comparison between the simulations and the experiment have been done using the measurements of the muon charge ratio with the WILLI detector in Bucharest. The results of the Monte Carlo simulations of the muon flux for the geographical positions of Hiroshima and Bucharest are compared with the semi-analytical formulae of Judge and Nash, and of Gaisser for different angles of incidence between 0 deg and 70 deg and with experimental results of the Bess experiment (vertical incidence). Various sensitivities of the approach of Judge and Nash, in particular to variations of the pion and kaon production spectra have been studied.

1. Introduction

The muon belongs to the family of elementary particles known as leptons. Like the electron it may be positively or negatively charged and has a spin $\frac{1}{2}$. However its mass is about 100 MeV, more than two orders of magnitude larger than that of the electron, and about one order of magnitude less than of the proton. It is produced mainly by the decay of pions and kaons generated by high-energy collisions of cosmic rays with the atoms of the Earth atmosphere. Muons are unstable decaying to electrons and positrons and neutrinos (electron (ν_e) and muon (ν_μ) neutrinos) with a half - life of $\tau_\mu = 2.2\mu s$.

2. The air shower simulation program CORSIKA

The simulation tool CORSIKA has been originally designed for the four dimensional simulation of extensive air showers with primary energies around 10^{15} eV. The particle transport includes the particle ranges defined by the life time of the particle and its cross-section with air. The density profile of the atmosphere is handled as continuous function, thus not sampled in layers of constant density.

Ionization losses, multiple scattering, and the deflection in the local magnetic field are considered. The decay of particles is simulated in exact kinematics, and the muon polarization is taken into account.

In contrast to other air shower simulations tools, CORSIKA offers alternatively six different models for the description of the high energy hadronic interaction and three different models for the description of the low energy hadronic interaction. The threshold between the high and low energy models is set by default to $E_{Lab} = 80$ GeV/n.

3. Calculation of atmospheric muon flux

The calculation of muon flux proceeds by a full 3D-simulation (CORSIKA). The simulations have been done using for the primary particle's spectrum the expression: $J_p(E) \sim E^{-2.78}$.

The differential particle flux

$$J_\mu = \frac{dN}{dt \cdot dA \cdot d\Omega \cdot dP} \quad (cm^{-2} \cdot s^{-1} \cdot sr^{-1} \cdot (GeV/c)^{-1}) \quad (1)$$

resulting from the simulation was calculated by dividing the number of particles detected by the surface of the particle collection area (cm^2), solid angle, momentum bin size, and equivalent sampling time of the CR flux.

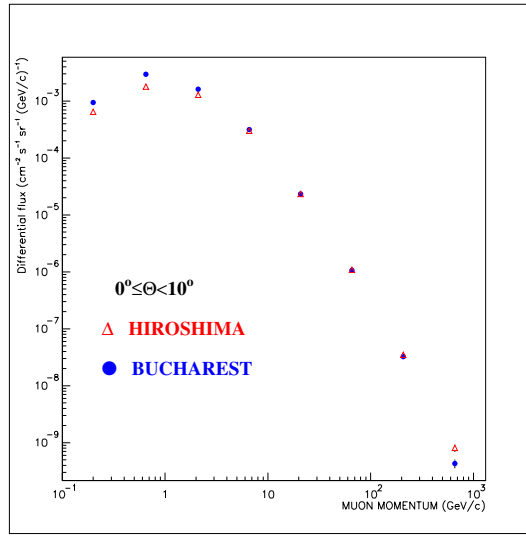


Figure 1. Differential flux of the muons for $0^\circ \leq \theta < 10^\circ$

4. Semi-analytical approaches

There are several empirical approximations describing the fluxes in by analytical expressions like power-law distributions (see P.Grieder[4]). Recent approaches by T.K. Gaisser[1] display explicitly the dependence on primary energy, but with complicated mathematical procedures and valid only for muon energies above 10 GeV. This holds also for the simplification given in Gaisser's Book:

$$\phi_\mu = \frac{0.14}{cm^2 \cdot s \cdot sr \cdot GeV} \cdot (E/GeV)^{-2.7} \left[\frac{1}{1 + \frac{E \cdot \cos\theta}{110 GeV}} + \frac{0.37}{1 + \frac{E \cdot \cos\theta}{760 GeV}} \right] \quad (2)$$

used for example by Unger[5]. In Fig.2 this formula is compared with the the results of the Monte Carlo simulations , displaying the disagreement in particular at lower energies.

The approach by Judge and Nash[2] uses as input the production spectra of parent pions and kaons and calculates the flux resulting from pion and kaon decay by:

$$D_{\pi}(E_{\mu}, \theta) = \frac{A_{\pi} \cdot W_{\mu} \cdot E_{\pi}^{-\gamma_{\pi}} \cdot H_{\pi}}{E_{\pi} \cdot \cos\theta + H_{\pi}} \quad (3)$$

$$D_{k}(E_{\mu}, \theta) = \frac{A_{k} \cdot W_{\mu} \cdot E_{k}^{-\gamma_{k}} \cdot H_{k}}{E_{k} \cdot \cos\theta + H_{k}} \quad (4)$$

There $H_{\pi,k}$ and H_{μ} are parameters accounting for the propagation of the particles in the atmosphere. The parameters $A_{\pi,k}$ are the normalisations of the pion and kaon production spectra. There are several other parameters entering in the approximation: the absorption lengths of the primary particle λ_p , of the pions λ_{π} and kaons λ_k . There is clearly some influence, but in the present investigation the values have been fixed along the original proposal. Only the $A_{\pi,k}$ values have been changed in order to adjust the calculated fluxes to the results of the Monte Carlo simulations and to experimental data from the BESS[3] experiment.

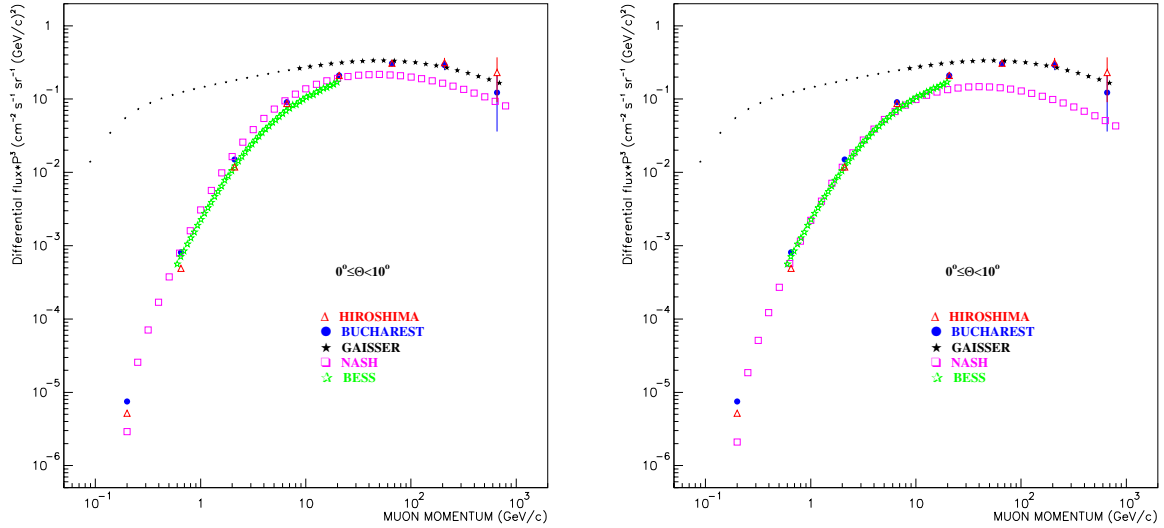


Figure 2. Comparison of the results of Monte Carlo simulations and BESS data with predictions of simplified semi-analytical formulae. In the approach of Judge and Nash $A_{\pi} = 0.373$ and $A_k = 1.0$ (Fig. 1.a) and $A_{\pi} = 0.373$ and $A_k = 0.373$ (Fig. 1.b) is used.

5. Test of the simulation program by experimental results

The Monte Carlo program outlined in chapt. 2 and to be used for calculations of the muon fluxes at various locations has been checked by experimental results of accurate muon charge ratio measurements[6]. Fig.3 displays the comparison between measured results of the East -West effect performed with WILLI and with CORSIKA simulations. The values are compiled in tab.1.

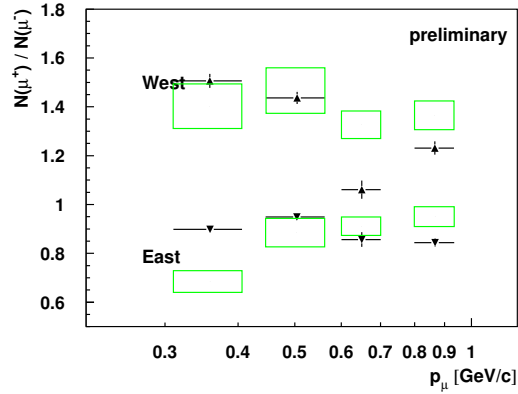


Figure 3. Comparison of the muon charge ratio and the East -West effect with the CORSIKA predictions

Table 1. Compilation of the numerical values displayed in fig.3

Azimuth	Momentum(GeV/c)	$\langle \theta_p \rangle$	R_{WILLI}	$R_{CORSIKA}$
EAST	0.36	35	0.89	0.68
	0.50	35	0.95	0.88
	0.65	35	0.85	0.91
	0.87	35	0.84	0.95
WEST	0.36	35	1.50	1.4
	0.50	35	1.43	1.46
	0.65	35	1.06	1.32
	0.87	35	1.23	1.36

6. Concluding remarks

Semi-analytical approaches[7] are able to reproduce globally the results of Monte Carlo simulations and experimental data, and in particular the approach of Judge and Nash does account for muon energies $< 10 GeV$. However, these approaches can be hardly modified in order to take into account also finer effect like the influence of the geomagnetic field. For that detailed Monte Carlo simulations have to be invoked.

References

- [1] T.K. Gaisser, *Astropart. Phys.* 16(2002)285
- [2] R.J.R.Judge and W.F.Nash, *Il Nuovo Cimento*, XXXV-4(1965)999
- [3] M. Motoki et al, *Astropart. Phys.* 19(2003)113-126
- [4] P.K.Grieder, *Cosmic Rays at Earth, Researcher's Reference Manual and Data Book*, Elsevier (2001)354-454
- [5] M.Unger, PhD thesis, Humboldt-Universitat zu Berlin, (2003)
- [6] I.M.Brancus et al, *Nucl. Phys.* A721(2003)1044c
- [7] B.Mitrica, Master Thesis, University Bucharest (2004)

Upper limit on the primary photon fraction from the Pierre Auger Observatory

The Pierre Auger Collaboration

Presenter: M. Risse (markus.risse@ik.fzk.de), ger-risse-M-abs2-he14-oral

Based on observations of the depth of shower maximum performed with the hybrid detector of the Auger Observatory, an upper limit on the cosmic-ray photon fraction of 26% (at 95% confidence level) is derived for primary energies above 10^{19} eV. Additional observables recorded with the surface detector array, available for a sub-set of the data sample, support the conclusion that a photon origin of the observed events is not favoured.

1. Introduction

One of the key observables to distinguish between model predictions on the origin of the highest-energy cosmic rays is the fraction of primary cosmic-ray photons. In non-acceleration (“top-down”) models a significant fraction of the generated particles are photons [1]. Air showers initiated by photons at energies above 10^{19} eV are in general expected to have a relatively large depth of shower maximum X_{\max} and fewer secondary muons compared to nuclear primaries. Previous upper limits on the photon fraction were derived from surface array data of the Haverah Park and AGASA experiments [2, 3, 4].

We report an analysis of data recorded by the Auger Observatory [5]. The photon upper limit derived here is based on the direct observation of the longitudinal air shower profile and makes use of the hybrid detection technique: X_{\max} is used as discriminant observable. The information from triggered surface detectors in hybrid events considerably reduces the uncertainty in shower track geometry.

For a sub-set of the event sample used in this analysis, a variety of surface detector observables is available. The additional discrimination power of these observables is demonstrated.

2. Data

The data are taken with a total of 12 fluorescence telescopes [6], situated at two different telescope sites, during the period January 2004 to April 2005. The number of deployed surface detector (SD) stations [7] grew from ~ 200 to ~ 800 during this time. For the analysis, hybrid events were selected, i.e. showers observed both by (at least one) surface tank and telescope [8]. Even for one triggered tank only, the additional timing constraint allows a significantly improved geometry fit to the observed profile which leads to a reduced uncertainty in the reconstructed X_{\max} . The following criteria are applied for event selection:

- to maximize the reconstruction quality: geometry and profile fits succeeded, X_{\max} observed, track length in field of view $>400 \text{ g cm}^{-2}$, minimum viewing angle $>18^\circ$, primary photon energy $\lg E/\text{eV} > 19.0$;
- to achieve comparable detector acceptance to photon and nuclear primaries: primary zenith angle $>35^\circ$, distance of telescope to shower axis $<24 \text{ km} + f(E)$, with $f(E) = 12 \text{ km} \cdot (\lg E/\text{eV} - 19.0)$.

The reconstruction is based on an end-to-end calibration of the fluorescence telescopes [9], on monitoring data of local atmospheric conditions [10, 11], and includes an improved subtraction of Cherenkov light [12] and reconstruction of energy deposit profiles for deriving the primary energy. The decreased fraction of missing energy in primary photon showers is accounted for. In total, 16 events with energies above 10^{19} eV are selected.

The total uncertainty $\Delta X_{\max}^{\text{tot}}$ of the reconstructed depth of shower maximum is composed of several contributions which, in general, vary from event to event. A conservative estimate of the current X_{\max} uncertainties gives $\Delta X_{\max}^{\text{tot}} \simeq 40 \text{ g cm}^{-2}$. Among the main contributions, each one in general well below $\Delta X_{\max} = 15 \text{ g cm}^{-2}$, are the statistical uncertainty from the profile fit, the uncertainty in shower geometry, the uncertainty in atmospheric conditions such as the air density profile, and the uncertainty in the reconstructed primary energy, which is taken as input for the primary photon simulation.

For each event, high-statistics shower simulations are performed for photons for the specific event conditions. Possible cascading of photons in the geomagnetic field is simulated with PRESHOWER [13]. Shower development in air, including the LPM effect [14], is calculated with CORSIKA [15]. The Particle Data Group extrapolation of the photonuclear cross-section [16] and QGSJET 01 [17] as hadron event generator are adopted.

A simulation study of the detector acceptance to photons and nuclear primaries has been conducted. For the chosen cuts, the ratio of the acceptance to photon-induced showers to that of nuclear primaries (proton or iron nuclei) is $\epsilon = 0.88$. A corresponding correction is applied to the derived photon limit.

3. Results

Fig. 1 shows as an example an event of 11 EeV primary energy observed with $X_{\max} = 744 \text{ g cm}^{-2}$, compared to the corresponding X_{\max} distribution expected for primary photons. With $\langle X_{\max}^{\gamma} \rangle = 1020 \text{ g cm}^{-2}$, photon showers are on average expected to reach maximum at depths considerably greater than observed. Shower-to-shower fluctuations are large due to the LPM effect (rms of 80 g cm^{-2}) and well in excess of the measurement uncertainty. For all 16 events, the observed X_{\max} is well below the average value expected for photons. The X_{\max} distribution of the data is also displayed in Fig. 1.

The statistical method for deriving an upper limit follows that introduced in [4]. In brief, for each event a χ^2 value is derived by comparing the observed X_{\max} to the prediction from photon shower simulations. Accounting for the limited event statistics, the chance probability $p(f_{\gamma})$ is calculated to obtain data sets with χ^2 values larger than observed as a function of the hypothetical primary photon fraction f_{γ} . The upper limit f_{γ}^{ul} , at a confidence level α , is then obtained from $p(f_{\gamma} \geq \epsilon f_{\gamma}^{\text{ul}}) \leq 1 - \alpha$, where the factor $\epsilon = 0.88$ accounts for the different detector acceptance to photon and nuclear primaries.

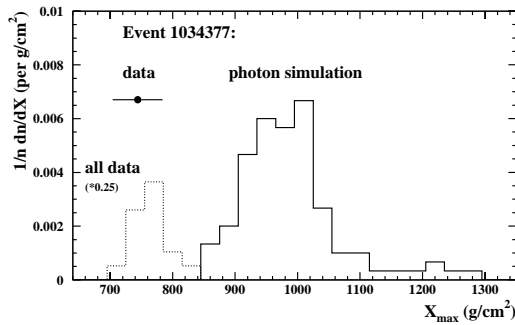


Figure 1. Example of X_{\max} measured in an individual shower of 11 EeV (point with error bar) compared to the X_{\max} distribution expected for photon showers (solid line). Also shown the X_{\max} distribution of the data sample (dashed line; normalization changed as indicated).

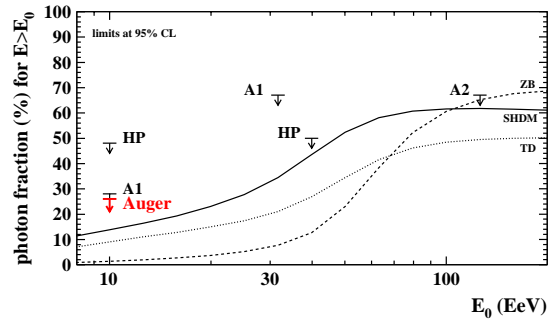


Figure 2. Upper limits (95% CL) on cosmic-ray photon fraction derived in the present analysis (Auger) and previously from AGASA (A1) [3], (A2) [4] and Haverah Park (HP) [2] data compared to some estimates based on non-acceleration models [1].

For the Auger data sample, an upper limit on the photon fraction of 26% at a confidence level of 95% is derived. In Fig. 2, this upper limit is plotted together with previous experimental limits and some estimates based on non-acceleration models. The presented 26% limit confirms and improves the existing limits above 10^{19} eV.

4. Discrimination power of surface array observables

In 5 out of the 16 selected events, the number of triggered surface detectors is large enough to perform a standard SD reconstruction [7]. Several observables can be used for primary photon discrimination [18], e.g.:

- *rise time*: For each triggered tank, we define a rise time as the time for the integrated signal to go from 10% to 50% of its total value. By interpolation between rise times recorded by the tanks at different distances to the shower core, the rise time at 1000 m core distance is extracted after correcting for azimuthal asymmetries in the shower front. Compared to nuclear primaries, where the rise time is relatively short due to muons that do not suffer from multiple scattering as shower electrons do, rise times in muon-poor photon showers are expected to be significantly larger.
- *curvature*: The shower front shape is fitted to a sphere (expanding at speed of light as the shower propagates) using the start times of the FADC traces of each station. Then the curvature for the event is defined as the inverse of the radius of the sphere at the shower core position on ground. As the photon-initiated showers in general develop deeper in the atmosphere, the shower front curvature is expected to be larger than that of nuclear primaries.

As an example, for the specific event shown in Fig. 1, the measured rise time and curvature data are compared to the simulated distributions in Figs. 3 and 4. For this and the other SD reconstructed hybrid events, the SD observables are well separated from the predictions for primary photons. These results provide independent information to the photon limit derived by the hybrid analysis. They support the conclusion that a photon origin of the observed events is not favoured.

The SD data statistics at these energies is considerably larger than the hybrid statistics, as the duty cycle of the fluorescence telescopes is $\sim 10\%$. To exploit the excellent statistical power, which will allow us to test

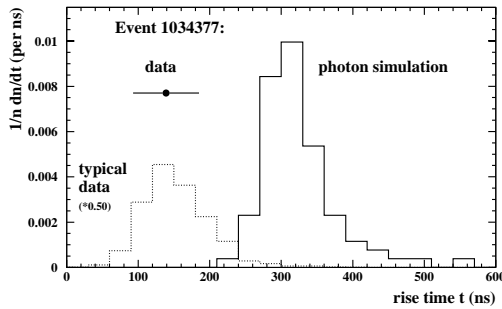


Figure 3. Example of rise time measured in an individual shower (same as in Fig. 1) (point with error bar) compared to the X_{\max} distribution expected for photon showers (solid line). The typical data distribution from SD events at comparable zenith angle is also given (dashed line; normalization changed as indicated).

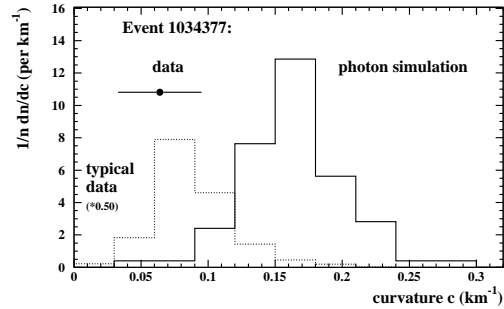


Figure 4. Example of curvature measured in an individual shower (same as in Fig. 1) (point with error bar) compared to the X_{\max} distribution expected for photon showers (solid line). The typical data distribution from SD events at comparable zenith angle is also given (dashed line; normalization changed as indicated).

hypothetical primary photon fractions that are significantly smaller, current studies are performed on subtleties specific to an SD-only analysis: (i) event trigger and reconstruction are not fully efficient for photons at 10^{19} eV; (ii) the primary energy estimation is mass dependent, which could lead to a selection bias.

5. Outlook

The photon bound derived in this work is mainly limited by the small number of events. The data statistics of hybrid events will considerably increase in the near future, and much lower primary photon fractions can be tested. Moreover, the larger statistics will allow us to increase the threshold energy of 10^{19} eV chosen in the present analysis to energy ranges where even larger photon fractions are predicted by some models.

The discrimination power of surface detector observables will be further exploited. If hybrid detection is not required then statistics is significantly increased. Ways to reduce a possible selection bias in SD-only analyses are being investigated. Also, the technique introduced in [2] where event rates of near-vertical and inclined showers are compared to each other, can be further developed.

The uncertainty in extrapolating the photonuclear cross-section to highest photon energies imposes a systematic uncertainty in photon shower simulations both for fluorescence light and ground particle observations [19, 4]. Related systematic studies are ongoing.

References

- [1] G. Gelmini, O.E. Kalashev, and D.V. Semikoz, astro-ph/0506128 (2005), and references therein.
- [2] M. Ave *et al.*, Phys. Rev. Lett. **85**, 2244 (2000); M. Ave *et al.*, Phys. Rev. **D65**, 063007 (2002).
- [3] K. Shinozaki *et al.*, Astrophys. J. **571**, L117 (2002).
- [4] M. Risse *et al.*, astro-ph/0502418 (2005).
- [5] J. Abraham *et al.*, P. Auger Collaboration, Nucl. Instrum. Meth. **A 523**, 50 (2004).
- [6] J. Bellido for the P. Auger Collaboration, these proceedings (aus-bellido-J-abs1-he14-oral)
- [7] X. Bertou for the P. Auger Collaboration, these proceedings (arg-bertou-X-abs1-he14-oral)
- [8] M.A. Mostafá for the P. Auger Collaboration, these proceedings (usa-mostafa-M-abs1-he14-oral)
- [9] A.C. Rovero *et al.*, P. Auger Collaboration, these proceedings (arg-rovero-AC-abs1-he15-poster)
- [10] B. Keilhauer *et al.*, P. Auger Collaboration, these proceedings (ger-keilhauer-B-abs2-he14-poster)
- [11] M. Roberts *et al.*, P. Auger Collaboration, these proceedings (usa-roberts-M-abs1-he15-poster)
- [12] F. Nerling *et al.*, P. Auger Collaboration, these proceedings (ger-nerling-F-abs2-he14-poster)
- [13] P. Homola *et al.*, astro-ph/0311442 (2003).
- [14] L.D. Landau and I.Ya. Pomeranchuk, Dokl. Akad. Nauk SSSR **92**, 535 & 735 (1953); A.B. Migdal, Phys. Rev. **103**, 1811 (1956).
- [15] D. Heck *et al.*, Reports **FZKA 6019 & 6097**, Forschungszentrum Karlsruhe (1998).
- [16] S. Eidelmann *et al.*, Particle Data Group, Phys. Lett. **B592**, 1 (2004).
- [17] N.N. Kalmykov, S.S. Ostapchenko, and A.I. Pavlov, Nucl. Phys. B (Proc. Suppl.) **52B**, 17 (1997).
- [18] X. Bertou, P. Billoir, and S. Dagoret-Campagne, Astropart. Phys. **14**, 121 (2000).
- [19] M. Risse *et al.*, Nucl. Phys. B (Proc. Suppl.), in press; astro-ph/0410739 (2004).

Atmospheric Profiles at the Southern Pierre Auger Observatory and their Relevance to Air Shower Measurement

J. Blümer, R. Engel, D. Gora, P. Homola, B. Keilhauer, H. Klages, J. Pekala, M. Risse, M. Unger, B. Wilczynska, H. Wilczynski for the Pierre Auger Collaboration*

Presenter: B. Keilhauer (bianca.keilhauer@ik.fzk.de), ger-keilhauer-B-abs2-he14-poster

The dependence of atmospheric conditions on altitude and time have to be known at the site of an air shower experiment for accurate reconstruction of extensive air showers and their simulations. The height-profile of atmospheric depth is of particular interest as it enters directly into the reconstruction of longitudinal shower development and of the primary energy and mass of cosmic rays. For the southern part of the Auger Observatory, the atmosphere has been investigated in a number of campaigns with meteorological radio soundings and with continuous measurements of ground-based weather stations. Focusing on atmospheric depth and temperature profiles, temporal variations are described and monthly profiles are developed. Uncertainties of the monthly atmospheres that are currently applied in the Auger reconstruction are discussed.

1. Introduction

The Pierre Auger Observatory measures extensive air showers (EAS) induced by ultra-high energy cosmic rays using a hybrid technique [1]. One detection method is the registration of secondary particles of EAS at ground with water Cherenkov tanks [2]. The second technique is the observation of the longitudinal development of EAS with fluorescence telescopes [3]. Especially for the detection and reconstruction of fluorescence light emission of EAS, knowledge of actual atmospheric conditions at the site of the experiment is necessary.

Therefore, several meteorological systems have been installed at the site of the Pierre Auger Observatory and additionally, data from publicly available databases of atmospheric measurements are used. The data recorded at the site are compared to the US Standard Atmosphere 1976 (US-StdA), which had been commonly used.

The longitudinal development of EAS can be described by the number of particles at a given atmospheric depth. The atmospheric depth at which a shower exhibits its maximum, X_{\max} , is well correlated with the mass of the primary particle. However, using the fluorescence technique for detecting EAS, these quantities cannot be observed directly. The fluorescence telescopes (FD) observe the light within a fixed field of view. Thus, the simulated shower profiles have to be transformed from a description based on vertical atmospheric depth to geometrical height. For a physical interpretation of detected EAS events, the conversion has to be done vice versa. Therefore, the transformation between atmospheric depth and geometrical altitude is a crucial point in the simulation and reconstruction of EAS and the relation between atmospheric depth and height follows from the air density profile [4]. Atmospheric conditions also have a major impact on the fluorescence emission process itself, and on the details of light propagation from the emitting region to the telescope.

2. Atmospheric conditions at the southern Pierre Auger Observatory

Since August 2002, meteorological radio soundings have been performed in several campaigns near Malargüe, Argentina. The radiosondes are launched above the site of the experiment on helium-filled balloons. A set of data is taken about every 20 m during ascent up to 25 km a.s.l. in average. Despite changing wind conditions, the radiosondes stay mostly directly above the array up to 10 km a.s.l., covering the more interesting part of the

* Observatorio Pierre Auger, Av. San Martin Norte 304, 5613 Malargüe, Argentina, <http://www.auger.org/auger-authors.pdf>

profiles for EAS development. More than 100 atmospheric profiles, including data for temperature, pressure, relative humidity, and wind speed and direction, were collected. Day-night variations are very small in this area. Only temperature changes up to 10 K may occur in the lowest 1000 m above ground which is roughly at 1420 m a.s.l. in our case. The important profile of atmospheric depth hardly changes on day-night time scales. From day to day, the extent of variation is strongly seasonal dependent. During austral summer, the conditions are much more stable than during winter. At ground, differences in atmospheric depth up to 5 g cm^{-2} have been found which are related to pressure variations. At higher altitudes, between 6 and 12 km a.s.l., even variations of $10 - 15 \text{ g cm}^{-2}$ are recorded. Over a period of days, the temperature may shift by 15 K. Seasonal effects are, of course, the largest. For individual days, the difference in atmospheric depth between summer and winter can be as large as 20 g cm^{-2} at ground and reach approximately 30 g cm^{-2} at altitudes between 6 and 9 km a.s.l.

Apart from these intermittent profile measurements, ground-based weather stations record temperature, pressure, relative humidity, and wind data every 5 min. At completion of the southern Observatory stations will be located at every FD building and the central laser facility. Up to now, data from 2 stations are available. While the atmospheric profiles are mainly used for simulation and reconstruction of the longitudinal shower development, the continuous ground-based data are applied in the calculation of trigger efficiencies of the water Cherenkov tanks. An example of the pressure distribution within a single day is given in Fig. 1. In Figures 2 and 3, atmospheric depth and temperature data of the year 2004 are shown. Additionally to these local measurements, information from public databases are included in our analysis. The UK Met Office, through the

British Atmospheric Data Centre [5], maintains a database of atmospheric radio soundings worldwide. The stations closest to Malargüe are Cordoba and Santa Rosa, at a distance of 500 - 650 km.

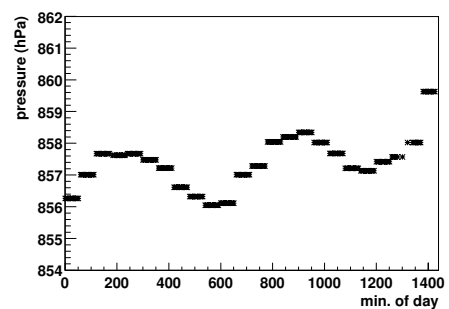


Figure 1. Pressure distribution at the FD building Los Leones at April 3rd, 2004.

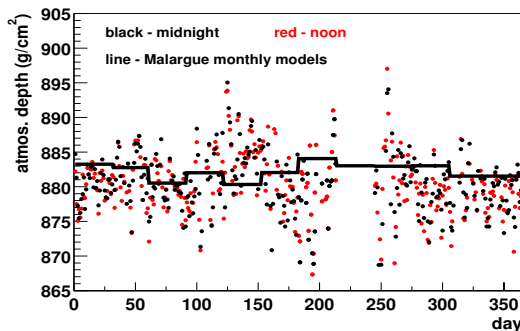


Figure 2. Atmospheric depth data at the FD Los Leones from the year 2004. The plotted data are recorded at noon and midnight local time. The line indicates the values of the Malargüe Monthly Models at the same altitude.

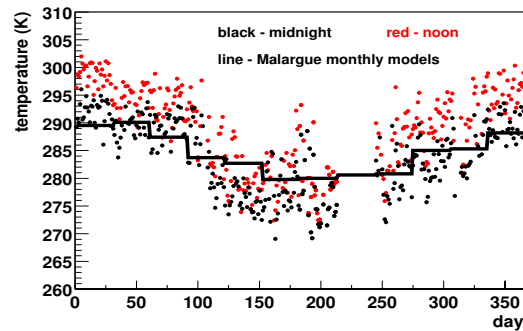


Figure 3. Temperature data at the FD Los Leones from the year 2004. The plotted data are recorded at noon and midnight local time. The line indicates the values of the Malargüe Monthly Models at the same altitude.

The investigation of locally measured atmospheric profiles and the comparison of them to data from the UK Met Office shows that monthly parameterisations can give a good description of the atmospheric variations. To obtain such parameterisations, once-a-day measurements of Cordoba and Santa Rosa are averaged within each month and also between these two stations. The resulting monthly profiles describe the atmosphere near

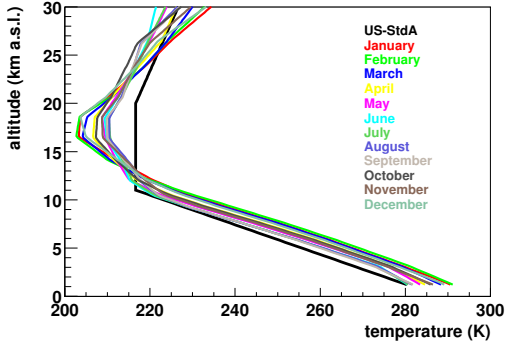


Figure 4. Temperature profiles of the Malargüe Monthly Models.

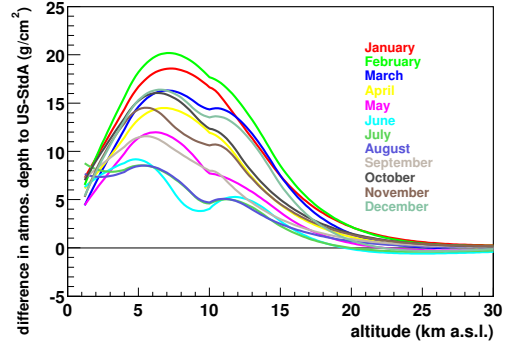


Figure 5. Profiles of atmospheric depth of the Malargüe Monthly Models in difference to the US-StdA.

Malargüe already quite well. Further adjustments are calculated using the information from the local radio soundings. The obtained monthly models are shown in Figures 4 and 5. These profiles, called Malargüe Monthly Models, are employed in the Auger simulation and reconstruction of EAS events [6].

3. Effects on longitudinal profiles

For the physical interpretation of EAS, the position of shower maximum and the energy of the primary particle are important features. Using the fluorescence technique, the shower maximum can be observed directly while the energy of the primary particle has to be deduced from the deposited ionisation energy in the atmosphere.

In Figure 6, the shower development represented by the energy deposit profile can be seen for an average of 100 Fe-ind. showers with 10^{19} eV and 60° incidence. The profiles are plotted versus altitude developing in the US-StdA, Malargüe February, August, and annual average atmospheres. The figure reveals that the position of shower maximum is shifted due to atmospheric conditions. To clearly demonstrate the effect, the inclination angle ϑ is chosen to be 60° , since the extent of the shift is enlarged by a factor $1/\cos\vartheta$. In particular, the Malargüe atmospheres give a systematic shift of the position of X_{\max} towards higher altitudes which is

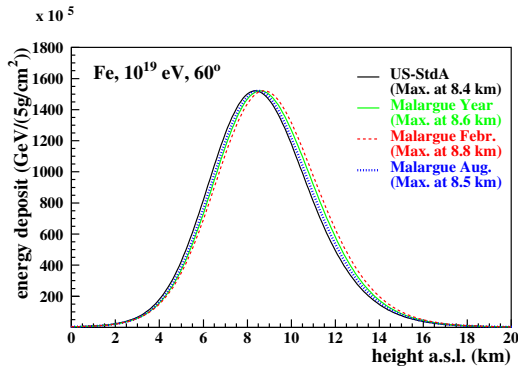


Figure 6. Energy deposit profile for an average of 100 EAS. The black-solid line shows the profile expected in the US-StdA. The coloured curves are for the two extrema of the Malargüe Monthly Models and the annual average.

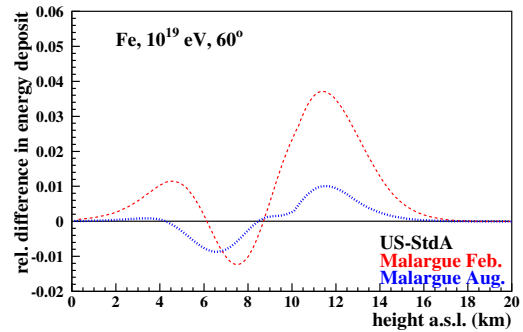


Figure 7. Difference of the profiles shown in Fig. 6 to the US Standard atmosphere divided by the energy deposit at shower maximum. The profiles are shifted in height to bring all shower maxima to the same position (see text).

equivalent to smaller values of atmospheric depth. However, not only the average position of the shower maximum is a measure of the type of the primary particle. Also the width of the distribution of this position for a large number of EAS is systematically different for proton and iron induced showers. The daily variations of the atmosphere lead to a broadening of the X_{\max} distribution by about 25% for iron but only 4% for proton induced showers, again $\vartheta = 60^\circ$, as compared to the expectation for the time-independent US-StdA [4].

For estimating changes in the reconstruction of the primary energy of EAS, the distortion of profiles due to atmospheric variations has to be checked. In Fig. 7, differences of two Malargüe profiles to the US-StdA are plotted. To remove obvious differences, the profiles are shifted in height such that all maxima are at the position of the maximum for the US-StdA. The variation of the total energy is negligible since the integral over each curve is small in comparison to the entire amount of deposited energy of the EAS.

4. Discussion of remaining uncertainties

Firstly, the influence of applying Malargüe Monthly Models instead of US-StdA is analysed with about 2700 hybrid events. The position of shower maximum is shifted on average by $\approx -15 \text{ g cm}^{-2}$, see Fig. 8, right panel. The change of the reconstructed primary energy is only 0.7%, see Fig. 8, left panel.

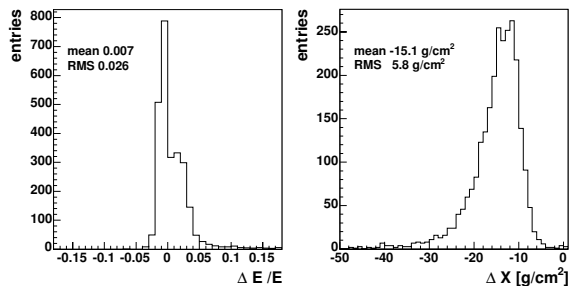


Figure 8. Difference of reconstruction using Malargüe Monthly Models to reconstruction in US-StdA is shown. Left: primary energy. Right: position of shower maximum.

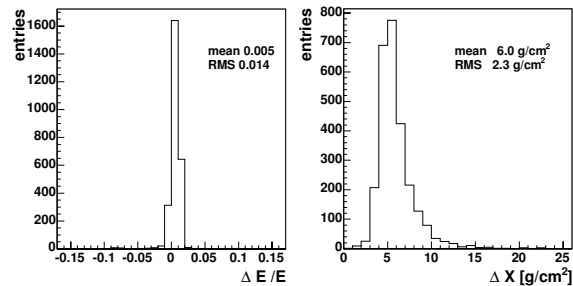


Figure 9. Comparison between normal reconstruction and reconstruction applying a one- σ error to the atmospheric profiles. Left: primary energy. Right: X_{\max} position.

Secondly, the remaining uncertainties due to day-to-day variations of the atmospheric conditions within each month have been studied using the same set of events. For this purpose, modified monthly profiles are used in the analysis that represent the uncertainty bound of one standard deviation of the Malargüe Monthly Models. The position of X_{\max} , Fig. 9, right panel, and the primary energy, Fig. 9, left panel, are compared between the normal reconstruction and the modified reconstruction. The uncertainty of the depth of maximum of EAS is about 6 g cm^{-2} and of the reconstructed primary energy 0.5%. Finally it should be noted that the calculation of fluorescence photon profiles is included in the standard Auger reconstruction chain. The fluorescence photon yield is dependent on temperature and pressure according to the used atmospheric models.

References

- [1] Mostafa, M., for the Pierre Auger Collaboration, usa-mostafa-M-abs1-he14-oral
- [2] Bertou, X., for the Pierre Auger Collaboration, arg-bertou-X-abs1-he14-oral
- [3] Bellido, J., for the Pierre Auger Collaboration, aus-bellido-J-abs1-he14-oral
- [4] Keilhauer B. et al., *Astropart. Phys.* 22 (2004) 249
- [5] British Atmospheric Data Center, <http://badc.nerc.ac.uk/data/radiosglobe/radhelp.html>
- [6] Paul, T. et al., for the Pierre Auger Collaboration, usa-paul-T-abs1-he15-poster

Validation of the Real and Simulated Data of the Pierre Auger Fluorescence Telescopes

A.Ewers^a, H.Geenen^a, K-H Kampert^a, L. Perrone^a, S. Robbins^a, V. Scherini^a, M Unger^b
for the Pierre Auger Collaboration

(a) Universität Wuppertal, Fachbereich Physik, D-42097 Wuppertal, Germany

(b) Forschungszentrum Karlsruhe, Institut für Kernphysik, 76021 Karlsruhe, Germany

Presenter: L. Perrone (perrone@physik.uni-wuppertal.de), ger-kampert-K-abs3-he14-poster

The fluorescence detector (FD) of the Pierre Auger Observatory is currently operating 18 fluorescence telescopes of the 24 that will be employed in the completed detector. These telescopes, grouped in 4 eyes each consisting of 6 telescopes, measure the longitudinal profile of cosmic ray showers with a 14% duty cycle. The reconstruction capability and triggering efficiency have been studied using a complete simulation and reconstruction production chain, employing both simulated CORSIKA showers and parameterised Gaisser-Hillas profiles. The propagation through the atmosphere and the detector response are taken into account and simulated in detail. These simulated data have been generated in a preliminary analysis using the method of importance sampling to efficiently cover the energy region of 0.3 - 300 EeV, various shower geometries and impact points and different primary particles. The distributions of observables have then been investigated in both real and simulated data, facilitating the validation of the reconstruction and simulation software. Comparisons of real and simulated data are discussed and used to assess their impact on the data analysis.

1. The CORSIKA simulation sample

This paper discusses the performance of the Auger fluorescence telescope, which has been studied with a large sample of fully simulated CORSIKA showers [1]. A detailed description of the Fluorescence Detector simulation program is given in [2]; the reconstruction was performed using the Auger Offline software [3]. To obtain a sufficiently large number of events the CORSIKA showers have been taken from the shower database generated in the Lyon computing centre for simulation studies with the Auger detector. The shower sample consists of 3850 proton showers and 4150 iron showers with zenith angles of 0°, 18°, 26°, 37°, 45°, 60° and energies ranging between $10^{17.5}$ and $10^{20.5}$ eV in steps of 0.25 or 0.5 in the logarithmic scale. The CORSIKA showers have been simulated in a slice of 2° in the field of view of Bay4 (Los Leones Eye), with uniformly distributed core distances. This choice has been made in order to optimise the reconstruction and trigger efficiency study as a function of core distance, rather than simulating the true distribution of cosmic ray landing points (uniformly distributed on surface). In order to minimise the inefficiency due to low energy showers landing far away from the eye (with a negligible probability of being triggered), the maximum distance of the generated impact points was chosen to depend on the shower energy and ranges from 5 km up to a maximum of 60 km. The sensitivity of reconstructed energy to the atmospheric properties has been investigated by assuming two extreme atmospheres with aerosol horizontal attenuation lengths at sea level of 12.5 km and 24 km and scale height of 2 km.

2. Trigger efficiency and energy resolution with a given shower geometry

The Pierre Auger Observatory employs two independent detection techniques, allowing the reconstruction of extensive air showers with two complementary measurements. Indeed, the combination of information from the surface array and the fluorescence telescopes enhances the reconstruction capability of these so called "hy-

brid” events with respect to the individual detector components. A description of the hybrid performance of the Pierre Auger Observatory is given in [4].

In this study, the energy resolution of the fluorescence detector has been estimated for the case of known fixed shower geometry. This assumption is justified by the argument that hybrid reconstruction benefits from a more accurate shower geometry with respect to the monocular fluorescence reconstruction. Setting the geometry to the true value then provides a realistic estimate of the energy resolution for the hybrid mode. Assumptions for the atmosphere, detector calibration and fluorescence yield calculation have been made consistently throughout the simulation-reconstruction chain. Fig. 1 shows the trigger efficiency as a function of energy

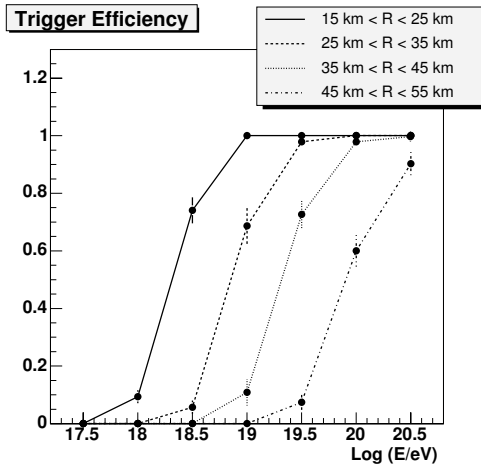


Figure 1. Trigger efficiency as a function of energy for increasing core distances ranges (all zenith angles merged).

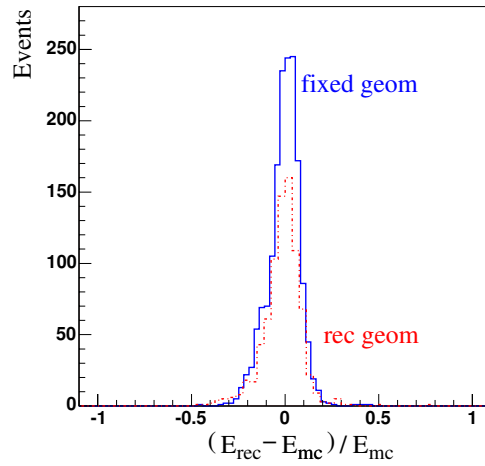


Figure 2. Energy resolution for the simulated data sample with true geometry (blue line, 1607 events, RMS=9%) and reconstructed monocular geometry (red dot-dashed line, 798 events, RMS=11%).

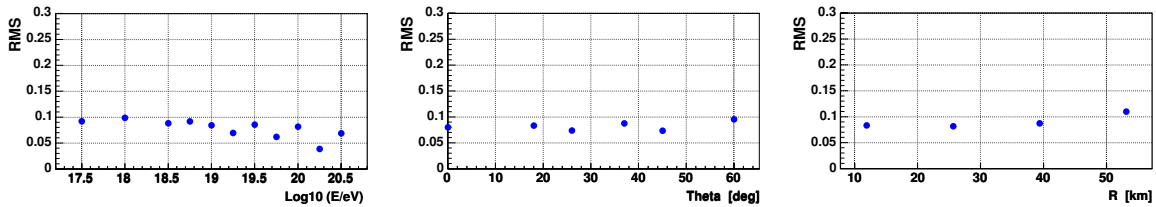


Figure 3. RMS of the residual distribution as a function of true energy (left), zenith angle (middle) and core distance (right) for fixed geometry.

for increasing core distance ranges (all zenith angles merged). The trigger efficiency is 100% up to a distance of 25 km for showers with energy of 10^{19} eV. A detailed calculation of the fluorescence detector aperture for different detector configurations and using analytical shower profiles (Gaisser-Hillas functions) is given in [6]. The method adopted here for the reconstruction of shower longitudinal profiles and energies with the Auger Fluorescence telescope is described in [5]. In order to focus on ”reconstructible” events only, the observed profile and reconstructed shower depth at maximum (X_{max}) are required to satisfy the following conditions:

- a successful Gaisser-Hillas fit with $\chi^2/Ndof < 5$ for the reconstructed longitudinal profile

- minimum observed depth $< X_{max} <$ maximum observed depth
- a reconstructed longitudinal profile wider than 200 g cm^{-2} .

Fig. 2 shows the residual distribution of the reconstructed energy, $(\text{reconstructed energy} - \text{true energy}) / (\text{true energy})$, for events with fixed geometry (blue line) and with reconstructed geometry (red dot-dashed line). The energy resolution improves from 11% to 9% in terms of RMS and the number of selected events increases - by a factor 2 - if the geometry is set to the true value. This demonstrates how much the performance of the Auger Observatory can improve when operating in hybrid mode. The RMS of the residual for the case of fixed geometry is shown in Fig. 3 as a function of true energy (left), zenith angle (middle) and core distance (right). It depends weakly on the energy (improving slightly with increasing energy) and has a stable average value of about 9% over the studied core distance and zenith angle range. The energy resolution shown has been calculated for proton primaries and for a clean atmosphere (aerosol horizontal attenuation length at sea level of 24 km and scale height of 2 km). A test performed with a different atmosphere (aerosol horizontal attenuation length at sea level of 12.5 km and scale height of 2 km) shows that the energy resolution may degrade from 11% to 13% for the proton case.

Finally, the residual of the reconstructed depth at shower maximum $(\text{reconstructed } X_{max} - \text{true } X_{max})$ is shown for fixed geometry in Fig. 4 for proton (black line, $\text{RMS}=25 \text{ g cm}^{-2}$) and iron (red dot-dashed line, $\text{RMS}=22 \text{ g cm}^{-2}$).

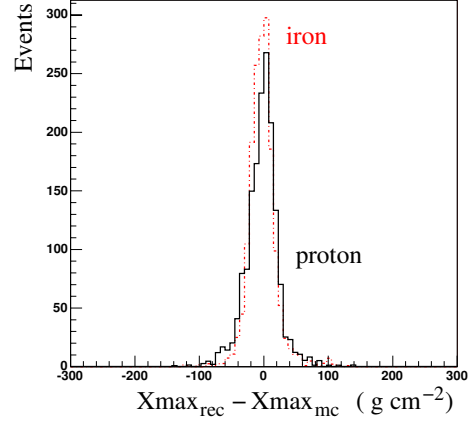


Figure 4. Residual distribution of the reconstructed depth at shower maximum (reconstructed X_{max} - true X_{max}) - fixed geometry -, for proton (black line) and iron (red dot-dashed line).

3. Comparison with experimental data

The trigger simulation has been validated by comparing the predicted number of triggered events to the experimental data. The Monte Carlo sample has the following characteristics:

- 250000 events (50% iron, 50 % proton primaries), analytical shower profiles (Gaisser-Hillas functions)
- energy spectrum generated from $10^{17.5} \text{ eV}$ up to $10^{20.5} \text{ eV}$ according to a power-law spectrum with differential spectral index -2
- zenith angles generated according to $dN/d\cos\theta \propto \cos\theta$ between 0° and 60°
- events simulated in the field of view of Bay 4 of the Los Leones eye with landing points distributed uniformly on the surface.

To make the Monte Carlo sample comparable with the experimental data, the events have been re-weighted according to particular physical assumptions. This study used a power law cosmic ray spectrum with a break at 10^{18} eV ($\gamma = -3.3$ for $E < 10^{18} \text{ eV}$ and $\gamma = -3$ for $E > 10^{18} \text{ eV}$, motivated by [7]) and with isotropically distributed arrival directions. Two months of data (Los Leones, Bay 4, August-September 2004) have been used, with an estimated total livetime of $T_l = 708000 \text{ s} \pm 10\%$. The expected number of events has been compared with the collected data at different levels: geometry reconstructed (level 1), profile reconstructed (level 2) and after applying physical cuts as described in section 2 (level 3). The result is plotted in Fig. 5 (left) as a function of the reconstruction level; the red boxes show the Monte Carlo prediction and the black histogram the

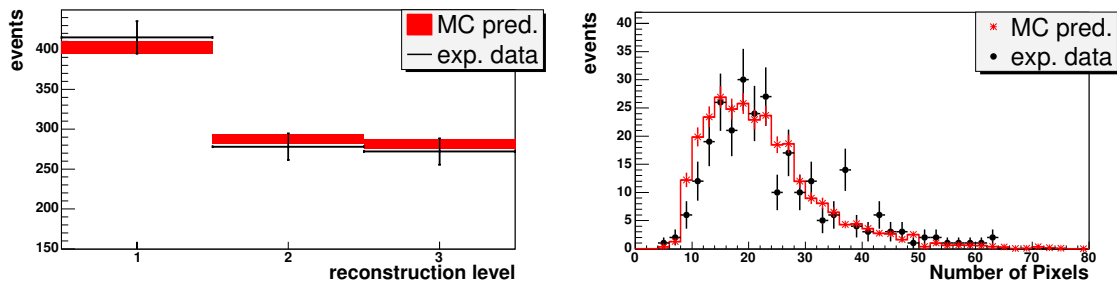


Figure 5. Left: Expected number of events (after weighting) (red boxes) and experimental data (black line) at different reconstruction levels: geometry reconstructed (level 1) profile reconstructed (level 2) and physical cuts as described in section 2 applied (level 3). The Monte Carlo prediction includes the estimated uncertainty on livetime. Only statistical errors are given for data. Right: Predicted and experimental data distribution of pixels used for the longitudinal profile reconstruction.

experimental data. The uncertainty on the Monte Carlo expectation includes statistical and systematic errors, dominated by the estimated uncertainty on the total livetime; only statistical errors are given for data. The experimental data and prediction agree at each reconstruction level within their uncertainties, demonstrating that the trigger simulation is well understood. As an example of the detailed consistency between data and simulation, the distribution of the number of pixels used for the longitudinal profile reconstruction is shown in Fig. 5 (right) at the last reconstruction level.

4. Conclusions

The performance of the Auger fluorescence detector has been studied using a large number of simulated CORSIKA showers. The energy resolution has been estimated for the case of known fixed shower geometry which provides a realistic estimate for the hybrid operation of the Pierre Auger Observatory. In this case, the energy resolution improves and the number of reconstructible events is larger by a factor 2 with respect to the case of the pure monocular reconstruction. The overall energy resolution depends weakly on the shower energy and remains stable with an average value (RMS) of 9% over the studied range of zenith angles ($0^\circ - 60^\circ$) and core distances (5 - 60 km). The overall resolution of the atmospheric depth at shower maximum is at the level of 22 g cm^{-2} for iron and 25 g cm^{-2} for protons.

Finally, a comparison between simulation and data has been carried out at trigger level for a large sample of analytical shower profiles (Gaisser-Hillas functions); agreement has been observed at each reconstruction level.

References

- [1] D. Heck *et al*, Report FZKA 6019, (1998).
- [2] L. Prado Jr. *et al*, Nucl. Instr. Meth. A 545, 632 (2005)
- [3] S. Argirò *et al*, for the Pierre Auger Collaboration, at this Conference, usa-paul-T-abs1-he15-poster.
- [4] M. Mostafà for the Pierre Auger Collaboration, at this Conference. usa-mostafa-M-abs1-he14-oral.
- [5] J. Bellido for the Pierre Auger Collaboration, at this Conference, aus-bellido-J-abs1-he14-oral.
- [6] S. Petrera *et al*, for the Pierre Auger Collaboration, at this Conference, ita-ptera-S-abs1-he15-poster.
- [7] A. Zech for the HiRes Collaboration, Nucl. Phys. B (Proc. Suppl.) 136 (2004)

Impact of a new Cherenkov light parameterisation on the reconstruction of shower profiles from Auger hybrid data

F. Nerling^a, J. Blümer^{a,b}, R. Engel^a, M. Unger^a for the Pierre Auger Collaboration^c

(a) Forschungszentrum Karlsruhe, Institut für Kernphysik, 76021 Karlsruhe, Germany

(b) Universität Karlsruhe, Institut für Experimentelle Kernphysik, 76021 Karlsruhe, Germany

(c) for the Auger authors list see these proceedings

Presenter: F. Nerling (frank.nerling@ik.fzk.de), ger-nerling-F-abs2-he14-poster

The light signal measured by fluorescence telescopes receives - strongly depending on the shower geometry with respect to the detector - a non-negligible contribution from additionally produced Cherenkov light. This Cherenkov contribution has to be accounted for to determine primary parameters properly. In comparison to the previous ansatz used by other experiments, the impact of a new analytical description of Cherenkov light production in EAS on the Auger event reconstruction is investigated.

1. Introduction

The Pierre Auger Observatory [1] applies the fluorescence technique for calorimetric measurement of longitudinal shower profiles of high-energy EAS. For the determination of primary parameters based on fluorescence observations, a knowledge of the Cherenkov light contribution to the measured light signal is mandatory. The amount of Cherenkov light in the fluorescence detector signal depends on the viewing angle with respect to the shower axis because the Cherenkov photons are emitted mainly in the forward direction. Due to the steep angular distribution of charged particles in a shower only at small viewing angles a significant amount of so-called *direct Cherenkov light* is detected. However, direct Cherenkov light can outnumber the fluorescence light by far. At larger viewing angles, the Cherenkov light contribution is dominated by photons emitted along the shower axis that are scattered into the field of view of the detector. This is illustrated in Fig. 1, where a shower simultaneously detected by two Auger fluorescence telescopes under different viewing angles is shown. As can be seen, one detector receives a large amount of Cherenkov light. Clearly, a precise model of Cherenkov light production is needed to infer the energy E and position of shower maximum X_{\max} of such a shower. Parameterisations going back to Hillas [2] are typically used for calculating analytically the Cherenkov light

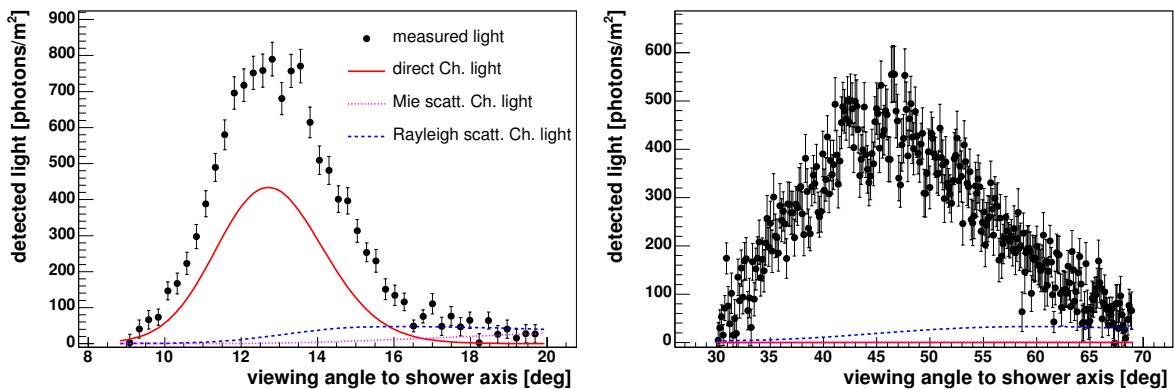


Figure 1. Measured light profiles and reconstructed Cherenkov light of an Auger event observed by two telescopes under different viewing angles (and from different distances).

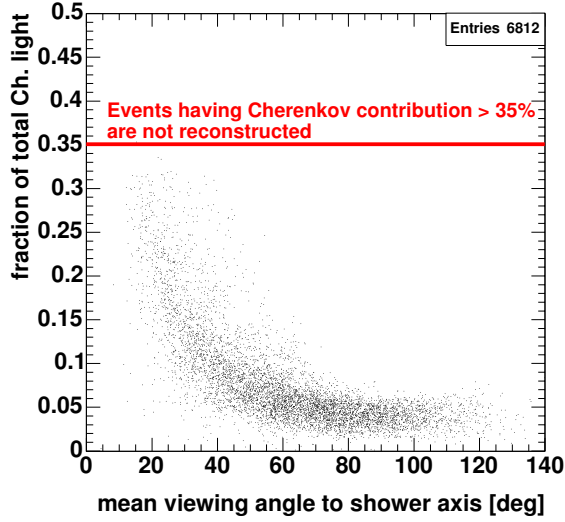


Figure 2. Distribution of reconstructed fraction of Cherenkov light contribution to the total shower signal.

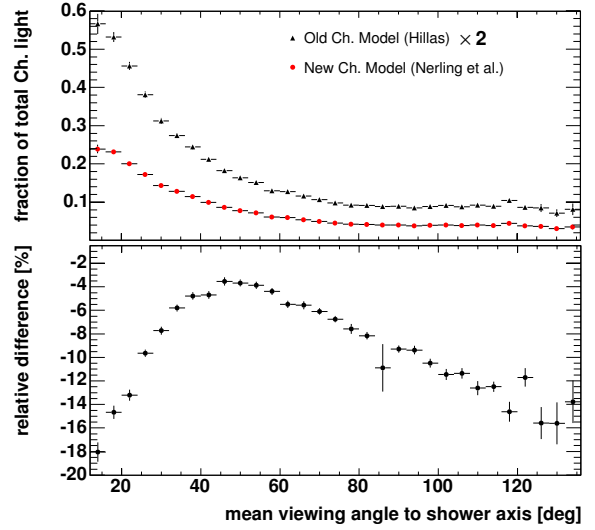


Figure 3. Mean fraction of the reconstructed Cherenkov light contribution. Data points based on the previous Cherenkov model are scaled by a factor of two.

contribution to light signals measured in fluorescence observations, see e.g. [3, 4]. Based on CORSIKA [5], QGSJET01 [6] simulations, a new parameterisation of Cherenkov light production providing both the direct and scattered Cherenkov light contributions, has been introduced recently [7].

2. Reconstructed fraction of Cherenkov light

Hybrid fluorescence data from 01/04 to 04/05 have been analysed, using the Auger Offline [8] reconstruction framework, for studying the differences in reconstructed event properties due to the new Cherenkov calculation instead of the one described in [3]. To ensure a reasonable reconstruction quality, the following selection criteria are applied to the data. The χ^2/ndof of the shower profile fit with a Gaisser-Hillas function is demanded to be less than 3 and the estimated statistical relative uncertainties of reconstructed E and X_{max} are required to be smaller than 30%. The differences in reconstructed event properties ΔP_{rec} as shown in the following are always calculated on an event-by-event basis as $\Delta P_{\text{rec}} = P_{\text{rec}}(\text{new}) - P_{\text{rec}}(\text{old})$, and relative differences are always given relative to the results of the new Cherenkov model. The viewing angle under which a single event is seen by the detector changes with shower development. Therefore, we define an effective viewing angle as the angle between the normal vector of that triggered pixel having the mean trigger time with respect to the total shower observation time and the shower axis. This mean viewing angle is chosen for the studies presented. From Fig. 2 it can be seen that currently only light profiles with less than about 35% Cherenkov light are passing the full reconstruction with given quality cuts. In Fig. 3 the reconstructed fraction of total (superposition of direct and scattered) Cherenkov light, defined as $f_{Ch} = N_{\gamma}^{Ch}/(N_{\gamma}^{Ch} + N_{\gamma}^{Fl})$, is shown as a function of the mean viewing angle. Here N_{γ}^{Ch} is the number of reconstructed Cherenkov photons and $N_{\gamma}^{Ch} + N_{\gamma}^{Fl}$ the measured light signal (Cherenkov and fluorescence photons). The application of the new model results in smaller fractions of the total Cherenkov light over the whole angular range. The differences

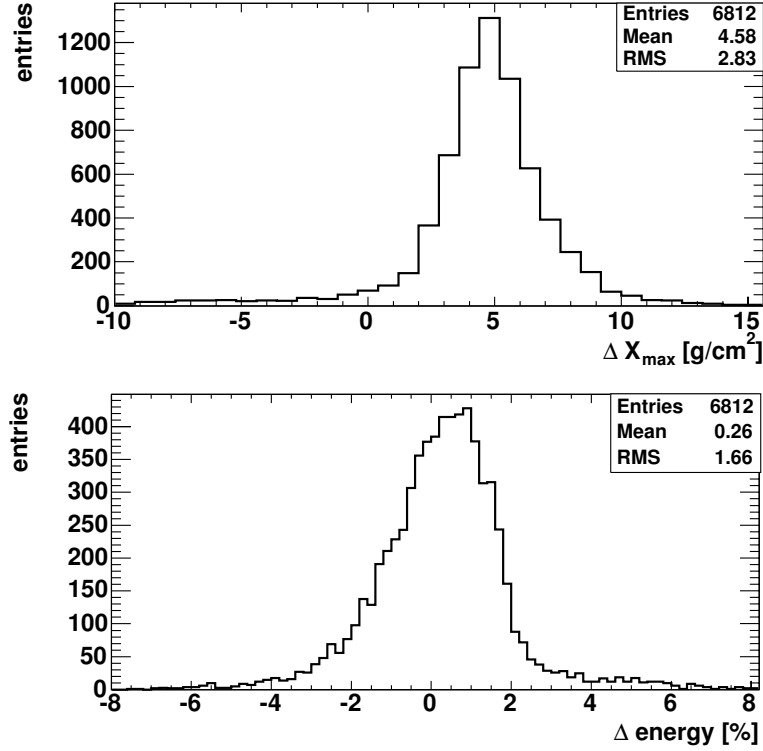


Figure 4. Impact of the new Cherenkov calculation on reconstructed primary energy and position of shower maximum.

range from about -3% up to -15% at large viewing angles. For viewing angles smaller than about 40°, the differences increase strongly, approaching -20%. They are expected to be even larger for viewing angles smaller than 10°. However, the comparison is hampered in this phase space by the limited statistics. It can be concluded that the new model predicts significantly less Cherenkov light depending systematically on viewing angle.

3. Impact on reconstructed primary parameters

The impact of the new Cherenkov calculation on the reconstruction of E and X_{\max} is shown in Fig. 4 and Fig. 5. The differences in depth of maximum, ΔX_{\max} , are given in g/cm² and energy, ΔE , in percent. The mean difference averaged over the complete data set amounts to about +5 g/cm² and +0.3%, respectively. As the differences of the reconstructed fraction of Cherenkov light depend on viewing angle, a similar dependence is observed for the primary parameters. This study is shown in Fig. 5, where ΔE and ΔX_{\max} are given versus the mean viewing angle. The difference in reconstructed energy E can be as large as +6% for smaller angles. The reconstructed depth of maximum increases by about +5 g/cm² for viewing angles larger than about 30°. For viewing angles smaller than about 30° the application of the new Cherenkov calculation results in smaller X_{\max} values, with the difference increasing up to about -10 g/cm² at small viewing angles. For angles smaller than about 10°, the impact of the new model on inferred primary parameters is expected to be even

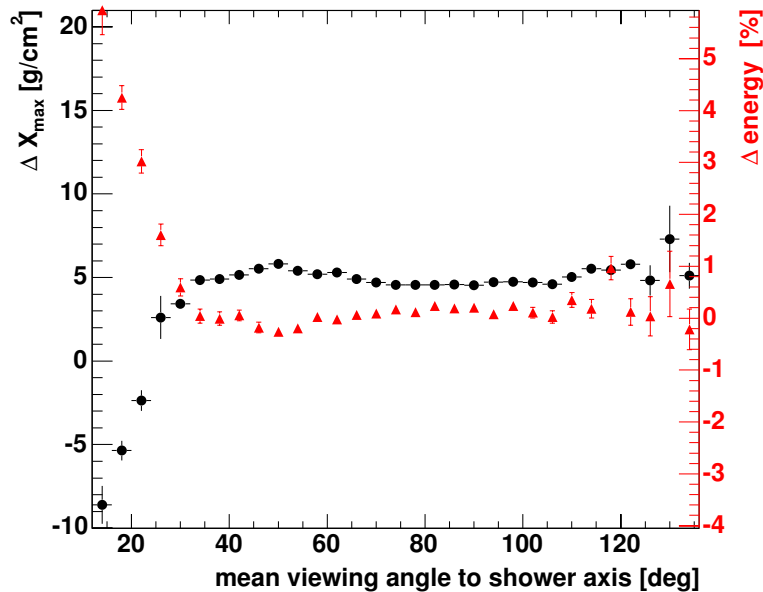


Figure 5. Differences of reconstructed energy and position of shower maximum due to the new Cherenkov calculation as a function of mean viewing angle.

larger. However, currently shower profiles comprising Cherenkov fractions larger than 35 % are rejected in the standard Auger reconstruction.

4. Conclusions

A new Cherenkov light parameterisation [7] has been applied for shower profile reconstruction of the Auger hybrid data. The reconstructed energy and depth of shower maximum have been compared to the traditional treatment [3, 4] on an event-by-event basis. The resulting differences are significant and depend systematically on the viewing angle. Events detected at small viewing angles are more sensitive to the model applied for describing Cherenkov light production.

References

- [1] J. Abraham et al., Pierre Auger Collaboration, Nucl. Instr. Meth. A 523, 50 (2005).
- [2] A. M. Hillas, J. Phys. G 8, 1461 (1982).
- [3] R. M. Baltrusaitis et al., Nucl. Instr. Meth. A240, 410 (1985).
- [4] T. Abu-Zayyad et al., HiRes Collaboration, Astropart. Phys., 16, 1 (2001).
- [5] D. Heck et al., Report FZKA 6019 (Forschungszentrum Karlsruhe) (1998).
- [6] N. N. Kalmykov, S. S. Ostapchenko, A. I. Pavlov, Nucl. Phys. B (Proc. Suppl.), 52, 17 (1997).
- [7] F. Nerling et al., astro-ph/0506729 (2005).
- [8] S. Argiro et al., Pierre Auger Collaboration, these proceedings, usa-paul-T-abs1-he15-poster (2005).

Lateral width of shower image in the Auger fluorescence detector.

H. Barbosa, V. de Souza, C. Dobrigkeit, R. Engel, D. Góra, D. Heck,
P. Homola, H. Klages, G. Medina-Tanco, J.A. Ortiz, J. Pękala,
M. Risse, B. Wilczyńska, and H. Wilczyński for the Pierre Auger Collaboration
Presenter: V. de Souza (vitor@astro.iag.usp.br), bra-desouza-V-abs1-he14-poster

The impact of the lateral distribution of light in extensive air showers on the detection and reconstruction of shower profiles is investigated for the Auger fluorescence telescopes. Based on three-dimensional simulations, the capability of the Auger telescopes to measure the lateral distribution of light is evaluated. The ability to infer the actual lateral distribution is confirmed by the comparison of detailed simulations with real data. The contribution of pixels located far from the axis of the shower image is calculated and the accepted signal is rescaled in order to reconstruct a correct shower profile. The analysis presented here shows that: (a) the Auger telescopes are able to observe the lateral distribution of showers and (b) the energy corrections to account for the signal in outlying pixels can exceed 10%, depending on shower geometry.

1. Introduction

The Pierre Auger Observatory is a hybrid detector based on fluorescence telescopes and water Cerenkov tanks [1]. The basic configuration of the Auger telescopes is a Schmidt camera consisting of a 1.1 m radius aperture (including a ring of corrector lenses), and a spherical mirror with a $30^\circ \times 30^\circ$ of field of view. The fluorescence light is detected by an array of 440 photomultipliers, each with 1.5° diameter field of view. The signal is sampled in time slots of 100 ns.

The amount of fluorescence light produced by a shower particle is proportional to the energy it deposits in air via ionization losses. As can be seen in reference [2], the energy deposited by the particles in an air shower has a wide lateral distribution. According to that work, electrons and positrons at distances between 100 and 1000 meters from the shower axis account for 15 to 20% of the energy released in air by a shower.

Figure 1 shows examples of two events measured by the Auger telescopes. Both events had reconstructed energies of 2.2 EeV. The shower illustrated in the left panel landed with a core 10.5 km from the telescope while the shower illustrated in the right panel landed only 4.5 km away. Note the difference in lateral spread of the signal in these showers.

In this paper, we investigate how the Pierre Auger telescopes detect the lateral distribution of particles in the shower. We compare the simulated lateral spread of light on the camera with that seen in real events. Finally, a correction is proposed for the reconstructed shower energy, to take account of the fraction of light falling into pixels located far from the axis of the image.

2. Detection of the Lateral Distribution by the Auger Telescopes

A three-dimensional shower simulation program CORSIKA [3] was used to evaluate the lateral distribution of particles in the shower and consequently the lateral spread of the signal on the camera. The energy deposited by particles in the atmosphere as given by CORSIKA can be converted to fluorescence photons and propagated to the telescope aperture.

The telescope simulation and the shower reconstruction have been done using the official Auger collaboration programs described in references [4, 5].

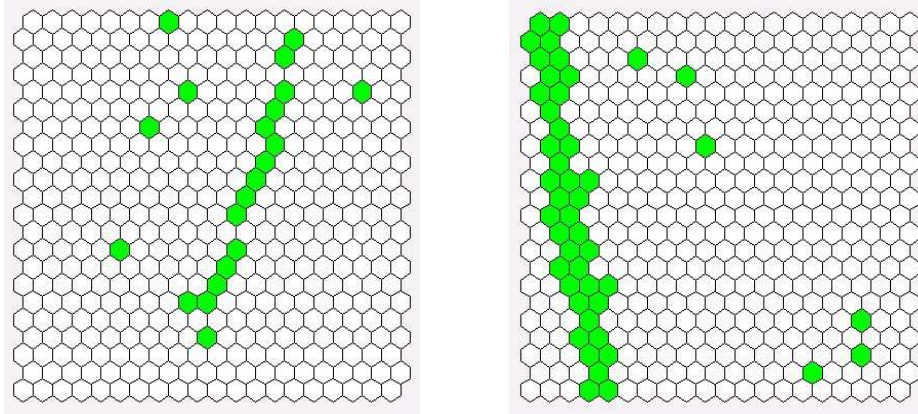


Figure 1. Image of two showers in the photomultiplier camera. The reconstructed energy of both showers is 2.2 EeV. The shower on the left had a core 10.5 km from the telescope, while that on the right landed 4.5 km away. Note the number of pixels and the lateral spread in the image in each shower.

In order to investigate the capability of the Auger telescopes to measure the lateral distribution of showers, we have simulated two sets of 100 vertical showers initiated by 10^{19} eV protons. One set was simulated with the three-dimensional approach and the other with a one-dimensional simulation using a Gaisser-Hillas function for the longitudinal profile.

Two parameters have been investigated in this study: the number of triggered pixels and the ζ angle. The ζ angle is the radius of a circle (measured in degrees) on the photomultiplier camera which maximizes the signal to noise ratio, S/N for collected light. The distribution of triggered pixels on the camera allows us to determine the main track of the shower by fitting a line to the hit pixels. Signal from a pixel is included in the measured light flux if the pixel center lies within an angle ζ from the track axis. The value of ζ is varied to search for a maximum S/N . After the search, ζ is set to a fixed value for the entire track.

Figure 2 shows the expectation for the number of triggered pixels and ζ , obtained for one and three-dimensional simulations as a function of the distance between the telescope and the core position of the shower. Figure 2 shows that for cores closer than 10 km the lateral distribution of the particles in the shower produces a measurable and important spread of the signal on the photomultiplier camera at primary energies of 10^{19} eV. Real data are also shown in the figures, from showers measured to have energy between $10^{18.5}$ and $10^{19.5}$ eV, and these data follow the expectation from the three-dimensional simulation. This shows the capability of the telescopes to measure the lateral distribution of the signal produced by showers.

3. Influence of the Lateral Distribution in the Energy Reconstruction

The primary energy of the shower is calculated based on the amount of fluorescence light recorded by the fluorescence telescope. The standard reconstruction procedure sums the measured charge in each time slot (for pixels within the radius ζ) and converts it to the number of photons at the telescope aperture using calibration constants.

However, this method is most suitable for distant showers where the light collected within the radius ζ corresponds to about 100% of the total signal. Some differences between the signal within ζ and the total signal produced by a shower may exist for nearby showers.

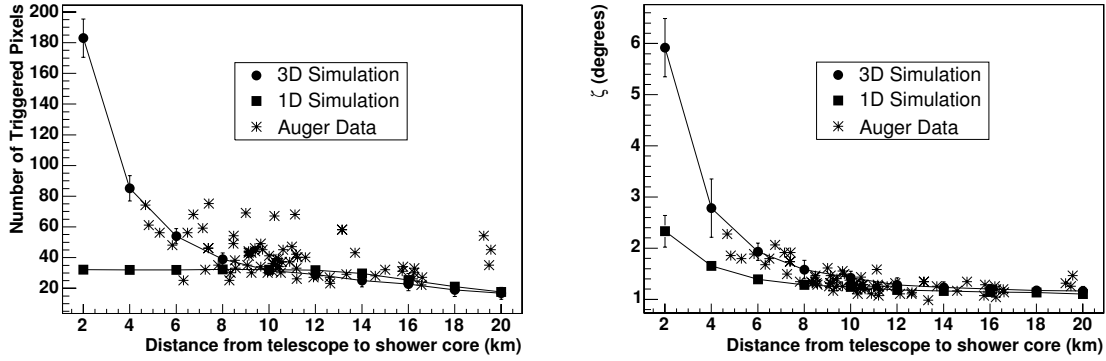


Figure 2. Number of pixels and ζ as a function of the distance between the telescope and the shower core.

As can be seen in reference [6], the fraction of energy deposited $F(r)$ within a distance r , measured in Molière units, can be well parameterized as a function of an effective shower age parameter only.

We have used this parameterization to calculate the total signal produced by the passage of the shower, which may be distributed among several neighboring detector pixels. For a given geometry of the shower, we find the collected signal $L_\zeta(t)$ within the angular distance ζ at each time interval. Then, for the given ζ and the detector-to-shower distance R_0 , the effective radius around the shower axis for which the produced signal will be accounted for in the standard energy reconstruction is given by $r_0 = R_0 \tan(\zeta)$.

The fraction of energy deposited in air within r_0 , and therefore the amount of fluorescence light, can be calculated according to reference [6]. Finally, the signal outside r_0 can be considered in the energy reconstruction by rescaling $L_\zeta(t)$ according to the formula $L_{total}(t) = L_\zeta(t)/F(r_0)$.

Figure 3 shows four events measured by the Auger telescopes to which this procedure has been applied. It is seen that for Event1 $F(r_0)$ changes from 89% for a distance to the shower of $R_0 = 7.0$ km to 87% for $R_0 = 6.0$ km. Accepting only a fraction of the signal contained within ζ directly influences the reconstructed primary energy of the shower. In Table 1 we present the influence of the correction on the Gaisser-Hillas fit to the reconstructed number of particles in the showers. It is seen that this correction changes both the number of particles at the shower maximum and the position of the shower maximum. These changes lead to different estimates of primary energy. In the last column of Table 1 the relative differences $k_E = (E_0^{total} - E_0^\zeta)/E_0^\zeta$ are listed. One sees that k_E is always positive and decreases from 14% for a distance to shower maximum of $R_0=6.5$ km to 2% for $R_0=23$ km.

4. Conclusion

The Pierre Auger fluorescence telescopes are able to detect the lateral distribution of particles in close-by showers and an energy correction must be applied due to this effect. The correction can exceed 10%, as shown in Table 1, depending on the geometry of the shower.

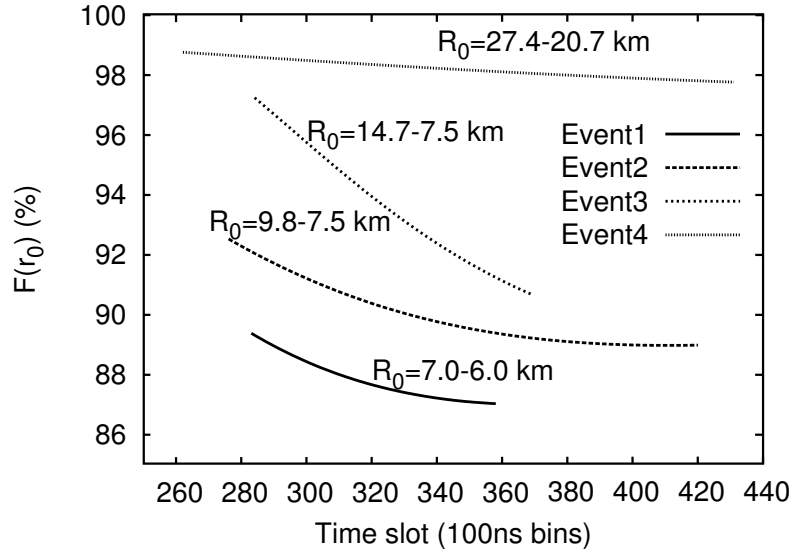


Figure 3. Fraction of light collected within the angle ζ versus time for four events measured by the Auger telescopes.

Table 1. Comparison of Gaisser-Hillas function parameters based on the $L_{total}(t)$ and $L_{\zeta}(t)$ light profiles and their influence on primary energy.

Event	R_0 (km)	N_{max}^{ζ} (10^9)	N_{max}^{total} (10^9)	X_{max}^{ζ} (g/cm^2)	X_{max}^{total} (g/cm^2)	E_0^{ζ} (EeV)	E_0^{total} (EeV)	k_E (%)
Event1	6.4	0.93	1.06	701	706	1.370	1.562	14
Event2	8	6.57	6.88	759	767	9.853	10.40	6
Event3	11	2.12	2.19	637	642	2.950	3.100	5
Event4	23	12.85	13.10	752	753	19.20	19.57	2

5. Acknowledgments

This work was partially supported by the Polish Committee for Scientific Research under grants No. PBZ KBN 054/P03/2001 and 2P03B 11024, in Germany by the DAAD under grant No. PPP 323 and in Brazil by CNPq and FAPESP.

References

- [1] Auger Collaboration, Nucl. Instr. Meth. **A523** (2004) 50
- [2] M. Risse et al., Astroparticle Phys. **20** (2004) 661
- [3] D. Heck et al., Report FZKA 6019, (1998).
- [4] L. Prado et al., Nucl. Instr. Meth. A **545** (2005) 632.
- [5] T. Paul et al. for the Pierre Auger Collaboration, these proceedings.
- [6] D. Góra et al., these proceedings.

Universality of the lateral distribution of energy deposit in extensive air showers

D. Góra^a, R. Engel^b, D. Heck^b, P. Homola^a, H. Klages^b,
J. Pękala^a, M. Risse^b, B. Wilczyńska^a, and H. Wilczyński^a

(a) Institute of Nuclear Physics PAN, Radzikowskiego 152, 31-342 Krakow, Poland

(b) Forschungszentrum Karlsruhe, Institut für Kernphysik, 76021 Karlsruhe, Germany

Presenter: D. Góra (Dariusz.Gora@ifj.edu.pl), pol-gora-D-abs1-he14-oral

Using the CORSIKA air shower simulation package, the spatial distribution of ionization energy deposited by high energy showers in the atmosphere is calculated. The fraction of total energy deposit versus distance from the shower axis is derived. If the lateral distance is measured in Molière units the energy deposit is, to a good approximation, independent of primary energy, primary particle type and zenith angle. It depends only on the shower age and can well be parametrized as a function of an effective shower age parameter only.

1. Introduction

One of the methods of extensive air shower (EAS) detection is recording fluorescence light emitted by nitrogen molecules in the air along the shower path. For very high energies of the primary particle, enough fluorescence light is produced so that the shower can be recorded from a distance of many kilometers by an appropriate optical detector system [1, 2]. As the amount of fluorescence light is proportional to the ionization energy deposit in air, it provides a calorimetric measure of the primary energy.

Given an optical imaging system for recording the light emitted by the shower, the size of shower image is defined as the minimum angular diameter 2α of the image spot containing a certain fraction $F(\alpha)$ of the total light recorded by the detector. The intensity distribution of light in this image, $f_\gamma(\alpha)$, is proportional to the lateral distribution of the emitted fluorescence light around the shower axis [2, 3]. Therefore the fraction of light recorded $F(\alpha)$ can be obtained from the corresponding fraction of light emitted around the shower axis

$$F(\alpha) \equiv \int_0^\alpha f_\gamma(\alpha') 2\pi\alpha' d\alpha' \sim \int_0^r f(r') 2\pi r' dr' \equiv F(r), \quad (1)$$

where $f(r)$ is the (normalized) lateral distribution of fluorescence light emitted. The main task is therefore to derive $f(r)$ and calculate the corresponding fraction of light $F(r)$.

2. Method

In this paper, we study the lateral distribution of energy deposit density in air showers, as it is directly proportional to the number of expected fluorescence photons. The amount of light can be obtained by using the energy deposit $dE(X)/dX$ as a function of atmospheric slant depth interval dX together with a density- and temperature-dependent fluorescence yield $Y(\rho, T)$ [4]. In this approximation the distribution of photons emitted around the shower axis is proportional to the lateral distribution of energy deposit, $f(r) \sim \frac{dE(X, r)}{dX_v}$ at a given stage of shower evolution, where $dX_v = dX \cos(\theta)$ is the vertical depth interval and θ is the shower zenith angle. The distribution of energy deposit $dE(X, r)/dX_v$ is calculated with the CORSIKA shower simulation package [5, 6] as the sum of the energy released by charged particles with energies above the simulation threshold and the releasable energy fraction of particles discarded due to the simulation energy threshold [6].

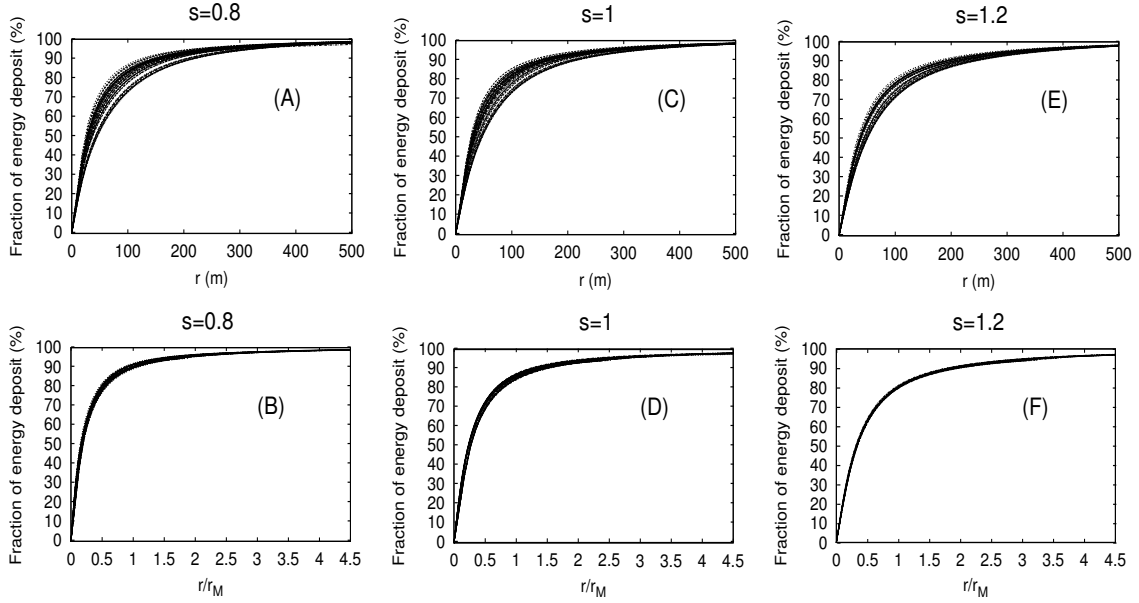


Figure 1. Integral of the energy deposit density for different age parameters and for 10 individual proton and 5 individual iron showers with different zenith angles ($\theta = 0^\circ, 45^\circ, 60^\circ$) and energy 10 EeV; (A), (C), (E) Integral of energy deposit density versus distance from shower axis; (B), (D), (F) Integral of energy deposit density versus distance measured in Molière units.

Using CORSIKA, a two-dimensional energy deposit distribution around the shower axis is stored in histograms during the simulation process for 20 different vertical atmospheric depths. Each of the 20 horizontal layers has a thickness of $\Delta X_v = 1 \text{ g/cm}^2$ and corresponds to a certain atmospheric depth: the first one to $X_1 = 120 \text{ g/cm}^2$ and the last one to $X_{20} = 870 \text{ g/cm}^2$. Linear interpolation between the observation levels is performed in order to get the lateral distribution at a given vertical depth X_n located between two CORSIKA observation levels X_k and X_{k+1} . The fraction of energy deposit $F(r)$ is calculated by numerically integrating the histograms up to the lateral distance r .

3. Discussion

In the following we study the dependence of the lateral distribution of energy deposit density on energy, primary particle and zenith angle. A natural transverse scale length in air showers, which proves to be useful for obtaining a universal parameterization of the lateral distribution, is given by the Molière radius [7]

$$r_M \equiv E_s \frac{X_l}{\epsilon_0}, \quad (2)$$

where $E_s \simeq 21 \text{ MeV}$ is the scale energy, $\epsilon_0 = 81 \text{ MeV}$ the critical energy and $X_l = 37 \text{ g/cm}^2$ the radiation length in air. The local Molière radius in units of length at a given atmospheric depth (at altitude h) can be obtained by dividing Eq. (2) by the air density, $\rho(h)$, and is approximately given by $r_M = 9.6 \text{ gcm}^{-2}/\rho(h)$.

It is also well known that the distribution of particles in a shower at a given depth depends on the history of the changes of r_M along the shower path rather than on the local r_M value at this depth. To take this into

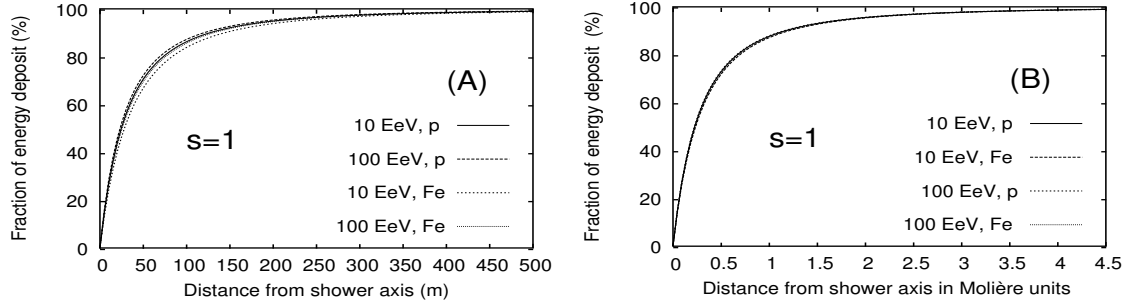


Figure 2. (A) Integral of energy deposit density versus distance from shower axis; (B) The integral profiles versus distance measured in Molière units; The profiles are shown for vertical showers (at $s=1$) with different primary particle type and energy.

account, the r_M value is calculated at 2 radiation lengths above the considered depth [7]. Using the value of the Molière radius calculated based on the atmospheric profile (the US Standard Atmosphere) for vertical depth $X_n - 2X_l \cos(\theta)$, the fraction of energy deposit density $F(r^*)$ versus the distance in Molière units $r^* = r/r_M$ is found. The knowledge of $F(r^*)$ gives a possibility to study the variation of the shape of energy deposit density due to properties of the atmosphere. The variation of the density of the atmosphere along the path of a shower affects the Molière radius and consequently also the radial particle distribution. To characterize the development stage of a shower, we use the shower age parameter $s \equiv 3X/(X + 2X_{max})$, where X_{max} is the atmospheric depth of shower maximum extracted from simulated data¹. A shower reaches its maximum at $s = 1$.

In Figure 1 we present the integral of the energy deposit density for different age parameters for 10 individual proton and 5 individual iron showers with different zenith angles ($\theta = 0^\circ, 45^\circ, 60^\circ$) and energy 10 EeV. The shower-to-shower fluctuations are strongly reduced for a given age when we correct $F(r)$ profiles for the atmospheric effect, i.e. consider $F(r^*)$. Also, there are very little differences in the shape of $F(r^*)$ for showers with different zenith angles and primary particle type. The analysis of Figs. 1 and 2 leads to the following conclusion: *the lateral shape of the energy deposit density versus distance from shower axis measured in Molière units is independent of the primary energy, primary particle type and zenith angle. It depends, to a good approximation, only on the shower age.*

This means that it is possible to find a universal function which describes the shape of the energy deposit density as a function of shower age only. Following our earlier work [8] we will use the function

$$F(r^*) = 1 - (1 + a(s)r^*)^{-b(s)}, \quad (3)$$

where the parameters $a(s)$ and $b(s)$ are assumed to be functions of shower age. Fits of this functional form to the integral of energy deposit density were performed for the data from Figures 1B, D, F. The values of the parameters $a(s)$ and $b(s)$ for different shower ages are presented in Figure 3. The age dependence of $a(s)$ and $b(s)$ is well described by

$$a(s) = 5.151s^4 - 28.925s^3 + 60.056s^2 - 56.718s + 22.331, \quad (4)$$

$$b(s) = -1.039s^2 + 2.251s + 0.676. \quad (5)$$

¹ X_{max} was determined by fitting a Gaisser-Hillas type function to the CORSIKA longitudinal profile of energy deposit.

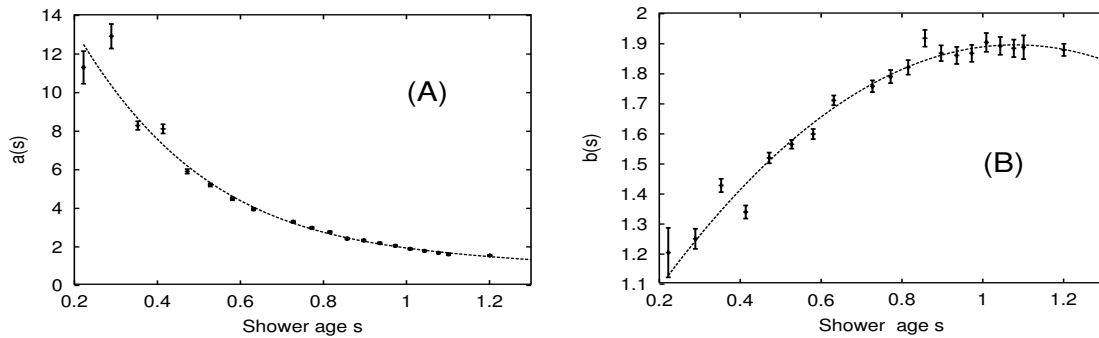


Figure 3. Values of parameters $a(s)$ and $b(s)$ of Eqs. (4) and (5) obtained based on integral of CORSIKA energy deposit density for vertical showers at energy 10 EeV.

Thus, Eqs. (3), (4) and (5) provide a model to describe the fraction of energy deposit within a specified distance from the shower axis for different energies, zenith angles and primary particles. Similarly, a dependence of the lateral distribution of particles on shower age was found in [9].

4. Conclusions

In this work, the distribution of light in the shower optical image is analyzed, based on the lateral distribution of energy deposited by the shower as derived from CORSIKA simulations. The lateral distribution of deposited energy is parameterized with a functional form inspired by the NKG distribution. The angular distribution of photons arriving simultaneously at the detector (i.e. the intensity distribution of light in the instantaneous image of the shower) is obtained. The shape of this distribution can be approximated by a universal function that depends on the shower age only. The results presented here are described in more detail in [10].

5. Acknowledgements

This work was partially supported by the Polish Committee for Scientific Research under grants No. PBZ KBN 054/P03/2001 and 2P03B 11024 and in Germany by the DAAD under grant No. PPP 323.

References

- [1] R.M. Baltrusaitis et al., Nucl. Instr. Meth. **A240** 410 (1985).
- [2] P. Sommers, Astropart. Phys. **3** 349 (1995).
- [3] D. Góra et al., Astropart. Phys. **16** 129 (2001).
- [4] M. Nagano et al., Astropart. Phys. **20** 293 (2003).
- [5] D. Heck et al., Report FZKA 6019, Forschungszentrum Karlsruhe, (1998).
- [6] M. Risse and D. Heck, Astropart. Phys. **20** 661 (2004).
- [7] K. Greisen, Prog. Cosmic Ray Phys. **3** 1 (1956).
- [8] D. Góra et al., Astropart. Phys. **22** 29 (2004).
- [9] M. Giller et al., to appear in Intern. Journ. Mod. Phys. A (2005).
- [10] Góra et al., preprint astro-ph/0505371 (2005).

Atmospheric multiple scattering of fluorescence and Cherenkov light from air shower

J. Pękala^a, D. Góra^a, P. Homola^a, M. Risse^{a,b}, B. Wilczyńska^a, H. Wilczyński^a

(a) *Institute of Nuclear Physics PAN, Radzikowskiego 152, 31-342 Kraków, Poland*

(b) *Forschungszentrum Karlsruhe, Institut für Kernphysik, 76021 Karlsruhe, Germany*

Presenter: H. Wilczyński (Henryk.Wilczynski@ifj.edu.pl), pol-wilczynski-H-abs1-he14-poster

Atmospheric scattering of light emitted by an air shower contributes to the direct fluorescence light from the shower, rather than just attenuating it. So far only direct and singly-scattered Cherenkov photons have been taken into account in analyses of the optical image of an air shower. In this paper a Monte Carlo method of evaluating the contribution of scattered light to the optical image is presented. Preliminary results of these simulations are shown.

1. Introduction

Charged particles of an extensive air shower produce a large number of fluorescence and Cherenkov photons on their way through the atmosphere. Fluorescence light coming directly from the shower to the detector provides information needed for determining shower size at different points along the shower track. Scattering of light in the atmosphere results in attenuation of the fluorescence signal, but also contributes to the signal received by the detector. The scattered light (both fluorescence and Cherenkov photons) must be regarded as a background for the direct fluorescence signal, because its intensity relates to history of shower development rather than to current number of particles in the shower.

In most cases, the optical image of a shower consists mainly of direct fluorescence and singly-scattered Cherenkov photons. Direct Cherenkov light makes a significant contribution to the signal in the fluorescence detector only when the shower lands close to the detector site. Scattered light may be relatively strong in all geometrical configurations, especially in the late stages of shower development. Fluorescence and Cherenkov photons produced by the shower may undergo scattering at different angles. A small part of them gets directly to the detector and is recorded together with the direct fluorescence light. Other photons, after traveling some distance in the atmosphere may scatter again, this time in direction of the detector. It is possible that shower photons may reach the detector after a longer series of scatterings. This light is expected to be distributed over larger area of the sky than the direct light from the shower, and due to its longer path it is also respectively delayed [1].

Until now neither scattered fluorescence photons, nor multiple scattering of Cherenkov light have been taken into account in shower reconstruction procedures. The objective of this paper is to find out how much light contributes to the shower signal due to these effects.

2. Method of simulation

Multiple scattering of fluorescence and Cherenkov photons was simulated using the "Hybrid_fadc" program [2]. In the program, calculations are done in steps corresponding to a change of 0.04° in shower position on the sky, as seen by the detector. In each step the program calculates the shower size (using the Gaisser-Hillas parameterization) and the number of emitted photons. Based on these, fluorescence and Cherenkov light (both

direct and singly-scattered) are calculated. The shower is assumed to have no lateral distribution. Calculations are done in 16 wavelength bins covering the range from 276 to 420 nm.

In calculations concerning multiple scattering of fluorescence and Cherenkov photons produced in a given step it is impossible to trace all photons separately, so that some simplifications are inevitable. The total photon number is divided into smaller "packets" (typically 10 thousand packets in each step and each wavelength bin). All following calculations are done for each packet. A packet starts from the shower axis at the point corresponding to a current shower development step, with either isotropic (fluorescence) or exponential (Cherenkov) angular distribution [3]. Assuming that all photons in a packet scatter at one point, the point of first scattering, either by Rayleigh or Mie processes, is randomly chosen. From the two calculated points, the closer one is chosen as the place where the scattering occurs. Knowing the geometry of the event and also the angular distribution of scattering (Rayleigh or Mie respectively), including attenuation factor for the path toward the eye, the signal at the detector due to a portion of the packet is calculated. With the information about the whole path in the atmosphere, the time of arrival is found. In order to trace the rest of the photons in a packet, it is assumed that they continue their flight together. For this smaller packet, a direction is randomly chosen and all calculations, just as for the first scattering, can be repeated several times. These calculations give as output information about each packet: size of signal, arrival direction on the sky and time of arrival to the detector.

3. Preliminary results

With the program described above simulations were made for different shower configurations, namely for all combinations of:

- energy - 10^{18} , 10^{19} , 10^{20} , 10^{21} eV;
- core distance - 3, 7, 15, 25 km;
- ψ angle within the shower-detector plane - 30, 50, 70, 90, 110, 130, 170 degrees for vertical SDP;
- SDP inclination - 30, 45, 60, 70 degrees with $\psi = 90^\circ$.

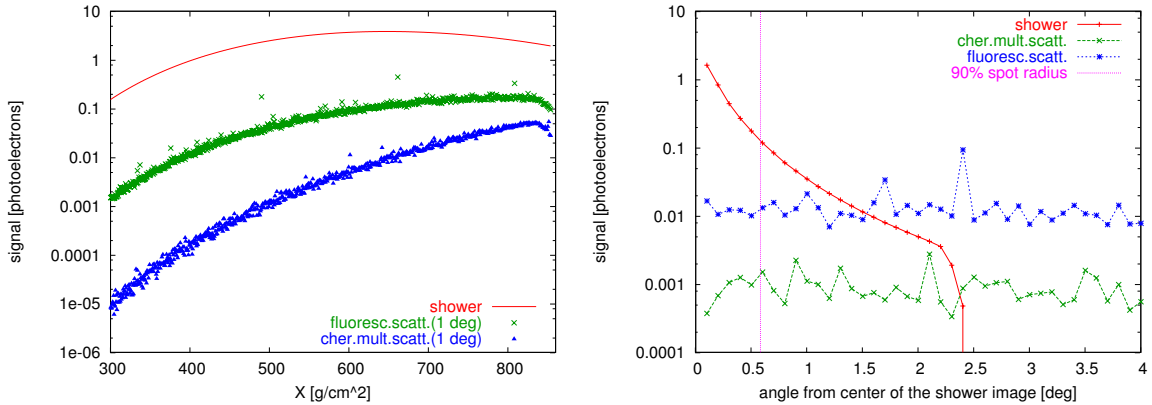


Figure 1. Example of simulation results (vertical 10^{19} eV shower landing 15 km from detector). Shower longitudinal profile and scattered light contribution in 1° -radius circle is shown on the left panel. The "shower" curve includes direct fluorescence, direct and singly scattered Cherenkov photons. On the right panel the distribution of light on the sky (integrated in rings 0.1° wide) in shower maximum is shown. The vertical line marks the radius of the spot containing 90% of the signal.

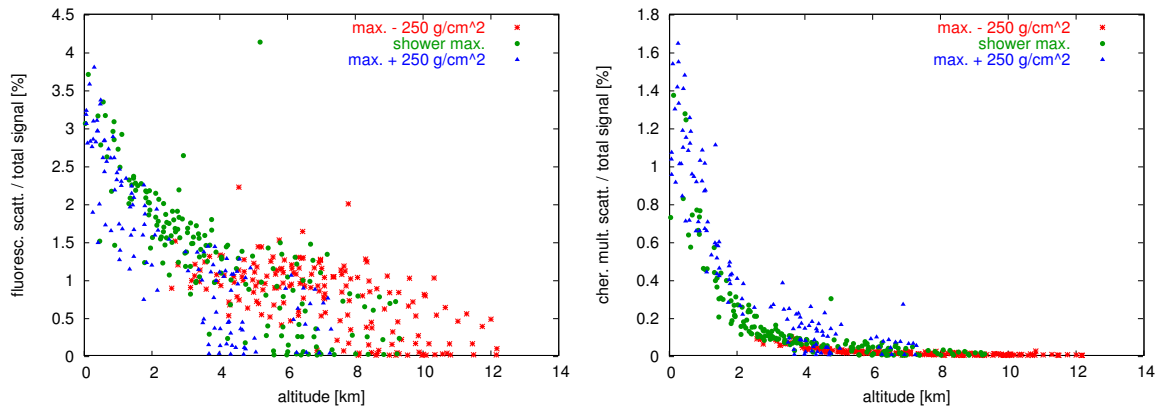


Figure 2. Contribution of scattered fluorescence (left) and multiply scattered Cherenkov (right) to total shower signal plotted versus altitude above ground.

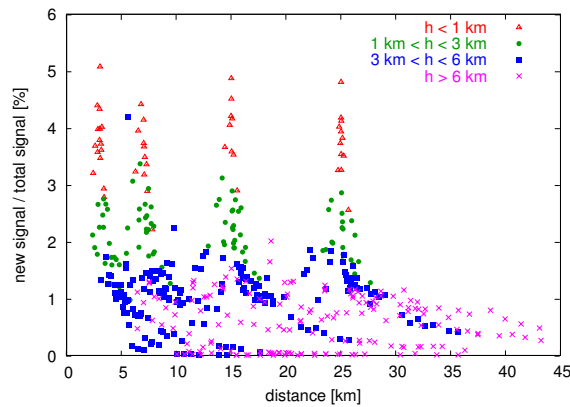


Figure 3. Contribution of scattered light to total shower signal versus the shower-detector distance, in different altitude ranges. The "new signal" includes scattered fluorescence and multiply scattered Cherenkov photons. The points at low altitudes have largest contributions of the scattered light, and are grouped at distances corresponding to chosen core distances of simulated showers.

Example of results from a single simulation run is shown in fig. 1. The signal from multiply scattered light is larger at later stages of shower development, and may finally reach few percent of the total signal from the shower. The contribution of scattered fluorescence light (including single scattering) is at all stages larger than from multiple scattering of Cherenkov light. In order to precisely calculate the contribution from scattered photons, we must know exactly the size of the area on the sky, from which shower light is recorded. When compared to size of shower image, scattered light has very broad distribution, and so the ratio of scattered light contribution to shower signal depends strongly on the light collecting solid angle. To compare contributions of scattered light in various shower geometries, the presented results show contribution of scattered fluorescence and multiply scattered Cherenkov light within a circle containing 90% of light coming directly from the air shower. In analyses of experimental data, the detector characteristics must also be taken into account.

Results from the whole set of simulations performed are presented in figures 2 and 3. Shown are contributions from multiply scattered light for all shower maxima and points 250 g/cm^2 before and after the maximum (if above ground). This contribution appears to be strongly correlated with altitude above ground, rather than with distance from shower to detector. Results from different simulations, representing maxima and points earlier and later in shower development that are at the same altitude, show also comparable contribution of scattered light. This may mean that a simple parameterization, independent of shower age and geometry, is possible. At the lowest altitudes the contribution from multiply scattered light reaches up to 5% of the total signal, therefore it should be taken into account in analysis of experimental data from fluorescence detectors.

In order to investigate the impact of some assumptions made in the simulations, namely atmospheric profile and Cherenkov emission model, on contribution of multiply scattered light, smaller sets of simulations were made. Compared were the US Standard Atmosphere Model [4] (used in all previous simulations) and models of atmosphere in January and July at the southern Pierre Auger Observatory in Malargüe (Argentina). Results of simulations show that changing atmospheric models has little influence on final results. Compared were also results of simulations using different models of angular distribution of Cherenkov emission: simple, one-exponential distribution [3] with more realistic two-exponential one [5]. Also, no significant change of results can be seen.

4. Conclusions

Scattering of fluorescence light and multiple scattering of Cherenkov photons makes a contribution to the signal received by the fluorescence detector, that must be taken into account in analysis of experimental data. The contribution of multiple scattering to the image spot containing 90% of the light received from the shower was presented here. This contribution, which depends on the instantaneous altitude of the shower above the ground, can reach $\sim 5\%$ of the shower signal. Since the multiple-scattering contribution changes with altitude, after this correction the shape of shower profile (and with it depth of shower maximum) may also change. The multiply scattered light has a very broad distribution, and so the exact estimation of its contribution requires information about the solid angle from which light is collected.

Acknowledgements. This work was partially supported in Poland by the State Committee for Scientific Research, grants No. PBZ KBN 054/P03/2001 and 2P03B 11024 and in Germany by the DAAD grant No. PPP 323.

References

- [1] J. Pękala et al., Proc. 28th ICRC Tsukuba, 2 551 (2003).
- [2] B. Dawson, private communication (1998).
- [3] R. M. Baltrusaitis et al., Nucl. Instr. Meth. A240 410 (1985).
- [4] US Standard Atmosphere Model, http://nssdc.gsfc.nasa.gov/space/model/atmos/us_standard.html
- [5] F. Nerling, private communication (2004).

Parameterisation of Cherenkov light production in high-energy showers

F. Nerling^a, J. Blümer^{a,b}, R. Engel^a, M. Risse^a

(a) Forschungszentrum Karlsruhe, Institut für Kernphysik, 76021 Karlsruhe, Germany

(b) Universität Karlsruhe, Institut für Experimentelle Kernphysik, 76021 Karlsruhe, Germany

Presenter: F. Nerling (frank.nerling@ik.fzk.de), ger-nerling-F-abs1-he14-oral

A new analytical description of Cherenkov light production in high energy showers is presented. It describes both the total amount and the angular distribution of the emitted Cherenkov photons as a function of the shower age. A universal parameterisation of electron energy distribution is used for calculating the total number of Cherenkov photons. Based on universality features of the angular distribution of electrons, a parameterisation of produced Cherenkov photons for a given angle to the shower axis is introduced. Thus, a complete analytical description is derived which allows the calculation of direct and scattered Cherenkov contributions to light profiles measured by experiments using the fluorescence technique. The results are compared to CORSIKA simulations and to other parameterisations.

1. Introduction

For correct shower profile reconstruction from light signals measured using the air fluorescence technique, a precise knowledge of the Cherenkov light contribution to the fluorescence detector signal is mandatory. In contrast to the isotropically radiated fluorescence light, the Cherenkov photons are emitted mostly in the forward direction. Therefore, the amount of Cherenkov light in the measured signal depends on the shower geometry with respect to the detector. It leads to systematic uncertainties in the determination of primary properties like energy and position of shower maximum unless accounted for properly. The analytical calculation of the amount of Cherenkov light received by fluorescence detectors needs the total number of Cherenkov photons produced and their angular distribution with respect to the shower axis. The so-called *scattered Cherenkov light* contribution, i.e. those photons which originally would not have reached the detector but are scattered into the field of view, depends mainly on the former and is nearly independent of the shower geometry. The amount of Cherenkov photons directly hitting the detector, the so-called *direct Cherenkov light*, depends on both the total amount of produced Cherenkov photons and their angular distribution with respect to the shower axis.

The total number of Cherenkov photons dN_γ produced per interval of slant depth dX and angle $d\theta$ with respect to the shower axis can be calculated in good approximation by [1, 2]

$$\frac{dN_\gamma}{dX d\theta}(X, \theta, h) = A_\gamma(X, \theta, h) \cdot N(X) \int_{\ln E_{\text{thr}}} y_\gamma(h, E) f_e(X, E) d \ln E. \quad (1)$$

Here, $N(X)$ is the charged particle number as function of depth X , E_{thr} the local Cherenkov energy threshold, which depends on the refractive index $n = n(h)$ of air, and $f_e(X, E)$ is the differential electron energy spectrum at depth X normalised to unity above the energy threshold E_{cut} adopted in the simulation (1 MeV in the examples shown here), cf. [1, 2]. $A_\gamma(\theta, X, h)$ is the angular distribution of Cherenkov photons per angular bin with respect to the shower axis, normalised to one photon and averaged over azimuth

$$A_\gamma(\theta, X, h) \cdot \frac{dN_\gamma}{dX} = \frac{dN_\gamma}{d\theta dX}(\theta, X, h), \text{ with } \int_0^\pi A_\gamma d\theta = 1. \quad (2)$$

For a given shower geometry, $h = h(X)$ follows from the atmospheric model (US-StdA used in the following).

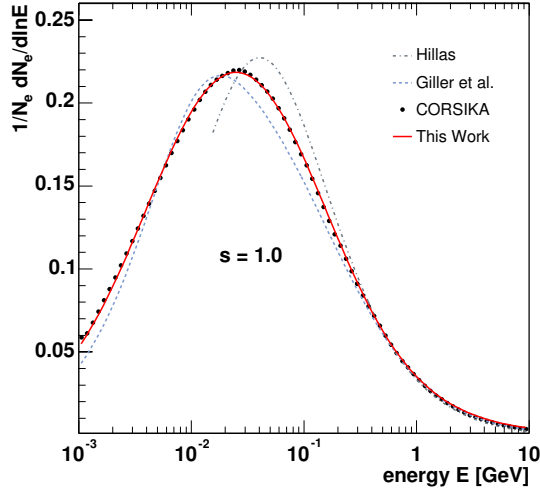


Figure 1. Mean electron energy spectrum CORSIKA, different parameterisations (see text) for $s = 1.0$.

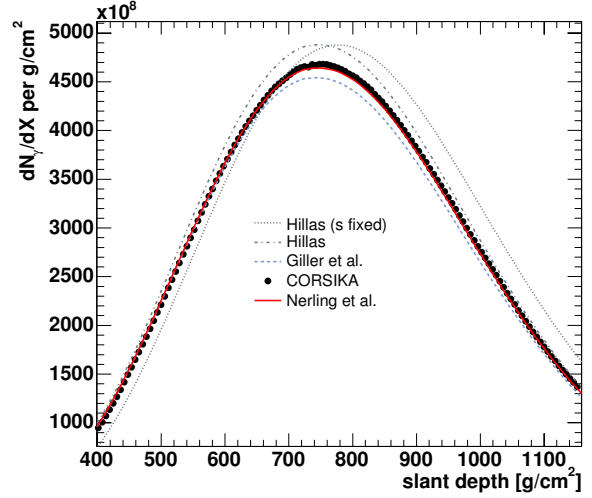


Figure 2. Longitudinal Cherenkov photon profile obtained by CORSIKA, different parameterisations (see text).

2. Total number of Cherenkov photons produced

Applying a parameterisation of the electron energy spectrum, the total number of Cherenkov photons produced per slant depth dX can be calculated analytically based on ansatz (1) when the shower size profile is provided by EAS simulations or by fluorescence observations. A parameterisation of the electron energy spectrum depending only on the shower age $s = 3X/(X + 2X_{\max})$ was first provided by Hillas [3]. Two new approaches have recently proposed [4, 1] based on CORSIKA [5] simulations applying QGSJET01 [6] as interaction model. For high-energy showers $> 10^{17}$ eV, the electron spectrum has shown to be universal, i.e. it does not depend significantly on the primary energy or particle type [4, 1, 2] and is also largely independent of the shower zenith angle [2]. In Fig. 1 different parameterisations of the electron energy spectrum are compared to the Monte Carlo result for $s = 1$. The comparison of the full Monte Carlo Cherenkov profile calculation with the model calculation applying the different parameterisations for ansatz (1) is shown in Fig. 2. The parameterisation given by Nerling et al. also accounts for different E_{cut} , which is important to be consistent with $N(X, E > E_{\text{cut}})$. The calculation labelled “Hillas (s fixed)” employs the parameterisation given in [3] for $s = 1$ only, as often used (see e.g. [7, 8]).

3. Angular distribution of electrons and Cherenkov photons

Electrons in a shower undergo multiple Coulomb scattering, which broadens their angular distribution with respect to the shower axis: The higher the mean electron energy, the smaller is the mean electron angle to the shower axis. In Fig. 3 the energy dependent angular distribution of electrons is shown exemplarily for an individual proton shower of 10^{19} eV for three different shower ages. It can be seen that the distribution is strongly depending on the particle energy, and is to a large extent independent of the shower age within the statistical fluctuations. As the electron energy spectra are universal in high-energy showers and the electron scattering angle is mostly determined by the particle energy, the electron angular distribution is also approximately independent of shower energy and primary particle type [2]. This is illustrated in Fig. 4 where the electron angular distributions of many individual proton and iron showers of different energies ($10^{18}, 10^{19}$ eV) are shown at

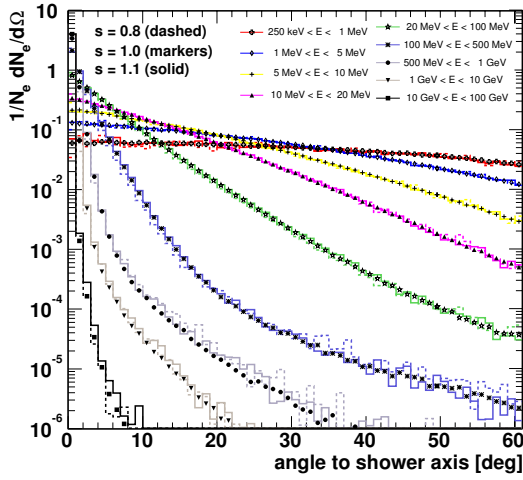


Figure 3. Normalised electron angular distribution with respect to the shower axis, shown for an individual proton shower of 10^{19} eV for three different shower ages and various different ranges of electron energies.

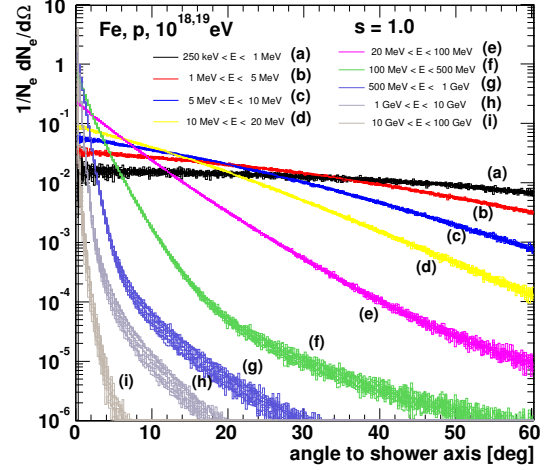


Figure 4. Universality of electron angular distributions, shown for numerous individual proton and iron showers of 10^{18} and 10^{19} eV and various different ranges of electron energies.

shower maximum, cf. also [9]. The distributions of individual showers do not differ much, larger (statistical) fluctuations occur merely at large angles. The distribution of electrons in the GeV-region show a larger spread, which is in agreement with the energy spectra of GeV-electrons showing larger fluctuations as well [2].

The Cherenkov photons are emitted under the Cherenkov emission angle, which slightly changes with altitude and amounts about 1° in air. This angle is negligible compared to the broad distribution of electrons. Consequently, the Cherenkov photon angular distribution is determined mainly by the electron energy spectrum and two dependencies occur. The photon angular distribution depends on height h due to the dependence of $E_{\text{thr}}(h)$, and on the shower age s because of the dependence of $f_e(E, s)$. It is common to describe the height dependence by an exponential function, where the scaling angle θ_0 is a function of E_{thr} , see e.g. [7]. Traditionally this approximation is applied for calculating the Cherenkov contamination of fluorescence light signals from high-energy showers, see e.g. [7, 8]. Generalising this ansatz in order to take into account both the dependence on h as well as on s we write $A_\gamma(\theta, h, s) = A_\gamma(s) \cdot A_\gamma(\theta, h)$, where $A_\gamma(s)$ is a polynomial of second order in shower age and the exponential term depends on altitude only. To enlarge the range of validity up to 60° and improve the data description around 30° this factorised ansatz is extended to [2]

$$A_\gamma(\theta, h, s) = a_s(s) \frac{1}{\theta_c(h)} e^{-\theta/\theta_c(h)} + b_s(s) \frac{1}{\theta_{cc}(h)} e^{-\theta/\theta_{cc}(h)}. \quad (3)$$

In this expression, the age dependence is included by the polynomials $a_s(s)$ and $b_s(s)$, and the height dependence is taken into account by $\theta_c(h) = \alpha \cdot E_{\text{thr}}^{-\beta}$ and $\theta_{cc}(h) = \gamma \cdot \theta_c(h)$ with $\gamma = \alpha' + \beta' \cdot s$, where E_{thr} is given in MeV. As shown in Fig. 5 and Fig. 6 respectively, the CORSIKA results are described properly using the parameters given in [2].

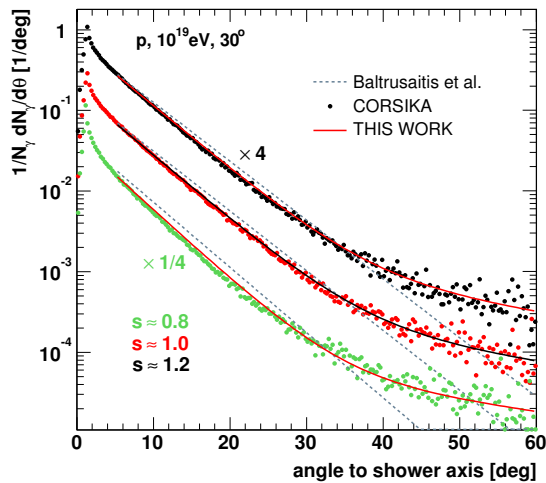


Figure 5. Angular distribution of Cherenkov photons with respect to the shower axis. Shown are the simulated distributions for an individual proton shower for different shower ages, [7] and the new parameterisation Eq. (3) [2].

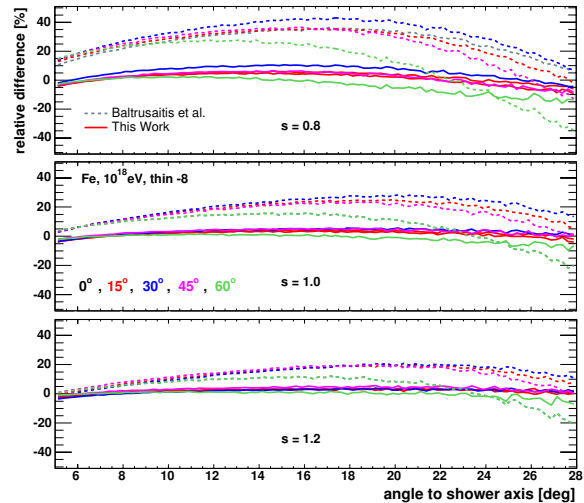


Figure 6. Quality of description: Relative differences of different approaches ([7] and Eq. (3) [2]) to CORSIKA results, shown for 5 individual iron showers and different zenith angles.

4. Conclusions

Based on universality features of high-energy showers, an analytical description of the Cherenkov light production in EAS has been introduced providing both, the total number of produced Cherenkov photons as well as their angular distribution with respect to the shower axis. It offers the calculation of the direct and scattered Cherenkov contributions to measured fluorescence light profiles, see [10]. The achieved accuracy in reproducing the CORSIKA predictions in terms of the number of Cherenkov photons produced per slant depth and angle with respect to the shower axis is (within shower-to-shower fluctuations) better than a few percent ($< 10\%$ for $s=0.8$, $< 5\%$ for $s=1.0$, $< 3\%$ for $s=1.2$). The differences compared to the traditionally used approach result in significant and systematic differences in reconstructed energy and position of shower maximum, if the new model is applied for shower profile reconstruction as has been shown for Auger hybrid data [10].

References

- [1] F. Nerling et al., Proc. 28th Int. Cos. Ray Conf., Tsukuba (Japan), 2 (2003) 611.
- [2] F. Nerling et al., astro-ph/0506729 (2005).
- [3] A. M. Hillas, J. Phys. G: Nucl. Part. Phys. 8 (1982) 1461.
- [4] M. Giller et al., J. Phys. G: Nucl. Part. Phys. 30 (2004) 97; Proc. 28th Int. Cos. Ray Conf., Tsukuba (Japan), 2 (2003) 619. Note: Parameters used here are different from that published, a new set of parameters [Giller et al. 2005, private communication] is used.
- [5] D. Heck et al., Report FZKA 6019, Forschungszentrum Karlsruhe (1998).
- [6] N. N. Kalmykov, S. S. Ostapchenko, A. I. Pavlov, Nucl. Phys. B (Proc. Suppl.), 52B (1997) 17.
- [7] R. M. Baltrusaitis et al., Nucl. Instr. Meth. A 240 (1985) 410.
- [8] T. Abu-Zayyad et al., HiRes Collaboration, Astropart. Phys., 16 (2001) 1.
- [9] M. Giller et al., Int. J. Mod. Phys. A: Proc. 19th European Cos. Ray Symp., Florence (Italy) (2004).
- [10] F. Nerling et al., Pierre Auger Collaboration, these proceedings, ger-nerling-F-abs2-he14-poster (2005).

Variability of atmospheric depth profiles

B. Wilczyńska^a, D. Góra^a, P. Homola^a, B. Keilhauer^b, H. Klages^c, J. Pękala^a, M. Risse^{a,c},
H. Wilczyński^a

(a) *Institute of Nuclear Physics PAN, ul. Radzikowskiego 152, 31-342 Kraków, Poland*

(b) *Universität Karlsruhe, Institut für Experimentelle Kernphysik, 76021 Karlsruhe, Germany*

(c) *Forschungszentrum Karlsruhe, Institut für Kernphysik, 76021 Karlsruhe, Germany*

Presenter: B. Wilczyńska (Barbara.Wilczynska@ifj.edu.pl), pol-wilczynska-B-abs1-he14-poster

Variation of profiles of atmospheric depth is studied based on the UK Met Office radiosonde data. The seasonal variation at different sites (Salt Lake City, USA; Mendoza, Argentina) is compared to daily variation within a given month in a season. Year-to-year variations of monthly average profiles are also presented. It is demonstrated that daily, local monitoring of the atmosphere is needed for precise shower reconstruction.

1. Introduction

Development of extensive air showers depends on the properties of the atmosphere itself, in particular on distribution of mass in the atmosphere. Since the atmosphere serves both as a target in which primary cosmic rays interact and the medium in which showers develop, as precise as possible knowledge of properties of the atmosphere is extremely important for studies of high energy cosmic rays. Therefore, the local distribution of air density along the shower path is of primary importance. In the fluorescence detection technique the longitudinal profile of shower development is reconstructed as a function of altitude above ground. To extract such important quantities like depth of shower maximum, X_{max} , an accurate conversion of the altitude into atmospheric depth is necessary.

The US Standard Atmosphere Model [1] is widely used in air shower simulation codes and in analyses of shower measurements. This model provides the temperature and pressure profiles at the northern hemisphere, for mid-latitude average atmosphere. The 1976 extension of the Model provides also the northern mid-latitude winter and summer atmospheric distributions. An important question is, however, how well does the US Standard Atmosphere Model approximate local conditions at the sites of air shower detectors, and what is the time variability of the local atmosphere? In other words, is the annual or seasonal average adequate for a particular day at a particular location? It is now well known [2, 3] that a good knowledge of atmospheric depth profiles is essential for precise shower reconstruction.

In this analysis we use the UK Met Office data [4] which contain temperature and pressure profiles measured by radiosondes at the stations located worldwide. A radiosonde, carried by a small balloon, typically reaches altitudes up to 20-30 km. At higher altitudes, the COSPAR International Reference Atmosphere (CIRA86) [5] is used, which provides temperature and pressure profiles at many latitudes at both hemispheres. In the following we present an analysis of data collected at the station in Salt Lake City (USA) and at the station in Mendoza (Argentina) located near the southern Pierre Auger Observatory site. The atmospheric depth at an altitude h is the integral of density of overlying air: $X(h) = \int_h^\infty \rho(h)dh$, where $\rho(p, T) = pM_{mol}/(RT)$ is the air density, p is the measured pressure, T - measured temperature, M_{mol} is the molar mass of air and R the universal gas constant.

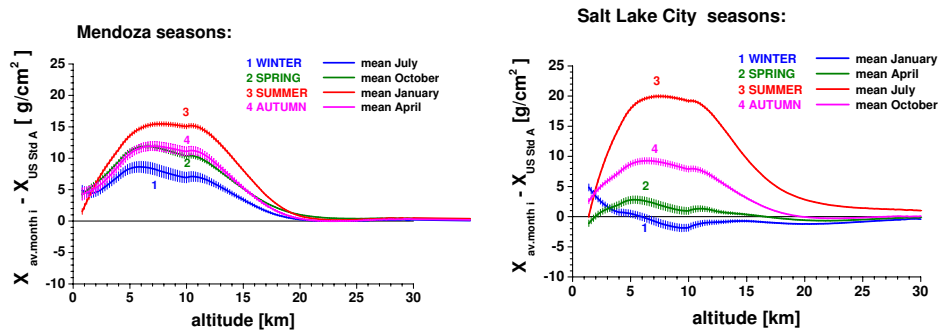


Figure 1. Average seasonal atmospheric depth profiles, relative to US Standard Atmosphere, at Mendoza (Argentina) and Salt Lake City (USA).

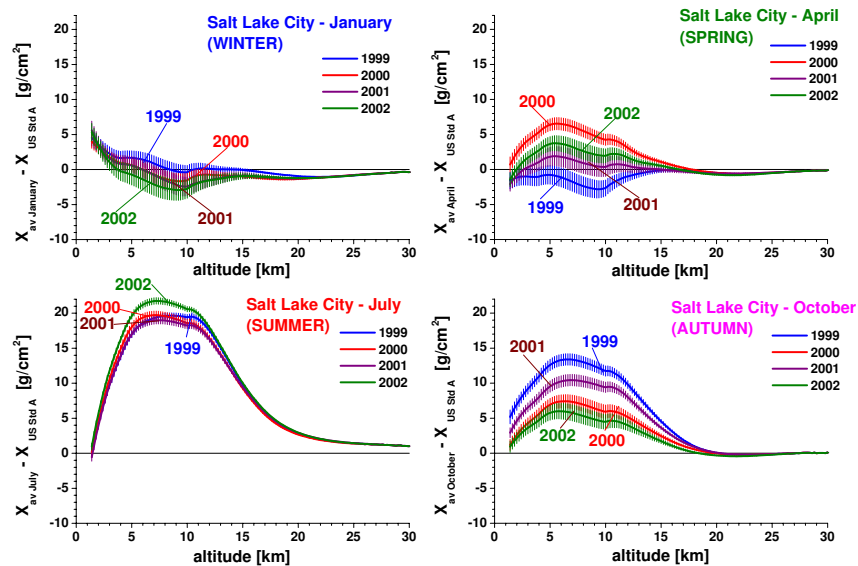


Figure 2. Year-to-year variability of monthly average profiles at Salt Lake City.

2. Seasonal variation of atmospheric profiles

Seasonal variations of the atmospheric depth profiles $X(h)$ for both sites analyzed (Mendoza and Salt Lake City) are shown in Fig.1. Differences of the average monthly profiles in four seasons, relative to the US Standard Atmosphere, are shown. One can see that seasonal profiles strongly depend on the site. In Salt Lake City the differences among seasons are much larger than in Mendoza. The seasonal profiles shown in Fig.1 are the four-year averages of the months shown. The average monthly profiles vary from year to year, as shown in Fig.2. The year-to-year variability of the average monthly profiles can reach 10 g/cm^2 , as shown for April and October.

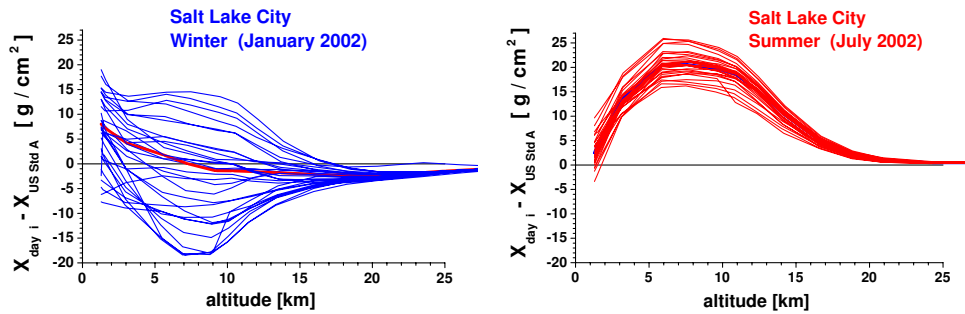


Figure 3. Daily variation of atmospheric depth profiles in winter and summer at Salt Lake City.

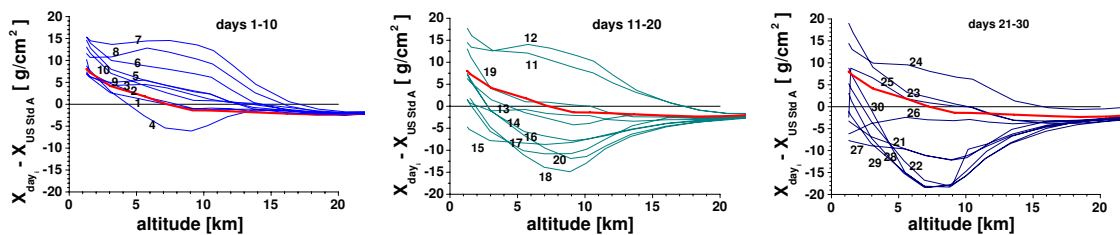


Figure 4. Profiles of individual days in January 2002 at Salt Lake City.

3. Day-to day variation within a month

Apart from the seasonal variation of the atmosphere, a strong variation is observed on the time scale of a day. In Fig.3 the differences of atmospheric depth profiles for individual days relative to the US Standard Atmosphere Model are presented for winter (January 2002) and summer (July 2002) at Salt Lake City. The range of profile variability is larger in winter than in summer. To examine closer this variability, the profiles of individual days of January 2002 are shown in Fig.4 with ten consecutive days shown in each panel. The numbers denote the date of each day. The four-year average of January is shown by the red heavy line.

One can note that the profiles of consecutive days differ typically by 3–5 g/cm², with profiles of neighboring days grouped together. Occasionally, a large change is observed from a day to a next one (e.g. days 12-13, days 18-19-20, days 22-23, etc.). Most of the daily profiles in the first decade of January lay above the monthly average, while in the rest of the month the profiles lay predominantly below the average. The character of the daily variability in other seasons and sites is very similar to that shown in Fig.3, but the range of variability is sometimes smaller. As an example, the daily profiles at Mendoza in winter and summer are shown in Fig.5.

The data presented in Figures 1–5 clearly demonstrate that taking into account the seasonal variation is not sufficient for precise shower reconstruction. The day-to-day variation within a month is equally important and should be accounted for.

4. Day-night variation

Observations of extensive air showers using the fluorescence technique are done only during nights. However, some of the balloon launching stations usually make balloon soundings during days only. A question therefore

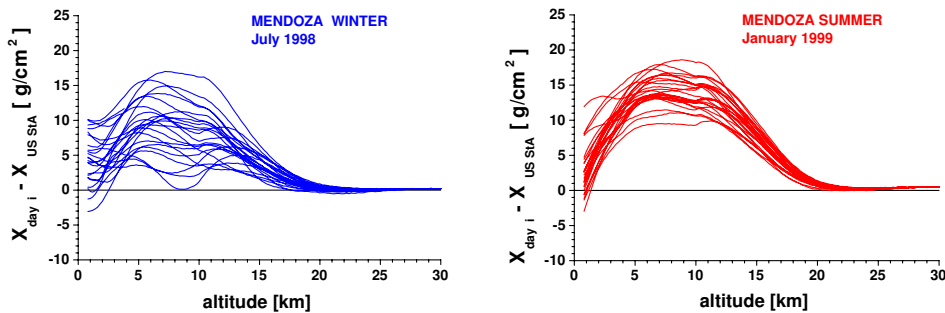


Figure 5. Daily variation of atmospheric profiles in winter and summer at Mendoza.

arises whether one can calculate accurately enough an atmospheric depth profile for the night, based on the radiosonde data collected during the day. The station at Salt Lake City routinely makes two radiosonde soundings during daytime (11.00 and 12.00 hrs) and two soundings during night (23.00 and 0.00 hrs). The day-night atmospheric variation can therefore be studied at Salt Lake City.

Using profiles of two consecutive days, an interpolation is made to get a "night interpolated" profile, which is then compared to the profile actually measured during that night. The standard deviation of the distribution of differences between measured and interpolated nightly profiles stay below $\sim 3 \text{ g/cm}^2$. One can therefore conclude that the nightly profiles can be adequately determined from measurements done during neighboring days.

5. Summary

The profiles of atmospheric depth exhibit a seasonal variation of up to $10\text{--}20 \text{ g/cm}^2$, both at Mendoza and at Salt Lake City. The average monthly profiles vary year-to-year within a few g/cm^2 . This variation is due to fluctuations of daily profiles. The day-to-day variation within a month is as important for shower studies as the seasonal variation: the ranges of the seasonal and daily variations are similar. Therefore, a daily local monitoring of the atmosphere is needed for precise shower reconstruction. The day-night variation, which reflects the day-to-day variation, is reasonably small.

Acknowledgements. The access to the UK Met Office data, granted to us by the British Atmospheric Data Centre is gratefully acknowledged. This work was partially supported in Poland by the State Committee for Scientific Research, grants No. PBZ KBN 054/P03/2001 and 2 P03B 11024 and in Germany by the DAAD under grant No. PPP323.

References

- [1] US Standard Atmosphere Model, http://nssdc.gsfc.nasa.gov/space/model/atmos/us_standard.html
- [2] B.Keilhauer et al., *Astropart. Phys.* 22 249 (2004)
- [3] B.Wilczyńska et al., *Proc. 28th ICRC, Tsukuba, 2, 571* (2003)
- [4] British Atmospheric Data Centre, <http://badc.nerc.ac.uk/data/radiosglobe/radhelp.html>
- [5] COSPAR International Reference Atmosphere, <http://nssdc.gsfc.nasa.gov/space/model/atmos/cospar1.html>

Nitrogen fluorescence yield in dependence on atmospheric conditions

B. Keilhauer^a, R. Engel^b, H. Klages^b, T. Waldenmaier^b

(a) University of Karlsruhe, Institute for Experimental Nuclear Physics, Karlsruhe, Germany

(b) Forschungszentrum Karlsruhe, Institute for Nuclear Physics, Karlsruhe, Germany

Presenter: B. Keilhauer (bianca.keilhauer@ik.fzk.de), ger-keilhauer-B-abs1-he14-oral

The effective fluorescence yield in air is a crucial quantity for the reconstruction of extensive air showers detected with fluorescence telescopes. Several laboratory experiments provide results for the fluorescence yield that is typically measured in small scintillation chambers. These data are compared to a theoretical description of the dependence on atmospheric conditions.

1. Introduction

In several air shower experiments (e.g. HiRes, Pierre Auger Observatory, TA [1]), the fluorescence technique for detecting extensive air showers is employed. Measuring the fluorescence light that nitrogen molecules emit after being excited by charged particles traversing the atmosphere, is the most direct method of detecting the longitudinal shower profile. For the reconstruction procedures of the air shower experiments, the value of fluorescence yield FY_λ and its dependence on atmospheric conditions are crucial parameters.

The theory of fluorescence light emission is based on the *Franck-Condon principle* and the theory of molecular motion. The absolute value of FY_λ is measured by different laboratory experiments. In this article, we want to compare results of different laboratory measurements with theoretical calculations, accounting for the atmospheric conditions.

2. Theoretical description of fluorescence emission and comparison of measurements

The N_2 fluorescence spectrum is characterized by an electronic band system. Light is emitted isotropically mainly in the wavelength region between 300 and 400 nm. Up to now, there are 19 strong emission bands separated, 18 of them are belonging to the second positive (2P) system and the other to the first negative system (1N). Nitrogen molecules are excited mainly by electrons which are most numerous charged particles in extensive air showers. During de-excitation some non-radiative processes have to be taken into account. Therefore, the quantum efficiency of fluorescence is defined as

$$\frac{\text{rate of de-excitation via radiation}}{\text{total rate of de-excitation}} = \frac{\tau_c}{\tau_0 + \tau_c}, \quad (1)$$

where the rate of de-excitation is proportional to the reciprocal of the life time. The mean life time of a radiative transition to any lower state is τ_0 , and to collisional quenching τ_c . The collisional quenching depends on the collision rate and, therefore, on the mean velocity of molecules $\bar{v} = \sqrt{\frac{8kT}{\pi M}}$:

$$\tau_c = (\sqrt{2} \cdot \rho_n \cdot \sigma_{NN} \cdot \bar{v})^{-1} = \sqrt{(\pi M/kT)} \cdot (4\rho_n \cdot \sigma_{NN})^{-1}, \quad (2)$$

where ρ_n is the particle number density, σ_{NN} the collisional cross section between nitrogen molecules, T the temperature, k the Boltzmann constant, and M the molecular mass. Now the fluorescence efficiency can be defined as

$$\varepsilon_\lambda(p, T) = \frac{\varepsilon_\lambda(p \rightarrow 0)}{1 + (p/p'_\nu(T))} = \frac{\text{radiated energy in the form of fluorescence photons}}{\text{energy deposit in the observed medium}} = \frac{n \cdot E_\gamma}{E_{dep}}, \quad (3)$$

with $\varepsilon_\lambda(p \rightarrow 0)$ being fluorescence efficiency at wavelength λ without collisional quenching, n denoting the number of photons, and $p/p'_\nu = \tau_{0,\nu}/\tau_{c,\nu}$. The pressure p is that of the observed medium (e.g. air), p'_ν is a

reference pressure, $\tau_{0,\nu}$, and $\tau_{c,\nu}$ are the mean life times for excitation level ν . Applying actual atmospheric conditions, with air presumed to be a two-component gas, the relation between p and p' can be written as

$$\frac{p}{p'_\nu} = \tau_{0,\nu} \cdot \left(\frac{1}{\tau_{NN,\nu}(\sigma_{NN,\nu})} + \frac{1}{\tau_{NO,\nu}(\sigma_{NO,\nu})} \right) = \frac{\tau_{0,\nu} p_{\text{air}} \cdot N_A}{R \cdot T} \cdot \sqrt{\frac{kTN_A}{\pi}} \cdot \left(4 \cdot \text{vol}\%(\text{N}_2) \cdot \sigma_{NN,\nu} \sqrt{\frac{1}{M_{m,N}}} + 2 \cdot \text{vol}\%(\text{O}_2) \cdot \sigma_{NO,\nu} \sqrt{2 \left(\frac{1}{M_{m,N}} + \frac{1}{M_{m,O}} \right)} \right), \quad (4)$$

with Avogadro's number N_A , the masses per mole for nitrogen $M_{m,N}$ and oxygen $M_{m,O}$, and the cross sections for collisional de-excitation for nitrogen-nitrogen $\sigma_{NN,\nu}$ and nitrogen-oxygen $\sigma_{NO,\nu}$.

The here shown calculations are based on theoretical expectations and some free parameters which have been obtained by fluorescence measurements. Values for $\varepsilon_\lambda(p \rightarrow 0)$, see table 2, are given in [2] and also the deactivation constants, see Table 1, are taken from [2] or partly exchanged by recent data from [3].

Table 1. Deactivation constants for air in the lower atmosphere

	Bunner [2]			Ulrich et al. [3]		
	σ_{NO} in m^2	σ_{NN} in m^2	τ_0 in 10^{-8} s	σ_{NN} in m^2	$\sigma_{N\text{vapor}}$ in m^2	τ_0 in 10^{-8} s
1N $\nu = 0$	13×10^{-19}	4.37×10^{-19}	6.58	-	-	-
2P $\nu = 0$	2.1×10^{-19}	1.0×10^{-20}	4.45	1.82×10^{-20}	8.53×10^{-19}	4.17
$\nu = 1$	5.0×10^{-19} ^a	3.5×10^{-20}	4.93	3.77×10^{-20}	8.04×10^{-19}	4.17
$\nu = 2$	7.0×10^{-19} ^a	8.8×10^{-20}	4.45	-	-	-
$\nu = 3$	8.0×10^{-19} ^a	1.2×10^{-19}	6.65	-	-	-

^aThis value is determined by the given results of [2] and not given in his original publication.

Wavelength-dependent results of fluorescence yield measurements have been provided by 3 experiments [2, 4, 5]. Bunner lists several intermediate values: $\varepsilon_\lambda(p \rightarrow 0)$, $\varepsilon_\lambda^{s.l.}(p, T)$ in %, and the fluorescence efficiency $\varepsilon_{E_{dep}}^{s.l.}$ in units of photons/MeV of deposited energy = $\varepsilon_\lambda^{s.l.}(p, T) \cdot (\lambda/hc)$, with λ = wavelength, c = speed of light, h = Planck's constant, at sea level (*s.l.*). The values for $\varepsilon_\lambda^{s.l.}(p, T)$ and $\varepsilon_{E_{dep}}^{s.l.}$ given explicitly in [2] are not reproduced by the here shown calculations, see Table 2. Possible reasons are rounding uncertainties by Bunner or the use of deviating numbers for variables concerning air conditions. Davidson and O'Neil list results for $\varepsilon_\lambda^{s.l.}(p, T)$ for wavelengths above 328 nm [4]. It should be mentioned that the results in [4] are given for $p = 800$ hPa. However, the pressure dependence is not so strong in this region from sea level with $p = 1013$ hPa to $p = 800$ hPa. Nagano et al. report directly the values for FY_λ at sea level for 0.85 MeV electrons [5], however, only 10 contributing emission bands are listed. For comparing the results of all authors, 0.85 MeV electrons are chosen as exciting particles, so the ionization energy deposit is $dE/dX = 0.1677$ MeV/kg·m⁻² [6]. It is assumed that the fluorescence yield is proportional to the energy deposit as indicated by experiments [7, 8]. Air is taken to be a composition of 78.8 % N₂ and 21.1 % O₂ [6]. The resulting fluorescence yield can be written as

$$FY_\lambda = \varepsilon_\lambda(p, T) \cdot \frac{\lambda}{hc} \cdot \frac{dE}{dX} \cdot \rho_{\text{air}} \left[\frac{\text{photons}}{\text{m}} \right]. \quad (5)$$

A comparison of the obtained FY_λ values at sea level is shown in Table 2.

Kakimoto et al. provide a formula for calculating the fluorescence yield between 300 and 400 nm, which gives at sea level $3.275 \frac{\text{photons}}{\text{m}}$ [7]. This value is smaller by 11 % compared to the results of Nagano et al. The HiRes

Table 2. Fluorescence yields at sea level in the US Std. Atmosphere. Details see text.

Wave-length λ (nm)	Band	ε_λ ($p \rightarrow 0$) (%)	Fluorescence Yield $FY_\lambda^{s.l.}$				Nagano et al. [5] ($\frac{\text{photons}}{\text{m}}$)
			Bunner [2] ($\frac{\text{photons}}{\text{m}}$)	Davidson & O'Neil [4] ($\frac{\text{photons}}{\text{m}}$)	this work with Tab. 1 <i>Bunner</i> ($\frac{\text{photons}}{\text{m}}$)	this work with Tab. 1 <i>Ulrich</i> ($\frac{\text{photons}}{\text{m}}$)	
311.7	2P (3-2)	.005	0.008	-	0.009	0.009	- ^a
313.6	2P (2-1)	.029	0.090	-	0.094	0.094	- ^a
315.9	2P (1-0)	.050	0.224	-	0.240	0.279	0.549
328.5	2P (3-3)	.0154	0.027	0.035	0.029	0.029	0.180
330.9	2P (2-2)	.002	0.007	- ^a	0.007	0.007	- ^a
333.9	2P (1-1)	.0041	0.019	- ^a	0.021	0.024	- ^a
337.1	2P (0-0)	.082	0.887	1.173	1.169	1.109	1.021
346.9	2P (3-4)	.0063	0.012	0.015	0.013	0.013	- ^a
350.0(1) ^b	2P (2-3)	.004	0.014	0.013	0.014	0.014	- ^a
353.7	2P (1-2)	.029	0.146	0.188	0.156	0.181	0.130
357.7	2P (0-1)	.0615	0.707	0.889	0.930	0.882	0.799
367.2	2P (3-5)	.0046	0.009	0.012	0.010	0.010	- ^a
371.1	2P (2-4)	.010	0.037	0.047	0.038	0.038	- ^a
375.6	2P (1-3)	.0271	0.150	0.187	0.155	0.180	0.238
380.5	2P (0-2)	.0213	0.261	0.328	0.343	0.325	0.287
389.4	2P (3-6)	.003	0.006	- ^a	0.007	0.007	- ^a
391.4	1N (0-0)	.33	0.281	0.454	0.315	0.315	0.302
394.3	2P (2-5)	.0064	0.025	0.032	0.026	0.026	0.063
399.8	2P (1-4)	.016	0.090	0.119	0.097	0.113	0.129
sum of $\lambda = (300 - 400)$ nm			3.001	3.490 ^c	3.672	3.653	3.698
sum of all Nagano-wavelengths			2.798	3.404 ^c	3.460	3.438	3.698

^aThis transition has not been measured.

^bIn the work of Davidson & O'Neil, the wavelength for this transition is given with 350.1 nm.

^cOnly measurements above 328 nm.

Collaboration uses a value of about $5 \frac{\text{photons}}{\text{m}}$ per charged particle in an air shower [9]. For these charged particles, an average energy deposit of $0.22 \text{ MeV/kg m}^{-2}$ is assumed [2], which leads to a corresponding fluorescence yield at s.l. of $3.811 \frac{\text{photons}}{\text{m}}$ for a 0.85 MeV electron. Assuming that the HiRes value refers to 5 km a.s.l., one would obtain at s.l. $3.6 - 3.7 \frac{\text{photons}}{\text{m}}$. The calculations shown here reproduce the measured values from Nagano very accurately and the partly varying deactivation constants do not affect the final result much. However, this holds only for the comparison of the whole wavelength region between 300 and 400 nm. One difficulty in these measurements is the treatment of interference filter which have a bandwidth of about 10 nm [5]. The 10 contributions of Nagano et al. are given after subtracting additional contributions by smaller emissions. Thus, for a direct comparison, one has to take into account only the 10 wavelengths reported in [5] and in this case, the calculations differ by approximately -7%.

3. Altitude dependence of the fluorescence yield

The formulas given in Sec. 2, provide directly the fluorescence yield in dependence on pressure and temperature. Other authors deduce parameterizations of functional forms based on the same equations [5, 7]:

$$FY_\lambda^{[5]} = \frac{dE}{dX} \cdot \left(\frac{A_\lambda \rho}{1 + \rho B_\lambda \sqrt{T}} \right), \quad FY_{300-400 \text{ nm}}^{[7]} = \frac{dE}{dX} \cdot \rho \left(\frac{A_1}{1 + \rho B_1 \sqrt{T}} + \frac{A_2}{1 + \rho B_2 \sqrt{T}} \right). \quad (6)$$

Both types of ansätze predict similar height dependence, see Fig. 1. The parameterization differs from the direct calculation by less than 1.5 %. In Fig. 2, the variation of the altitude dependence due to seasonal effects is illustrated. The two exemplarily chosen atmospheres are representatives for conditions in Argentina at the southern site of the Pierre Auger Observatory [10]. The relative difference to the US Std. Atmosphere is shown in Fig. 3. During winter, the variation is smallest and below 1.5 %. However during summer, the difference is about -2.5 to -3 % in the altitude range most important for air shower detection.

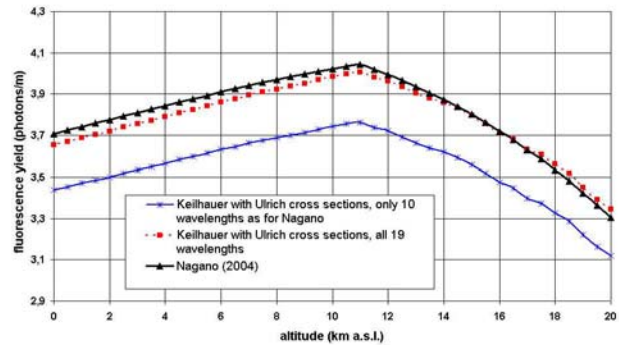


Figure 1. FY in dependence on altitude in the US Std. Atmosphere.

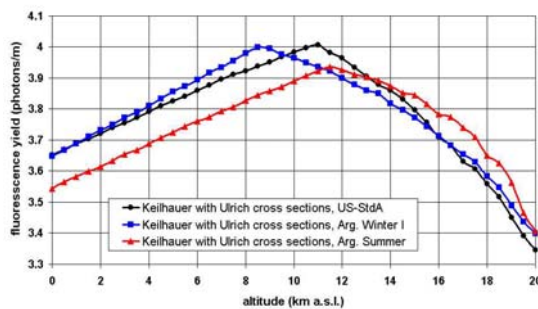


Figure 2. Fluorescence yield as function of altitude in three different atmospheres as given in [10].

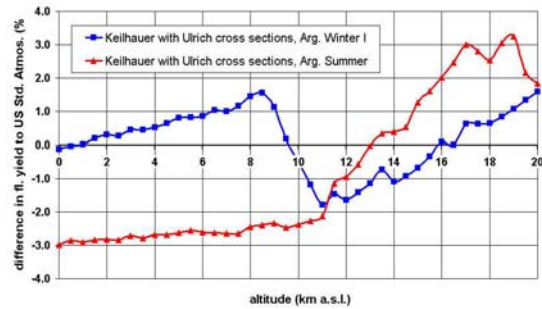


Figure 3. Difference in FY of two representative Argentine atmospheres to the US Std. Atmosphere.

For the 337.1 nm emission band, the effect of quenching due to water vapor has been studied. Applying the constants from Tab. 1 by Ulrich et al. and assuming 100 % rel. humidity, the emission at sea level is reduced by $\approx 20\%$, at 4 km a.s.l. by $\approx 5\%$, and at 8 km a.s.l. just by 0.3 %.

References

- [1] R. Engel, H. Klages, C. R. Physique **5**, 505, (2004)
- [2] A. N. Bunner, Cosmic Ray Detection by Atmospheric Fluorescence, PhD Thesis, Cornell University, Ithaca, NY, USA, (1967)
- [3] A. Morozov, R. Krücken, J. Wieser, and A. Ulrich, Eur. Phys. J. D **33**, 207, (2005)
- [4] G. Davidson, R. O'Neil, J. Chem. Phys. **41**, No. 12, 3946, (1964)
- [5] M. Nagano, K. Kobayakawa, N. Sakaki, and K. Ando, Astropart. Phys. **22**, 235, (2004)
- [6] M. Nagano, K. Kobayakawa, N. Sakaki, and K. Ando, Astropart. Phys. **20**, 293, (2003)
- [7] F. Kakimoto et al., Nucl. Instr. and Meth. in Phys. Res. A **372**, 527, (1996)
- [8] M. Bohcova et al., these proceedings, cz-bohcova-M-abs1-he14-poster
- [9] R. U. Abbasi et al. (HiRes Collab.), Astrophys. J. **622**, 901, (2005)
- [10] B. Keilhauer et al., Astropart. Phys. **22**, 249, (2004)

Measurement of the Air Fluorescence Yield with the AirLight Experiment

T. Waldenmaier^a, J. Blümer^{a,b}, B. Keilhauer^b, H. Klages^a, S. Klepser^c

(a) Forschungszentrum Karlsruhe, Institut für Kernphysik, P.O. Box 3640, 76021 Karlsruhe, Germany

(b) Universität Karlsruhe (TH), Institut für Experimentelle Kernphysik, P.O. Box 3640, 76021 Karlsruhe, Germany

(c) DESY Zeuthen, Platanenallee 6, 15738 Zeuthen, Germany

Presenter: B. Keilhauer (bianca.keilhauer@ik.fzk.de), ger-keilhauer-B-abs3-he15-poster

For the detection of ultrahigh energy cosmic rays, many experiments rely on the fluorescence technique to measure the longitudinal development of extensive air showers in the atmosphere. The key quantity for the energy reconstruction of the primary particle is the fluorescence yield which depends on pressure, temperature as well as the composition (e.g. water vapor) of the air. The AirLight Experiment at Forschungszentrum Karlsruhe aims for a measurement of the fluorescence yield using electrons emitted by a ⁹⁰Sr source. The usable energy of the electrons ranges from 250 keV to 2 MeV. Different gas mixtures can be tested at pressures between 5 hPa and 1000 hPa. The current status and first results will be presented.

1. Introduction

Due to the extremely low particle fluxes, very-high energy cosmic rays can be detected only indirectly by observing extensive air showers (EAS). Apart from their detection by large detector arrays on the ground, very-high energy EAS can also be measured with the aid of their fluorescence light emissions. This technique utilizes the atmosphere as a scintillator with the advantage of being able to directly access fundamental shower parameters, as the longitudinal development of the total electromagnetic energy deposit along the shower axis, without relying on theoretical interaction models. Therefore the longitudinal shower profile provides complementary information to the lateral particle distributions at ground, measured by the large detector fields. Challenging is the need of a very good understanding of the entire fluorescence detector, including the atmosphere and the fluorescence emission process.

If all the fluorescence photons are assumed to be emitted along the shower axis, the number of observed photons in the detector dN_γ per unit path length dx is obtained by

$$\frac{dN_\gamma}{dx} = \int \frac{d^2 N_\gamma^0}{d\lambda dx} \cdot \varepsilon_{\text{atm}}(\lambda, x) \cdot \varepsilon_{\text{FD}}(\lambda, x) d\lambda, \quad (1)$$

where ε_{atm} and ε_{FD} are the total efficiencies of the atmosphere and the fluorescence detector respectively, which have to be monitored very carefully. The number of produced fluorescence photons at the shower axis dN_γ^0 per wavelength bin $d\lambda$ is assumed to be related to the deposited energy dE_{dep} in the layer dx according to [1, 2]:

$$\frac{d^2 N_\gamma^0}{d\lambda dx} = y(\lambda, T, p) \cdot \frac{dE_{\text{dep}}}{dx}. \quad (2)$$

The quantity $y(\lambda, T, p)$ is the fluorescence yield, which depends on the wavelength λ of the emitted fluorescence light as well as on temperature $T(x)$ and pressure $p(x)$ of the air at the position of emission. If Eq. (2) is valid, the fluorescence yield $y(\lambda, T, p)$ does not depend on the energy of the ionizing particles and Eq. (1) transforms to the simple form

$$\frac{dN_\gamma}{dx} = \frac{dE_{\text{dep}}}{dx} \int y(\lambda, T, p) \cdot \varepsilon_{\text{atm}}(\lambda, x) \cdot \varepsilon_{\text{FD}}(\lambda, x) d\lambda. \quad (3)$$

Thus, the fluorescence light output of an EAS is directly related to the energy deposited along its shower axis.

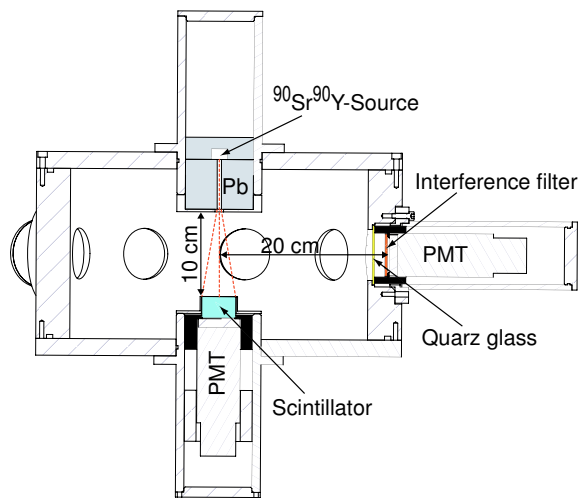


Figure 1. Experimental setup of the AirLight Experiment.

2. The AirLight Experiment

Most of the fluorescence emissions in air, in the wavelength range between 300 nm and 400 nm, are originating from excited N_2 and N_2^+ molecules [3]. In an EAS nearly all of the nitrogen excitations are caused by electrons and positrons with energies below 1 GeV [2]. About 13 % of the deposited energy in the atmosphere comes from low-energy electrons between 250 keV and 2 MeV [2]. The aim of the AirLight Experiment is to measure the relation between the fluorescence emission and the ionization energy deposit of electrons, Eq. (2), in this energy regime for atmospheric pressures, ranging from 5 hPa to 1000 hPa. Furthermore, the influence of water vapor will be investigated.

In Fig. 1, the experimental setup of the AirLight experiment is shown. The experiment consists of a cylindrical aluminum chamber with seven photomultipliers (PMT) mounted perpendicular to the chamber axis at a radius of 20 cm. Six PMTs are equipped with narrow band interference filters (FWHM ~ 10 nm) matched to the most important nitrogen transition bands as it is illustrated in Fig. 2. One PMT has a M-UG6 absorption filter as it is used in the fluorescence detectors of the Pierre Auger Observatory [5] to measure the integral fluorescence spectrum between 300 nm and 420 nm. The chamber is black anodized to suppress photons scattered off the chamber walls which would bias the acceptance of the PMTs. The electrons are emitted from a ^{90}Sr - ^{90}Y beta source with an endpoint energy of 2.3 MeV. The source has an activity of 37 MBq and is located behind a lead collimator of 6 cm length at the top of the chamber. Once the electrons have passed the collimator they traverse 10 cm of test gas (normally air or pure nitrogen) and are finally stopped in a scintillation detector at the bottom of the chamber. The scintillator measures the energy of the electrons and was calibrated by the measurement of the two well-known Compton-edges in the energy spectrum of a ^{22}Na gamma emitter. Analyzing the smearing of the Compton spectrum, the energy resolution of the scintillator turned out to be about $(E/\text{MeV})^{-0.5} \cdot 10\%$.

The measuring procedure takes advantage of the coincidence between the electron signal in the scintillator and the signal of the induced fluorescence photons. The resulting distribution of time differences between the electrons and the coincident PMT signals is shown in Fig. 3 for the 337 nm band. Since the relaxation of the excited states follows an exponential decay law, the signal can be fitted with a Gauss convoluted exponential function taking into account the experimental time resolution of about 0.8 ns. Accidental coincidences can be

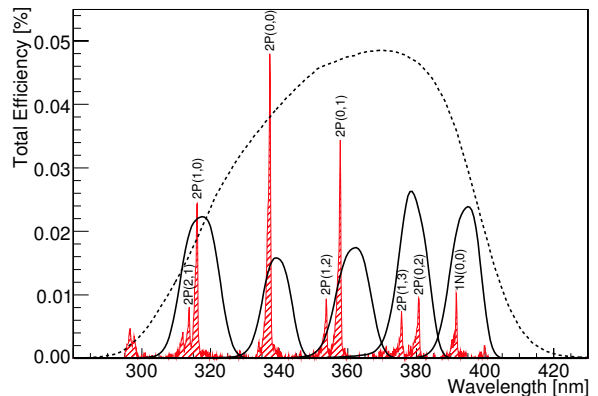


Figure 2. Total efficiencies of the different wavelength bands. The dashed line belongs to the M-UG6 filter and the solid lines represent the interference filters. The most prominent nitrogen transitions are labeled in the sketched spectrum measured by Ulrich et al. [4] (not calibrated).

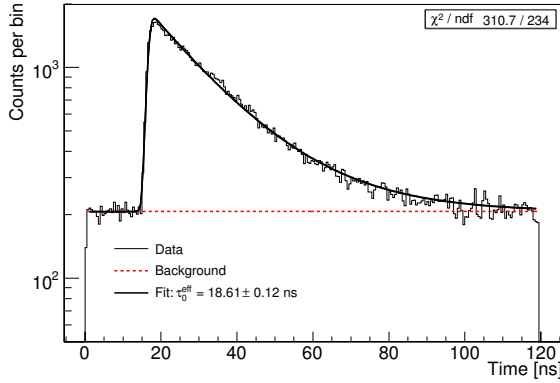


Figure 3. Fluorescence signal of the 2P(0,0) transition (337 nm band) in pure nitrogen at a pressure of 100 hPa and 20 °C.

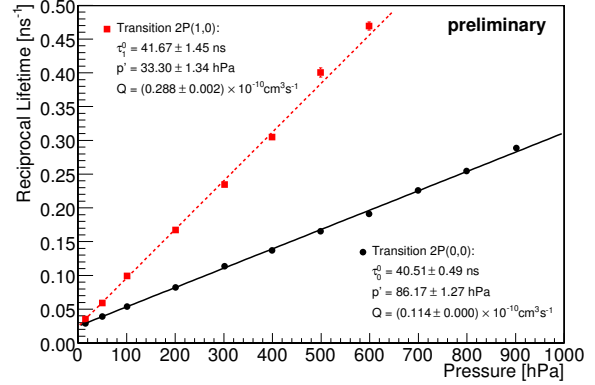


Figure 4. Reciprocal lifetimes $1/\tau_{v'}^{eff}$ for the 2P(0,0) and 2P(1,0) transitions in pure nitrogen vs. pressure at 20 °C. The Q-values are the quenching rate constants for the nitrogen self-quenching.

subtracted as flat background from the fluorescence signals because of their missing time correlation with the scintillator signal.

3. Some theory and first results

The data taking and the analysis are still ongoing. Nevertheless, some first results will be discussed in this section. As one can see in Fig. 2, the nitrogen spectrum consists of a variety of bands. Each band belongs to a transition between the vibrational states of a certain electronic transition. For example 2P(0,1) labels the transition between the vibrational states $v' = 0$ and $v'' = 1$ of the second positive electronic nitrogen transition system ($C^3\Pi_u \rightarrow B^3\Pi_g$). The broadening of the bands is due to the rotational substructure which is not resolved in Fig. 2. The relative intensities of the single vibrational bands, which belong to a certain electronic transition, are given by the Einstein transition probabilities $A_{v',v''}$ which have been calculated by Gilmore et al. [6]. Therefore the radiative lifetime $\tau_{v'}$ of a vibrational state v' can be calculated from the sum over all radiative transition probabilities $1/\tau_{v'} = \sum_{v''} A_{v',v''}$.

Since the excited nitrogen molecules suffer collisions with other molecules, there is a competition between radiative transitions and radiationless deactivations (quenching). The probability of collisional deactivation of the state v' can be expressed by $1/\tau_{v'}^c$, where $\tau_{v'}^c$ is the mean time between such collisions. $\tau_{v'}^c$ depends on the collisional cross sections as well as on temperature T and pressure p of the gas and hence it follows from kinetic gas theory $\tau_{v'}^c \propto \sqrt{T}/p$ [3]. The relaxation rate $\frac{dN_{v'}}{dt}$ and the effective lifetime $\tau_{v'}^{eff}(p, T)$ of an excited state are therefore:

$$\frac{dN_{v'}}{dt} = - \left(\frac{1}{\tau_{v'}^0} + \frac{1}{\tau_{v'}^c} \right) \cdot N_{v'}(t), \quad \tau_{v'}^{eff} = \frac{\tau_{v'}^0 \tau_{v'}^c}{\tau_{v'}^0 + \tau_{v'}^c} = \frac{\tau_{v'}^0}{1 + \frac{p}{p'_{v'}}}. \quad (4)$$

$\tau_{v'}^0$ is the observed lifetime at zero pressure which has not to be necessarily equal to the radiative lifetime $\tau_{v'}$, due to internal quenching effects. If the pressure p reaches the reference pressure $p'_{v'}$, the collisional deactivations are getting stronger than the optical transitions. The probability for an excited state v' to relax into a lower state v'' of the band system through the emission of an optical photon results to be $A_{v',v''} \cdot \tau_{v'}^{eff}(p, T)$.

If the number of excited states is proportional to the local deposited energy ($N_{v'} = f_{v'} \cdot E_{dep}$), the fluorescence yield of the transition $v' \rightarrow v''$ can be expressed as

$$y(v' \rightarrow v'', p, T) = f_{v'} \cdot A_{v', v''} \cdot \tau_{v''}^{\text{eff}}(p, T), \quad (5)$$

where $f_{v'}$ is the number of excited states v' per deposited energy. As one can see in Fig. 2, the fluorescence spectrum of nitrogen in the wavelength range between 300 nm and 400 nm consists almost entirely of vibrational transitions within the second positive system (2P) with $v' = 0, 1$ and the first negative system (1N) with $v' = 0$. Thus the total nitrogen fluorescence yield can be expressed in first approximation as the superposition of three contributions

$$y_{tot}(p, T) \approx \sum_{v''} y_{2P}(0 \rightarrow v'', p, T) + y_{2P}(1 \rightarrow v'', p, T) + y_{1N}(0 \rightarrow v'', p, T), \quad (6)$$

where all the transitions of one contribution have the same quenching behavior. Since in Eq. (6) there are only contributions with $v' = 0, 1$ it is sufficient to study the quenching just for the 2P(0,0), 2P(1,0) and 1N(0,0) bands. This is shown in Fig. 4, where the reciprocal lifetimes $1/\tau_{v''}^{\text{eff}}$ for the 2P system are plotted against the pressure in pure nitrogen. For the 2P(1,0) transition the contribution of the other two bands in the filter range is not taken into account because of their rather low intensities. The values obtained for this two transitions are in good agreement with other published data [7, 8]. Some filters, especially the filters at 360 nm and 380 nm, happen to match with two nitrogen bands. For these cases, the fit shown in Fig. 3 has to be done with two components using fixed lifetimes taken from the 2P(0,0) and 2P(1,0) data. The measurement of the 1N bands is much more complicated because of their large lifetimes at low pressures and their low intensities at high pressures. The corresponding analysis for this transition is still ongoing.

4. Status and Outlook

The experimental setup of the AirLight Experiment at Forschungszentrum Karlsruhe has almost been completed. First measurements have been performed in pure nitrogen at 20 °C. The data analysis is in progress and first results about the quenching mechanism are in agreement with previous data. Future work will concentrate on the measurement of the quenching constants for different air constituents and on the absolute calibration of the PMTs, to be able to determine the excitation yields $f_{v'}$. In addition GEANT4-simulations [9] of the energy deposition in the chamber and the PMT acceptances are in progress.

Acknowledgements: The authors thank Günter Wörner who constructed the chamber and provided excellent expertise in technical matters.

References

- [1] M. Nagano et al.: *Astropart. Phys.* **20**, 293 (2003)
- [2] M. Risse, D. Heck: *Astropart. Phys.* **20**, 661 (2004)
- [3] A.N. Bunner: *Cosmic Ray Detection by Atmospheric Fluorescence*.
PhD Thesis, Cornell University, Ithaca, New York (1967)
- [4] A. Ulrich: private communication
- [5] Auger Collab., J. Abraham et al.: *Nucl. Inst. and Meth. A* **523**, 50 (2004)
- [6] F.R. Gilmore, R.R. Laher, P.J. Espy: *J. Phys. Chem. Ref. Data* **21**, 1005 (1992)
- [7] S.V. Pancheshnyi et al.: *J. Chem. Phys.* **262**, 349 (2000)
- [8] A. Morozov, A. Ulrich et al.: *Eur. Phys. J. D* **33**, 207 (2005)
- [9] Geant4 Collab., S. Agostinelli et al.: *Nucl. Inst. and Meth. A* **506**, 250 (2003)

Top-Down Reconstruction of Ultrahigh Energy Air Showers

F. Schüssler^a, J. Blümer^{a,b}, R. Engel^b, M. Unger^b

(a) *University of Karlsruhe, Institut für exp. Kernphysik Postfach 6980 76128 Karlsruhe, Germany*

(b) *Forschungszentrum Karlsruhe, Institut für Kernphysik, Postfach 3640, 76021 Karlsruhe, Germany*

Presenter: R. Engel (ralph.engel@ik.fzk.de), ger-engel-R-abs1-hep14-poster

Based on the new air shower simulation tool CONEX, we evaluate the potential of a top-down reconstruction of ultrahigh energy air showers measured with the fluorescence telescopes of the Pierre Auger Observatory. A large number of simulated longitudinal shower profiles are passed to a complete fluorescence simulation chain, consisting of the production of fluorescence and Cherenkov light, light propagation in the atmosphere and a detailed simulation of the detector response including realistic resolutions, fluctuations and efficiencies. Using χ^2 test statistics, the simulated detector output is then directly compared to measured fluorescence signals. To test this method, it is applied to signals from simulated air showers and the reconstructed shower parameters are compared with the true ones.

1. Introduction

Due to the great importance of air shower measurements at the very end of the cosmic ray spectrum for the theoretical understanding of the highest energy phenomena in our universe, it is vital to be able to reconstruct these rare events as accurately and completely as possible.

In a conventional reconstruction procedure of fluorescence measurements as developed by the pioneering experiment Fly's Eye [1], first the event geometry is reconstructed and in a next step the shower profile is determined. Only subsets of the complete event information are used in each reconstruction step and correlations between reconstructed geometry and shower profile are disregarded.

The presented top-down reconstruction procedure takes into account the whole information available after the detection of an air shower by a single fluorescence telescope, namely the full ADC-traces of each triggered pixel (ADC-counts as function of time), the information about the atmospheric conditions at the time of measurement (atmospheric profile, attenuation and scattering parameters) and the knowledge about the detector itself, i.e. pointing directions and calibration constants of each camera pixel.

2. Top-Down reconstruction procedure

Top-down approaches use Monte Carlo simulations to derive the parameters of the air shower and its primary particle. Based on rough first estimates of the shower geometry and energy, provided usually by the standard algorithms, a large number of extensive air showers is simulated in the phase space around the estimated shower parameters and the response of the fluorescence detector to these simulated signals is derived. Statistical tests are then employed in order to find the most probable values of the parameters of the air shower and its primary particle including their errors and correlations.

In order to allow a sufficiently accurate reconstruction of the shower parameters, the simulated showers have to cover a wide range of phase space as close as possible. The ranges adopted here can be found in table 1 and equal about $\pm 3\sigma$ of the obtained resolution.

The potential of this method is evaluated by applying it to simulated showers inspired by the most energetic event detected by the Pierre Auger Observatory so far [2].

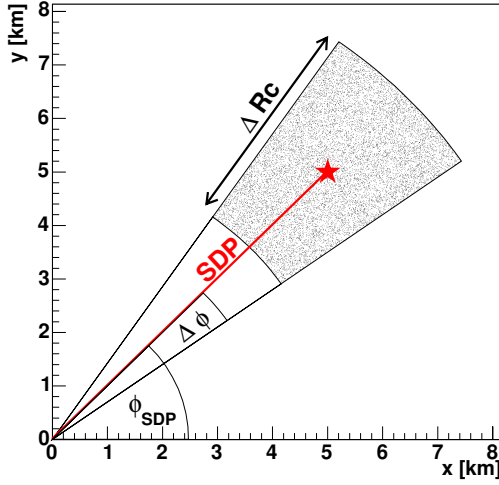


Figure 1. Construction of core position range around the first guess (red star) with the fluorescence detector situated at the origin.

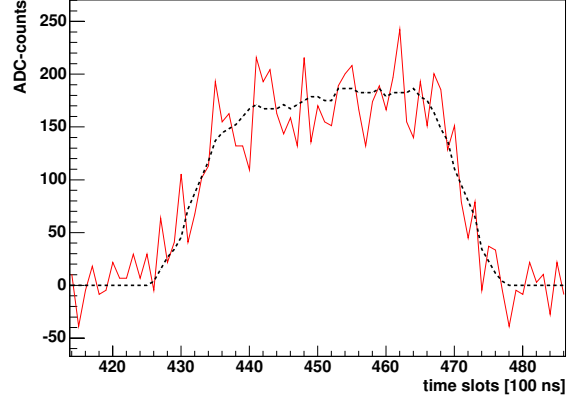


Figure 2. Example of an ADC-trace of a single camera pixel after the trigger simulation (red solid line) in comparison to the original trace (black dashed line).

Air shower simulation: CONEX [3] is applied to simulate longitudinal energy deposit profiles of extensive air showers. It combines both MC techniques and numerical solutions of the underlying cascade equations in order to reduce the needed computing time considerably. In this first simulation step, QGSJET01 [4] has been selected as high energy interaction model and air showers were produced with an energy spectrum constant in $\log_{10}(E)$. All other shower parameters, e.g. X_{\max} , were obtained naturally during the shower simulation.

Fluorescence light simulation: FDSim [5] has been used for the simulation of emission and propagation of fluorescence and Cherenkov light produced by these showers.

The distance between shower core and detector, R_{core} , corresponding to the core position inside the shower-detector-plane (SDP), has been chosen while taking into account possible variations of the SDP-direction itself, described through the angle ϕ_{SDP} with respect to the Auger site coordinate system (see figure 1).

In order to completely define the position of the shower in the atmosphere, the azimuth and zenith angle, ϕ and θ respectively, have also been chosen randomly in a fixed range around the first estimation given by the standard reconstruction.

Parameter	Range
Energy	$\pm 25\%$
R_{core}	± 2 km
ϕ_{SDP}	$\pm 1.5^\circ$
θ	$\pm 3^\circ$
ϕ	$\pm 3^\circ$

Table 1. Parameter ranges used for the shower simulations.

Detector simulation: As first step of the detector simulation, signal fluctuations based on background light and readout electronics are simulated. For the first one, a number of photons derived from night sky background measurements at the Auger site are distributed over the camera surface. The total number of photons at each pixel is then converted into photoelectrons and Poissonian fluctuations are applied, before simulating the noise caused by the electronics itself.

Using measured calibration constants, the photoelectrons are then translated into ADC-counts and passed through the same trigger algorithms as implemented in the actual data taking of the Auger detectors. The

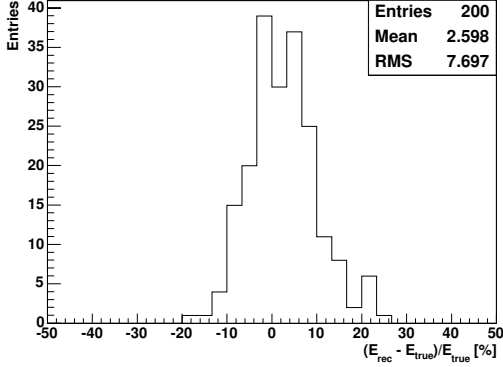


Figure 3. Primary energy resolution for the top-down reconstruction of mono fluorescence events (preliminary).

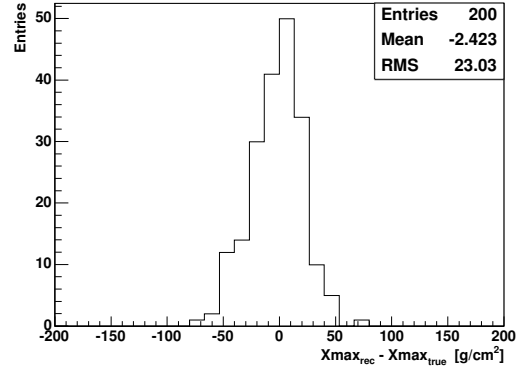


Figure 4. Depth at shower maximum resolution for the top-down reconstruction of mono fluorescence events (preliminary).

simulated output is translated into the Auger DAQ format and stored together with the original ADC-traces carrying no detector noise (see figure 2).

Comparison: After extraction of the ADC-traces of all triggered pixels, a χ^2 -value and corresponding probability $P(\chi_S^2, \text{ndof})$ is assigned to each MC shower through comparison with the measured traces:

$$\chi_S^2 = \sum_{\text{pixel } i} \sum_{\text{time } t} \frac{(F_D(i, t) - F_{MC}(i, t))^2}{\sigma_B^2(i) + \sigma_{MC}^2(i, t)} \quad (1)$$

$$P(\chi_S^2, \text{ndof}) = \int_{\chi_S^2}^{\infty} f_{\text{ndof}}(\chi^2) d\chi^2 \quad (2)$$

$F_D(i, t)$ and $F_{MC}(i, t)$ denote the ADC-signal of the data and MC shower, respectively. $f_{\text{ndof}}(\chi^2)$ stands for the χ^2 probability density function. In order to account for possible boundary effects of the pulses, the integration time window of each camera pixel has been chosen to be 50% larger than the reconstructed ADC-pulse. The error related to the noise background of the measurement can be estimated from the data itself through determining the RMS of the background fluctuations in a region outside the pulse: $\sigma_B(i) = \sqrt{\text{RMS}_{\text{noise}}}$. Using the MC ADC-trace without noise fluctuations, the signal error is caused only by Poissonian fluctuations of the photoelectrons and can be written as $\sigma_{MC}(i, t) = \sqrt{k_i \cdot F_{MC}(i, t)}$, where k_i denotes the conversion factor between ADC-counts and photoelectrons and has been derived from calibration measurements.

The *top-down reconstruction result* is given by the shower with minimal χ_S^2 and its corresponding parameters. The related uncertainties are determined by the maximal deviations of the parameters obtained from all showers falling inside $\chi_{\text{min}}^2 + 1$.

3. Preliminary results

Based on this MC study, namely the top-down reconstruction of simulated air showers, first preliminary results of the presented method can be derived. Only simulated data from one fluorescence detector has been used in this *monocular reconstruction*. All shower parameters have been varied within the boundaries given in table 1 and determined during the reconstruction process. No additional quality cuts have been used. As example the

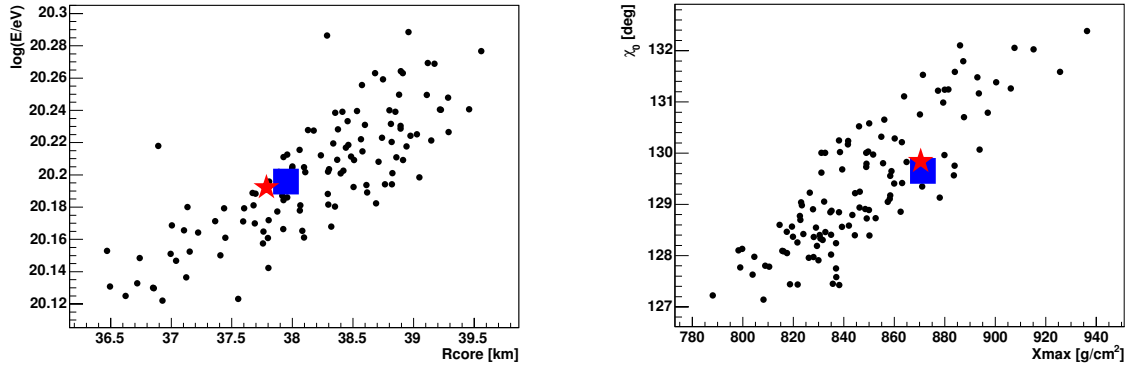


Figure 5. Reconstruction example of one event: Correlation between reconstructed energy and distance between detector and shower core (left panel) and correlation between the reconstructed angle between shower axis and ground plane χ_0 inside the shower detector plane and the position of shower maximum X_{\max} (right panel). The *reconstruction results* are shown as blue squares, the true values are given as red stars. In addition all MC showers having a probability $P > 5\%$ are shown.

obtained energy resolution ($\text{RMS} \approx 8\%$) and the corresponding residual of the depth at shower maximum ($\text{RMS} \approx 23 \text{ g/cm}^2$) are shown in figure 3 and 4, respectively for 200 reconstructed showers. Simultaneous reconstruction of the shower geometry results in $\text{RMS}(\theta) \approx \text{RMS}(\phi) \approx 1^\circ$ and $\text{RMS}(R_{\text{core}}) \approx 0.6 \text{ km}$.

Another possible application of top-down reconstruction algorithms is the systematic study of the correlation between parameter uncertainties. Using the reconstruction of a single shower, one can, for example, check the correlation between reconstructed energy and core distance, or the correlation between shower angle χ_0 and depth at shower maximum X_{\max} as demonstrated in figure 5. Only MC showers having a probability $P(\chi^2_{\text{S}}, \text{ndof})$ greater than 5% are shown.

Although based only on monocular observations of air showers, the presented top-down reconstruction method provides superior resolution and realistic, asymmetric error estimates in comparison to standard reconstruction algorithms, see for example [6]. Its application will nevertheless be limited to some of the highest energy events due to the computational requirements needed to perform the calculations.

References

- [1] R. M. Baltrusaitis et al., Fly’s Eye Collab., *Nucl. Instr. Meth.* A240 (1985) 410.
- [2] M. Ave et al., Pierre Auger Collab., these proceedings, usa-ave-pernas-M-abs1-he14-oral.
- [3] S. Ostapchenko et al., these proceedings, ger-ostapchenko-S-abs2-he14-poster; T. Pierog et al., astro-ph/0411260.
- [4] N.N. Kalmykov, S.S. Ostapchenko, and A.I. Pavlov, *Nucl. Phys. B (Proc. Suppl.)* 52B (1997) 17.
- [5] L. Prado Jr. et al., *Nucl. Instr. Meth.* A545 (2005) 632.
- [6] L. Perrone et al., Pierre Auger Collab., these proceedings, ger-kampert-K-abs3-he14-poster.

Measurement of the Lateral Distribution Function of UHECR Air Showers with the Pierre Auger Observatory

D. Barnhill, P. Bauleo, M.T. Dova, J. Harton, R. Knapik, J. Knapp, J. Lee, M. Manceñido, A.G. Mariazzi, I.C. Mariş, D. Newton, M. Roth, T. Schmidt, A.A. Watson for the Pierre Auger Collaboration

Presenter: P. Bauleo (bauleo@lamar.colostate.edu), usa-bauleo-PM-abs2-he14-poster

1. Introduction

The Pierre Auger Observatory [1] is being used to study cosmic rays with energies larger than 10^{19} eV with unprecedented precision and statistics. An essential quantity that must be deduced from data is the lateral distribution function (LDF) that describes the decreasing of the signals in the water-tanks as a function of distance. Knowledge of the LDF is important for the reconstruction of the shower core and the shower direction. It can also be compared with model calculations to give useful information relating to primary mass. Here we describe how the LDF is measured using the large sample of events recorded with the surface detector (SD) array and with a small sample observed with the fluorescence detectors (FD). For hybrid events, in which SD and FD measurements of the same shower are available, the core position is much better constrained than for SD-only events, thus providing an important cross-check on the LDF determined from SD measurements alone.

2. The Fitting Method

The water-Cherenkov detectors provide information about Cherenkov photons, which are produced when charged particles cross the tanks. The number of Cherenkov photons collected is to a good approximation proportional to the energy deposit in the tank. The signal is calibrated in units of *vertical equivalent muons* (VEM) [9]. The energy deposit, however, depends strongly on the particle type and the conversion from the Cherenkov signal back to the number of particles in the tank is not obvious. For large tank signals (> 15 VEM) this is not crucial since the uncertainty $\sigma(S)$ of a signal S (in VEM) was determined from data of two detectors positioned 11 meters apart [5] to be $\sigma(S) = 1.06 \sqrt{S}$. But for small tank signals the number of effective particles, n , is needed since their Poissonian fluctuation dominates the uncertainty of the signal and is required for the maximum likelihood fit. We have introduced a function that gives n for a measured signal $S(r)$: $n = P(r, \theta, E, A) \times S(r)$ where the conversion factor P is called the *Poisson factor* and is presently assumed to be independent of the primary energy, E , and mass, A , for any distance, r , and zenith angle, θ . The factor reflects the different energy deposits of different secondaries and is determined by simulations. Finally we set up a maximum likelihood fit to determine the parameters of a trial LDF functional form and, at the same time, the position of the shower core, by comparing each tank signal, with its fluctuations, to the value expected from the trial function, S_{th} . $L = \prod_i f_P(n_i, \mu_i) \times \prod_k f_G(n_k, \mu_k) \times \prod_l F_{sat}(n_l, \mu_l) \times \prod_m F_{zero}(n_m, \mu_m)$. The individual factors of the likelihood function are determined using the information of tanks at their respective distance r . The Poissonian probability density, $f_P(n_i, \mu_i)$, is calculated for small signals ($S_i < 15$ VEM). For larger signals the Gaussian approximation is used, $f_G(n_k, \mu_k)$. The effective particle number n of a saturated tank represents a lower limit of the actual signal and we have to integrate f_G over all possible values larger than n , to estimate the detecting probability of a signal larger than n . In case of tanks without a signal we have to sum over all Poissonian probabilities with a predicted particle number μ_i and actual effective particle number $n_i \leq 3$.

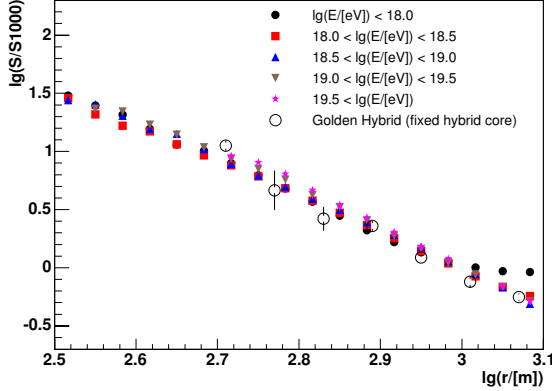


Figure 1. Averaged LDF for $\sec \theta \in [1.2, 1.4]$ (NKG fit and floating slope).

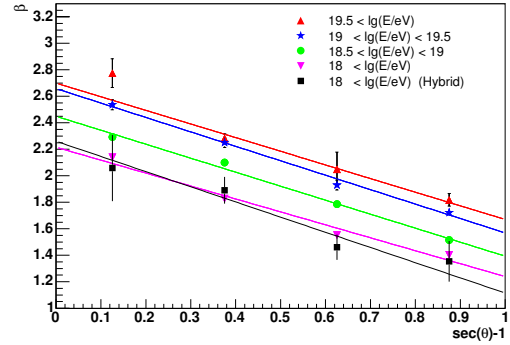


Figure 2. Slope β vs zenith angle as function of energy for SD-only or hybrid geometry. Fits to the slope parameter for different energy bins are shown

3. LDF Measurements

In contrast to $S(1000)$ the shape of the lateral distribution does not change much with energy [8]. Therefore, the normalisation constant is decoupled from the shape parameter and showers of different energies are combined. The LDF was deduced from experimental data using SD-only and Hybrid events. Data from January 2004 to April 2005 have been used for the following analysis. High-quality events have been selected, which had a successful directional reconstruction with $\theta < 60^\circ$, at least 6 stations with signal above detection threshold, and a core position well inside the SD array. Using SD-only events the following LDFs have been investigated: (i) a power law: $S(r) = S(1000) \cdot (r/1000 \text{ m})^{-\nu}$, with a θ dependent index $\nu = a + b(\sec \theta - 1)$, (ii) a NKG-like function [6]: $S(r) = A \cdot [(r/r_s) \cdot (1 + r/r_s)]^{-\beta}$ with $A = S(1000) \cdot 3.47^\beta$, $\beta = a + b(\sec \theta - 1)$ and $r_s = 700 \text{ m}$ (since β and r_s are strongly correlated, we have fixed $r_s = 700 \text{ m}$ and left β to vary), and (iii) a function used by the Haverah Park experiment [3]: $S(r) = k r^{-(\eta+r/r_s)}$, if $r < 800 \text{ m}$, else $(\frac{1}{800})^\delta k r^{-(\eta+r/r_s)+\delta}$ with fixed δ , the shape parameter η varying with zenith angle, and $r_s = 4000 \text{ m}$. These forms were fitted to individual events using a maximum likelihood fit of core location and LDF at the same time (see section 2). Two SD-only analyses were performed. First, in a four-parameter fit, besides the core location x and y , the slope parameters ν , β and η , respectively, have been varied together with the scale factor $S(1000)$. Then a parameterisation of ν , β and η as function of θ was determined, which was then used in a second analysis fitting only x , y , and $S(1000)$. Figure 1 shows the averaged LDF for $\sec \theta \in [1.2, 1.4]$ when the NKG assumption is used. For comparison a hybrid derived average LDF is shown too (see below for details). An energy dependent threshold effect is apparent at large radii

sec θ range	number of events		NKG						power law				Haverah Park			
	hy	sd	β free (hy)		β free (sd)		β fixed (sd)		ν free		ν fixed		η free		η fixed	
			m	σ	m	σ	m	σ	m	σ	m	σ	m	σ	m	σ
[1.0, 1.2]	5	367	0.27	2.12	0.04	0.48	-0.07	1.45	-0.03	0.55	-0.07	1.45	-0.17	1.27	-0.21	1.0
[1.2, 1.4]	14	549	-0.18	1.71	0.06	0.53	-0.04	1.30	-0.27	0.81	-0.04	1.30	-0.03	0.95	0.14	1.2
[1.4, 1.6]	17	624	-0.07	2.00	0.07	0.55	0.04	1.02	-0.12	0.65	0.05	1.02	-0.09	1.04	0.03	1.6
[1.6, 1.8]	8	576	-0.04	1.40	0.09	0.59	-0.07	0.80	-0.07	0.81	-0.14	0.92	0.01	1.27	0.23	1.4
[1.8, 2.0]	6	493	-0.26	1.34	0.11	0.61	-0.11	0.98	-0.11	0.98	-0.21	1.15	-0.21	1.28	-0.24	1.9

Table 1. Moments (mean, σ) of residual distribution of exp. data with various LDFs. Only events with ≥ 6 stations were used in the present analysis. For the NKG-like LDF both SD and Hybrid moments are shown, denoted by “sd” and “hy” respectively.

and reflects upward fluctuations of signals close to the trigger threshold of single tanks. In case of this NKG-like function with a free slope parameter, β , the fit results for $E > 10^{18}$ eV are given in Table 2. The energy dependence of β is shown in Figure 2 and described by $\beta(E) = a(E) + b(\sec \theta - 1)$, with $a(E) = 2.26 + 0.195 \log_{10}(E/\text{EeV})$ and $b = -0.98$. To quantify the quality of the fits the residuals, $(S - S_{\text{th}})/\sigma_{\text{th}}$, and their distributions are computed. For a good LDF the residuals should scatter symmetrically around 0 with $\sigma = 1$. Means and standard deviations of the residual distribution are used to compare different LDFs and are given in Table 1. For simplicity only residuals up to 1500m are taken into account, resulting in a variance smaller than the expectation value of 1 to avoid systematic biases of upward fluctuating signals. The NKG-like function fits the data best, which can be seen from the smallest mean residuals and the smallest residual variances.

Complementarily to the SD analysis, a hybrid LDF analysis was performed. The hybrid reconstruction exploits the independent knowledge of the core position to determine the shower axis geometry and distance from each detector to the shower core. A maximum likelihood fit (section 2) is used to determine only $S(1000)$ and the LDF slope parameter (β). A NKG-like function was studied in the hybrid analysis.

Hybrid triggers usually include a relatively large number of accidental stations, which in the case of low multiplicity events could even outnumber the number of stations that are part of the event making the identification of accidentals and candidate stations a difficult task. Therefore, strict quality cuts were imposed and only events with at least 6 triggered stations were included in the analysis. That reduces the sample size, but at the same time, selecting events with a large number of active stations, prevents biasing the LDF slope due to signal fluctuations. Moreover, as the quality cuts imposed on the hybrid analysis are similar to those used on the SD-only analysis the comparison is straightforward. Figure 2 shows also how β varies with θ for hybrid events. Despite the limited statistics of the hybrid sample the agreement between SD and Hybrid is encouraging. The Hybrid data sub-sample is not large enough as to accurately quantify the dependence of β with energy at the time of writing.

	SD	Hybrid
Intercept a	2.24 ± 0.01	2.26 ± 0.17
Slope b	-0.98 ± 0.02	-1.1 ± 0.3

Table 2. Comparison between SD and Hybrid analysis on the parameterisation of the LDF slope (NKG-like function; $E > 10^{18}$ eV).

4. Uncertainty in $S(1000)$

High statistics are required to accurately describe the LDF, both to reduce the statistical and systematic uncertainties. Hybrid measurements (though with much reduced statistics) are a useful tool to help identify sources of systematic uncertainty, and it is certain that, as the Auger exposure increases, the functional form of the LDF will evolve and become increasingly accurate. Increasing accuracy will lead to much smaller uncertainties in the reconstructed core position, but the ground parameter, $S(1000)$ which is used to determine the energy of the primary CR, is very robust to inaccuracies in the LDF. It can be shown that by measuring $S(r)$ at 1000 m, fluctuations in the ground parameter due to a lack of knowledge of the LDF are minimised. The result of analysing one SD event many times, whilst allowing the slope parameter to vary by $\pm 8\%$ is shown in figure 3. This was chosen as a reasonable value for the magnitude of the shower-to-shower fluctuations, based on measurements made at Haverah Park where the precision was sufficient to measure intrinsic shower-to-shower fluctuations [4]. Analysing the shower with different assumed values for the slope parameter, results in a shift in the reconstructed core position, but by choosing to measure the ground parameter $S(r)$ at the point where the LDFs intersect, (at ~ 1000 m), the effect of the changing slope parameter is minimised. At this point the ground parameter is independent of the LDF. Analysing many showers in this way shows that r_{opt} , the optimum ground

parameter has very little dependence on zenith angle, energy, or the form of the LDF used to reconstruct the showers. For example, an analysis of ~ 500 Auger SD events with energies $10^{18.5}$ eV $< E < 10^{19}$ eV and zenith angles $0^\circ < \theta < 60^\circ$ gives a distribution of r_{opt} with mean 940 m and a rms of 110 m. An analysis of simulated events at 10^{20} eV gives a mean of 930 m and a rms deviation of 40 m. The presence of a saturated station (predominantly in vertical, high energy events) tends to push r_{opt} out by several hundred metres, and after an analysis of many showers, at different zenith angle and energy, $S(1000)$ was chosen as a robust ground parameter to measure all showers at. At 1000 m from the core the mean uncertainty in $S(r)$ (across all events) is minimised, and furthermore, for the few showers where r_{opt} lies far from 1000 m, the uncertainty in $S(1000)$ can easily be estimated.

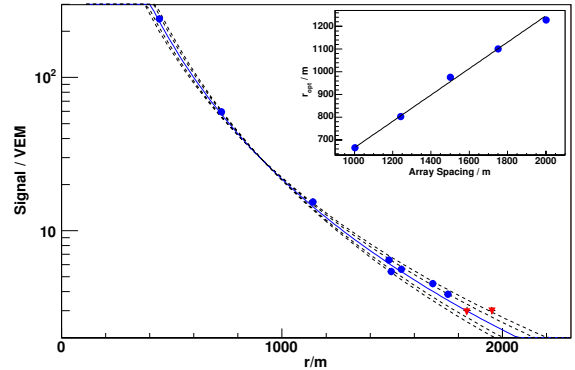


Figure 3. LDFs of an Auger SD event, analysed with different slope parameters. Red points indicate stations with zero signal. The inset shows how the optimum ground parameter r_{opt} varies with the array spacing.

5. Summary and Outlook

The lateral distribution function of EAS observed using the Auger Observatory has been derived. Different functions have been tested and it is concluded that an NKG-like LDF describes the data well. The dependence of the function on atmospheric depth has been described. It should be emphasized that the global shower observables, like the lateral distribution of particles, are not affected by the geomagnetic field for zenith angles $\theta < 70^\circ$. However, for the case of very inclined showers which are dominated by muons, the density at ground is rendered quite asymmetric by the geomagnetic field and the LDF approach is not longer valid [2, 7].

References

- [1] Abraham J. et al., (Auger Collaboration), Nucl. Instr. Meth. A 523 (2004) 50-95
- [2] Ave M. et al., Astropart. Phys. 14 (2000) 91
- [3] Coy R.N. et al., Astropart. Phys. 6 (1997) 263
- [4] Coy R.N. et al., Proc. 17th ICRC, Paris (1981) vol.6.
- [5] Ghia P. et al. for the Auger Collaboration, these proceedings (ita-ghia-P-abs1-he14-oral)
- [6] Greisen K, Progress in Cosmic Ray Physics 3 (1956) North Holland Publ.
Kamata K and Nishimura J. Prog. Theoret. Phys. Suppl. 6 (1958) 93
- [7] Hillas A.M. et al., Proc. 11th ICRC, Budapest (1969), Acta Physica Academiae Scientiarum Hungaricae 29, Suppl. 3, (1970) 533
- [8] Roth M. for the Auger Collaboration, Proc. 28th ICRC, Tsukuba (2003) 333.
- [9] Salazar H. for the Auger Collaboration, Proc. 27th ICRC, Hamburg (2001) 752.

The Offline Software Framework of the Pierre Auger Observatory

S. Argirò, S.L.C. Barroso, S. Dagoret-Campagne, J. Gonzalez, L. Nellen, T. Paul,
T. Porter, L. Prado Jr., M. Roth, R. Ulrich and D. Veberič
for the Pierre Auger Collaboration

Presenter: T. Paul (tom.paul@cern.ch), usa-paul-T-abs1-he15-poster

The Pierre Auger Observatory is designed to unveil the nature and origin of the highest energy cosmic rays through the analysis of extensive air showers. The large and geographically dispersed collaboration of physicists and the wide-ranging collection of simulation and reconstruction tasks pose some special challenges for the offline analysis software. We have designed and implemented a general purpose framework which allows Auger collaborators to contribute algorithms and configuration instructions to build up the variety of applications they require. The framework includes machinery to manage these user codes, to organise the abundance of user-contributed configuration files, to facilitate multi-format file handling, and to provide access to event and time-dependent detector information residing in many data sources. A number of utilities are also provided, including a novel geometry package allowing manipulation of abstract geometrical objects independent of coordinate system choice. The framework is implemented in C++ and takes advantage of object oriented design and common open source tools, while keeping the user-side simple enough for C++ novices to learn in a reasonable time. The distribution system incorporates unit and acceptance testing in order to support rapid development of both the core framework and the contributed user codes.

1. Introduction

The offline software framework of the Pierre Auger Observatory provides machinery to support simulation, reconstruction and analysis work carried out by members of the collaboration. The requirements of the experiment place rather strong demands on this software. Most importantly, the framework must be flexible and robust enough to support the collaborative effort of a large number of physicists developing a variety of applications over a 20 year experimental run. It must also handle a number of data formats in order to deal with event and monitoring information as well as the output of air shower simulation codes. Additionally it is desirable to ensure that all physics code is “exposed” in the sense that any user must be able to replace existing algorithms with his own in a straightforward manner. Furthermore, while the underlying framework may exploit the full power of C++ and object-oriented design, the portions of the code directly used by physicists should not assume a particularly detailed knowledge of C++.

The offline framework was designed with these principles in mind. Implementation of the code has taken place over the last two years, and it is now being employed in analysis of data gathered by the observatory.

2. Design overview

The offline framework comprises three principal parts: a collection of processing *modules* which can be assembled and sequenced through instructions provided in an XML file, an *event* structure through which modules can relay data to one another and which accumulates all simulation and reconstruction information, and a *detector description* which provides a gateway to data describing the configuration and performance of the observatory as well as atmospheric conditions as a function of time. These principal ingredients are depicted in Figure 1.

2.1 User code, configuration, and run control

Experience has shown that most tasks of interest to the Pierre Auger Collaboration naturally break down into sequences of well-defined processing steps. Physicists prepare such processing algorithms in so-called modules, which they can insert into the framework by adding a registration macro to their code. This modular design allows collaborators to easily exchange code, compare algorithms and build up a wide variety of applications by combining modules in various sequences.

Run-time control over module sequences is afforded through a *run controller* which invokes the various processing steps according to instructions provided in a sequencing file. We have chosen to use XML [1] to write the sequencing files as it is very easy to learn, yet grammatically rich enough to allow sequencing instruction that have enough detail to accommodate most analysis applications.

Cuts, parameters and configuration instructions used by modules or by the framework itself are also stored in XML files. A central directory points modules to their configuration file(s) by pathname or URL and creates parsers to assist in reading information from these files. The configuration mechanism can also concatenate and store all configuration files accessed during a run. This allows the creation of subsequent runs using the exact configuration employed in the original run. To check configuration files for errors we exploit schema [2] validation, in which an auxiliary XML file is provided which defines a set of rules that must be obeyed by the configuration file. This saves a considerable amount of coding, since users do not have to write error checking code themselves. Furthermore, XML schema allows users to easily effect much more detailed checking than they are likely to implement on their own.

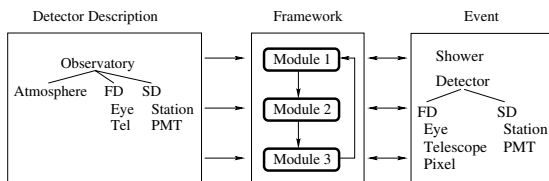


Figure 1. Simulation and reconstruction tasks are broken down into modules. Each module is able to read information from the detector description and/or the event, process the information, and write the results back into the event.

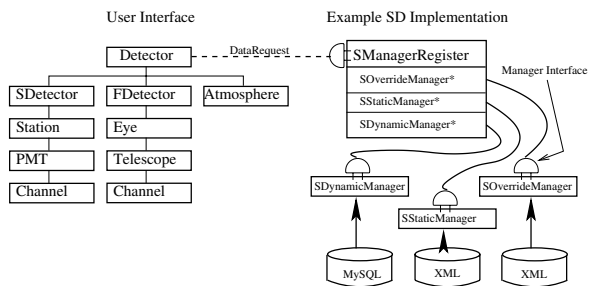


Figure 2. Machinery of the detector description. The user interface (left) relays requests for data to a registry of managers (right) which handle multiple data sources.

2.2 Event Description

The *event* data structure contains all raw, calibrated, reconstructed and Monte Carlo data and acts as the principal backbone for communication between modules. The event structure is built up dynamically as needed, and is instrumented with functions allowing modules to interrogate the event at any point to discover its current constituents.

The event representation in memory is decoupled from the representation on disk. This design choice is intended to allow one to change the underlying serialization mechanism, which maps complex objects in memory onto flat files on disk. It is prudent to maintain a design in which serialization technology can be changed without affecting existing code, as a standard serialization mechanism could be introduced into the C++ language in the future [3]. Currently, serialization is implemented using the ROOT [4] toolkit.

A set of simple-to-use input/output utilities allow users to transfer part or all of the event from memory to a file at any stage in the processing, and to reload the event to continue processing from that point onward. These utilities also support the multi-format reading and writing required to deal with different event and monitoring formats as well as the formats used by the AIRES [5], CONEX [6] and CORSIKA [7] air shower simulation packages.

2.3 Detector Description

The *detector description* provides an intuitive interface from which module authors may retrieve information about the detector configuration and performance. The interface is organized following the hierarchy normally associated with the observatory instruments. Requests for data are passed by this interface to a registry of so-called *managers*, each of which is capable of extracting a particular sort of information from a particular data source. In this way, the user sees only a single interface even though the data sought may reside in any number of different sources. Generally, we choose to store static detector information in XML files, and time-varying monitoring and calibration data in MySQL [8] databases. The structure of the detector description machinery is illustrated in Figure 2.

Note that it is possible to implement more than one manager for a particular sort of data. In this way, a special manager can override data from a general manager. For example, a user can decide to use a database for the majority of the description of the detector, but override some data by writing them in an XML file which is read by the special manager. The specification of which data sources are accessed by the manager registry and in what order they are queried is detailed in a configuration file. The configuration of the manager registry is transparent to the user code.

2.4 Utilities

The offline framework is built on a collection of utilities, including a XERCES-based [9] XML parser, an error logger, and a set foundation classes to represent objects such as signal traces, tabulated functions and particles. The utilities collection also provides a geometry package in which objects such as vectors and points keep track of the coordinate systems in which they are represented. This allows for abstract manipulation of these objects, as any coordinate transformations which may be required in an operation between objects are performed automatically. The geometry package also includes support for geodetic coordinates.

2.5 Maintainability and External Packages

To help ensure code maintainability and stability in the face of a large number of contributors and a long experimental run, unit and acceptance testing are integrated into the offline framework build and distribution system. This sort of quality assurance mechanism is crucial for any software which must continue to grow and develop over a timescale of years.

Our build system is based on the GNU autotools [10], which provide hooks for integrating tests with the build and distribution system. A substantial collection of unit tests has been developed, each of which is designed to comprehensively test a single framework component. These unit tests are run at regular intervals and in particular prior to releasing a new version of the software. We have employed the CppUnit [11] testing framework as an aid in implementing these unit tests. We are currently in the process of developing more involved acceptance tests which will be used to verify that modules and framework components working in concert continue to function properly during ongoing development.

The choice of external packages upon which to build the offline framework was dictated not only by package features, support, and the requirement of being open-source, but also by our best assessment of prospects for longevity.

3. Summary

We have implemented an offline software framework for the Pierre Auger Observatory. It provides machinery to help collaborators work together on data analysis problems, compare results, and carry out production runs of large quantities of simulated or real data. The framework is configurable enough to adapt to a diverse set of applications, while the user side remains simple enough for C++ non-experts to learn in a reasonable time. The modular design allows straightforward swapping of algorithms for quick comparisons of different approaches to a problem. The interfaces to detector and event information free the users from having to deal individually with multiple data formats and data sources. This software, while still undergoing vigorous development and improvement, is now being used in analysis of data gathered by the Pierre Auger Observatory. We believe our approach and general system design may be applicable to other experiments involving large collaborations and detectors of similar complexity.

References

- [1] <http://www.w3.org/XML>
- [2] <http://www.w3.org/XML/Schema>
- [3] see for example <http://www.boost.org>
- [4] <http://root.cern.ch>
- [5] S. Sciutto, AIREs User's Manual and Reference Guide,
<http://www.fisica.unlp.edu.ar/auger/aires>
- [6] T. Pierog *et al.*, to appear in proceedings of 13th International Symposium on Very High-Energy Cosmic Ray Interactions at the NESTOR Institute, Pylos, Greece, 6-12 Sep 2004, [arXiv:astro-ph/0411260].
- [7] D. Heck, J. Knapp, J.N. Capdevielle, G. Schatz, T. Thouw, Report FZKA 6019 (1998).
- [8] <http://dev.mysql.com>
- [9] <http://xml.apache.org/xerces-c>
- [10] <http://www.gnu.org/software/autoconf>
<http://www.gnu.org/software/automake>
<http://www.gnu.org/software/libtool>
- [11] <http://cppunit.sourceforge.net/doc/1.8.0>

Derivation of upper limit on the photon fraction using the highest-energy AGASA cosmic rays

M. Risse^{a,b}, P. Homola^b, R. Engel^a, D. Góra^b, D. Heck^a,
J. Pękala^b, B. Wilczyńska^b, and H. Wilczyński^b

(a) Forschungszentrum Karlsruhe, Institut für Kernphysik, 76021 Karlsruhe, Germany

(b) Institute of Nuclear Physics, Polish Academy of Sciences, ul. Radzikowskiego 152, 31-342 Kraków, Poland

Presenter: M. Risse (markus.risse@ik.fzk.de), ger-risse-M-abs1-he14-poster

A new method to derive an upper limit on photon primaries for small data sets of air showers is described which accounts for shower properties varying with the primary energy and arrival direction. Applying this method to the highest-energy AGASA data, an upper limit on the photon fraction of 51% (67%) at a confidence level of 90% (95%) for primary energies above $1.25 \cdot 10^{20}$ eV is derived.

1. Introduction

Robust experimental limits on the cosmic-ray photon component might be a key to distinguish between theoretical source models for the highest-energy cosmic rays. In particular, some non-acceleration models, usually fitted to the AGASA data at the high-energy end of the spectrum, predict photon dominance above 10^{20} eV [1]. We compare the muon densities measured in AGASA events $> 10^{20}$ eV to simulations of air showers induced by photons, taking photon conversion in the geomagnetic field into account.

To statistically quantify the level of agreement between the primary photon fraction predicted by a model and the observed air shower data, a method is required that accounts for (i) event-by-event fluctuations in the considered shower observable (here: the muon density) for fixed primary parameters (ii) a possible change of average shower properties for the different events in the data sample (e.g. different photon conversion probabilities depending on the direction of the observed event) (iii) the limited event statistics (which is unavoidable at the high-energy end of the cosmic-ray spectrum).

We describe such a method that allows one to test the contribution of photon primaries or any other particle type to cosmic rays and to possibly set an upper limit on the primary fraction with well-defined confidence level. Since only a limit on the primary *fraction* is placed, this method does not rely on a knowledge of the absolute cosmic-ray flux. Moreover, no potential signal background from other primary particle types has to be considered, as only the rejection power to photons is quantified: Any photon-like contributions from other primaries would just weaken the rejection power to photons and increase the numerical value of the derived upper limit. As a consequence, this analysis of photon primaries is also less severely affected by uncertainties from hadronic interaction models usually present in cosmic-ray composition studies.

Applying the new method to AGASA data allows us to exclude photon dominance at highest cosmic-ray energies at 90% confidence level. Thus, it is difficult to obtain a consistent description of the AGASA high-energy data in certain non-acceleration models which, therefore, are disfavoured as the sole explanation for the highest-energy cosmic rays.

A detailed description of the new method and the analysis is given in [2]. In the following, we provide a brief summary with the focus put on the statistical method.

2. Data and simulation

AGASA [3] consisted of 111 array detectors spread over $\simeq 100 \text{ km}^2$ area and 27 muon detectors with an energy threshold of 0.5 GeV for vertically incident muons. The primary energy was determined from the array data with a statistical accuracy of $\simeq 25\%$ for hadron primaries [4]. Assuming photon primaries, the energies reconstructed this way were found to be underestimated by $\simeq 20\%$ for the most-energetic events [3]. Six events were reconstructed with $> 100 \text{ EeV}$ which had more than one muon detector within 800-1600 m distance from the shower core [3]. The muon density ρ_j at 1000 m core distance was obtained for each event $j=1 \dots 6$ with an uncertainty of 40% [3]. The shower parameters of these events are given in Tab. 1.

Electromagnetic cascading of photons in the geomagnetic field is simulated for the AGASA site with the new PRESHOWER code [5]. The atmospheric shower is simulated with CORSIKA 6.18 [6] as a superposition of subshowers initiated by the preshower particles or, if no preshower occurred, with the original primary photon. Electromagnetic interactions are treated by the EGS4 code [7], which was upgraded [6] to take photonuclear reactions as well as the Landau-Pomeranchuk-Migdal (LPM) effect [8] into account. For the photonuclear cross-section, the Particle Data Group extrapolation is chosen [9]. The influence when using different extrapolations is discussed in [2]. Hadronic interactions are simulated with QGSJET 01 [10].

3. Method and Results

In contrast to previous approaches, the information about individual event topologies is used in the new method. For each AGASA event, 100 primary photon showers are generated. The reconstructed primary parameters [4] are adopted as simulation input, taking for the primary energy the statistical experimental resolution and the systematic underestimation in case of photon primaries into account. The distribution ρ_j^s of simulated muon densities obtained from CORSIKA for each AGASA event is compared in Fig. 1 to the data. The average values $\langle \rho_j^s \rangle$ and standard deviations $\Delta \rho_j^s$ are listed in Tab. 1. The average muon densities for primary photons are a factor 2-7 below the data. Qualitatively, a photon origin of most of the observed events is disfavoured.

To assess the agreement of data and photon expectation, a χ_j^2 value is calculated for each event j as

$$\chi_j^2 = \frac{(\rho_j - \langle \rho_j^s \rangle)^2}{(\Delta \rho_j)^2 + (\Delta \rho_j^s)^2} \quad (1)$$

with $\Delta \rho_j$ being the measurement uncertainty, $\Delta \rho_j = 0.4 \cdot \rho_j$ [3]. To account for possible deviations of the simulated muon densities from a Gaussian distribution, the probability $p_j(\chi^2 \geq \chi_j^2)$ of a photon-initiated shower

Table 1. Reconstructed shower parameters of the AGASA events [3] (upper part of the Table) and simulation results (lower part). The energies are increased by 20% to account for the case of photon primaries [3]. The azimuth angle is given clockwise from north for the incoming direction.

primary energy [EeV]	295	240	173	161	126	125
zenith angle [°]	37	23	14	35	33	37
azimuth angle [°]	260	236	211	55	108	279
ρ_j [m^{-2}]	8.9	10.7	8.7	5.9	12.6	9.3
preshower occurrence [%]	100	100	96	100	93	100
$\langle \rho_j^s \rangle$ [m^{-2}]	4.3	3.1	2.1	2.3	1.7	1.8
$\Delta \rho_j^s$ [m^{-2}]	1.1	1.0	0.9	0.6	0.5	0.5
χ_j^2	1.6	3.0	3.4	2.2	4.6	4.0
p_j [%]	20.8	8.3	6.4	13.9	3.1	4.6

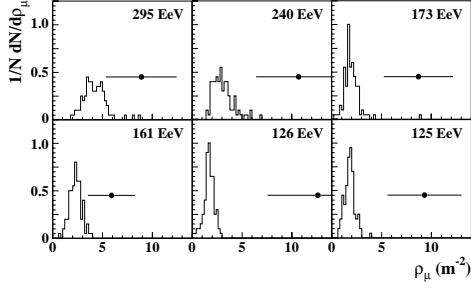


Figure 1. Observed muon densities (points with error bars) compared to the muon densities expected for primary photons (histograms) for the six events. Assigned to each event the primary energy (see Tab. 1). The measured values are above the predictions from primary photon simulations.

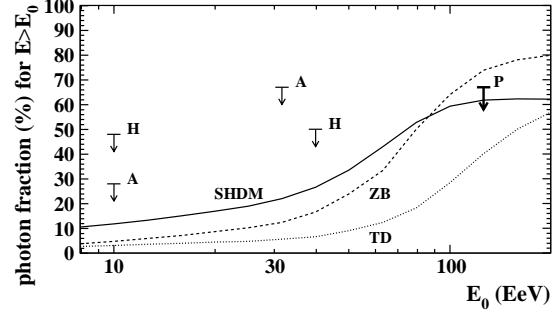


Figure 2. Upper limits on photon fraction (95% CL) from the present analysis (P) and previously from AGASA (A) [3] and Haverah Park (H) [11] compared to some predictions based on super-heavy dark matter (SHDM) [12], Z-bursts (ZB) and topological defect (TD) [13] models.

to yield a value $\chi^2 \geq \chi_j^2$ is determined by a Monte Carlo technique: A simulated muon density value is taken at random from the distribution ρ_j^s , a random shift is performed according to the experimental resolution $\Delta\rho_j$, and a χ^2 value is calculated with Eq. (1), replacing ρ_j by the artificial muon density value. Repeating this many times then gives $p_j(\chi^2 \geq \chi_j^2)$. The values χ_j^2 and p_j are listed for the six events in Tab. 1. The probabilities p_j range from 3% to 21%.

Correspondingly, the probability $p(\chi^2 \geq \sum_{j=1}^6 \chi_j^2)$ of six photon-initiated events to yield a χ^2 value larger or equal to the measured one can be determined as $p = 0.5\%$. Thus, it is unlikely that all cosmic rays at these energies are photons (rejection with 99.5% confidence). An upper limit on the photon fraction F_γ can be set.

It should be noted that, due to the small event statistics, the upper limit cannot be smaller than a certain value. Assuming a fraction F_γ of photons in the primary flux, a set of n_m primaries picked at random is expected to *ab initio* contain no primary photon with probability $(1 - F_\gamma)^{n_m}$. For $n_m=6$, this probability is $\simeq 5\%$ for $F_\gamma=40\%$. Thus, in the present case only hypothetical photon fractions $F_\gamma \geq 40\%$ could in principle be tested at a confidence level $\alpha = 95\%$. In general, the relation between the minimum possible fraction F_γ^{\min} that could be excluded for a given event number n_m (or in turn: the minimum event number n_m^{\min} required to possibly exclude a certain fraction F_γ) is given by

$$F_\gamma^{\min} = 1 - (1 - \alpha)^{1/n_m}, \text{ and } n_m^{\min} = \frac{\ln(1 - \alpha)}{\ln(1 - F_\gamma)}. \quad (2)$$

with α being the confidence level of rejection. This theoretical limit is reached only if for each event j , the observations allowed us to exclude a photon origin ($p_j \rightarrow 0$). Some numerical examples are listed in Tab. 2.

For deriving an upper limit $F_\gamma^{\text{ul}} < 100\%$, scenarios have to be tested in which $n_\gamma=0 \dots n_m$ showers out of n_m events might be initiated by photons. For a hypothetical photon fraction F_γ , the probability q that a set of n_m

Table 2. Numerical examples for minimum fraction $F_\gamma^{\min}(n_m)$ that could be excluded with n_m events (or: minimum number of events $n_m^{\min}(F_\gamma)$ required to exclude fraction F_γ) for a confidence level $\alpha = 95\%$.

6 ev \leftrightarrow 39.3%	10 ev \leftrightarrow 25.9%	30 ev \leftrightarrow 9.5%	100 ev \leftrightarrow 3.0%	300 ev \leftrightarrow 1.0%	1000 ev \leftrightarrow 0.3%
------------------------------	-------------------------------	------------------------------	-------------------------------	-------------------------------	--------------------------------

events contains n_γ photons is $q(F_\gamma, n_\gamma, n_m) = F_\gamma^{n_\gamma} (1 - F_\gamma)^{n_m - n_\gamma} \binom{n_m}{n_\gamma}$. This probability is multiplied by the probabilities $p_\gamma(n_\gamma) \cdot p_{\bar{\gamma}}(n_m - n_\gamma)$, with $p_\gamma(n_\gamma)$ being the probability that the n_γ most photon-like looking events are generated by photons, and $p_{\bar{\gamma}}(n_m - n_\gamma)$ being the probability that the remaining $n_m - n_\gamma$ events are due to non-photon primaries. $p_\gamma(n_\gamma)$ is determined by the MC technique as the probability to obtain values $\chi^2 \geq \sum_{i=1}^{n_\gamma} \chi_{k_i}^2$, with $p_\gamma(0)=1$ and with $\chi_{k_i}^2 = \chi_j^2$ from Tab. 1, where index k_1 refers to the event with smallest value χ_j^2 , and $\chi_{k_i}^2 \leq \chi_{k_{i+1}}^2$. To derive an upper limit on photons, the probabilities $p_{\bar{\gamma}}(n_m - n_\gamma)$ are set to unity. Summing over all possibilities $n_\gamma=0 \dots n_m$ then gives the probability $P(F_\gamma)$ to obtain χ^2 values at least as large as found in the data set,

$$P(F_\gamma) = \sum_{n_\gamma=0}^{n_m} q(F_\gamma, n_\gamma, n_m) \cdot p_\gamma(n_\gamma) \cdot p_{\bar{\gamma}}(n_m - n_\gamma). \quad (3)$$

This probability depends on the assumed photon fraction F_γ . For the considered AGASA data set one obtains $P(F_\gamma=51\%) = 10\%$ and $P(F_\gamma=67\%) = 5\%$. Therefore, the upper limit on the primary photon fraction is $F_\gamma^{\text{ul}} = 51\%$ (67%) at 90% (95%) CL. The derived bound is the first limit on the photon contribution above the GZK cutoff energy. The limit refers to the photon fraction integrated above the primary photon energy that corresponds to the lowest-energy event in the data sample, which in the present analysis is 125 EeV.

In Fig. 2, upper limits derived previously at lower energy and the current bound are compared to some predictions based on non-acceleration models. Models predicting photon dominance at highest energies are disfavoured by the presented upper limit.

The new method can easily be applied also to data from other air shower experiments, see e.g. [14].

Acknowledgments. We are grateful to K. Shinozaki for helpful discussions about the AGASA data. This work was partially supported by the Polish State Committee for Scientific Research under grants No. PBZ KBN 054/P03/2001 and 2P03B 11024 and in Germany by the DAAD under grant No. PPP 323.

References

- [1] P. Bhattacharjee, G. Sigl, Phys. Rep. **327**, 109 (2000).
- [2] M. Risse *et al.*, astro-ph/0502418 (2005).
- [3] K. Shinozaki *et al.*, Astrophys. J. **571**, L117 (2002).
- [4] M. Takeda *et al.*, Astropart. Phys. **19**, 447 (2003); N. Hayashida *et al.*, astro-ph/0008102 (2000); M. Takeda *et al.*, Astrophys. J. **522**, 225 (1999); <http://www-akeno.icrr.u-tokyo.ac.jp/AGASA>
- [5] P. Homola *et al.*, astro-ph/0311442 (2003).
- [6] D. Heck *et al.*, Reports **FZKA 6019** and **FZKA 6097**, Forschungszentrum Karlsruhe (1998).
- [7] W.R. Nelson, H. Hirayama, D.W.O. Rogers, Report **SLAC 265**, Stanford Linear Accel. Center (1985).
- [8] L.D. Landau, I.Ya. Pomeranchuk, Dokl. Akad. Nauk SSSR **92**, 535 & 735 (1953) (in Russian); A.B. Migdal, Phys. Rev. **103**, 1811 (1956).
- [9] S. Eidelmann *et al.*, Particle Data Group, Phys. Lett. **B592**, 1 (2004).
- [10] N.N. Kalmykov, S.S. Ostapchenko, A.I. Pavlov, Nucl. Phys. B (Proc. Suppl.) **52**, 17 (1997).
- [11] M. Ave *et al.*, Phys. Rev. Lett. **85**, 2244 (2000); M. Ave *et al.*, Phys. Rev. **D65**, 063007 (2002).
- [12] R. Aloisio, V. Berezhinsky, M. Kachelrieß, Phys. Rev. **D69**, 094023 (2004).
- [13] G. Sigl, hep-ph/0109202 (2001).
- [14] Pierre Auger Collaboration, "Upper limit on the primary photon fraction from the Pierre Auger Observatory", these proceedings.

Contributions of the Pierre Auger Collaboration (abstracts only)

Performance of the Pierre Auger Observatory Surface Array

X. Bertou for the Pierre Auger Collaboration

Presenter: X. Bertou (bertou@auger.org.ar), arg-bertou-X-abs1-he14-oral

The surface detector of the Pierre Auger Observatory is a 1600 water Cherenkov tank array on triangular 1.5km grid. The signals from each tank are read out using three 9. photomultipliers and processed at a sampling frequency of 40 MHz, from which a local digital trigger efficiently selects shower candidates. GPS signals are used for time synchronization and a wireless communication system connects all tanks to the central data acquisition system. Power is provided by a stand-alone solar panel system. With large ambient temperature variations, that can reach over 20 degrees in 24 hours, high salinity, dusty air, high humidity inside the tank, and remoteness of access, the performance and reliability of the array is a challenge. Several key parameters are constantly monitored to ensure consistent operation. The Surface Array has currently over 750 detectors and has been in reliable operation since January 2004. Good uniformity in the response of different detectors and good long term stability is observed.

Performance of the Fluorescence Detectors of the Pierre Auger Observatory

The Pierre Auger Collaboration

Av. San Martin Norte 304, (5613) Malargüe, Argentina

Presenter: J. A. Bellido (jbellido@physics.adelaide.edu.au), aus-bellido-J-abs1-he14-oral

Fluorescence detectors of the Pierre Auger Observatory have been operating in a stable manner since January 2004. After a brief review of the physical characteristics of the detectors, the associated atmospheric monitoring, the calibration infrastructure and the detector aperture, we will describe the steps required for the reconstruction of fluorescence event data, with emphasis on the shower profile parameters and primary energy.

The Hybrid Performance of the Pierre Auger Observatory

Pierre Auger Collaboration

Observatorio Pierre Auger, Av. San Martin Norte 304, Malargüe, (5613) Mendoza, Argentina

Presenter: Miguel A. Mostafá (mostafa@phys.unm.edu), usa-mostafa-M-abs1-he14-oral

The Pierre Auger Observatory detects ultra-high energy cosmic rays by implementing two complementary airshower techniques. The combination of a large ground array and fluorescence detectors, known as the *hybrid* concept, means that a rich variety of measurements can be made on a single shower, providing much improved information over what is possible with either detector alone. In this paper the hybrid reconstruction approach and its performance are described.

Statistical and systematic uncertainties in the event reconstruction and S(1000) determination by the Pierre Auger surface detector

Pierre Auger Collaboration

Pierre Auger Observatory, Av. San Martin Norte 304, (5613), Malargüe, Argentina

Presenter: Piera L. Ghia (piera.ghia@lngs.infn.it) ita-ghia-P-abs1-he14-oral

We discuss the statistical and systematic uncertainties in the event reconstruction (core location, and determination of S(1000), i.e., the signal at a distance of 1000 m from the shower core) by the Pierre Auger surface detector for showers with zenith angle less than 60 degrees. The method is based on a maximum likelihood method where the reference lateral distribution function is obtained through the experimental data. We also discuss S(1000) as primary energy estimator.

First Estimate of the Primary Cosmic Ray Energy Spectrum above 3 EeV from the Pierre Auger Observatory

P. Sommers for the Pierre Auger Collaboration

Presenter: P. Sommers (sommers@physics.utah.edu),usa-sommers-P-abs1-he14-oral

Measurements of air showers are accumulating at an increasing rate while construction proceeds at the Pierre Auger Observatory. Although the southern site is only half complete, the cumulative exposure is already similar to those achieved by the largest forerunner experiments. A measurement of the cosmic ray energy spectrum in the southern sky is reported here. The methods are simple and robust, exploiting the combination of fluorescence detector (FD) and surface detector (SD). The methods do not rely on detailed numerical simulation or any assumption about the chemical composition.

A description of some ultra high energy cosmic rays observed with the Pierre Auger Observatory

J. Matthews for the Pierre Auger Collaboration

Presenter: J. Matthews (matthews@phys.lsu.edu) usa-matthews-James-abs2-he14-oral

A discussion is given of the highest energy events so far recorded by the Pierre Auger Observatory. We present these to illustrate the quality of the information that they contain. The surface detectors are used to measure a rich set of parameters that will eventually help characterise the mass of the incoming primary particle.

Detection of Very Inclined Showers with the Auger Observatory

L. Nellen for the Pierre Auger Collaboration

Observatorio Pierre Auger, Av. San Martin Norte 304, (5613) Malargüe, Argentina

Presenter: Lukas Nellen (lukas@nucleares.unam.mx), mex-nellen-L-abs1-he14-oral

The Pierre Auger Observatory can detect air showers with high efficiency at large zenith angles with both the fluorescence and surface detectors. Since half the available solid angle corresponds to zeniths between 60 and 90 degrees, a large number of inclined events can be expected and are indeed observed. In this paper, we characterise the inclined air showers detected by the Observatory and we present the aperture for inclined showers and an outlook of the results that can be obtained in future studies of the inclined data set.

Anisotropy Studies around the Galactic Center at EeV Energies with Auger Data

The Pierre Auger Collaboration

Presenter: A. Letessier-Selvon (Antoine.Letessier-Selvon@@in2p3.fr), fra-letessier-selvon-A-abs1-he14-oral

The Pierre Auger Observatory data have been analyzed to search for excesses of events near the direction of the galactic center in several energy ranges around EeV energies. In this region the statistics accumulated by the Observatory are already larger than that of any previous experiment. Using both the data sets from the surface detector and our hybrid data sets (events detected simultaneously by the surface detector and the fluorescence detector) we do not find any significant excess. At our present level of understanding of the performance and properties of our detector, our results do not support the excesses reported by AGASA and SUGAR experiments. We set an upper bound on the flux of cosmic rays arriving within a few degrees from the galactic center in the energy range from 0.8-3.2 EeV. We also have searched for correlations of cosmic ray arrival directions with the galactic plane and with the super-galactic plane at energies in the range 1-5 EeV and above 5 EeV and have found no significant excess.

Search for localized excess fluxes in Auger sky maps and prescription results

Pierre Auger Collaboration

Pierre Auger Observatory, Av. San Martin Norte 304, (5613) Malargüe, Argentina

Presenter: B. Revenu (revenu@iap.fr), fra-revenu-B-abs1-he14-oral

Using the first surface detector data of the Pierre Auger Observatory, we present the results of a blind search for overdensities in the cosmic ray flux with respect to isotropic expectations. We consider two energy bands: $1 \text{ EeV} \leq E \leq 5 \text{ EeV}$ and $E \geq 5 \text{ EeV}$ at two angular scales: 5° and 15° . We also report the results of searches for excesses in target directions already defined in a set of prescriptions presented at the ICRC in 2003. At the moment, both analyses give results that are compatible with isotropy.

Observing muon decays in water Cherenkov detectors at the Pierre Auger Observatory

P. Allison, F. Arneodo, X. Bertou, N. Busca, P.L. Ghia, C. Medina, G. Navarra, L. Nellen
H. Salazar Ibarguen, S. Ranchon, M. Urban, L. Villasenor
for the Pierre Auger Collaboration.

Presenter: N. Busca (ngb@uchicago.edu) usa-busca-N-abs1-he15-poster

Muons decaying in the water volume of a Cherenkov detector of the Pierre Auger Observatory provide a useful calibration point at low energy. Using the digitized waveform continuously recorded by the electronics of each tank, we have devised a simple method to extract the charge spectrum of the Michel electrons, whose typical signal is about 1/8 of a crossing vertical muon. This procedure, moreover, allows continuous monitoring of the detector operation and of its water level. We have checked the procedure with high statistics on a test tank at the Observatory base and applied with success on the whole array.

Calibration of the surface array of the Pierre Auger Observatory

M. Aglietta, P.S. Allison, F. Arneodo, D. Barnhill, P. Bauleo, J.J. Beatty, X. Bertou,
C. Bonifazi, N. Busca, A. Creusot, D. Dornic, A. Etchegoyen, A. Filevitch,
P.L. Ghia, C.M. Grunfeld, I. Lhenry-Yvon, M.C. Medina, E. Moreno, G. Navarra,
D. Nitz, T. Ohnuki, S. Ranchon, H. Salazar, T. Suomijärvi, D. Supanitsky,
A. Tripathi, M. Urban, L. Villasenor for the Pierre Auger Collaboration
Pierre Auger Observatory, Av. San Martin Norte 304, (5613) Malargue, Argentina
Presenter: P.S. Allison (barawn@auger.org.ar), usa-Allison-PS-abs1-he14-poster

The ground array of the Pierre Auger Observatory will consist of 1600 water Cherenkov detectors, deployed over 3000 km². The remoteness and large number of detectors required a simple, automatic remote calibration procedure. The primary physics calibration is based on the average charge deposited by a vertical and central throughgoing muon, determined with good precision at the detector via a novel rate-based technique and later with higher precision via charge histograms. This value is named the vertical-equivalent muon (VEM). The VEM and the other parameters needed to maintain this calibration over the full energy range and to assess the quality of the detector are measured every minute. This allows an accurate determination of the energy deposited in each detector when an atmospheric cosmic ray shower occurs.

Response of the Pierre Auger Observatory Water Cherenkov Detectors to Muons

M. Aglietta, P. Allison, E.C. Andres, F. Arneodo, X. Bertou, C. Bonifazi, N. Busca, A. Creusot, O. Deligny, D. Dornic, B. Genolini, P.L. Ghia, C.M. Grunfeld, I. Lhenry-Yvon, P.O. Mazur, E. Moreno, G. Perez, H. Salazar, T. Suomijärvi
for the Pierre Auger Collaboration
Pierre Auger Observatory, Av. San Martin Norte 304, (5613) Malargue, Argentina
Presenter: T. Suomijärvi (tiina@ipno.in2p3.fr), fra-suomivi-T-abs1-he14-poster

Two test detectors similar to the Pierre Auger Observatory Water Cherenkov Detectors have been installed at the Observatory site and at the Institute de Physique Nucleaire d'Orsay. The signals from the tanks are read out using three 9. photomultipliers and analyzed by both a digital oscilloscope with high sampling frequency and the Auger surface detector electronics. Additionally, the detectors are equipped with plastic scintillators serving as muon telescopes. The trigger is provided either by the muon telescope or by the coincidence of the three PMTs. The scintillators are movable allowing the study of the detector response to atmospheric muons arriving with different incident angles. In this paper, the results of measurements for vertical and inclined background muons are presented. These results are compared to simulations and important calibration parameters are extracted. The influence of the direct light detected by the PMTs, particularly important for inclined showers, is discussed.

Observation of the Long Term Stability of Water Stations in the Pierre Auger Surface Detector

I. Allekotte, K. Arisaka, D. Barnhill, X. Bertou, C. Bonifazi, M.D. Healy, J. Lee
C. Medina, T. Ohnuki, A. Tripathi, for the Pierre Auger Collaboration
Presenter: M.D. Healy (healymd@physics.ucla.edu), usa-healy-MD-abs1-he15-poster

The results of a study examining the long-term behaviour of Pierre Auger surface detectors are presented. The station properties, such as water quality, liner reflectivity and the water level must be continuously monitored. Such monitoring provides information on the long-term stability of the detectors, which have been designed to operate for twenty years. Using pulse height and shapes of cosmic ray muons, water quality changes are monitored and a technique developed to identify and monitor long-term trends in the array.

Fluorescence and Hybrid Detection Aperture of the Pierre Auger Observatory

J.A. Bellido, D. D'Urso, H. Geenen, F. Guarino, L. Perrone, S. Petrera, L. Prado Jr.,
F. Salamida for the Pierre Auger Collaboration
Presenter: S. Petrera (sergio.petrera@aquila.infn.it), ita-petrera-S-abs1-he15-poster

The aperture of the Fluorescence Detector (FD) of the Pierre Auger Observatory is evaluated from simulated events using different detector configurations: mono, stereo, 3-FD and 4-FD. The trigger efficiency has been modelled using shower profiles with ground impacts in the field of view of a single telescope and studying the trigger response (at the different levels) by that telescope and by its neighbours. In addition, analysis cuts imposed by event reconstruction have been applied. The hybrid aperture is then derived for the Auger final extension. Taking into account the actual Surface Detector (SD) array configuration and its trigger response, the aperture is also calculated for a typical configuration of the present phase.

The Performance of the Corrector Lenses for the Auger Fluorescence Detector

Ricardo Sato, Carlos O. Escobar,
for the Pierre Auger Collaboration

(a) Instituto de Física Universidade Estadual de Campinas, Campinas, Brasil

Presenter: C. O. Escobar (escobar@i_unicamp.br), bra-escobar-co-bas1-he15-poster

We present an analysis of the effect that the corrector lenses (Schmidt Optics) has on the overall performance of the Auger Fluorescence Detector. The analysis uses real data from the telescopes. Figures of merit for the corrector lenses performance include shower trigger rate and the distribution of the distance of closest approach to the shower axis. As a result of this analysis we may say that the effective light collection area of a telescope nearly doubles with the use of a corrector lens at its aperture.

Optical Relative Calibration and Stability Monitoring for the Auger Fluorescence Detector

C. Aramo, J. Brack, R. Caruso, D. D'Urso, D. Fazio, R. Fonte, H. Gemmeke,
M. Kleifges, R. Knapik, A. Insolia, J. A. J. Matthews, A. Menshikov, W. Miller,
P. Privitera and J. Rodriguez Martino for the Pierre Auger Collaboration

(a) Pierre Auger Observatory, Av. San Martin Norte 304, (5613) Malargu, Argentina

Presenter: A. Insolia (antonio.insolia@ct.infn.it), ita-insolia-A-abs1-he15-poster

The stability of the fluorescence telescopes of the Pierre Auger Observatory is monitored with the optical relative calibration setup. Optical fibers distribute light pulses to three different diffuser groups within the optical system. The total charge per pulse is measured for each pixel and compared with reference calibration measurements. This allows monitoring the short and long term stability with respect of the relative timing between pixels and the relative gain for each pixel. The designs of the LED calibration unit (LCU) and of the Xenon flash lamp used for relative calibration, are described and their capabilities to monitor the stability of the telescope performances are studied. We report the analysis of relative calibration data recorded during 2004. Fluctuations in the relative calibration constants provide a measure of the stability of the FD.

Absolute Calibration of the Auger Fluorescence Detectors

P. Bauleo, J. Brack, L. Garrard, J. Harton, R. Knapik, R. Meyhandan, A.C. Rovero,
A. Tamashiro, and D. Warner, for the Auger Collaboration

Presenter: A.C. Rovero (rovero@iafe.uba.ar), arg-rovero-AC-abs1-he15-poster

Absolute calibration of the Pierre Auger Observatory fluorescence detectors uses a light source at the telescope aperture. The technique accounts for the combined effects of all detector components in a single measurement. The calibrated 2.5 m diameter light source fills the aperture, providing uniform illumination to each pixel. The known flux from the light source and the response of the acquisition system give the required calibration for each pixel. In the lab, light source uniformity is studied using CCD images and the intensity is measured relative to NIST-calibrated photodiodes. Overall uncertainties are presently 12%, and are dominated by systematics.

Quality studies of the data taking conditions for the Auger Fluorescence Detector

R. Caruso, R. Fonte, A. Insolia, S. Petrera and J. Rodriguez Martino, for the Auger Collaboration
Presenter: J. Rodriguez Martino (julio.rodriguez@roma2.infn.it), ita-rodriguezmartino-J-abs1-he15-poster

As more than half of the Fluorescence Detector (FD) of the Auger Observatory is completed, data taking is becoming a routine job. It is then necessary to follow strict procedures to assure the quality of the data. An overview of the data taking methods is given. The nature of the FD background signal is due to the night sky brightness (stars and planet faint light, moonlight, twilight, airglow, zodiacal and artificial light) and to the electronic background (photomultiplier and electronic noise). The analysis of the fluctuations in the FADC signal (variance analysis), directly proportional to the background mean light level, performed for each night of data taking is used to monitor the FD background signal. The data quality is analysed using different techniques, described in detail. Examples of trigger rates, number of stereo events, dead time due to moonlight, weather or hardware problems are given. The analysis comprises several months of data taking, giving an overview of the FD capabilities, performance and allowing a systematic study of data and their correlation with the environment.

Measurement of the Sky Photon Background Flux at the Auger Observatory

R. Caruso, A. Insolia, S. Petrera, P. Privitera, F. Salamida and V. Verzi, for the Pierre Auger Collaboration
Presenter: S. Petrera (sergio.petrera@aquila.infn.it), ita-petrera-S-abs2-he15-poster

The sky photon background flux has been measured at the southern Auger site in Malargue, Argentina, using the observatory's fluorescence detectors (FD). The analysis is based on ADC variances of pixels not triggered by the First Level Trigger. Photon fluxes are calculated for each individual pixel at each telescope. The statistics from each night of data taking allows a study of local variations in the photon flux. Results show a clear dependence of the flux on elevation angle. Time variations, possibly related to different atmospheric conditions, do not mask this dependence. In particular the flux excess above the horizon shows a rather stable and reproducible behaviour with elevation. Correlation of this dependence with atmospheric parameters can be of interest as it offers the promise of extracting those parameters directly from FD data, thus allowing cross checks with independent methods based on different monitoring devices.

The Central Laser Facility at the Pierre Auger Observatory

F. Arqueros, J. Bellido, C. Covault, D. D'Urso, C. Di Giulio, P. Facal, B. Fick, F. Guarino, M. Malek, J.A.J. Matthews, J. Matthews, R. Meyhandan, M. Monasor, M. Mostafa, P. Petrinca, M. Roberts, P. Sommers, P. Travnicek, L. Valore, V. Verzi, L. Wiencke for the Pierre Auger Collaboration.

Presenter: M. Malek malek@fnal.gov, usa-malek-M-abs1-he15-poster

The Central Laser Facility is located near the middle of the Pierre Auger Observatory in Argentina. It features a UV laser and optics that direct a beam of calibrated pulsed light into the sky. Light scattered from this beam produces tracks in the Auger optical detectors which normally record nitrogen fluorescence tracks from cosmic ray air showers. The Central Laser Facility provides a test beam to investigate properties of the atmosphere and the fluorescence detectors. The laser can send light via optical fiber simultaneously to the nearest surface detector tank for hybrid timing analyses. We describe the facility and show some examples of its many uses.

Atmospheric aerosol monitoring at the Pierre Auger Observatory

R. Cester, M. Chiosso, J. Chirin, R. Clay, B. Dawson, B. Fick, A. Filipcic, B. Garcia, A. Grillo, M. Horvat, M. Iarlori, M. Malek, J. Matthews, J. A. J. Matthews, D. Melo, R. Meyhandan, M. Mostafa, R. Mussa, M. Prouza, B. Raefert, V. Rizi, M. Roberts, J. Rodriguez, M. Santander, G. Sequeiros, A. Smith, P. Sommers, L. Wiencke, L. Valore, D. Veberic, M. Zavrtanik, D. Zavrtanik for the Auger Collaboration

(a) Observatorio Pierre Auger, Av. San Martin Norte 304, (5613) Malargue, Argentina

Presenter: M. Roberts (roberts@cosmic.utah.edu), usa-roberts-M-abs1-he15-poster

For a ground based cosmic-ray observatory the atmosphere is an integral part of the detector. Air fluorescence detectors (FDs) are particularly sensitive to the presence of aerosols in the atmosphere. These aerosols, consisting mainly of clouds and dust, can strongly affect the propagation of fluorescence and Cherenkov light from cosmic-ray induced extensive air showers. The Pierre Auger Observatory has a comprehensive program to monitor the aerosols within the atmospheric volume of the detector. In this paper the aerosol parameters that affect FD reconstruction will be discussed. The aerosol monitoring systems that have been deployed at the Pierre Auger Observatory will be briefly described along with some measurements from these systems.

Detecting gamma-ray bursts with the Pierre Auger Observatory using the single particle technique

D. Allard, E. Parizot, X. Bertou, J. Beatty, M. Du Vernois, D. Nitz, G. Rodriguez
for the Pierre Auger Collaboration

Presenter: Denis Allard (denis@oddjob.uchicago.edu), arg-bertou-X-abs2-og24-poster

During the past ten years, gamma-ray Bursts (GRB) have been extensively studied in the keV-MeV energy range but the higher energy emission still remains mysterious. Ground based observatories have the possibility to investigate energy range around one GeV using the single particle technique. The aim of the present study is to investigate the capability of the Pierre Auger Observatory to detect the high energy emission of GRBs with such a technique. According to the detector response to photon showers around one GeV, and making reasonable assumptions about the high energy emission of GRBs, we show that the Pierre Auger Observatory is a competitive instrument for this technique, and that water tanks are very promising detectors for the single particle technique.

Angular Resolution of the Pierre Auger Observatory

C. Bonifazi for Pierre Auger Collaboration

Pierre Auger Observatory, Av. San Martin Norte 304, (5613) Malargue, Argentina

Presenter: C. Bonifazi (bonifazi@cbpf.br), bra-bonifazi-C-abs1-he14-oral

We studied the angular resolution of the Pierre Auger Detector using data collected from January 2004 to May 2005. The detector consists of two independent components, the fluorescence detector and the surface detector. Hybrid events, observed simultaneously by both components, have smaller reconstruction uncertainties than the events observed with only one component. The hybrid resolution is extracted from artificial showers generated by laser shots, while the surface detector angular accuracy is then determined from the comparison of the hybrid geometrical fit with the one obtained from the surface detector alone. We used adjacent surface detector stations to cross check our methods. The angular reconstruction accuracy of the surface detector events is given as a function of station multiplicity.

Aperture calculation of the Pierre Auger Observatory surface detector

D. Allard, I. Allekotte, E. Armengaud, J. Aublin, X. Bertou, A. Chou, P. L. Ghia,

M. G'omez Berisso, J.C. Hamilton, I. Lhenry-Yvon, C. Medina, G. Navarra,

E. Parizot, A. Tripathi, for the Pierre Auger Collaboration

Observatorio Pierre Auger, Av San Martin Norte 304, (5613) Malargue, Argentina

Presenter: E. Parizot (parizot@ipno.in2p3.fr), fra-parizotE-abs1-he14-poster

We determine the instantaneous aperture and integrated exposure of the surface detector of the Pierre Auger Observatory, taking into account the trigger efficiency as a function of the energy, arrival direction (with zenith angle lower than 60 degrees) and nature of the primary cosmic-ray. We make use of the so-called Lateral Trigger Probability function (or LTP) associated with an extensive air shower, which summarizes all the relevant information about the physics of the shower, the water tank Cherenkov detector, and the triggers.

Studies of Signal Waveforms from the Water-Cherenkov Detectors of the Pierre Auger Observatory

P.S. Allison, H. Bui-Duc, J. Chye, S. Dagoret-Campagne, A. Dorofeev, J. Matthews,

D.F. Nitz, S. Ranchon, M. Urban, D. Veberic, A.A. Watson, and C. Wileman,

for the Pierre Auger Collaboration

(a) Observatorio Pierre Auger, Av. San Martin Norte 304, (5613) Malargue, Mendoza, Argentina

Presenter: J. Matthews (matthews@phys.lsu.edu), usa-matthews-James-abs1-he14-poster

The ground array of the Pierre Auger Observatory will consist of 1600 water-Cherenkov detectors. Such detectors give signals which can help differentiate between muons and electrons in extensive air showers. The relative numbers of muons and electrons is sensitive to the type of primary particle which initiated the shower. Results are presented using methods which describe the muon content and related information, such as the time structure of the shower front.

Coverage and large scale anisotropies estimation methods for the Pierre Auger Observatory

J.-Ch. Hamilton for the Pierre Auger Collaboration

Av. San Martin Norte 304, (5613) Malargue, Argentina

Presenter: J.-Ch. Hamilton (hamilton@in2p3.fr), fra-hamilton-JC-abs1-he14-oral

When searching for anisotropies in the arrival directions of Ultra High Energy Cosmic Rays, one must estimate the number of events expected in each direction of the sky in the case of a perfect isotropy. We present in this article a new method, developed for the Auger Observatory, based on a smooth estimate of the zenith angle distribution obtained from the data itself (which is essentially unchanged in the case of the presence of a large scale anisotropy pattern). We also study the sensitivity of several methods to detect large-scale anisotropies in the cosmic ray arrival direction distribution: Rayleigh analysis, dipole fitting and angular power spectrum estimation.

Timing Calibration and Synchronization of Surface and Fluorescence Detectors of the Pierre Auger Observatory

P. Allison, J. Bellido, X. Bertou, C.E. Covault, B.E. Fick, H. Gemmeke, M. Kleifges, M. Mostafa, A. Menshikov, F. Meyer, C. Pryke, P. Sommers, E. Vanderpan, F. Vernotte and L. Wiencke for the Auger Collaboration

Presenter: C.E. Covault (corbin.covault@case.edu), usa-covault-C-abs2-he15-poster

Reconstruction of cosmic ray arrival directions for Surface Detectors (SD) and Fluorescence Detectors (FD) of the Pierre Auger Observatory requires accurate timing (25 nanoseconds or better) between measurements at individual detectors and instrument triggers. Timing systems for both SD and FD are based on Motorola Oncore UT+ GPS receivers installed into custom-built time-tagging circuits that are calibrated in the laboratory to a statistical precision of better than 15 ns. We describe timing calibration and synchronization methods applied in the field for both the SD and the FD systems in four areas: (1) checks of timing offsets within the SD using co-located station pairs and timing residuals on reconstructed showers, (2) calibration within the FD using a custom-build LED calibration system, (3) calibration between SD and FD using laser signals fed simultaneously into an SD station and across the FD via the Central Laser Facility (CLF), and (4) studies of synchronization between FD and SD through the analysis of events detected by both systems, called hybrid events. These hybrid events allow for a much more accurate reconstruction of the shower and for relatively tight constraints on timing calibration offsets. We demonstrate that statistical and systematic timing uncertainties have no significant impact on the event reconstruction.

The trigger system of the Pierre Auger Surface Detector: operation, efficiency and stability

D. Allard, E. Armengaud, I. Allekotte, P. Allison, J. Aublin, M. Ave, P. Bauleo, J. Beatty, T. Beau, X. Bertou, P. Billoir, C. Bonifazi, A. Chou, J. Chye, S. Dagoret-Campagne, A. Dorofeev, P.L. Ghia, M. Gomez Berisso, A. Gorgi, J.C. Hamilton, J. Harton, R. Knapik, C. Lachaud, I. Lhenry-Yvon, A. Letessier-Selvon, J. Matthews, C. Medina, R. Meyhandan, G. Navarra, D. Nitz, E. Parizot, B. Revenu, Z. Szadkowski, T. Yamamoto for the Pierre Auger Collaboration

(a) Pierre Auger Observatory, Av San Martin Norte 304,(5613) Malargue, Argentina

Presenter: I. Lhenry-Yvon (lhenry@ipno.in2p3.fr), usa-lhenry-yvon-I-abs1-he14-poster

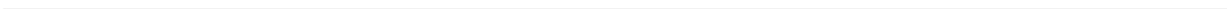
The trigger system of the Surface Detector (SD) of the Pierre Auger Observatory is described, from the identification of candidate showers ($E > 1 \text{ EeV}$) at the level of a single station, among a huge background (mainly single muons), up to the selection of real events and the rejection of random coincidences at a higher central trigger level (including the reconstruction accuracy). Efficiency of a single station trigger is evaluated using real data, and the high performance of event selection hierarchy will be demonstrated.

Education and Public Outreach of the Pierre Auger Observatory

B. Garcia and G. Snow for the Pierre Auger Observatory Collaboration

Presenter: B. Garcia (bgarcia@frm.utn.edu.ar), arg-garcia-B-abs1-he15-poster

The Auger collaboration's broad mission in education, outreach and public relations is coordinated in a separate task. Its goals are to encourage and support a wide range of outreach efforts that link schools and the public with the Auger scientists and the science of cosmic rays, particle physics, and associated technologies. This report focuses on recent activities and future initiatives.



An analysis of super-high energy cosmic-ray propagation in the Galaxy

J.R. Hörandel^a, N.N. Kalmykov^b, A.V. Timokhin^c

(a) *Institute for Experimental Nuclear Physics, University of Karlsruhe, P.O. Box 3640, 76021 Karlsruhe, Germany*

(b) *Skobeltsyn Institute of Nuclear Physics, Lomonosov Moscow State University, Russia*

(c) *Faculty of Physics, Lomonosov Moscow State University, Russia*

Presenter: J.R. Hörandel (hoerandel@ik.fzk.de), ger-hoerandel-J-abs1-og13-poster

Calculations of the cosmic-ray energy spectrum and the propagation pathlength in the energy range $10^{14} - 10^{19}$ eV have been performed within the framework of a combined approach based on a diffusion model and a simulation of particle trajectories in the Galaxy. The obtained escape pathlength and the interaction probability for nuclei in the Galaxy are discussed. The resulting spectrum for protons at Earth is compared to experimental data.

1. Introduction

The origin of super-high energy cosmic rays (CRs) is one of the most important problems in astrophysics. Since the spectrum at the sources is not identical to the spectrum observed at Earth, a study of sources is closely connected to the investigation of CR propagation processes in the Galaxy. This necessitates knowledge about the structure of the galactic magnetic fields. Unfortunately, there is no standard field configuration, different magnetic field models are able to describe available experimental data [1, 2, 3, 4]. How CRs are accelerated to extremely high energies is another open question. Although the popular model of CR acceleration by shock waves in expanding shells of supernovae (for example [5, 6, 7]) is almost recognized as "standard theory", there are still a number of unresolved problems in this model. Furthermore, the question about the role of other acceleration mechanisms is not quite clear, and could lead to different CR energy spectra at the sources [1].

The validity of various concepts is verified by the calculation of the primary CR energy spectrum, making assumptions on the density distribution of CR sources, the energy spectrum at the sources, and the configuration of the galactic magnetic fields. The diffusion model can be used in the energy range up to 10^{17} eV, where the spectrum is calculated using the diffusion equation for the density of CRs in the Galaxy. At higher energies this model ceases to be valid, and it becomes necessary to carry out numerical calculations of particle trajectories for the propagation in the magnetic fields. This method works best for the highest-energy particles, since the time for the calculations required is inversely proportional to the particle energy. Therefore, the calculation of the CR spectrum in the energy range $10^{14} - 10^{19}$ eV has been performed within the framework of a combined approach, the use of a diffusion model and the numerical integration of particle trajectories.

2. Assumptions

High isotropy and a comparatively long retention of CRs in the Galaxy ($\sim 10^7$ years for the disk model) reveal the diffusion nature of particle motion in the interstellar magnetic fields. This process is described by a corresponding diffusion tensor [1, 3, 8]. The steady-state diffusion equation for the CR density $N(r)$ is (neglecting nuclear interactions and energy losses)

$$-\nabla_i D_{ij}(r) \nabla_j N(r) = Q(r), \quad (1)$$

with the source term $Q(r)$ and the diffusion tensor $D_{ij}(r)$.

Under the assumption of azimuthal symmetry and taking into account the predominance of the toroidal component of the magnetic field, eq. 1 is presented in cylindrical coordinates as

$$\left[-\frac{1}{r} \frac{\partial}{\partial r} r D_{\perp} \frac{\partial}{\partial r} - \frac{\partial}{\partial z} D_{\perp} \frac{\partial}{\partial z} - \frac{\partial}{\partial z} D_A \frac{\partial}{\partial r} + \frac{1}{r} \frac{\partial}{\partial r} r D_A \frac{\partial}{\partial z} \right] N(r, z) = Q(r, z), \quad (2)$$

where $N(r, z)$ is the CR density averaged over the large-scale fluctuations with the characteristic scale $L \sim 100$ pc [3]. $D_{\perp} \propto E^m$ is the diffusion coefficient, where m is much less than one ($m \approx 0.2$), and $D_A \propto E$ is the Hall diffusion coefficient. Thus, the influence of Hall diffusion becomes predominant at sufficiently high energies ($> 10^{15}$ eV). The sharp enhancement of the diffusion coefficient leads to the excessive leakage of CRs from the Galaxy at energies exceeding 10^{17} eV. For investigations of the CR propagation at such energies it is necessary to carry out numerical calculations of the trajectories for individual particles.

The calculation is based on the solution of the equation of motion for a charged particle in the magnetic field of the Galaxy. In this work the calculation was carried out using a fourth order Runge-Kutta method. Trajectories of CRs were calculated until they left the Galaxy. While testing the differential scheme that is used in the calculation, it was found that the accuracy of the obtained trajectories for protons with an energy of 10^{15} eV after passing a distance of 1 pc amounts to $5 \cdot 10^{-8}$ pc. The retention time of a proton with such an energy averages to about 10 million years, hence, a total error for the trajectory approximation by the differential scheme used is about 0.5 pc.

The magnetic field of the Galaxy consists of a large-scale (regular) and a chaotic component $\vec{B} = \vec{B}_{reg} + \vec{B}_{irr}$. A purely azimuthal magnetic field was assumed for the regular field $B_z = 0$, $B_r = 0$, $B_{\phi} = 1 \mu\text{G} \cdot \exp(-z^2/z_0^2 - r^2/r_0^2)$, where $z_0 = 5$ kpc and $r_0 = 10$ kpc are constants [3]. The irregular field was constructed according to an algorithm used in [9], that takes into account the correlation of magnetic field intensity in adjacent cells. The radius of the Galaxy is assumed to be 15 kpc and the galactic disk had a half-thickness of 200 pc. The position of the Solar system was defined at $r = 8.5$ kpc, $\phi = 0^\circ$, and $z = 0$ kpc. A radial distribution of supernovae remnants along the galactic disk was considered as sources [10].

3. Results

The obtained pathlength in the Galaxy for protons as function of energy is presented in Fig. 1 (left). The interstellar matter density was taken as $n_d = 1 \text{ cm}^{-3}$ for the galactic disk and $n_h = 0.01 \text{ cm}^{-3}$ for the halo. For heavier nuclei with charge Z the pathlength scales with the rigidity, i.e. is related to the values for protons $\lambda(E)$ as $\lambda(E, Z) = \lambda(E/Z)$. At the corresponding knees, the amount of traversed material is less than 1 g/cm^2 . The dashed dotted line indicates a trend at lower energies according to $\lambda \propto E^{-\delta}$. To reach values of about 10 g/cm^2 as obtained around 1 GeV [11], one needs a relatively small slope $\delta \approx 0.2$ — much lower than the value usually assumed ($\delta \approx 0.6$).

Measurements of the ratio of secondary to primary CR nuclei at energies in the GeV regime are successfully described using leaky box models, e.g. [11, 12]. Both examples are compared to the predictions of the diffusion model in Fig. 1 (left). Extrapolating these relations to higher energies, the strong dependence of the pathlength on energy ($\propto E^{-0.6}$) leads to extremely small values at PeV energies. Above 10^5 GeV the traversed matter would be smaller than the pathlength accumulated on a straight line from the galactic center to the solar system $\lambda_{gc} = 8 \text{ kpc} \cdot 1 \text{ proton/cm}^3 \approx 0.04 \text{ g/cm}^3$. This value is indicated in the figure as dotted line. A similar conclusion can be derived from anisotropy measurements. Leaky box models, with their extremely steep decrease of the pathlength $\lambda \propto E^{-0.6}$, yield relative large anisotropies even at modest energies, which seem to be ruled out by the measurements [13].

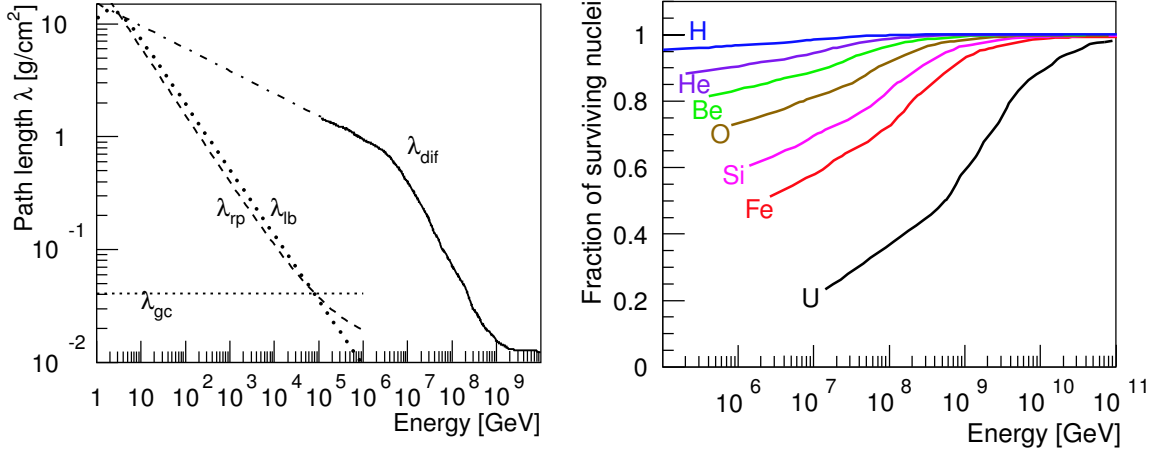


Figure 1. *Left:* Pathlength in the Galaxy for protons. The values for the diffusion model (λ_{dif}) are indicated by the solid line. They are extrapolated to lower energies by the dashed dotted line. The dashed and dotted lines indicate a leaky box model (λ_{lb} [11]) and a residual pathlength model (λ_{rp} [12]). The dotted line indicates the matter accumulated along a straight line from the galactic center (λ_{gc}). *Right:* Fraction of nuclei surviving without interaction in the Galaxy as function of energy for different elements.

The interaction probability for different nuclei has been calculated using the obtained pathlength and interaction parameters according to the QGSJET model [14]. Nuclear fragmentation is taken into account in an approximate approach [15]. It should be pointed out that a nuclear fragment conserves the trajectory direction of its parent if Z/A in question is the same as for the primary nucleus and for most stable nuclei the ratio Z/A is close to $1/2$. The resulting fraction of nuclei which survive without an interaction is presented in Fig. 1 (right) for selected elements. It turns out that at the respective knees ($\sim Z \cdot 4.5$ PeV) more than $\sim 50\%$ of the nuclei survive without interactions, even for the heaviest elements. This is an important result, since the *poly gonato* model relates the contribution of ultra-heavy CRs to the second knee in the all-particle spectrum around 400 PeV [16].

The results of the calculations of the proton spectrum are shown in Fig. 2. They were obtained using the diffusion model and numerical calculations of trajectories. Both methods give identical results up to about $3 \cdot 10^{16}$ eV. At higher energies there is a continuous decrease of the intensity in the "diffusion" spectrum, which corresponds to the excessive increase in the diffusion coefficient that results in a large leakage of particles from the Galaxy. An energy of 10^{17} eV can be accepted as the boundary for the applicability of the diffusion model. At this energy the results obtained with the two methods differ by a factor of 2 and for higher energies the diffusion approximation of CR propagation in the Galaxy becomes invalid.

The results from air shower experiments [18, 19] indicate a relatively pronounced knee at an energy of about 4 PeV. The spectra are compatible with the *poly gonato* model, see Fig. 2, with a change of the spectral index at the knee of $\Delta\gamma = 2.10 \pm 0.24$ [16]. The observed steepening of the energy spectrum should be compared with a value of $1 - m \approx 0.8$ as predicted by the diffusion model [3]. It is obvious that the experimental value of $\Delta\gamma$ is larger, hence, at least a part of the observed steepening should be related to a change of the shape of the spectrum at the sources.

The maximum energy reached during the acceleration process and the corresponding shape of the spectrum at these energies depend on the intensity of the magnetic fields in the acceleration zone and on assumptions for the feedback of CRs to the shock front. The uncertainties of the parameters used yield differences in the

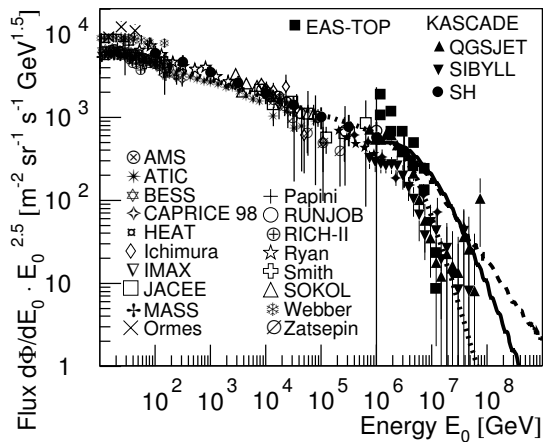


Figure 2. Calculated spectra for protons for the diffusion model (—) and the numerical trajectory calculations (---) compared to the flux obtained by various experiments, for references see [17], and the *polygono* model (- · -) [16].

maximum energy attained in the order of \pm one decade [6, 20]. In addition, the situation is complicated by the dependence of the escape pathlength on energy. As discussed above, the dependence $\lambda \propto E^{-0.6}$ can not be extrapolated to knee energies. On the other hand, a dependence $\propto E^{-0.2}$ requires additional assumptions for the spectral shape at the sources to explain the observed energy spectra. Thus, there is no agreement about a "standard model" scenario. At present, it is difficult to draw definite conclusions from the comparison of the observed spectra for different elemental groups with the standard model of CR acceleration at ultra high energies.

Acknowledgment: The authors are grateful to V.N. Zirakashvili and A.I. Pavlov for useful discussions. N.N.K. and A.V.T. acknowledge the support of the RFBR (grant 05-02-16401).

References

- [1] V.S. Berezinsky *et al.*, *Astrophysics of Cosmic Rays*, North-Holland (1990).
- [2] A.A. Ruzmaikin *et al.*, *Magnetic Fields of Galaxies*, Kluwer, Dordrecht (1988).
- [3] S.V. Ptuskin *et al.*, *Astron. & Astroph.* **268**, 726 (1993).
- [4] E.V. Gorchakov & I.V. Kharchenko, *Izv. RAN ser. phys.* **64**, 1457 (2000).
- [5] D.C. Ellison *et al.*, *Astrophys. J.* **488**, 197 (1997).
- [6] E.G. Berezhko & L.T. Ksenofontov, *JETP* **89**, 391 (1999).
- [7] L.G. Sveshnikova *et al.*, *Astron. & Astroph.* **409**, 799 (2003).
- [8] N.N. Kalmykov & A.I. Pavlov, *Proc. 26th Int. Cosmic Ray Conf., Salt Lake City* **4**, 263 (1999).
- [9] V.N. Zirakashvili *et al.*, *Izv. RAN ser. phys.* **59**, 153 (1995).
- [10] K. Kodaira, *Publ. Astron. Soc. Japan* **26**, 255 (1974).
- [11] N.E. Yanasak *et al.*, *Astrophys. J.* **563**, 768 (2001).
- [12] S.P. Swordy, *Proc. 24th Int. Cosmic Ray Conf., Rome* **2**, 697 (1995).
- [13] J.R. Hörandel, astro-ph/0501251 (2005).
- [14] N.N. Kalmykov *et al.*, *Nucl. Phys. B (Proc. Suppl.)* **52B**, 17 (1997).
- [15] N.N. Kalmykov & S.S. Ostapchenko, *Yad. Fiz.* **56**, 105 (1993).
- [16] J.R. Hörandel, *Astropart. Phys.* **19**, 193 (2003).
- [17] J.R. Hörandel, astro-ph/0407554 (2004).
- [18] H. Ulrich *et al.*, astro-ph/0505413 (2005).
- [19] M. Aglietta *et al.*, *Nucl. Instr. & Meth. A* **336**, 310 (1993).
- [20] J.R. Hörandel, *Astropart. Phys.* **21**, 241 (2004).

Energy Spectra of Heavy Cosmic Ray Nuclei from 0.5 GeV/amu to 10,000 GeV/amu

P.J. Boyle^a, M. Ave^a, F. Gahbauer^a, C. Höppner^a, J. Hörandel^b, M. Ichimura^c, D. Müller^a, A. Romero-Wolf^a, S. Wakely^a

(a) Enrico Fermi Institute, University of Chicago, 5640 South Ellis Avenue, Chicago, IL 60637

(b) University of Karlsruhe, Germany

(c) Hiroasaki University, Japan

Presenter: P.J. Boyle (jojo@donegal.uchicago.edu), usa-boyle-P-abs1-og11-oral

We present new results on the energy spectra of cosmic ray nuclei which are derived from the long-duration balloon flight of the TRACER detector in Antarctica in December, 2003. The measurements are corrected for detection efficiencies, interaction losses in the atmosphere and in the instrument, and for overlap effects due to limited energy resolution. Hence, we report the absolute intensities at the top of the atmosphere for the cosmic ray nuclei over the charge range from oxygen ($Z = 8$) to iron ($Z = 26$). The range of the individual energy spectra extends from about 0.5 GeV/amu to several 1000 GeV/amu for the more abundant species (O, Ne, Mg, Si, and Fe), and to about 1000 GeV/amu for the rarer species S, Ar, and Ca.

1. Introduction

The TRACER detector has observed heavy cosmic-ray nuclei ($8 \leq Z \leq 26$) in a 10-day balloon exposure in 2003. For each accepted event, the instrument records signals from the top and bottom scintillators, Cherenkov counter, the specific ionization (dE/dx), and the transition radiation detector (TRD), as well as details of the particle trajectory through the instrument. Characteristic correlations between these signals lead to the assignment of nuclear charge Z and energy E (or Lorentz factor $\gamma = E/mc^2$). At low energies, below about 10 GeV/amu, the energy measurement comes from the Cherenkov signal, while TRD and dE/dx determine the energy of highly relativistic particles. As an example, we show in Figure 1 the cross-correlation of TRD and dE/dx signals for eight different elements studied in this investigation. The charge Z for each element has been determined from the scintillator signals, and low energy particles are excluded by the additional constraint that the Cherenkov counter must be in saturation (for details see [1]).

The scatter plots show clearly how the signals of dE/dx and TRD are correlated, and increasing with energy along the 45 degree line until, at about 400 GeV/amu, transition radiation sets in and leads to a rapid increase in TRD signal. Hence, the very rare particles, with energies extending well into the 10^3 to 10^4 GeV/amu region, stand out in these scatter plots, and are well separated from low energy background.

2. Absolute Intensities

All accepted events are sorted into energy bins, using the response curves described by Höppner et al. [1]. The energy resolution is different for different energy regions, and generally improves with increasing charge Z because the relative signal fluctuations decrease typically with $1/Z$ (as can be seen explicitly in the data of figure 1). The width of the energy bins must be commensurate with or larger than the energy resolution of the detector.

In order to obtain absolute particle intensities, we must determine the geometric aperture and the efficiencies of the various analysis cuts on the raw data as accurately as possible. The aperture of the instrument has been

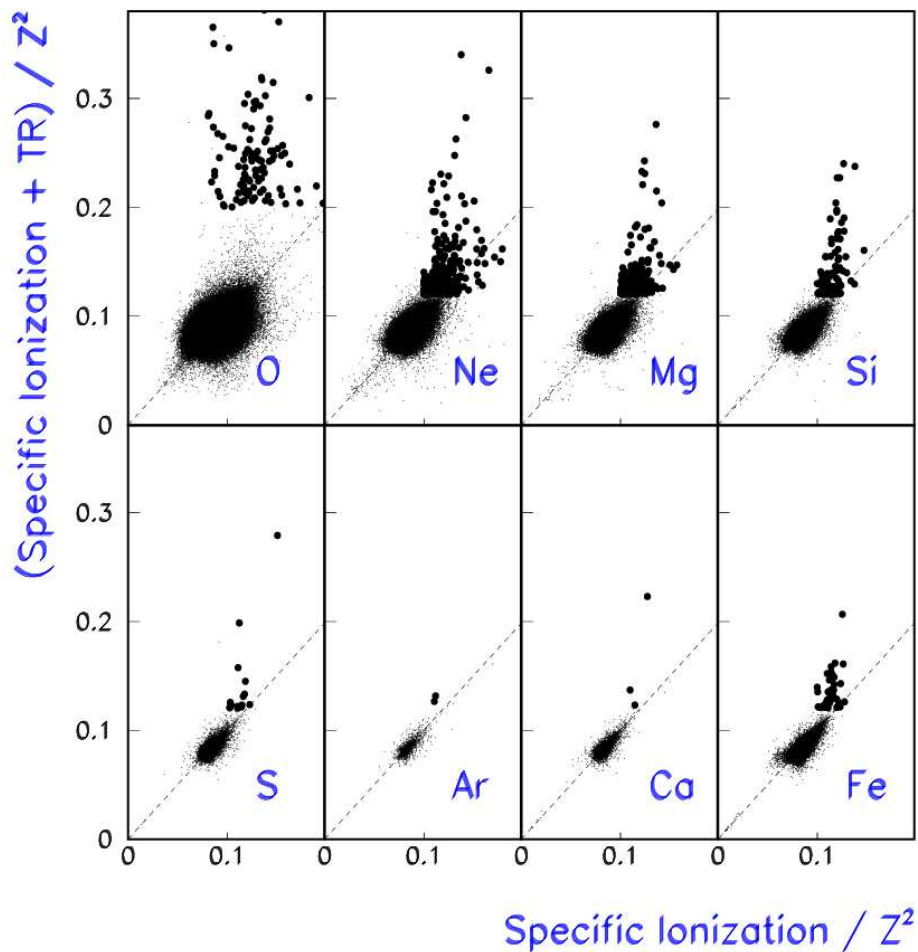


Figure 1. Scatter plot of $(TR + dE/dx)$ against dE/dx for different elements. Note that all signals are normalized by Z^2 . The highlighted points represent the highest energy events measured with the TRD. As expected, all the transition radiation events have signals in the dE/dx detector which are well above the minimum ionization level.

determined analytically and verified by a computer simulation which also takes certain “dead” counter areas into account. Instrumental dead-time or data recording inefficiencies were negligible. A number of efficiency factors are derived from the flight data themselves. These include the efficiencies for the charge selection cuts and Cherenkov cuts. Other cuts, for instance the criteria for trajectory selection, require a detailed computer simulation of the entire instrument [2].

Relatively significant, and increasing with Z , are losses of nuclei due to nuclear spallations in the detector material, and due to spallations in the residual atmosphere above the balloon. These can be reliably calculated with known energy-independent cross sections [3], [4]. As an example, Table 1 shows some typical efficiency factors for oxygen and iron nuclei.

Finally, “overlap corrections” in energy must be taken into account, i.e., the number of events in a given energy

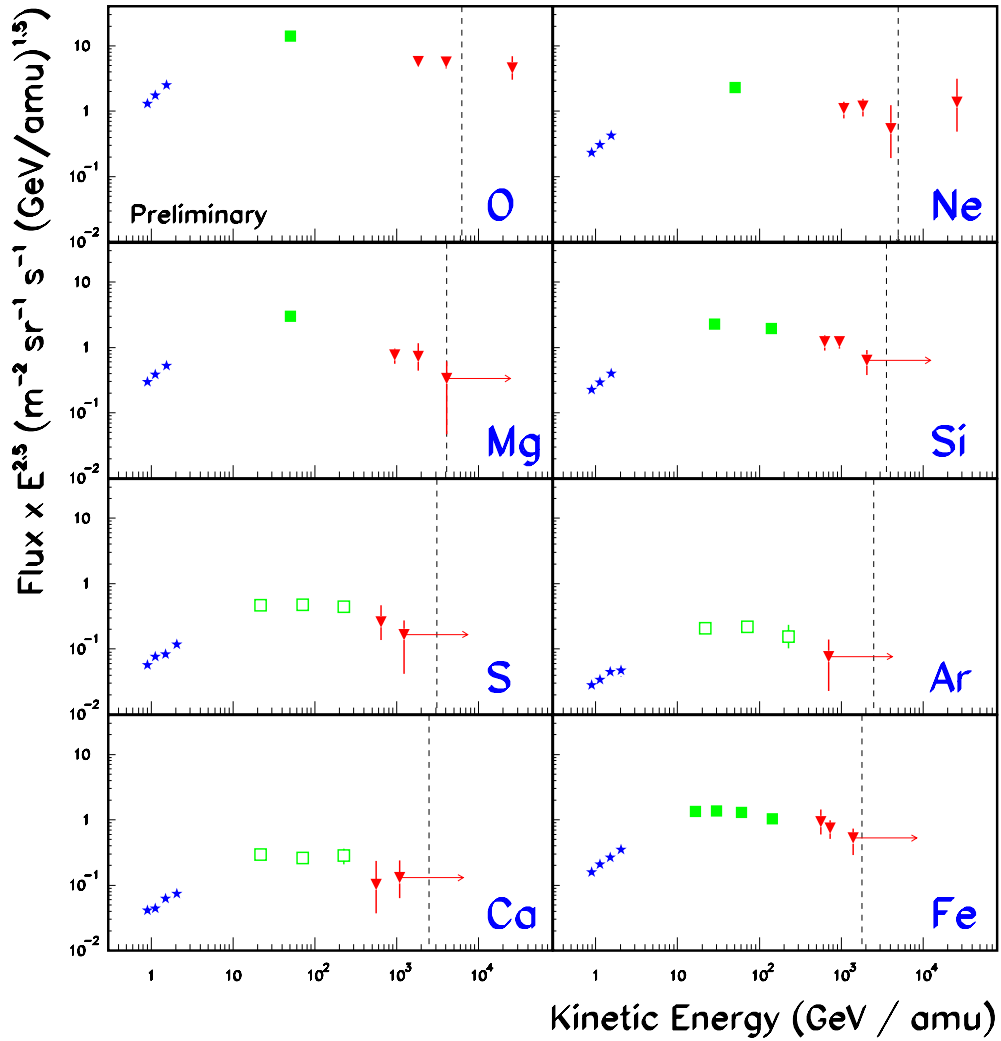


Figure 2. Differential energy spectra for the cosmic ray nuclei O, Ne, Mg, Si, S, Ar, Ca and Fe. Note the fluxes are multiplied by $E^{2.5}$. Energy assignments come from the Cerenkov counter (stars), from the specific ionization (squares), or from TR measurements (triangles). The error bars are statistical. The dashed line indicates a total Energy of 10^{14} eV.

bin that should have been assigned to a neighboring bin due to fluctuations in response. We determine these in an extensive computer model that generates a set of simulated raw data which are then subjected to the same analysis as the real data. We choose the width of the energy bins such that, in general, the overlap corrections are not larger than 10-20%.

Table 1. Efficiencies, i.e. fractions of surviving particles, for oxygen and iron.

	Oxygen	Iron
Interaction - Atmosphere	82%	72%
Interaction - Instrument	65%	48%
Charge Selection	89%	90%
Tracking Efficiency	95%	95%

3. Resulting Energy Spectra

Figure 2 shows the energy spectra obtained for eight different elemental species. We emphasize that the data analysis is still ongoing and hence, that the spectra shown in the figure must still be regarded as preliminary. The intensities are multiplied with $E^{2.5}$ and are plotted as a function of kinetic energy/amu. For all elements, the dashed line indicates a total energy of 10^{14} eV per particle. We note that for each element, the intensities are given by three groups of data points, low energy data from the Cherenkov counter (\star), moderately high energies from the relativistic increase in dE/dx (\square), and very high energies from the TRD signals (∇). Altogether, the data cover up to four decades in energy, from a few GeV/amu, to more than 10 TeV/amu. In absolute energy, the results for oxygen and neon exceed 10^{14} eV per particle. We emphasize again that all values given are absolute intensities, without any arbitrary normalization. The error bars are statistical, and for the lower energies, are smaller than the size of the symbols in figure 2.

4. Conclusion

We have presented preliminary energy spectra obtained with the TRACER Cosmic Ray detector during a successful long duration balloon campaign in Antarctica 2003. The individual energy spectra for the major elements (O, Ne, Mg, Si and Fe) extend from 0.5 GeV/amu to several 1000 GeV/amu and for S, Ar and Ca from 0.5 GeV/amu to 1000 GeV/amu. These results represent the highest energies for which spectral measurements with individual charge resolution have been reported. In terms of total energy per particle, the TRACER data reach or exceed 10^{14} eV for most of the elements.

These results, while still preliminary, show that the transition radiation technique adopted in TRACER is capable of providing the cosmic-ray composition up to very high energies. The interplay of complementary detection techniques permits an excellent separation of low, moderate and high energy particles, covering over four decades in energy. With some modifications of the TRD system [5], and with sufficient exposure time, such measurements can reach the knee in the cosmic-ray spectrum.

This work has been supported by NASA grants NAG5-5305 and NN04WC08G.

References

- [1] Höppner, C. et al., 29th ICRC, Pune (2005) OG1.1
- [2] Romero-Wolf, A. et al., 29th ICRC, Pune (2005) OG1.1
- [3] Heckman, H.H. et al., Phys Rev C 17:1735-1747, 1978
- [4] Westfall, G.D. et al., Phys Rev C 19:1309-1323, 1979
- [5] Wakely, S.P. et al, NIM A531, 435, 2004

The Response of the TRACER Detector: Design, Calibrations and Measurements

C. Höppner^a, M. Ave^a, P. Boyle^a, F. Gahbauer^a, J. Hörandel^b,
M. Ichimura^c, D. Müller^a, A. Romero-Wolf^a, S. Wakely^a

(a) Enrico Fermi Institute, University of Chicago, 5640 South Ellis Avenue, Chicago, IL, 60637

(b) University of Karlsruhe, Germany

(c) Hiroasaki University, Japan

Presenter: C. Höppner (hoppner@uchicago.edu), usa-hoeppner-C-abs1-og11-oral

TRACER (“Transition Radiation Array for Cosmic Energetic Radiation”) is currently the largest detector system for direct measurements of cosmic-ray nuclei on balloons. The instrument combines arrays of single-wire proportional tubes for measurements of specific ionization and transition radiation with large-area plastic scintillators and acrylic Cherenkov counters. We shall describe the response functions of the individual detector elements, and the correlations between them which make possible an unambiguous identification of heavy cosmic-ray nuclei ($8 \leq Z \leq 26$) by charge Z and energy E or Lorentz factor $\gamma = E/mc^2$, covering an energy range of four decades.

1. Introduction

Measurements of the cosmic-ray composition to energies approaching the “knee” above 10^{15} eV have been a long-standing goal of cosmic-ray astrophysics. However, experimental progress has been slow because of the rapidly falling intensities which require observations with exposure factors of the order of at least several m^2 ster year for the nuclei heavier than helium. These are difficult if not impossible to accomplish on balloons with traditional instruments, but may be approached in repeated long-duration flights of systems that use transition radiation detectors (TRD) for energy measurements. As a step in this direction, the TRACER instrument has been developed and exposed successfully in a one-day test flight in 1999 [1], and in a 10-day Antarctic long-duration flight in 2003 [2]. The instrument has a geometric factor of $5 m^2$ ster.

2. Description of the Detector

The TRACER concept is based on electromagnetic detection techniques. It achieves a large detector area-to-weight ratio because a nuclear interaction of the particle is not required. The instrument is composed of two plastic scintillation counters, an acrylic Cherenkov detector, and an array of 1600 single-wire proportional tubes. In its current configuration, TRACER is tuned for measurements of the heavier cosmic-ray nuclei, from oxygen ($Z = 8$) to iron ($Z = 26$).

A schematic drawing is shown in figure 1. The scintillators on top and at the bottom of the instrument measure the charge Z of the particles and also serve as trigger. The Cherenkov counter is sensitive to particles with energy above 0.5 GeV/amu and is used to identify low energy particles. The proportional tube array provides energy measurements for highly relativistic particles. It consists of two components: The upper half of the array measures the specific ionization signal (“proportional tube array” in figure 1 which serves as “dE/dx” detector). The lower half which is interspersed with transition radiator material (blankets of plastic fibers) measures specific ionization with X-ray transition radiation (TR) superimposed (“transition radiation detector” in the figure). The use of proportional tubes as ionization and X-ray detectors, rather than more conventional multi-

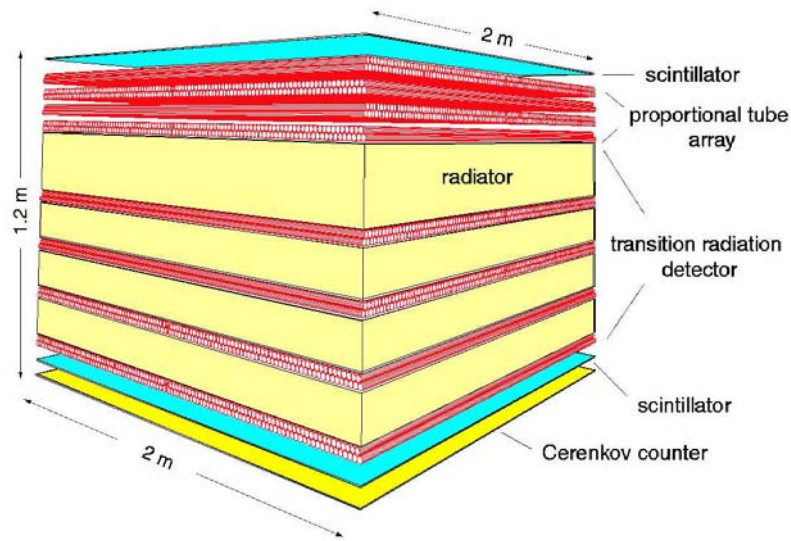


Figure 1. Schematic drawing of TRACER

wire proportional chambers (MWPCs), permits the operation of the detector in a low-pressure environment, thus making the use of a heavy pressure vessel unnecessary.

3. Detector Response

Each of the sub-detectors generates a signal which is essentially proportional to the square of the particle charge and which exhibits a characteristically different response to the energy E or Lorentz factor $\gamma = E/mc^2$ of the particle. It is the interplay between the detectors that permits the precise identification of charge and energy of cosmic ray nuclei.

Cherenkov Response and Specific Ionization in Scintillators and Gas Counters

The two scintillation counters each consist of 8 sheets of BICRON 408 with each sheet measuring $100 \times 50 \text{ cm}^2$ in area. While the counters are only 0.5 cm thick, the light yield, detected with 24 photomultipliers (PMT) via wavelength shifter bars, is ~ 40 photoelectrons for singly charged particles, sufficient to provide single charge resolution for the heavier nuclei. The light yield increases with Z^2 but deviates from strict proportionality by 15 % for iron.

The Cherenkov counter is composed of four sheets of acrylic material ($100 \times 100 \times 1.27 \text{ cm}^3$) which is doped with blue wavelength shifter. The Cherenkov threshold is $\gamma \approx 1.35$, and the light output in saturation is about 2 - 3 photoelectrons per Z^2 , again measured with 24 PMTs via wavelength shifter bars. Figure 2 displays the "ideal" response for this material (labeled "CER").

As the counter is located at the bottom of the TRACER detector the response function is considerably modified due to δ -rays produced while the particle propagates through the detector material above the counter. The addition of the δ -rays leads to an enhancement of the signal and raises the saturation energy from $\gamma \approx 4$ to $\gamma \approx 10$. This effect is understood and has previously been studied quantitatively [3]. The modified response is

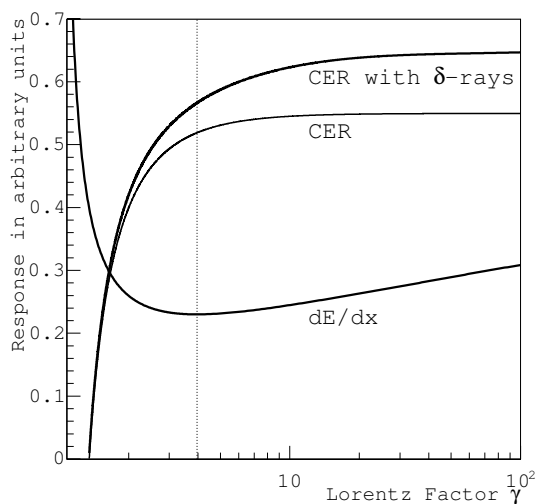


Figure 2. Energy response of the Cherenkov counter with and without taking into account the δ -rays and response function of the specific ionization detector. The dashed line indicates minimum ionization.

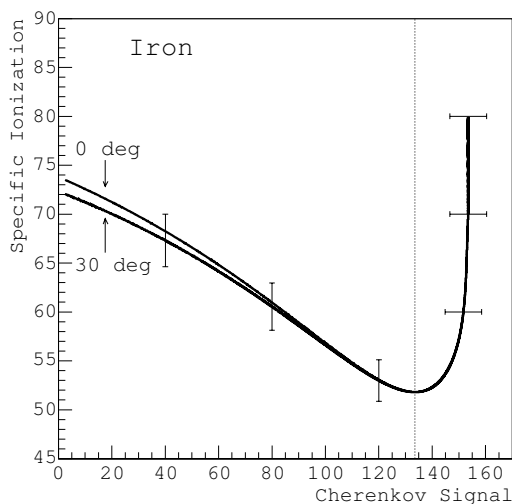


Figure 3. Correlation of specific ionization and Cherenkov signals. The error bars indicate 1σ fluctuations. The two lines on the low energy end represent 0° and 30° incidence angle (see text). The units are arbitrary.

displayed in figure 2 (labeled “CER with δ -rays”).

The prime purpose of TRACER is a measurement of cosmic-ray nuclei at the highest energies. This is accomplished with the dE/dx – TRD system which contains 1600 proportional tubes as active detector elements. Each tube has a wall of $150\ \mu\text{m}$ of aluminized mylar, is 200 cm long and 2 cm in diameter and is filled with a mixture of xenon and methane.

The TRD system is designed for measurements from $\sim 400\ \text{GeV/amu}$ to energies well exceeding 10,000 GeV/amu . Particles at these energies are extremely rare, and care must be taken to insure that no misidentification of particles with lower energies occurs due to fluctuations in response. To accomplish this the dE/dx system is essential. This system utilizes the relativistic rise in the specific ionization to discriminate highly relativistic particles from those with lower energies. The measurement of the specific ionization also provides an estimate of the particle energy from 10 - 400 GeV/amu .

However, the specific ionization response, well described by the Bethe-Bloch equation, is degenerate in energy below and above minimum ionization (see dE/dx curve in figure 2). The signal of the Cherenkov counter breaks this degeneracy. The correlation of dE/dx and Cherenkov detector is shown in figure 3. The dashed line indicates how a cut on the Cherenkov signal effectively suppresses low energy particles. In practice, this correlation also provides a normalization of the response curves of both the dE/dx detector and the Cherenkov counter [2]. As shown in figure 3 the correlation has a slight dependence on the zenith angle at the lowest energies. This dependence is due to the fact that particles on inclined trajectories traverse more material and hence, lose more energy by ionization on their way from the dE/dx detector to the Cherenkov counter.

Energy Measurement with the TRD

The key to using a TRD is that the energy response can be calibrated with singly charged particles at accelerators over a wide range of Lorentz factors. The radiators used to generate TR in TRACER are made from

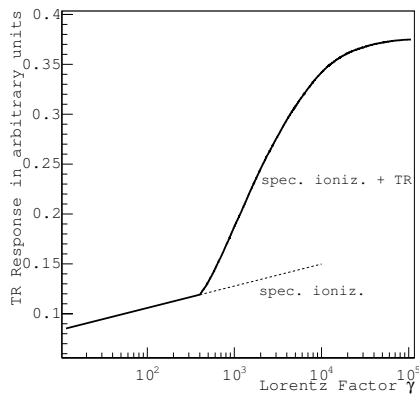


Figure 4. Energy response of the Transition Radiation Detector

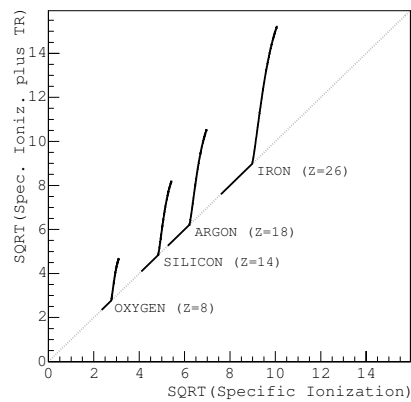


Figure 5. Correlation of responses of Transition Radiation and specific ionization detectors. Four elements are displayed to illustrate the charge dependence of the responses.

plastic fibers and are the same that were used on the Cosmic Ray Nuclei detector (CRN, [4]). The response for this detector is shown in figure 4.

In practice, the combined responses of dE/dx and TRD are used to measure the energy. The correlation of these two responses is displayed in figure 5. Up to 400 GeV/amu both the dE/dx and TRD signals are due to ionization only and are therefore the same. Above this energy TR becomes observable and lifts the correlation above the diagonal. This allows the identification of the very rare highest energy events with no low-energy background.

4. Outlook

The following three contributions to this conference will describe the analysis of the data obtained from the long-duration flight of TRACER in Antarctica [2] and the derivation of the energy spectra of the individual elemental species [5], and will discuss the relevance and astrophysical implications of the results [6].

This work has been supported by NASA grants NAG5-5305 and NN04WC08G.

We thank German Hermann (at MPIK Heidelberg, Germany) for numerous contributions to the design, construction and first flight of the instrument.

References

- [1] Gahbauer, F.H. et al. ApJ. 607, 333, 2004
- [2] Romero-Wolf, A. et al., 29th ICRC, Pune (2005) OG1.1
- [3] Gahbauer, F.H. et al., 28th ICRC, Tsukuba (2003) OG1.5, 2245
- [4] L'Heureux, J. et al., NIM Phys. Res., 295, 246, 1990
- [5] Boyle, P. et al., 29th ICRC, Pune (2005) OG1.1
- [6] Müller, D. et al., 29th ICRC, Pune (2005) OG1.1

Measurements with TRACER: Discussion of Results and Future Prospects

D. Müller^a, M. Ave^a, P.J. Boyle^a, F. Gahbauer^a, C. Höppner^a, J. Hörandel^b, M. Ichimura^c, A. Romero-Wolf^a, S. Wakely^a

(a) Enrico Fermi Institute, University of Chicago, 5640 South Ellis Avenue, Chicago, IL 60637

(b) University of Karlsruhe, Germany

(c) Hiroasaki University, Japan

Presenter: D. Müller (dmuller@uchicago.edu), usa-muller-D-abs1-og11-oral

The individual energy spectra and relative abundances measured with TRACER, are compared with previous measurements in space and balloons, and with interpretations of air shower data. From the individual spectral slopes, we discuss constraints on models of cosmic-ray propagation through the galaxy. We also discuss the extrapolated high-energy abundances of the elements at the cosmic ray sources. The TRACER instrument is currently being refurbished for a second long duration balloon flight. The dynamic range of the measurement will then be extended to include the lighter cosmic ray nuclei, down to boron ($Z = 5$).

1. Introduction

The measurements of the cosmic-ray composition with TRACER [1] cover a very wide range of energies, but the present discussion will concentrate on results at the highest energies, up to 10^4 GeV/amu. Key questions are how the current measurement extends previous results, how the data constrain models of cosmic-ray propagation in the Galaxy, how compatible direct measurements are with interpretations of air-shower observations, and what can be learned about the source composition of the sources of high-energy cosmic rays.

2. Comparison with other Measurements

At energies below 40 GeV/amu, we compare TRACER results with measurements in space on HEAO-3 [2] and at higher energies with data from CRN on the space shuttle [3]. Results from the passive balloon-borne detectors JACEE [4] and RUNJOB [5] extend to higher energies than the TRACER data, albeit with very limited statistics, and only for groups of elements. Figure 1 illustrates the generally good agreement in absolute intensity between the TRACER data and the results from the space-borne detectors. As absolute intensities are plotted, without any arbitrary normalizations, but multiplied with $E^{2.5}$, this agreement indicates that systematic uncertainties are small.

An exception are the relatively rare elements S, Ar and Ca. For these, the intensities obtained from the relativistic rise of specific ionization between 10 and 400 GeV/amu tend to be higher than the HEAO data would suggest. We believe that there could be contamination in our data in this region due to insufficient charge resolution. However, this affects only these three elements, and only in the intermediate energy region. The intensities derived from the TRD measurement at the highest energies are clearly separated in charge without contamination for all elements. The highest energy results for S, Ar, and Ca are the first that have been reported for these elements. The statistical errors of the TRACER results are smaller than those of CRN, and the TRACER data extend to higher energies. Unusual features in the spectra, such as flattening or steepening are not obvious and we do not observe a steep silicon spectrum as was suggested from early data from CRN and RUNJOB.

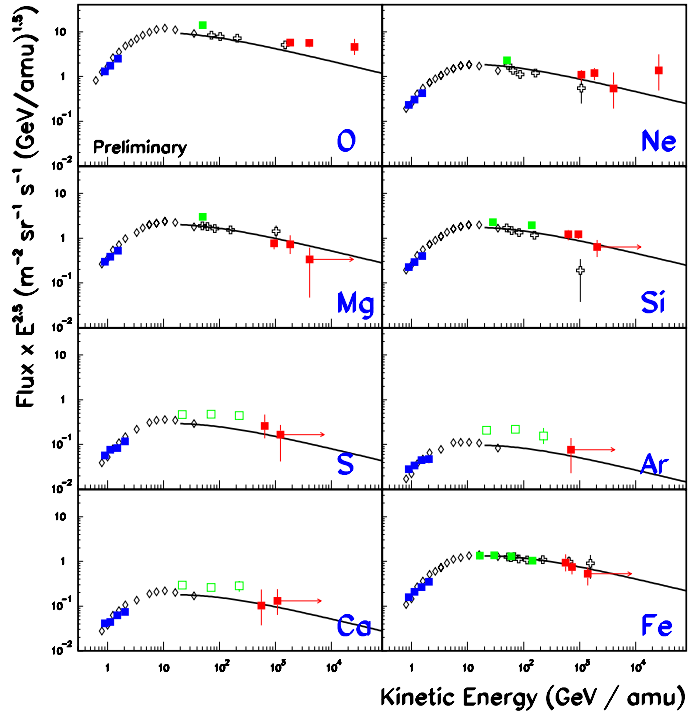


Figure 1. Differential energy spectra, multiplied by $E^{2.5}$, from TRACER (solid squares), HEAO-3 (open diamonds), and CRN (open crosses). The curves refer to predictions from a simple propagation model (see text).

In figure 2 the TRACER data for oxygen and iron are compared with results from the JACEE [6] and from the RUNJOB [5] balloon flights, and with spectra derived from indirect observations of the EAS-TOP collaboration [7], and of the KASCADE group assuming different nucleus-nucleus interaction models [8]. However, these groups do not report results for individual elements: the “CNO group” probably have about twice the intensity than oxygen alone, while the “iron group” probably is dominated by iron. Our results do not yet overlap with the energy region of the air shower data, but the gap is becoming smaller, in particular, for oxygen. Additional measurements will indeed lead to significant constraints on the air shower interpretations.

3. Propagation in the Galaxy

The results from HEAO-3 and CRN have previously been parameterized in a simple propagation model with differential source spectra $\propto E^{-2.2}$, and an escape path length $\Lambda \propto R^{-0.6}$ for rigidities $R > 20$ GV [9]. The spectral slope observed for a given species and energy would then result simply from the equilibrium between production in the source and loss by diffusion (diffusion coefficient $\propto E^{0.6}$) or spallation (energy-independent, but cross section increases with nuclear mass). Expected spectra according to this model are shown as curves in Figure 1. It is apparent that the new data from TRACER do not indicate a significant departure from this model.

However, it has often been argued that there might be an energy-independent residual pathlength Λ_0 in addition to the $E^{-0.6}$ dependence of the pathlength, i.e. $\Lambda(E) = AE^{-0.6} + \Lambda_0$. This would lead to a hardening of the energy spectra at the highest energies, as perhaps suggested in our oxygen data. A more detailed analysis of the TRACER data constrains the value of Λ_0 to $\Lambda_0 \leq 0.15 \text{ g/cm}^2$.

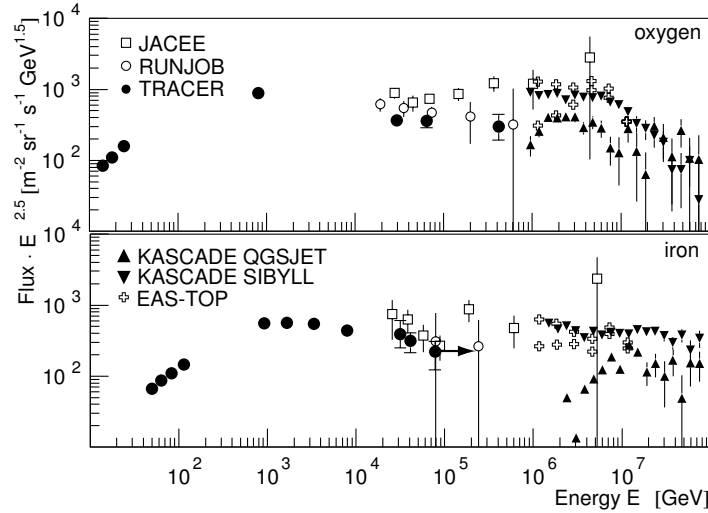


Figure 2. Energy Spectra from the balloon detectors TRACER, JACEE (as quoted in [6]), and RUNJOB, and from the interpretation of air shower data of KASCADE (for two different interaction models) and of EAS-TOP (two data points for each energy are given, representing upper and lower limits). The spectra are for oxygen and for iron for TRACER, but for the “CNO-group” and the “Fe-group” for the other observations. Note that the spectra are plotted versus total energy per particle.

4. Composition of the Cosmic-Ray Source

The elemental abundances of cosmic rays at lower energies, as compared to the solar system, favor elements with low first ionization potential (FIP), or “refractories” with high condensation temperature [10]. In the interstellar medium, the refractories are preferentially frozen out in dust [11]. Figure 3 shows the abundances of the elements at the cosmic ray source from our measurements around 100 and 1000 GeV/amu, assuming the same propagation model as illustrated in Figure 1. Compared with solar system abundances [12], the TRACER results again exhibit the familiar FIP/volatility correlation. This behavior perhaps is a little more pronounced for the CRN results, although these cover fewer elements and have inferior statistics.

5. Future Prospects

The TRACER measurements provide significant new information on high-energy cosmic-rays, but still remain statistics limited. Additional flights of TRACER will help to improve this situation, but the TRD technique must eventually be utilized in extended space flights. The current TRACER instrument is limited in dynamic range for measurements of the elements oxygen to iron. This limitation is not intrinsic to the technique but due

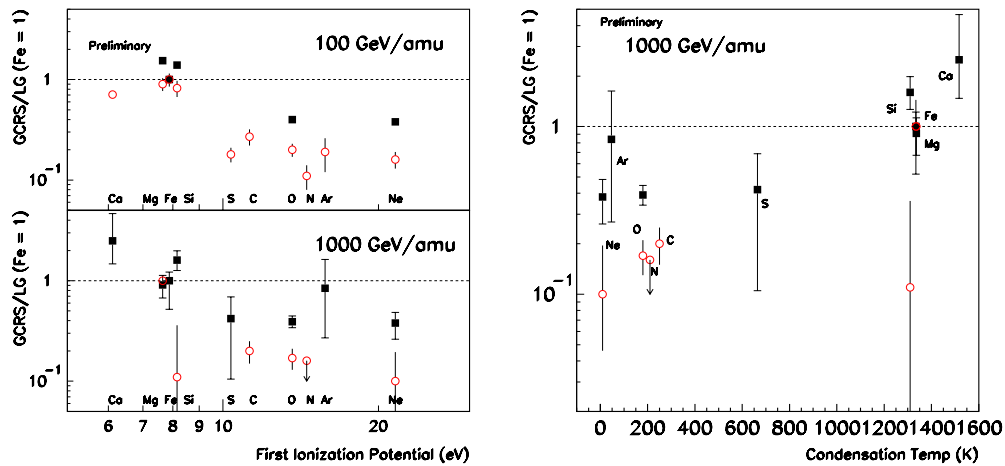


Figure 3. Abundances of the elements in the cosmic-ray source relative to local galactic abundances, plotted versus the first ionization potential (FIP), or versus the condensation temperature. Data from TRACER (squares) and CRN (open circles).

to the electronics used in the 2003 flight. An upgrade of the electronics, currently in progress, will extend the measurements down to boron ($Z = 5$) and hence, determine the propagation pathlength at high energies from the abundance of Boron relative to its "parents", mostly carbon and oxygen. Another long-duration balloon flight of the upgraded TRACER detector is planned for 2006.

This work has been supported by NASA grants NAG5-5305 and NN04WC08G.

References

- [1] Boyle, P.J. et al., 29th ICRC, Pune (2005) OG1.1
- [2] Engelmann, J.J. et al, *Astron. Astrophys.*, 233, 96, 1990
- [3] Müller, D. et al, *ApJ.* 372, 356, 1991
- [4] Takahashi, Y et al, *Nucl. Phys. B (Proc. Suppl.)* 60B, 83, 1998
- [5] Furukawa, M et al, *Proc. 28th ICRC Tsukuba*, 1, 203, 2003
- [6] Shibata, T. *Nucl. Phys. B (Proc. Suppl.)* 75A, 22, 1999
- [7] Navarra, G. et al, 28th ICRC Tsukuba, 1, 147, 2003
- [8] Antori, T. et al, *Astropart. Phys.*, in Press 2005, astro-ph/0505413
- [9] Swordy, S.P. et al, *ApJ.* 349, 625, 1990
- [10] Meyer, J.P. et al, *ApJ.* 487, 182, 1997
- [11] Ellison, D.C. et al, *ApJ.* 487, 192, 1997
- [12] Grevesse, N. et al, *ASP Conf. Ser.* 99, *Cosmic Abundances*, 117, 1996

Antarctic Balloon Flight and Data Analysis of TRACER

A. Romero-Wolf, M. Ave, P. Boyle, F. Gahbauer, C. Höppner, J. Hörandel^a,
M. Ichimura^b, D. Müller, S. Wakely

Enrico Fermi Institute, University of Chicago, 5640 South Ellis Avenue, Chicago, IL 60637

(a) University of Karlsruhe, Germany (b) Hirosaki University, Japan

Presenter: A. Romero-Wolf (afromero@uchicago.edu), usa-romero-wolf-A-abs1-og11-oral

The TRACER cosmic-ray detector was successfully flown from McMurdo, Antarctica in December 2003. The instrument has a geometric factor of $5 \text{ m}^2 \text{ ster}$ and provided measurements of cosmic ray nuclei from oxygen to iron ($Z=8$ to $Z=26$). The analysis of the data begins with the reconstruction of the trajectory of each nucleus through the instrument. Subsequently, the elemental charge Z and the particle energy are measured from 0.5 to 10,000 GeV/amu. This process uses known response functions and fluctuations in response of the individual detector elements, and the procedures are verified with extensive computer simulations. The analysis is able to cleanly select the very rare events at the highest energies without contamination due to low energy background which is more abundant by about a factor of $\sim 10^4$.

1. Introduction

The concept of the TRACER instrument for the detection of high-energy cosmic-ray nuclei was first demonstrated with a successful test flight from Fort Sumner, NM in 1999 [1]. To obtain data with much improved statistics, a long-duration balloon (LDB) flight is required, and was conducted from McMurdo, Antarctica in 2003, at the first opportunity when a launch vehicle compatible with the weight of TRACER ($\sim 1600\text{kg}$) was available at that site. The LDB flight yielded a total exposure of $50 \text{ m}^2 \text{ ster days}$ at an average altitude of 3.9 g/cm^2 . In contrast to Fort Sumner, the high geomagnetic latitude at McMurdo exposes TRACER to a large flux of low energy particles. The instrument must therefore avoid the mis-identification of low energy particles while retaining high efficiency for the detection of the rare high-energy events. Keeping this requirement in mind, the analysis procedure aims at identifying the particle species with single charge resolution and measuring the particle energy E , or Lorentz factor $\gamma=E/mc^2$, over four orders of magnitude.

2. Analysis Procedure

The data analysis proceeds by first determining the trajectory of each cosmic-ray particle through the detector system, then determining charge Z and energy E for each event, and finally, evaluating all efficiency losses due to the various cuts in the data. Monte Carlo simulations are necessary to test and refine the data analysis procedure. Extensive simulations of the TRACER detector as well as other analytical tools have been developed that run in parallel with each step in the analysis procedure. Wherever possible, the results of the simulations are verified with the measured data themselves.

2.1 Simulations

The TRACER simulation code (TSIM) is a GEANT4 [2] based simulation of the detector. The code includes the geometry of the individual instrument components and uses the “G4hIonisation” model of the energy deposited and δ -ray production in each part of the detector. The program generates a simulated cosmic-ray data set, which is then subjected to the same analysis procedures as the real flight data. In addition, simpler

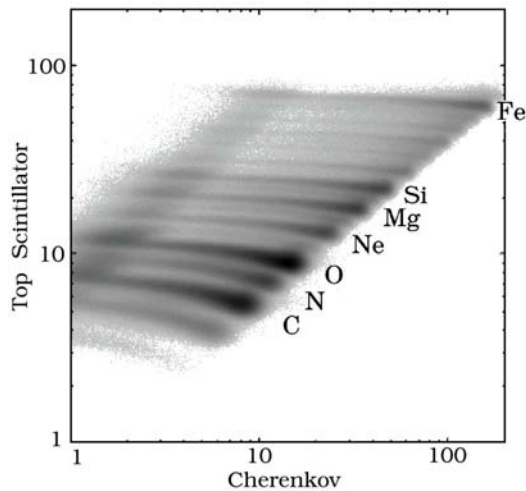


Figure 1. Scatter plot of top scintillator vs. Cherenkov signal in arbitrary units.

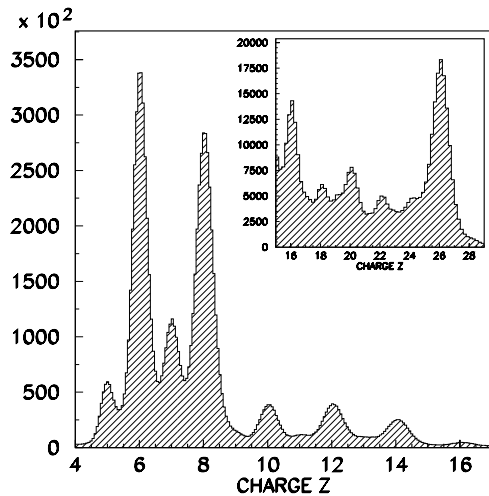


Figure 2. Charge histogram for all events measured in flight.

simulations have been developed to model fluctuations in the detector and δ -ray effects where TSIM was found to be impractical.

2.2 Trajectory Reconstruction

Each particle travels through sixteen layers of 2cm diameter proportional tubes (see figure 1 in [3]). These are oriented in two orthogonal directions and thus provide all details about the particle trajectory. Using the positions of the centers of all tubes that show signals above threshold, a first estimate of the trajectory is obtained. Due to the cylindrical shape of the tubes, the pathlength through each tube along the particle trajectory is generally different. However, the signal amplitude measured in each tube is proportional to the pathlength within statistical fluctuations. This fact is applied to determine a refined track fit. The average total pathlength through all tube layers is 24 cm for particles incident within the acceptance cone of the instrument.

Including the geometry of the proportional tube array in the simulation, the tracking accuracy is determined by comparing the simulated track with the track reconstructed by the analysis routine. Typically, the reconstructed track has an accuracy of 2mm in the impact parameter, and 8 mm (3 %) for the total pathlength through all tubes. The tracking efficiency is determined by counting the number of simulated events that pass the track quality cuts. The tracking efficiency is 95%.

2.3 Charge Identification

The charge of a particle traversing the instrument is determined primarily from the scintillator signals. Note that the scintillators are only 5 mm thick. Their response exhibits spatial non-uniformities which are mapped with muons on the ground and with flight data. The response maps, together with the trajectory information, are used to correct the signal for each event. The presence of low energy particles, with signals larger than minimum ionization, requires to combine the scintillator signals with an energy scale; otherwise the charge

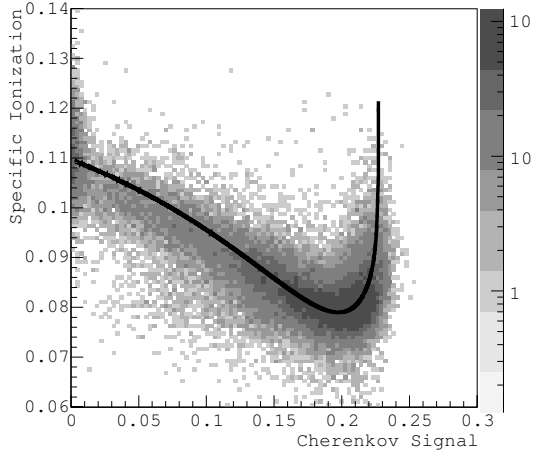


Figure 3. Scatter plot of dE/dx vs. Cherenkov signals for iron nuclei. The black line is the average response obtained from simulations. The units are arbitrary.

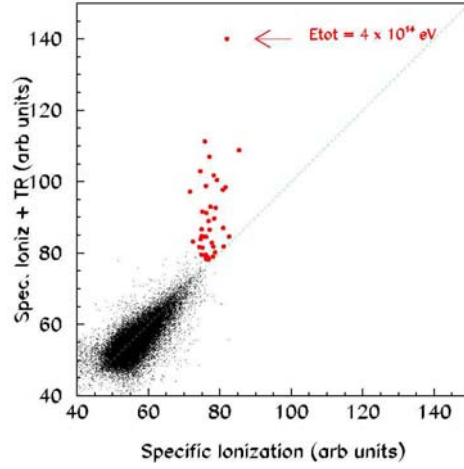


Figure 4. Scatter plot of TR vs. dE/dx signal for iron nuclei. The units are arbitrary.

resolution from scintillator measurements becomes smeared out. This scale is provided by the Cherenkov counter signal. Figure 1 shows the correlation plot of top scintillator signal vs. Cherenkov signal. From this scatter plot lines of constant charge are identified. By summation along these lines the charge histogram shown in figure 2 is obtained. The charge resolution (1σ) is 0.3 charge units for oxygen and 0.5 charge units for iron.

2.4 Energy Measurement

The energy measurement results from the combination of three types of detector covering a range of 0.5 GeV/amu to 10,000 GeV/amu: The Cherenkov counter measures the energy of a particle from 0.5 GeV/amu up to saturation around 10 GeV/amu. For higher energies the energy is obtained from the measurement of the specific ionization and its relativistic rise in the top eight layers of proportional tubes (dE/dx), or the detection of x-ray transition radiation in the bottom eight layers of proportional tubes (TRD). (For details of the configuration see [3].) To find the average dE/dx the signal ΔE_i in each tube along the particle trajectory is taken along with the corresponding pathlength Δx_i in the tube. The summation $dE/dx = \sum \Delta E_i / \sum \Delta x_i$ gives the overall value of the specific ionization. In this summation, the tubes with small pathlengths, $\Delta x_i < 1\text{cm}$, are excluded since fluctuations in the signal increase for shorter pathlength. The average TR signal is found in the same manner using tubes in the TRD layers.

With simulated data generated by TSIM the signal fluctuations in the proportional tube array are determined and compared to the fluctuations measured from the data. For instance, for iron the measured dE/dx fluctuations are 3% while the simulated fluctuations are 2%. The increase in the measured value is due to the tracklength uncertainty ($\sim 3\%$, see section 2.2). Hence, simulations and data agree quite well.

The energy deposit in a gas proportional tube is described by the Bethe-Bloch formula. It is degenerate in energy: a signal larger than minimum ionization could either be generated by a low-energy particle, or could be elevated due to the relativistic rise in dE/dx with energy. To break the degeneracy the energy scale provided

by the Cherenkov counter is used. Figure 3 shows a scatter plot of dE/dx vs. Cherenkov signals for iron nuclei. The correlation follows closely the pattern predicted by simulations [3]. With the combined signals of dE/dx and Cherenkov the minimum ionization point in the dE/dx signal is identified, and the corresponding Cherenkov signal distinguishes between low and high energy particles. The Cherenkov signal provides an energy measurement for particles below the minimum ionization energy.

Simulations have been used to study the effect of δ -rays generated while the particle traverses the detector. It is found that δ -ray contributions on proportional tube signals are negligible; however, they produce increased signals in the large-area scintillator and Cherenkov counters at the bottom of the instrument [4]. The effects of δ -rays are taken into account in the analysis and are verified with the data.

To measure the energy of a particle at higher energies, above 10 GeV/amu, the combined responses of TR and dE/dx are used. Figure 4 shows the correlation of the TR signal with the dE/dx signal for iron data. For events with energies below 400 GeV/amu, the onset of transition radiation, the signals are well correlated along the diagonal. The energy assigned to these events is obtained from a parameterization of the relativistic rise in the energy deposited in a gas tube [3]. Signals at energies higher than 400 GeV/amu have a significant contribution from transition radiation and are identified on the scatter plot in figure 4 by their location above the diagonal. The events are assigned an energy according to a parameterization of the TR response curve [3]. Note that these rare events at the highest energies (representing a fraction of the order of 10^{-4} of all detected iron nuclei) stand out in the scatter plot without any significant contribution of background.

The signal fluctuations for each component of the detector depend on the charge of the particle and its energy. For example, the corresponding energy resolution of the Cherenkov counter measurement for iron is 20% at 3 GeV/amu, but 40% with dE/dx at 20 GeV/amu and <10% for the TRD at 1,000 GeV/amu.

3. Conclusions

The long-duration balloon flight of TRACER has provided a statistically significant data set of cosmic ray nuclei from oxygen to iron up to TeV/amu energies, or even beyond. High energy events are clearly discriminated against the low energy background. The measurements cover four decades in energy with single charge resolution. The resulting energy spectra are presented in [5].

We gratefully acknowledge the services of the National Scientific Balloon Facility and of the NSF Antarctic Program. This work has been supported by NASA grants NAG5-5305 and NN04WC08G.

References

- [1] Gahbauer, F.H., et al., *Astrophysical Journal*, 607:333-341, 2004.
- [2] Agostinelli, S., et al., *Nucl. Instrum. Methods Phys. Res.*, 506, 250, 2003
- [3] Höppner, C., et al., 29th ICRC, Pune (2005), OG1.1
- [4] Gahbauer, F.H., et al., 28th ICRC, Tsukuba (2003), OG1.5, 2245
- [5] Boyle, P., et al., 29th ICRC, Pune (2005), OG1.1

Solar modulation of cosmic rays in the energy range from 10 to 20 GeV

I. Braun^{a,1}, J. Engler^a, J.R. Hörandel^a, J. Milke^a

(a) University and Forschungszentrum Karlsruhe, P.O. Box 3640, 76021 Karlsruhe, Germany

(1) now at Max Planck Institute for Nuclear Physics, P.O. Box 103980, 69029 Heidelberg, Germany

Presenter: J.R. Hörandel (hoerandel@ik.fzk.de), ger-hoerandel-J-abs3-sh34-poster

The flux of single muons with energies above 0.7 GeV has been recorded from 1993 to 2005 using a muon telescope, located in southern Germany. The registered events originate from primary cosmic rays with energies around 10 to 20 GeV, thus extending the energy range covered by neutron monitors to higher energies. Correlations of the time dependence of the muon flux with heliospheric parameters have been analyzed using data from the muon telescope and the worldwide neutron monitor network as well as simulations. Variations on time scales of the solar cycle, the solar rotation, and the Earth's rotation are investigated.

1. Introduction

Galactic cosmic rays traverse the heliosphere and interact with its varying fields yielding a variation of the cosmic-ray flux with solar activity. At energies up to about 10 GeV, the modulation effect is measured in detail by the well established world wide neutron monitor network. The present experiment uses secondary muons corresponding to more energetic cosmic-ray protons that are still modulated by the heliosphere. This allows to study energy dependent differences like in the amplitude of solar modulation. In addition, an annual modulation of cosmic rays can occur due to heliospheric anisotropies. The relative movement of the Earth around the sun and within the interstellar medium generates the Compton-Getting effect. Low energy cosmic-ray particles travel mainly along curved field lines in the heliospheric neutral current sheet (NCS), inward or outward according to the magnetic polarity of the heliosphere. These fields rotate with a period of approximately 27 days and overtake the Earth in its orbit creating a flux variation dependent on local time.

A muon telescope located at Forschungszentrum Karlsruhe, Germany (49°N, 8°E), consisting of two layers of scintillators separated by a lead filter, records the flux of single muons with energies above 0.7 GeV continuously since 1993. The experimental setup is described in detail in [1]. Simulations with CORSIKA (with the hadronic interaction model UrQMD) and GEANT 3.21 using a parametrized cosmic-ray spectrum at the top of the atmosphere [2] ($M = 750$ MV) revealed that the registered events originate from primary cosmic rays with energies around 10 to 20 GeV with a maximum at 15 GeV. 90% of the triggered events are caused by primary protons with zenith angles smaller than 15°.

The muon rate dN was iteratively corrected for an atmospheric pressure of 1013 hPa and a height of the typical muon production layer of 13.6 km (~ 150 g/cm²) for each year, yielding correction parameters of $dn/dp = (-0.12 \pm 0.04)$ %/hPa and $dn/dh = (-3.8 \pm 1.2)$ %/km. For a consistency check, a rough estimate of the muon lifetime can be deduced from these values, assuming that all muons are produced with the same energy at the same atmospheric depth. The obtained lifetime of 2 ± 0.5 μ s is consistent with the expected value.

2. Results

Variability on Timescales of the Solar Cycle

The traditional key parameter to quantify solar activity is the international sunspot number (ISSN), which is provided by the Sunspot Index Data Center [3]. As a measure for the correlation between cosmic-ray intensity

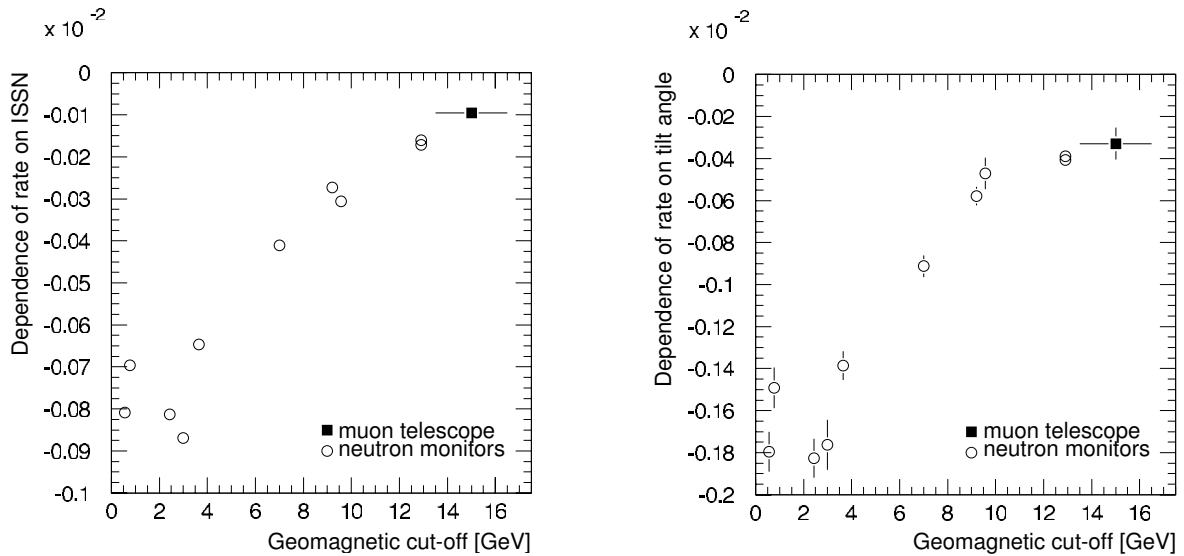


Figure 1. Dependence of neutron and muon count rate on the sunspot number (left) and on the tilt angle of the heliospheric neutral current sheet (right) for different cut-off parameters.

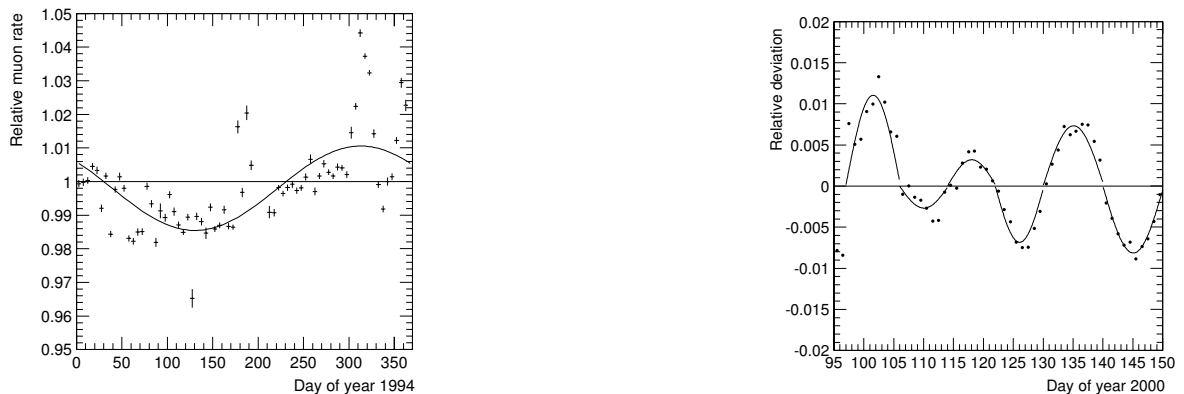


Figure 2. *Left:* Measured annual variation of the muon rate in 1994. *Right:* Example for the difference between the muon rate smoothed over 9 days and the rate smoothed over 29 days. Sine functions have been fitted to the data between subsequent zero crossings.

and solar activity, the slopes of linear fits to the muon and neutron count rates as a function of the sunspot number were used. The same was done for the dependency on the average tilt angle of the NCS over one Carrington rotation [4], which relates to the electromagnetic structure of the heliosphere. Fig. 1 shows the good correlation between both solar modulation parameters and the geomagnetic cut-off rigidity of several neutron monitor sites (open circles). The cut-off rigidity defines the typical energy of the primary particles. For the muon telescope, the typical primary energy has been derived from simulations. Its total flux variability of about $\pm 1.5\%$ over the solar cycle follows the trend of the neutron monitors. It is also consistent with a simulated value of $\pm 2.4\%$ using the spectral sensitivity of the instrument and a parametrized energy spectrum of cosmic rays [2] for modulation parameters obtained from [5].

Annual Variability

The muon flux after atmospheric correction was scanned for annual variation in the years 1994 to 2005. Only for 1994 a significant signal with an amplitude of $\pm 1.2\%$ could be detected (Fig. 2, left). This agrees with a decreasing strength of such a modulation seen in the neutron monitor data as well. The maximum in 1994 occurs on day 313 (November 9th). Averaging over all years we obtain a maximum at day 278 (October 5th) which coincides with the average maximum for the neutron monitors on the same day. The phase of this modulation seems to be nearly independent of energy, while the amplitude decreases with primary energy. For example, in 1993 the modulation amplitude of the neutron rate ranges from about 1.5% at 0.6 GV to 0.3% at 12.9 GV.

Solar Rotation

Effects following the solar rotation are expected to have time scales of approximately 25.7 to 33.5 days, depending on the heliospheric latitude of their origin. Half that periodicity is expected for disturbances symmetric to the solar rotation axis. In addition to irregular events on the solar surface, NCS crossings (the magnetic polarity surrounding the Earth) can cause variations on both time scales. Instead of a harmonical analysis, a more flexible method was used: a running mean over 29 days was subtracted from a running mean over nine days to eliminate effects on shorter and longer time scales. Between zero crossings, a sine-function was fitted to the data as indicated in Fig. 2, right. Amplitudes in the order of 0.5 – 3% were detected throughout the data, apparently with larger amplitudes when mayor drops in the NCS tilt angle occurred during the phase of rising solar activity. The average variation period of 22.0 days is shorter than expected.

Diurnal Variation

The hourly muon rates were normalized to a daily average and added up from October 1993 to May 2005. The sum of two sine-functions with twelve and 24 hour periodicity was fitted to analyze the dependence on local time. As seen in Fig. 3, the data are described well by the function $dN = 0.15\% \cdot \cos(2\pi/24 \cdot (h - 14.4)) + 0.05\% \cdot \cos(2\pi/12 \cdot (h - 0.2))$, where h is the local time. When separating the data into subsets of different heliospheric sectors according to [6], phase and amplitude of the diurnal variation stay the same within errors, while the semidiurnal component in the Toward-sector is stronger than in the Away-sector by a factor of three.

Individual Events

The high energy threshold of the muon telescope usually impedes direct detection of solar protons, but extremely energetic events as well as magnetic field disturbances could be detected as a drop in the muon rate. The strongest solar activity period so far occurred from October 19th to November 4th, 2003. The measured muon rate in comparison with the rate registered by the Climax neutron monitor is shown in Fig. 3 (right). Both instruments observe similar variations as a function of time, in particular a coincident drop in the rate on October 29th, 2003. This indicates the strength of this event, which influenced the proton flux even above 10 GeV.

3. Conclusion

Effects of solar modulation have been studied using neutron monitors with geomagnetic cut-off energies between 0.6 and 12.9 GV. The results were compared to data from a muon telescope sensitive to primary cosmic rays with energies from 10 to 20 GeV. For various observables the variations of the muon data follow the energy dependence indicated by the neutron monitors. This demonstrates that muon telescope data can be used to complement neutron monitor observations at high energies.

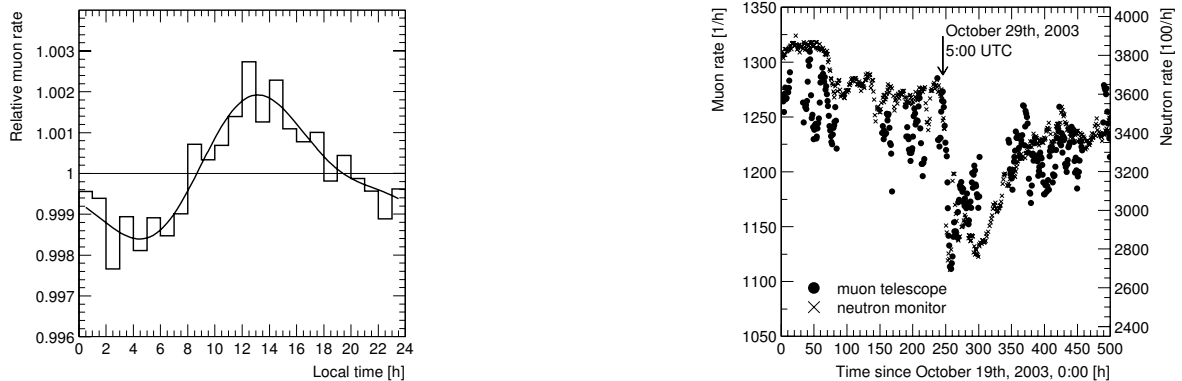


Figure 3. *Left:* Average diurnal variation of the muon rate after atmospheric correction and normalization to the daily average. *Right:* Muon rate (counts/hour) smoothed over 5 hours from October 19th to November 8th, 2003 compared to the Climax neutron monitor rate (counts/hour/100).

4. Acknowledgments

The neutron monitor data were kindly provided through the on-line databases of the Polar Geophysical Institute of the Russian Academy of Sciences (Apatity, geomagnetic cut-off 0.6 GV), the Sodankyl Geophysical Observatory of the University of Oulu, Finland (0.8 GV), the Solar-Terrestrial Physics Division of Izmiran, Russia (Moscow, 2.4 GV), the Space Physics Data System of the University of New Hampshire, USA (Climax, 3.0 GV and Haleakala, 12.9 GV), the Irkutsk Neutron Monitor, the Unit of Space Physics at North-West University Potchefstroom, South Africa (Potchefstroom: 7.0 GV and Tsumeb, Namibia: 9.2 GV), and the Institute of Space Physics Beijing, China (9.6 GV).

We are grateful to Mrs. Heike Bolz for the continuous operation of the muon telescope.

References

- [1] J. Engler et al., *Nuclear Instruments and Methods A* 427 (1999) 528.
- [2] I.H. Urch and L.J. Gleason, *Astronom. Space Sci.*, 426 (1972) 17.
- [3] Sunspot Index Data Center, Royal Observatory of Belgium (<http://sidc.oma.be>).
- [4] Wilcox Solar Observatory (<http://sun.stanford.edu/~wso/>).
- [5] I.G. Usoskin et al., *Proceedings 28th International Cosmic Ray Conference* (2003) 3803.
- [6] OMNIWeb Near-Earth Heliosphere Data, NSSDC Goddard Space Flight Center (<http://nssdc.gsfc.nasa.gov/omniweb/>).

Egret excess of diffuse galactic gamma rays as tracer of Dark Matter

C. Sander^a

(a) *Institut für Exp. Kernphysik (IEKP), Universität Karlsruhe, Wolfgang-Gaede-Str. 1, 76131 Karlsruhe, Germany*

Presenter: C. Sander (sander@ekp.physik.uni-karlsruhe.de) ger-sander-C-abs1-he23-oral

The public data from the EGRET space telescope on diffuse galactic gamma rays in the energy range from 0.1 to 10 GeV are reanalyzed with the purpose of searching for signals of Dark Matter annihilation (DMA). The analysis confirms the previously observed excess for energies above 1 GeV in comparison with the expectations from conventional galactic models. In addition, the excess was found to show all the key features of a signal from Dark Matter Annihilation (DMA): a) the excess is observable in all sky directions and has the same shape everywhere, thus pointing to a common source; b) the shape corresponds to the expected spectrum of the annihilation of non-relativistic massive particles into neutral π_0 mesons, which decay into photons. From the energy spectrum of the excess we deduce a WIMP mass between 50 and 100 GeV, while from the intensity of the excess in all sky directions the shape of the halo could be reconstructed. The DM halo is consistent with an almost spherical isothermal profile with substructure in the galactic plane in the form of toroidal rings at 4 and 14 kpc from the centre. These rings lead to a peculiar shape of the rotation curve, in agreement with the data, which proves that the EGRET excess traces the Dark Matter.

1. Introduction

Cold Dark Matter (CDM) makes up 23% of the energy of the universe, as deduced from the WMAP measurements of the temperature anisotropies in the Cosmic Microwave Background, in combination with data on the Hubble expansion and the density fluctuations in the universe (1). The Dark Matter has to be much more widely distributed than the visible matter, since the rotation speeds do not fall off like $1/\sqrt{r}$, as expected from the visible matter in the centre, but stay more or less constant as function of distance. For a "flat" rotation curve the DM has to fall off slowly like $1/r^2$ instead of the exponential drop-off for the visible matter. The fact that the DM is distributed over large distances implies that its properties must be quite different from the visible matter, since the latter clumps in the centre owing to its rapid loss of kinetic energy by the electromagnetic and strong interactions after infall into the centre. Since the DM apparently undergoes little energy loss, it can have at most weak interactions. In addition its mass is probably large, since it cannot be produced with present accelerators. Therefore it is generically called a WIMP, a Weakly Interacting Massive Particle.

Weakly interacting particles can annihilate, yielding predominantly quark-antiquark pairs in the final state, which hadronize into mesons and baryons. The stable decay and fragmentation products are neutrinos, photons, protons, antiprotons, electrons and positrons. From these, the protons and electrons disappear in the sea of many matter particles in the universe, but the photons and antimatter particles may be detectable above the background, generated by particle interactions. Such searches for indirect Dark Matter detection have been actively pursued, see e.g. the review by Bergström (2) or more recently by Bertone, Hooper and Silk (3).

The present analysis on diffuse galactic gamma rays differs from previous ones by considering simultaneously the complete sky map *and* the energy spectrum, which allows us to constrain both the halo distribution *and* the WIMP mass. More details have been given elsewhere (4; 5; 6; 7).

In the early universe all particles were produced abundantly and were in thermal equilibrium through annihilation and production processes. At temperatures below the mass of the WIMPS the number density drops exponentially. The annihilation rate $\Gamma = \langle \sigma v \rangle n_\chi$ drops exponentially as well, and if it drops below the

expansion rate, the WIMP's cease to annihilate. They fall out of equilibrium (freeze-out) at a temperature of about $m_\chi/22$ (8). For the present value of $\Omega_\chi h^2 = 0.113 \pm 0.009$ the thermally averaged total cross section at the freeze-out temperature of $m_\chi/22$ must have been around $2 \cdot 10^{-26} \text{cm}^3 \text{s}^{-1}$ (9). The observed annihilation rate will be compared with this generic cross section, which basically only depends on the expansion rate of the universe, i.e. on the value of the Hubble constant. However, it should be noted that this cross section may be energy dependent and the annihilation cross section in the present universe may be much smaller than the value deduced from the time of freeze out, when the temperature was $m_\chi/22 \approx$ several GeV. On the other hand the annihilation rate may be enhanced by the clustering of DM in "microhaloes", which increases the density locally. This unknown enhancement factor, usually called "boost factor", may vary from a few to a few thousand (10; 11). Given the uncertainty in the prediction of the boost factor, this can only be obtained from the data by keeping the normalization as free parameter.

2. Indirect Dark Matter Detection

The neutral particles play a very special role for indirect DM searches, since they point back to the source. The charged particles change their direction by the interstellar magnetic fields, energy losses and scattering. Therefore the gamma rays provide a perfect means to reconstruct the intensity (halo) profile of the DM by observing the intensity of the gamma ray emissions in the various sky directions. Of course, this assumes that one can distinguish the gamma rays from DM annihilation from the background, which is dominated by proton-proton interactions for gamma ray energies above 0.1 GeV. Both for DMA and pp collisions the gamma rays originate mainly from the decay of neutral pions, a light particle produced abundantly in the hadronization process of quarks into hadrons. However, the protons in the galaxies and consequently the quarks inside the protons have a steeply falling energy spectrum ($N \propto E^{-2.7}$). In contrast, the quarks from DM annihilation are mono-energetic, since the WIMPS annihilate almost at rest, so their mass is converted into kinetic energy of the quarks. Each quark thus obtains an energy corresponding to the mass of the WIMP, which yields a gamma ray spectrum with a sharp cut-off at the mass of the WIMP. So from the shape of the spectrum the WIMP mass can be deduced. The difference in spectral shape between DMA and background allows to obtain their absolute normalizations by fitting their shapes to the EGRET data. These shapes are well known from accelerator experiments and can be obtained e.g. from the PYTHIA code for quark fragmentation (12); the parameters in this code have been optimized to fit a wide variety of accelerator data with a single model, the string fragmentation model. The fit of the normalizations can be repeated in many different sky direction to obtain the halo profile of the DM. Given the WIMP *number density* in all directions from the flux of the excess and the WIMP *mass* from the spectrum allows to reconstruct the DM mass distribution in our galaxy, which in turn can be used to reconstruct the rotation curve.

A very detailed gamma ray distribution over the whole sky was obtained by the Energetic Gamma Ray Emission Telescope EGRET, one of the four instruments on the Compton Gamma Ray Observatory CGRO, which collected data during nine years, from 1991 to 2000. The EGRET telescope was carefully calibrated in the energy range of 0.02 to 10 GeV (13). It was already noticed in 1997 that the EGRET data showed an excess of gamma ray fluxes for energies above 1 GeV if compared with conventional galactic models (14).

Fitting the three contributions of galactic background, extragalactic background and DMA to the energy spectra of 180 independent sky directions yielded astonishingly good fits with the free normalization of the background agreeing reasonably well with the absolute predictions of the galactic models (15; 16) for the energies between 0.1 and 0.5 GeV. Above these energies a clear contribution from Dark Matter annihilation is needed, but the excess in different sky directions can be explained by a single WIMP mass. The fits for 3 different sky directions are shown in Fig. 1.

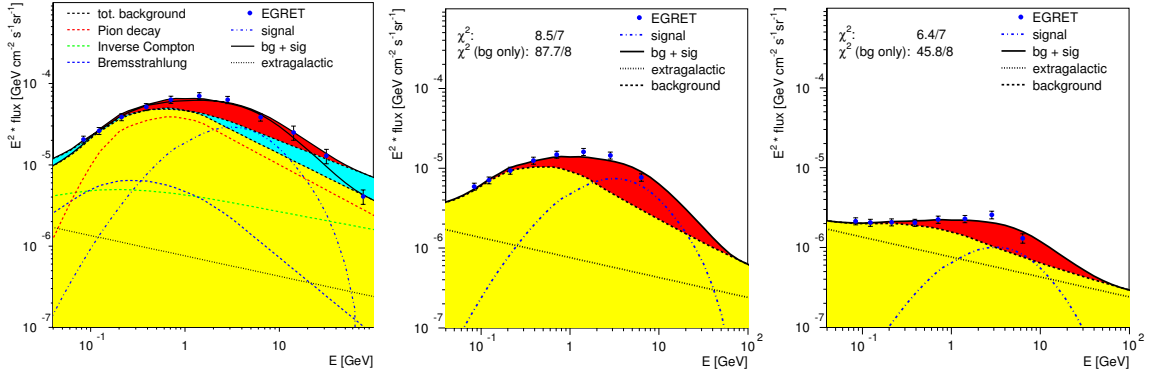


Figure 1. The diffuse gamma-ray energy spectrum of 3 angular regions: from left to right: towards the galactic centre (latitudes $0^\circ < |b| < 5^\circ$; longitudes $0^\circ < |l| < 30^\circ$), the galactic anticentre ($0^\circ < |b| < 10^\circ$; $90^\circ < |l| < 270^\circ$) and the pole regions ($60^\circ < |b| < 90^\circ$; $0^\circ < |l| < 360^\circ$), as measured by the EGRET space telescope. In the two panels on the right the solid straight line represents the fitted contribution from the extragalactic background, while the dotted line indicates the contribution from the annihilation from 65 GeV WIMPs. The total background (DMA) is indicated by the light (yellow) (dark (red)) shaded area, respectively. In the panel on the left the three data points above 10 GeV are for illustrative purposes. They were taken from Ref. (17), but due to the unknown systematic errors, they were not included in the fit. The various contributions to the background are indicated as well, while the uncertainties from the background are indicated by the medium shaded (blue) area. Here the upper edge of the medium shaded (blue) area corresponds to the hardest spectrum from Kamae et al. (18) with the power index of 2.5, while the lower edge corresponds to the shape of the conventional GALPROP model (17). Note that since the background normalization is left free, the low energy data (where only the background contributes) are always well fitted and different shapes only show up at larger energies.

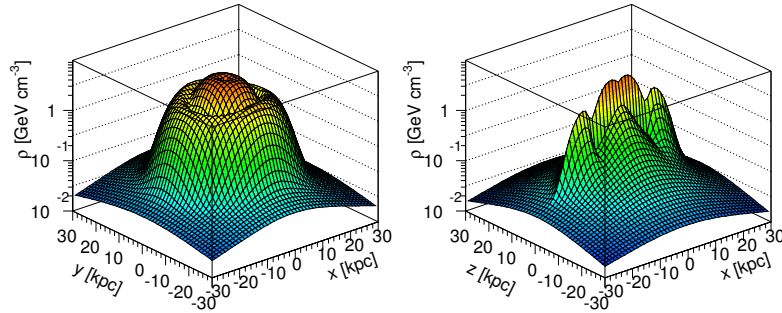


Figure 2. 3D-distributions of the haloprofile in the galactic xy-plane (left) and xz-plane (right). The ring structures at 4 and 14 kpc can be clearly seen.

Other ways to increase the excess would be to harden the spectra of the primary nuclei and electrons with respect to the locally measured spectra. Inhomogeneities in the spectra could happen e.g. by density fluctuations from the spiral arms or Supernovae explosions. However, such models do not describe the shape of the data very well, as can be seen e.g. from Fig. 9 of the so-called optimized model (17), which gives the best fit to the data so far, but still at energies above 2 GeV the model is below the data. Summing over more than 1400 data

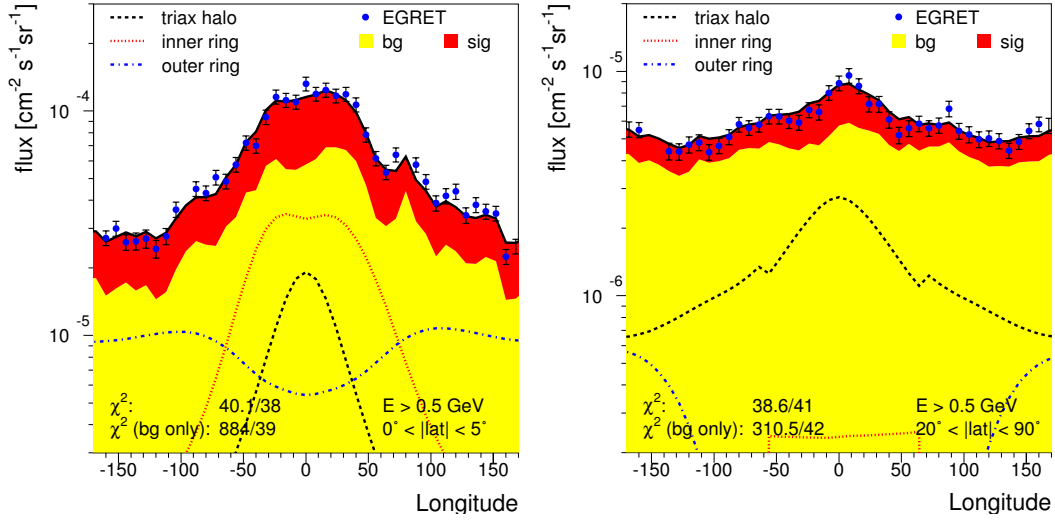


Figure 3. The longitude distribution of diffuse gamma-rays in the disk of the galaxy (left) and towards the galactic poles (right). The contributions of the inner ring, outer ring and isothermal triaxial halo to the excess in the disk can be clearly seen. The points represent the EGRET data.

points in 180 independent sky directions yields a probability for the fit of the spectral shape from the optimized model below 10^{-7} , if the error correlations between the different energy bands are taken into account. Details can be found elsewhere (6; 7). The problem of models without DMA: if the shape of the EGRET excess can be explained perfectly in all sky directions by a gamma contribution originating from the fragmentation of mono-energetic quarks, it is very difficult to replace such a contribution by an excess from nuclei (quarks) (or electrons) with a steeply falling energy spectrum.

From the excess in the various sky directions one can obtain the halo profile under the assumption that the clustering of the DM is similar in all sky directions. This is not necessarily true, since near the centre of the galaxy clumps may be tidally disrupted by the fly by of stars. The annihilation rate is in general proportional to $B\rho^n$, where B is the boost factor and n is between 1 and 2, depending on how much of the DM is clustered ($n=2$ for no clustering and $n=1$ if all DM is in clusters). Consequently one has many alternatives to fit, which are outside the scope of the present paper. Therefore we concentrate on a boost factor independent of r and $n = 2$, which turns out to yield a good fit.

The result is surprising: in addition to the isothermal profile the EGRET excess show a substructure in the form of toroidal rings at 4 and 14 kpc, as shown in Fig. 2: on the left hand side the contribution from the $1/r^2$ profile is shown, while for the right hand side the ring structure is added. Such enhanced gamma radiation at 4 and 14 kpc was already observed in the original paper on the EGRET excess (14). Note that the appearance of substructure would also be obtained if a radial dependence of n and B would have been taken. The analysis is sensitive to the radii of ringlike structures, since we are not located at the centre: assuming a constant flux along the ring yields automatically more flux from the nearest parts. The need for these additional rings is most easily seen by comparing the longitudinal profiles in the galactic plane and towards the galactic poles, as shown in Fig. 3. Note that for each bin only the flux integrated for data above 0.5 GeV has been plotted.

The position and shape of the outer ring coincides with the ring of stars, discovered in 2003 by several groups

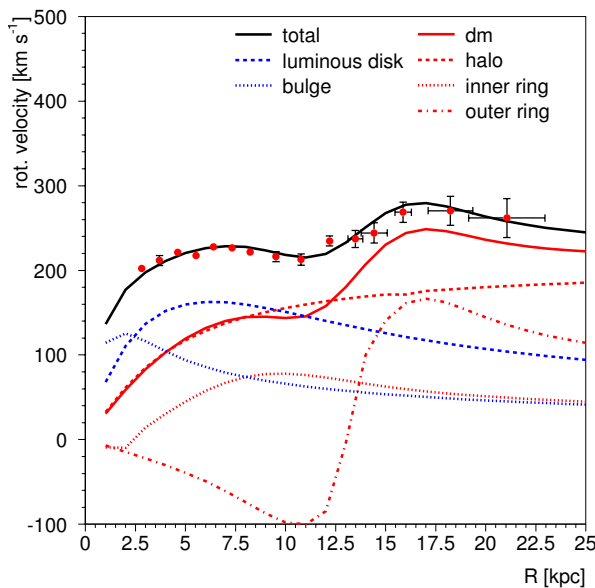


Figure 4. The rotation curve from our galaxy with the DM contribution determined from the EGRET excess of diffuse gamma rays. The data are averaged from Ref. (6).

(19; 20; 21). These stars show a much smaller velocity dispersion (10-30 km/s) and larger z -distribution than the thick disk, so they cannot be considered an extension of the disk. A viable alternative is the infall of a dwarf galaxy (19; 22), for which one expects in addition to the visible stars a DM component. From the size of the ring and its peak density one can estimate the amount of DM in the outer ring to be $\approx 10^{10} - 10^{11}$ solar masses. Since the gamma ray excess requires the full 360° of the sky, one can extrapolate the observed 100° of visible stars to obtain a total mass of $\approx 10^8 - 10^9$ solar masses (19; 20), so the baryonic matter in the outer ring is only a small fraction of its total mass.

The inner ring at 4.2 kpc with a width of 4.2 kpc in radius and 0.2 kpc perpendicular to the disk is more difficult to interpret, since the density of the inner region is modified by adiabatic compression and interactions between the bar and the halo. However, it is interesting to note that its radius coincides with the ring of cold dense molecular hydrogen gas, which reaches a maximum density at 4.5 kpc and with a width around 2 kpc (23; 14). Since molecular hydrogen forms in regions with dust (which provides shelter against dissociating UV radiation and allows atomic hydrogen to bond at the surfaces) suggests a gravitational potential well in this region, in agreement with the EGRET excess in this region.

To prove that the enhanced gamma ray density is indeed connected to non-baryonic mass the rotation curve was reconstructed from the excess of the diffuse gamma rays in the following way: since the flux determines the number density of DM for a given boost factor and since the mass of each WIMP is between 50 and 100 GeV, one can determine the relative masses of the components (rings plus spherical part) and consequently predict the shape of the rotation curve. The absolute value of the mass can be obtained by requiring that the rotation speed of the solar system is 220 km/s at 8.3 kpc. The two ring model describes the peculiar change of slope at 11 kpc well, as shown in Fig. 4. The contributions from each of the mass terms have been shown separately. The basic explanation for the negative contribution from the outer ring is that a tracer star at the

inside of the ring at 14 kpc feels an outward force from the ring, thus a negative contribution to the rotation velocity.

3. Objections to the DMA interpretation

The DMA interpretation of the EGRET excess would mean that DM is not so dark anymore, but DM is visible from the 30-40 flashes of energetic gamma rays for each annihilation. This would be great, but are there more mundane explanations? Attempts to modify the electron and proton spectra from the locally measured spectra do not describe the shape of the EGRET data in all sky directions, as discussed in detail before by comparing the EGRET data with the “optimized model”. Here we summarize some other possible objections.

a) Are the EGRET data reliable enough to make such strong conclusions? The EGRET detector was calibrated in a quasi mono-energetic gamma ray beam at an accelerator, so its response is well known. Also the monitoring during the flight was done carefully. We have only used data in the energy range between 0.1 and 10 GeV, where the efficiency is more or less flat. So we believe the 9 years flight provided accurate and reliable data, especially it would be hard to believe in an undetected calibration problem, which would only effect the data above 0.5 GeV and fake the gamma ray spectrum from the fragmentation of mono-energetic quarks.

b) Is it possible to explain the excess in diffuse gamma rays with unresolved point sources? This is unlikely, first of all since the known point sources are only a small fraction of the diffuse gamma rays and the majority of the resolved sources has a rather soft spectrum, typically well below 1 GeV, as can be seen from the plots in the Appendix. If this part of the spectrum would be dominated by unresolved sources, then the diffuse component below 1 GeV would be lower than assumed, which in turn would lead to a lower normalization of the background and a correspondingly stronger excess for a fixed background shape. So arguing against DMA by unresolved sources goes in the wrong direction.

c) The tracing of DM relies largely on the outer rotation curve of our galaxy, which has large uncertainties from the distance r_0 between the Sun and the galactic centre and is determined with a different method than the inner rotation curve. Can this fake the results? The outer rotation curve indeed depends strongly on r_0 , as shown in Ref. (24), who varied r_0 between 7 and 8.5 kpc. At present one knows from the kinematics of the stars near the black hole at the centre of our galaxy that $r_0 = 8 \pm 0.4$ kpc (25), so the distance is already reasonably well known. But whatever the value of r_0 , the change in slope around $1.3r_0$ is always present, indicating a ringlike DM structure is always needed. Furthermore the outer rotation curve shows first the same decrease as the inner rotation curve and only then changes the slope, so the different methods agree.

d) The outer ring at 14 kpc has a mass between 10^{10} and 10^{11} solar masses. This is around 30-50% of the total mass inside the ring and one may worry about the disk stability of the Milky Way by the infall of such a heavy galaxy. However, large spiral galaxies show bumps of similar size (26), so it seems not to be uncommon to have masses of this size forming ringlike structures. Note that only ringlike structures can form maxima and minima in the outer rotation curve, since the rotation velocity squared is proportional to the *derivative* of the gravitational potential.

e) One observes a ring of molecular hydrogen near the inner ring and a ring of atomic hydrogen near the outer ring. Could this excess of hydrogen not be responsible for the excess of the gamma rays? No, our method of fitting only the shapes with a free normalization implies that this analysis is insensitive to density fluctuations of the background, which change the normalization, not the shape.

f) How can one be sure that the outer ring originated from the tidal disruption of a rather massive satellite galaxy, so one can expect an enhanced DM density in the ring? One finds three independent ringlike structures: stars, atomic hydrogen gas and excess of gamma radiation. The stars show a scale height of several kpc and

a low velocity dispersion, so they cannot be part of the galactic disk. Therefore the infall of a satellite galaxy is the natural explanation. Since the tidal forces are proportional to $1/r^3$, the satellite will be disrupted most strongly at its pericentre, leaving behind gas, stars and DM. All three are found with more than 90% of the mass being DM.

g) Is it not peculiar that if a ringlike structure originates from the infall of dwarf galaxy, that it lies in the plane of the disk? In principle the infall can happen in all directions with respect to the plane, but the angular momenta of the inner halo and a baryonic disk tend to align after a certain time by tidal torques (27).

4. Summary

In summary, the EGRET data shows an intriguing hint of DM annihilation, since it explains many unrelated facts simultaneously:

a) An excess of diffuse galactic gamma rays which shows a *spectrum* consistent with the expectation from WIMP annihilation into gamma rays originating from the fragmentation of mono-energetic quarks.

b) The excess is present in *all* sky directions with the same spectrum, thus excluding that it originates from anomalous contributions in the centre of the galaxy.

c) The excess shows an strongly increased intensity at positions where extra DM is expected, namely at two toroidal structures at radii of 14 and 4 kpc from the centre of the galaxy. At 14 kpc one has observed a ring of stars thought to originate from the infall of a dwarf galaxy, while at 4 kpc one finds an enhanced concentration of molecular hydrogen thought to form from atomic hydrogen in the presence of dust or heavy nuclei, which can be collected in the gravitational potential of a ring of DM.

d) The mass in the rings can be obtained from the flux of the excess and describes the hitherto mysterious change of slope in the rotation curve at a distance of about 11 kpc, thus proving that the EGRET excess traces the Dark Matter.

In our analysis we only fit the known spectral shapes of the various processes with arbitrary normalizations, so the analysis becomes largely model independent. Interestingly, the normalization factors come out to be in agreement with expectations, both for the WIMP signal and the background.

The statistical significance of the EGRET excess of at least 10σ , if fitted to the shape of the conventional diffuse gamma ray background only, combined with all features mentioned above provides an intriguing hint that this excess is indeed indirect evidence for Dark Matter annihilation. The fact that we can calculate the peculiar shape of the rotation curve of our galaxy from the gamma rays proves that the excess indeed traces the Dark Matter.

I thank my close collaborators W. de Boer, A. Gladyshev, D. Kazakov and V. Zhukov for their contributions to this interesting project. Furthermore I thank V. Moskalenko, A. Strong and O. Reimer for numerous discussions on galactic gamma rays and analysis of EGRET data. This work was supported by the BMBF (Bundesministerium für Bildung und Forschung) via the DLR (Deutsches Zentrum für Luft- und Raumfahrt) and a grant from the DFG (Deutsche Forschungsgemeinschaft, Grant 436 RUS 113/626/0-1).

References

- [1] D.N. Spergel et al, 2003, ApJS, 148, 175;
C.L. Bennett et al., 2003, ApJS, 148, 1; See also: http://map.gsfc.nasa.gov/m_mm/pub_papers/firstyear.html

- [2] L. Bergström, Rept. Prog. Phys. **63** (2000) 793 [arXiv:hep-ph/0002126].
- [3] G. Bertone, D. Hooper and J. Silk, Phys. Rept. **405**, 279 (2005) [arXiv:hep-ph/0404175].
- [4] W. de Boer, M., Herold, C. Sander, and V. Zhukov, Eur. Phys. J. C, **33**(2003) 981; arXiv:hep-ph/0312037
- [5] W. de Boer et al., arXiv:astro-ph/0408272
- [6] W. de Boer, New Astron. Rev., **49** (2005) 213; arXiv:hep-ph/0408166.
- [7] C. Sander, Thesis University of Karlsruhe, 2005.
- [8] E. Kolb, M.S. Turner, The Early Universe, Frontiers in Physics, Addison Wesley, 1990.
- [9] G. Jungman, M. Kamionkowski and K. Griest, Phys. Rep. **267** (1996) 195.
- [10] V. Dokuchaev, these proceedings. V. Berezhinsky, V. Dokuchaev and Y. Eroshenko, Phys. Rev. D **68**, 103003 (2003); [arXiv:astro-ph/0301551].
- [11] J. Diemand, B. Moore, and J. Stadel, Nature, **433**(2005) 389.
- [12] T. Sjöstrand, P. Eden, C. Friberg, L. Lönnblad, G. Miu, S. Mrenna and E. Norrbin, Computer Phys. Commun. **135** (2001) 238.
- [13] D.J. Thompson et al., IEEE Trans. Nucl. Sci. **34** (1987) 36; J.A. Esposito et al., ApJ **123** (1987) 203.
- [14] Hunter, S. D. *et al.*, Astrophysical Journal **481**, 205 (1997)
- [15] A. W. Strong and I. V. Moskalenko, Astrophys. J. **509**, 212 (1998); [arXiv:astro-ph/9807150].
- [16] I. V. Moskalenko and A. W. Strong, Astrophys. Space Sci. **272** (2000) 247; [arXiv:astro-ph/9908032].
- [17] A. W. Strong, I. V. Moskalenko and O. Reimer, Astrophys. J. **613**, 962 (2004); [arXiv:astro-ph/0406254].
- [18] T. Kamae, T. Abe and T. Koi, ApJ, **620** (2005) 244, arXiv:astro-ph/0410617.
- [19] B. Yanny *et al.*, Astrophys. J. **588** (2003) 824 [Erratum-ibid. **605** (2004) 575]; [arXiv:astro-ph/0301029].
- [20] R. A. Ibata, M. J. Irwin, G. F. Lewis, A. M. N. Ferguson and N. Tanvir, Mon. Not. Roy. Astron. Soc. **340** (2003) L21; [arXiv:astro-ph/0301067].
- [21] J.D. Crane, et al., ApJ, **594** (2003) L119; arXiv:astro-ph/0307505.
- [22] D. Martinez-Delgado, J. Penarrubia, D. I. Dinescu, D. J. Butler and H. W. Rix, arXiv:astro-ph/0506012.
- [23] M. A. Gordon, and W. B. Burton, ApJ **208** (1976) 346.
- [24] M. Honma and Y. Sofue, Publ. of the Astronomical Society of Japan, **48** (1997) 103; arXiv:astro-ph/9611156.
- [25] F. Eisenhauer, *et al.*, ApJ, **597** (2003) L121; arXiv:astro-ph/0306220.
- [26] Y. Sofue, in "Galaxy Disks and Disk Galaxies", ASP Conf. Series, Vatican Conf. Rome 2000, eds. J. Funes, and E.M. Corsini, arXiv:astro-ph/0010595.
- [27] J. Bailin, J. et al., arXiv:astro-ph/0505523.

The performance of the AMS-02 Transition Radiation Detector

M. Schmanau^a

on behalf of the AMS-02 TRD collaboration^b

(a) *Institut für Exp. Kernphysik (IEKP), Universität Karlsruhe, Wolfgang-Gaede-Str. 1, 76131 Karlsruhe, Germany*

(b) *L.Phys.Inst. RWTH Aachen, INFN Rome, IEKP Univ. of Karlsruhe, LNS MIT, Kyungpook National Univ., Taegu, Korea*

Presenter: M. Schmanau (mike.schmanau@cern.ch), ger-schmanau-M-abs1-og15-oral

The Alpha Magnetic Spectrometer (AMS-02) [1] is scheduled for flight on board of the International Space Station (ISS) for measurements of the cosmic ray spectrum up to the TeV energy range. It includes a Transition Radiation Detector (TRD) for the identification of electrons and positrons in the range of 1-300 GeV. The expected proton rejection is 10^2 - 10^3 with the TRD alone and can be increased up to 10^5 together with the calorimeter. This proton rejection at an electron efficiency of 90% will be an important asset for the indirect Dark Matter search via an anomalous positron fraction from the Dark Matter annihilation. Funded by the German space agency (DLR): DLR Funding Contract 50000505.

1. Introduction

Data on high energy electron and positron fluxes have been obtained with the balloon experiment HEAT and a short precursor shuttle flight of AMS-01 [2, 3]. The positron fraction $e^+/(e^+ + e^-)$ is sensitive to the galactic propagation model [4, 5] where electrons are considered as primary particles generated in the supernovae explosions and positrons are the secondary particles appearing from proton interactions with the galactic gas. The deviation from this scenario can be a hint for new physics and particularly the relic Dark Matter (DM) annihilation in our galaxy. The stable products of this annihilation may contribute significantly to the cosmic ray fluxes at higher energies, since heavy cold DM particles will annihilate at rest, so the mass is transformed into kinetic energy of the decay products yielding a deviation from the background prediction at high energies. Indeed, the HEAT data on the positron fraction show a small excess at high energies over the background, predicted by the GALPROP model [4], as shown in Fig. 1. The excess can be explained by the annihilation of a neutralino of about 340 GeV [6, 7]. However, the high energy data was obtained with three short balloon flights of the HEAT detector, so the data is statistically limited. Here AMS-02 will be able to improve significantly, as shown in Fig. 1. The acceptance of AMS-02 for different particles is defined by the geometrical acceptance and the efficiency of particle reconstruction. The right hand side of Fig. 1 shows the simulated acceptances for antiprotons, positrons and gammas together with the background acceptances [8]. For positrons the main backgrounds are protons, which have the same electrical charge, but a factor 10^5 larger flux. Therefore one needs a proton rejection factor of $>10^5$ in order to see positrons. The electrons can also be misidentified as a positron in case of wrong charge assignment in the tracker; however, the electron flux is only ten times larger than the positron flux. The Transition Radiation Detector (TRD) and Electromagnetic CALorimeter (ECAL) are the key detectors for electron/positron identification and proton (hadron) rejection. This contribution is focused on the TRD performance. Details on the TRD construction can be found in Ref. [9].

2. Electron and Positron measurement with AMS-02

The AMS-02 is a general purpose spectrometer and consists of:

1. the Transition Radiation Detector (TRD) with 20 layers of proportional gas tubes each interleaved with fleece radiator.

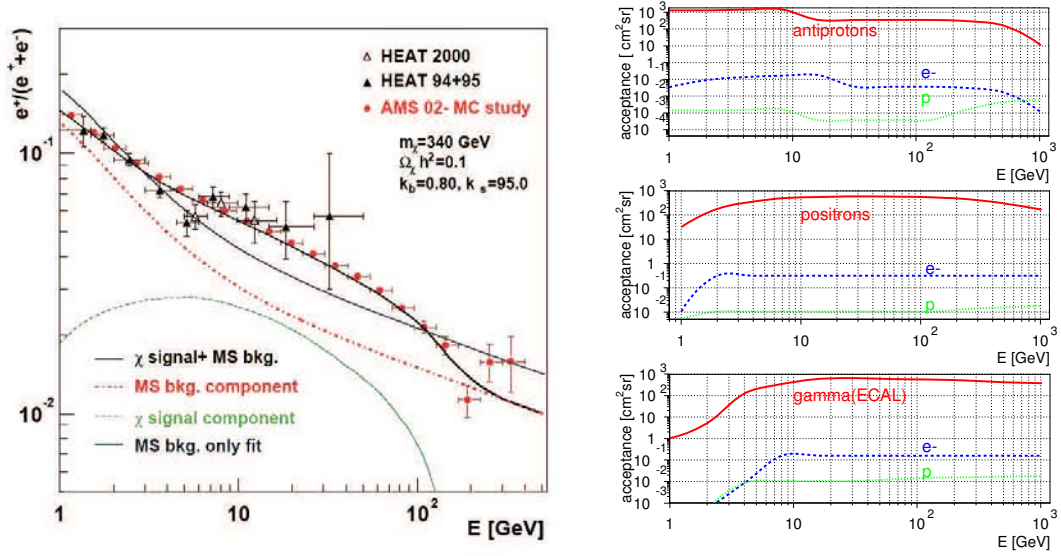


Figure 1. The $e^+/(e^+ + e^-)$ -fraction after one year of AMS-02 on the ISS in comparison with the data from the HEAT balloon experiment [2]. The ratio was modeled with the background from the GALPROP model [4, 5] and a DM annihilation signal of a 340 GeV neutralino [6]. The acceptance and the main contaminations for the AMS-02 detector [8] are shown on the right for some particles of interest for DM detection.

2. eight layers of silicon tracker inside a superconducting magnet with a maximum dipole field of 0.87 T.
3. the ring imaging Cherenkov detector (RICH) to measure velocities up to 20 GeV.
4. the electromagnetic calorimeter (ECAL) at the bottom of AMS-02, that measures lepton energies and provides lepton/hadron rejection of about 10^3 up to 1 TeV.
5. the Time of Flight (ToF) and veto scintillator hodoscope to provide a trigger, vetos and velocity measurements.

As mentioned in the Introduction, this note concentrates on the TRD performance. The physical principle of the TRD is based on the radiation of X-ray photons (TR) with energies in the 1-50 keV range which are emitted if a particle crosses the boundary between two media with a different dielectric constant ϵ . The TR energy is proportional to the relativistic γ -factor and the TR photon number can be increased by using multiple transitions, i.e. multilayer structures. Fig. 2 shows the total energy deposition in 20 TRD layers for electrons and protons; the peaks are clearly separated.

The performance of the AMS-02 TRD detector has been studied with a 20 layer prototype in test beams with electrons and protons and with Monte Carlo (MC) simulations. A Geant3 and Geant4 model [10] were used and tuned to reproduce the test beam data and improve rejection. The first algorithm considered a simple cluster counting method (counting the number of hits above 6.5 keV), but this yielded a relatively poor proton rejection (below 100 for energies above 200 GeV). Therefore a more sophisticated likelihood method was chosen [11], where the geometric mean $P_{e,p}^{mean} = \sqrt[n]{\prod_{k=1}^n P_{e,p}^k(E_{dep})}$ of probabilities for all n hits was calculated to build the likelihood L_e for the event to be electron like: $L_e = P_e^{mean} / (P_e^{mean} + P_p^{mean})$. The $-\ln(L_e)$ for each e^-

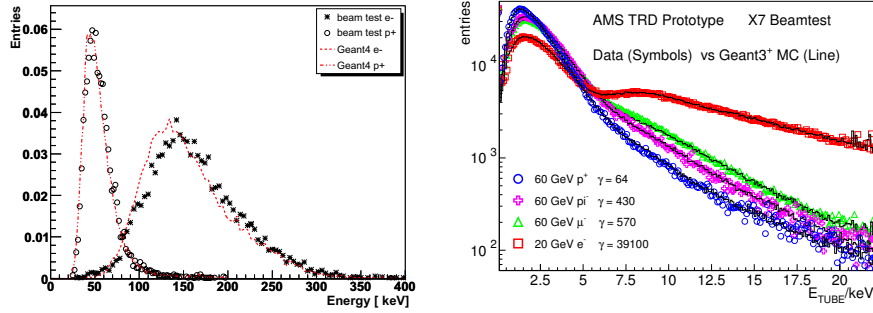


Figure 2. The left side shows the total energy deposition in 20 TRD layers for 20 GeV electrons and 100 GeV protons. A large γ -factor of about 40000 for the electrons compared to the small one of about 100 for the protons allows a clear separation. The test beam data are in reasonable agreement with the predictions of Geant4. TRD single layer spectra for different particles can be seen on the right side. Geant3 is also in good agreement with the test beam data. The different γ -factors of the particles lead to different TR contributions.

and p^+ -sample (for a given energy) were histogrammed. A cut on the distribution of the e^- -sample for 90% e^- -efficiency applied to the distribution of the p^+ -sample gave the fraction $N_{p,mis}$ of misidentified p^+ . With the total number of p^+ per sample with $N_{p,tot}$ protons the rejection factor was then defined as $N_{p,tot}/N_{p,mis}$.

The first simulation results with a Geant3 model [11] showed a disagreement between simulation and data at proton energies above 200 GeV: the rejection in real data was considerably lower than predicted by the simulation. This problem was solved by including the quasi elastic diffractive proton process $p + p \rightarrow (p + \pi^+ + \pi^-) + p$ with an adjusted cross section of $\sigma_{diff} = 15$ mb. The $\pi^+ + \pi^-$ pairs were produced with fixed energies of 40 MeV and emitted along the proton direction, thus producing more ionization and increasing the probability to fake TR of a relativistic electron. Geant4 [10] provides an XTR model [12] which is based on a theoretical formulation with parameters to adjust the process for irregular radiator structures like fleeces (used for AMS-02). Geant3 uses a parametrisation of the radiation process with tables generated by a separate program modelling irregular foil radiators. Moreover the Geant4 hadronic part is completely updated and includes many new processes and cross sections.

A comparison of the proton rejections derived by Geant4, Geant3 and the test beam data is presented in Fig. 3. The discrepancies at high energy occur for Geant4 in the same way as for the former Geant3 model, suggesting that also in Geant4 a process like diffractive scattering has to be added.

3. Summary

AMS-02 will be able to measure positron and electron spectra in a range of 1-300 GeV. The AMS-02 TRD will provide a proton rejection $>10^2$ for all energies and above 1000 for energies below 100 GeV. The latter energy range is the one of interest for indirect DM detection, if the hints from the existing data are correct, but also the range above 100 GeV is needed to exclude other origins for an excess in AMS-02 data. The AMS-02 Monte Carlo model is continuously improving and therefore the backgrounds will be better determined, which will lead to more efficient analysis methods with higher proton rejection factors. The much more sophisticated Geant4 model still suffers the same deficiencies as the former Geant3 model concerning the misidentification between protons and positrons at high energies. In Geant3 this could be solved by including an effective

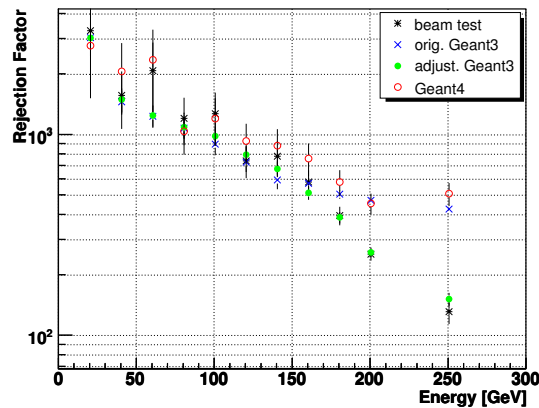


Figure 3. The rejection factor of protons for a 90% electron efficiency for the test beam data (points) as function of the beam energy. The original Geant3 and Geant4 rejection factor are clearly too optimistic at high energies, while the adjusted Geant3 including an effective diffractive proton-proton scattering describes the data.

diffractive proton-proton scattering as high as 15 mb. Since Geant4 does not include diffractive scattering, a similar approach may be needed here.

We wish to thank the many organisations and individuals listed in the acknowledgements of ref [1].

References

- [1] C. Lechanoine-Leluc, "AMS-02 A magnetic spectrometer on the International Space Station", these proceedings.
- [2] S. W. Barwick *et al.* [HEAT Collaboration], *Astrophys. J.* **482** (1997) L191, arXiv:astro-ph/9703192. M. A. Duvernois *et al.*, *ApJ* **559** (2001) 296.
- [3] J. Alcaraz *et al.* *Physics Letters B* **484** (2000) 10-22 .
- [4] A. W. Strong and I.V. Moskalenko, astro-ph/9812260.
- [5] I. V. Moskalenko *et al.* *Astroph. J.* **565** (2002) 28.
- [6] P. Maestro, Ph. D. Thesis, University of Siena, 2003, AMS Note 2003-01-0
- [7] W. de Boer, M. Herold, C. Sander and V. Zhukov, *Eur. Phys. J. C* **33**, (2004) 981, arXiv:hep-ph/0312037.
- [8] V. Zhukov in Proc. of the Eleventh Lomonosov Conference, Moscow, 2003, Ed. A. I. Studenikin, World Scientific.
- [9] Th.Kirn, Th. Siedenburg "The AMS transition radiation detector" *Nuclear Instruments and Methods A* **533** (2004) 165-170
- [10] Geant4 version7.0 (patch 01), as available from <http://wwwasd.web.cern.ch/wwwasd/geant4/geant4.html>, was used.
- [11] J. Orboeck, "The final 20-Layer-Prototype for the AMS Transition Radiation Detector.", Ph.D-Thesis, RWTH Aachen (2003).
- [12] V. M. Grichine, 7th Int. Conference, Advanced Technology and Particle Physics, Como 15-19 October 2001.

KASCADE Collaboration

(as of July 2005)

W.D. Apel^a, A.F. Badea^{a,1}, K. Bekk^a, A. Bercuci^b, H. Blümer^{a,c}, H. Bozdog^a, I.M. Brancus^b, A. Chilingarian^d, K. Daumiller^a, P. Doll^a, R. Engel^a, J. Engler^a, H.J. Gils^a, R. Glasstetter^{c,2}, A. Haungs^a, D. Heck^a, J.R. Hörandel^c, K.-H. Kampert^{c,a,2}, H.O. Klages^a, G. Maier^{a,3}, H.J. Mathes^a, H.J. Mayer^a, J. Milke^a, M. Müller^a, R. Obenland^a, J. Oehlschläger^a, S. Ostapchenko^{a,4}, M. Petcu^b, H. Rebel^a, A. Risse^e, M. Risse^a, M. Roth^c, G. Schatz^a, H. Schieler^a, H. Ulrich^a, J. van Buren^a, A. Vardanyan^d, A. Weindl^a, J. Wochele^a, J. Zabierowski^e

^a *Institut für Kernphysik, Forschungszentrum Karlsruhe, 76021 Karlsruhe, Germany*

^b *National Institute of Physics and Nuclear Engineering, 7690 Bucharest, Romania*

^c *Institut für Experimentelle Kernphysik, Universität Karlsruhe, 76021 Karlsruhe, Germany*

^d *Cosmic Ray Division, Yerevan Physics Institute, Yerevan 36, Armenia*

^e *Soltan Institute for Nuclear Studies, 90950 Lodz, Poland*

¹ *on leave of absence from Nat. Inst. of Phys. and Nucl. Engineering, Bucharest, Romania*

² *now at Fachbereich Physik, Universität Wuppertal, 42097 Wuppertal, Germany*

³ *now at University Leeds, LS2 9JT Leeds, United Kingdom*

⁴ *on leave of absence from Moscow State University, 119899 Moscow, Russia*

KASCADE-Grande Collaboration

(as of July 2005)

W.D. Apel^a, F. Badea^{a,1}, K. Bekk^a, A. Bercuci^b, M. Bertaina^c, J. Blümer^{a,d}, H. Bozdog^a, I.M. Brancus^b, M. Brüggemann^e, P. Buchholz^e, A. Chiavassa^c, K. Daumiller^a, F. Di Pierro^c, P. Doll^a, R. Engel^a, J. Engler^a, P.L. Ghia^f, H.J. Gils^a, R. Glasstetter^g, C. Grupen^e, A. Haungs^a, D. Heck^a, J.R. Hörandel^d, K.-H. Kampert^g, H.O. Klages^a, Y. Kolotaev^e, G. Maier^{a,2}, H.J. Mathes^a, H.J. Mayer^a, J. Milke^a, B. Mitrica^b, C. Morello^f, M. Müller^a, G. Navarra^c, R. Obenland^a, J. Oehlschläger^a, S. Ostapchenko^{a,3}, S. Over^e, M. Petcu^b, T. Pierog^a, S. Plewnia^a, H. Rebel^a, A. Risse^h, M. Roth^d, H. Schieler^a, O. Sima^b, M. Stümpert^d, G. Toma^b, G.C. Trinchero^f, H. Ulrich^a, S. Valchierotti^c, J. van Buren^a, W. Walkowiak^e, A. Weindl^a, J. Wochele^a, J. Zabierowski^h, S. Zagromski^a, D. Zimmermann^e

^a *Institut für Kernphysik, Forschungszentrum Karlsruhe, 76021 Karlsruhe, Germany*

^b *National Institute of Physics and Nuclear Engineering, 7690 Bucharest, Romania*

^c *Dipartimento di Fisica Generale dell'Università, 10125 Torino, Italy*

^d *Institut für Experimentelle Kernphysik, Universität Karlsruhe, 76021 Karlsruhe, Germany,*

^e *Fachbereich Physik, Universität Siegen, 57068 Siegen, Germany*

^f *Istituto di Fisica dello Spazio Interplanetario, INAF, 10133 Torino, Italy*

^g *Fachbereich Physik, Universität Wuppertal, 42097 Wuppertal, Germany*

^h *Soltan Institute for Nuclear Studies, 90950 Lodz, Poland*

¹ *on leave of absence from Nat. Inst. of Phys. and Nucl. Engineering, Bucharest, Romania*

² *now at University Leeds, LS2 9JT Leeds, United Kingdom*

³ *on leave of absence from Moscow State University, 119899 Moscow, Russia*

LOPES Collaboration

(as of July 2005)

W.D. Apel^a, F. Badea^{a,1}, L. Bühren^b, K. Bekk^a, A. Bercuci^c, M. Bertaina^d, P.L. Biermann^e, J. Blümer^{a,f}, H. Bozdog^a, I.M. Brancus^c, S. Buitink^g, M. Brüggemann^h, P. Buchholz^h, H. Butcher^b, A. Chiavassa^d, K. Daumiller^a, A.G. de Bruyn^b, C.M. de Vos^b, F. Di Pierro^d, P. Doll^a, R. Engel^a, H. Falcke^{b,e,g}, H. Gemmekeⁱ, P.L. Ghia^j, R. Glasstetter^k, C. Grupen^h, A. Haungs^a, D. Heck^a, J.R. Hörandel^f, A. Horneffer^{g,e}, T. Huege^{a,e}, K.-H. Kampert^k, G.W. Kant^b, U. Klein^l, Y. Kolotaev^h, Y. Koopman^b, O. Krömerⁱ, J. Kuijpers^g, S. Lafebre^g, G. Maier^{a,2}, H.J. Mathes^a, H.J. Mayer^a, J. Milke^a, B. Mitrica^c, C. Morello^j, G. Navarra^d, S. Nehls^a, A. Nigl^g, R. Obenland^a, J. Oehlschläger^a, S. Ostapchenko^{a,3}, S. Over^h, H.J. Pepping^b, M. Petcu^c, J. Petrovic^g, T. Pierog^a, S. Plewnia^a, H. Rebel^a, A. Risse^m, M. Roth^f, H. Schieler^a, G. Schoonderbeek^b, O. Sima^c, M. Stümpert^f, G. Toma^c, G.C. Trinchero^j, H. Ulrich^a, S. Valchierotti^d, J. van Buren^a, W. van Capellen^b, W. Walkowiak^h, A. Weindl^a, S. Wijnholds^b, J. Wochele^a, J. Zabierowski^m, J.A. Zensus^e, D. Zimmermann^h

^a *Institut für Kernphysik, Forschungszentrum Karlsruhe, 76021 Karlsruhe, Germany*

^b *ASTRON, 7990 AA Dwingeloo, The Netherlands*

^c *National Institute of Physics and Nuclear Engineering, 7690 Bucharest, Romania*

^d *Dipartimento di Fisica Generale dell'Università, 10125 Torino, Italy*

^e *Max-Planck-Institut für Radioastronomie, 53010 Bonn, Germany*

^f *Institut für Experimentelle Kernphysik, Universität Karlsruhe, 76021 Karlsruhe, Germany*

^g *Dept. of Astrophysics, Radboud University Nijmegen, 6525 ED Nijmegen, The Netherlands*

^h *Fachbereich Physik, Universität Siegen, 57068 Siegen, Germany*

ⁱ *Inst. Prozessdatenverarbeitung und Elektronik, Forschungszentrum Karlsruhe, Germany*

^j *Istituto di Fisica dello Spazio Interplanetario, INAF, 10133 Torino, Italy*

^k *Fachbereich Physik, Universität Wuppertal, 42097 Wuppertal, Germany*

^l *Radioastronomisches Institut der Universität Bonn, 53020 Bonn, Germany*

^m *Soltan Institute for Nuclear Studies, 90950 Lodz, Poland*

¹ *on leave of absence from Nat. Inst. of Phys. and Nucl. Engineering, Bucharest, Romania*

² *now at University Leeds, LS2 9JT Leeds, United Kingdom*

³ *on leave of absence from Moscow State University, 119899 Moscow, Russia*

Pierre Auger Collaboration Author List

J. Abraham⁵, M. Aglietta³⁷, C. Aguirre⁹, D. Allard⁶⁶, I. Allekotte³, P. Allison⁶³,
J. Alvarez-Muñiz⁵⁰, M. Ambrosio³⁴, L. Anchordoqui⁶², J. Anjos¹³, C. Aramo³⁴, S. Argiró³⁶,
K. Arisaka⁶⁵, E. Armengaud²¹, F. Arneodo³⁸, F. Arqueros⁵², J.C. Arteaga Velázquez⁴¹,
H. Asorey³, B.S. Atulugama⁶⁴, J. Aublin²³, M. Ave⁶⁶, G. Avila⁶, J. Bacelar⁴⁵, D. Badagnani²,
A. Barbosa¹³, H.M.J. Barbosa¹¹, D. Barnhill⁶⁵, S.L.C. Barroso¹¹, P. Bauleo⁵⁸, J. Beatty⁶³,
T. Beau²¹, K.H. Becker²⁹, J.A. Bellido⁸, T. Bergmann²⁶, X. Bertou³, P. Biermann³⁰, R. Bilhaut²⁴,
P. Billoir²², F. Blanco⁵², H. Blümer²⁶, M. Boháčová¹⁹, E. Bollmann²⁶, R.C. Bonifazi¹³,
R. Bonino³⁷, M. Boratav²², J. Brack⁶⁷, J.M. Brunet²¹, H. Bui Duc⁵⁵, N. Busca⁶⁶,
K.S. Caballero-Mora²⁸, L. Caggioni³³, B. Cai⁶⁸, D. Camin³³, J.N. Capdevielle²¹, R. Caruso³¹,
A. Castellina³⁷, L. Cazon⁵⁰, R. Cester³⁶, A. Chiavassa³⁷, J.A. Chinellato¹¹, M. Chiosso³⁶,
J. Chirinos Diaz⁶¹, A. Chou⁵⁹, J. Chye⁶¹, D. Claes⁶⁹, P.D.J. Clark⁵⁴, R. Clay⁸, S. Clay⁸,
F. Cohen²¹, S. Colonges²¹, F. Contreras⁶, A. Cordier²⁴, U. Cotti⁴², S. Coutu⁶⁴, C. Covault⁵⁶,
A. Creusot²³, J. Cronin⁶⁶, P. Da Silva²², S. Dagoret-Campagne²⁴, T. Dang Quang Thieu⁷²,
K. Daumiller²⁶, B. Dawson⁸, L.A. de Carvalho¹¹, C. De Donato³³, S. de Jong⁴⁶,
W.J.M. de Mello¹¹, I. De Mitri³⁹, M.A.L. de Oliveira¹⁸, L.V. de Souza¹², L. Del Peral⁵¹,
O. Deligny²³, A. Della Selva³⁴, C. Di Giulio³⁵, C. Dobrigkeit Chinellato¹¹, J.C. D'Olivo⁴³,
C. Donalek³⁴, D. Dornie²³, A. Dorofeev⁶¹, M.T. Dova², D. D'Urso³¹, M. DuVernois⁶⁸, R. Engel²⁶,
L. Epele², P. Eschstruth²⁴, C.O. Escobar¹¹, A. Etchegoyen¹, A. Ewers²⁹, P. Facal San Luis⁵⁰,
H. Falcke^{44,46}, A.C. Fauth¹¹, D. Fazio³¹, N. Fazzini⁵⁹, A. Fernández⁴⁰, S. Ferry⁴⁹, B. Fick⁶¹,
A. Filevich¹, A. Filipčić⁴⁹, R. Fonte³¹, W. Fulgione³⁷, B. García⁵, D. Garcia Pinto⁵²,
I.B. García-Ferreira⁴², L. Garrard⁵⁸, H. Geenen²⁹, G. Gelmini⁶⁵, H. Gemmeke²⁷, B. Genolini²³,
C. Germain-Renaud²⁴, P.L. Ghia³⁷, M. Giller⁴⁸, J. Gitto⁵, H. Glass⁵⁹, F. Gobbi⁵, M.S. Gold⁷⁰,
M. Gómez Berisso³, R. Gómez Herrero⁵¹, M. Goncalves do Amaral¹⁴, J.P. Gongora⁵,
J. Gonzalez⁶², D. Gora⁴⁷, P. Gouffon¹², V. Grassi³³, A. Grillo³⁸, C. Grunfeld², J. Grygar¹⁹,
F. Guarino³⁴, G. Guedes¹⁷, R. Gumbsheimer²⁶, J. Gutiérrez Muñoz⁵¹, C. Hamadache²¹,
J.C. Hamilton²², M.N. Harakeh⁴⁵, D. Harari³, J.L. Harton⁵⁸, M. Healy⁶⁵, D. Heck²⁶, C. Hojvat⁵⁹,
P. Homola⁴⁷, A. Horneffer⁴⁶, M. Horvat⁴⁹, M. Hrabovský¹⁹, M. Iarlori³², A. Insolia³¹,
M. Kaducak⁵⁹, K. H. Kampert²⁹, B. Keilhauer²⁸, E. Kemp¹¹, H. Klages²⁶, M. Kleifges²⁷,
J. Kleinfeller²⁶, R. Knapik⁵⁸, J. Knapp⁵⁵, A. Kopmann²⁷, J. Kuijpers⁴⁶, N. Kunka²⁷, A. Kusenko⁶⁵,
C. Lachaud²¹, N. Lahrichi²⁴, J. Lamblin²¹, J. Lee⁶⁵, A. Letessier-Selvon²², M. Leuthold⁶³,
I. Lhenry-Yvon²³, J. Lloyd-Evans⁵⁵, G. Longo³⁴, R. López⁴⁰, A. Lopez Agüera⁵⁰, A. Lucero⁵,
S. Maldera³⁷, M. Malek⁵⁹, M. Manceñido², D. Mandat¹⁹, P. Mantsch⁵⁹, A.G. Mariazzi⁵⁵,
I. Maris²⁸, D. Martello³⁹, N. Martinez², J. Martínez⁴¹, O. Martínez⁴⁰, R. Martínez⁴¹,
H. J. Mathes²⁶, J.A.J. Matthews⁷⁰, J. Matthews⁶⁰, G. Matthiae³⁵, G. Maurin²¹, D. Maurizio³⁶,
P. Mazur⁵⁹, T. McCauley⁶², M. McEwen⁶⁰, R. McNeil⁶⁰, M.C. Medina¹, G. Medina Tanco¹²,
A. Meli³⁰, D. Melo¹, M. Melocchi⁵, A. Menchikov²⁷, E. Menichetti³⁶, Chr. Meurer²⁶, F. Meyer²⁵,
R. Meyhandan⁶⁰, M.I. Micheletti¹, G. Miele³⁴, W. Miller⁷⁰, S. Mollerach³, M. Monasor^{51,50},
D. Monnier Ragaigne²⁴, B. Morales Ruiz⁴³, C. Morello³⁷, E. Moreno Barbosa⁴⁰, C. Morris⁶³,
M. Mostafa⁷⁰, M.A. Muller¹¹, R. Mussa³⁶, G. Navarra³⁷, L. Nellen⁴³, F. Nerling²⁶,
C. Newman Holmes⁵⁹, D. Newton⁵⁵, T.T. Nguyen Thi Thao⁷², R. Nichol⁶³, D. Nitz⁶¹,
H. Nogima¹¹, D. Nosek²⁰, L. Nožka¹⁹, J. Oehlschläger²⁶, T. Ohnuki⁶⁵, A. Olinto⁶⁶, L. Oliveira¹⁵,
V. Olmos-Gilbaja⁵⁰, H. Oros⁵, J.A. Ortiz¹², M. Ortiz⁵², S. Ostapchenko²⁶, L. Otero⁷, M. Palatka¹⁹,
J. Pallotta⁷, G. Parente⁵⁰, E. Parizot²³, M. Patel⁵⁵, T. Paul⁶², M. Pech¹⁹, J. Pekala⁴⁷, R. Pelayo⁴¹,
I.M. Pepe¹⁶, G. Perez⁴⁰, L. Perrone²⁹, S. Petrerá³², P. Petrinca³⁵, P. Pham Ngoc Diep⁷²,

D. Pham Ngoc Dong⁷², T.N. Pham Thi Tuyet Nhung⁷², T. Pierog²⁶, O. Pisanti³⁴, N. Playez²⁴, T. Porter⁶⁰, J. Pouthas²³, L. Prado Junior¹¹, P. Privitera⁶⁶, M. Prouza¹⁹, E.J. Quel⁷, B. Rafert⁵⁷, S. Ranchon²⁴, R. Randriatoamanana²², H.C. Reis¹², S. Reucroft⁶², B. Revenu²¹, J. Rídký¹⁹, A. Risi⁵, M. Risse²⁶, V. Rizi³², S. Robbins²⁹, M. Roberts⁷¹, C. Robledo⁴⁰, G. Rodriguez⁵⁰, D. Rodríguez Frías⁵¹, J. Rodriguez Martino³⁵, J. Rodriguez Rojo³⁵, S. Román⁴⁰, G. Ros Magán^{50,51}, L. Rosa⁴, M. Roth²⁸, C. Roucelle²², B. Rouillé-d'Orfeuille²², E. Roulet³, A.C. Rovero⁴, C. Rumbo⁵, F. Salamida³², H. Salazar⁴⁰, G. Salina³⁵, F. Sanchez³³, M. Santander⁵, S. Sarkar⁵³, R. Sato¹¹, V. Scherini²⁹, O. Scholten⁴⁵, P. Schovánek¹⁹, S.J. Sciutto², M. Scuderi³¹, D. Semikoz²¹, G. Sequeiros³⁶, R.C. Shellard¹³, B. Sieffert¹⁵, P. Skelton⁵⁵, W. Slater⁶⁵, N. Smetniansky De Grande¹, A. Smialkowski⁴⁸, R. Šmída¹⁹, G.R. Snow⁶⁹, P. Sommers⁷¹, J. Sorokin⁸, H. Spinka⁵⁹, R. Squartini⁶, F. Suarez³⁷, T. Suomijärvi²³, A.D. Supanitsky¹, J. Swain⁶², Z. Szadkowski^{29,48}, A. Tamashiro⁴, O. Tascou²⁹, G. Thornton⁸, R. Ticona¹⁰, C. Timmermans^{45a}, W. Tkaczyk⁴⁸, C.J. Todero Peixoto¹¹, A. Tonachini³⁶, J. Torres de Mello Neto¹⁵, D. Torresi³¹, P. Travnicek¹⁹, A. Tripathi⁶⁵, G. Tristram²¹, D. Tscherniakhovskii²⁷, P. Tuckey²⁵, M. Tueros², V. Tunnicliffe⁵⁴, R. Ulrich²⁸, M. Unger²⁶, M. Urban²⁴, J. F. Valdés Galicia⁴³, I. Valiño⁵⁰, L. Valore³⁴, A.M. Van den Berg⁴⁵, V. Van Elewyck⁴³, R.A. Vazquez⁵⁰, D. Veberic²⁴, D. Vega⁵¹, A. Velarde¹⁰, T. Venters⁶⁶, F. Vernotte²⁵, V. Verzi³⁵, M. Videla⁵, L. Villaseñor⁴², P. Vitale⁶, S. Vorobiov²¹, L. Voyvodic⁵⁹, T. Waldenmaier²⁶, P. Walker⁵⁴, D. Warner⁵⁸, A.A. Watson⁵⁵, C. Wiebusch²⁹, G. Wieczorek⁴⁸, L. Wiencke⁷¹, B. Wilczynska⁴⁷, H. Wilczynski⁴⁷, C. Wileman⁵⁵, J. Xu²⁷, T. Yamamoto⁶⁶, P. Younk⁶¹, E. Zas⁵⁰, D. Zavrtnik⁴⁹, M. Zavrtnik⁴⁹, A. Zepeda⁴¹, M. Zha⁵⁵

- 1 *Laboratorio Tandam, (CNEA). CONICET, Av. Gral. Paz 1499, (1650) San Martín, Buenos Aires, Argentina*
- 2 *Universidad Nacional de la Plata, Facultad de Ciencias Exactas, Departamento de Física and IFLP/CONICET, C.C. 67, (1900) La Plata, Argentina*
- 3 *Centro Atómico Bariloche (CNEA). Instituto Balseiro (CNEA and UNC). CONICET - 8400 San Carlos de Bariloche, Río Negro, Argentina*
- 4 *Instituto de Astronomía y Física del Espacio – (CONICET), CC 67, Suc. 28, (1428) Buenos Aires, Argentina*
- 5 *Universidad Tecnológica Nacional (Regs.Mendoza and San Rafael) CONICET - Rodríguez 273 Mendoza, Argentina*
- 6 *Pierre Auger Southern Observatory, Av. San Martin Norte 304, (5613) Malargue, Prov. De Mendoza, Argentina*
- 7 *Centro de Investigaciones en Laseres y Aplicaciones (CITEFA and CONICET) - Juan B. de La Salle 4397, Villa Martelli, Buenos Aires, Argentina*
- 8 *University of Adelaide, Department of Physics and Mathematical Physics, South Australia 5005, Australia*
- 9 *National Academy for Sciences, Av. 16 Julio 1732, POB 5829, La Paz, Bolivia*
- 10 *Universidad Mayor de San Andrés. Av. Villazón N° 1995 Monoblock Central, Bolivia*

- 11 *Universidade Estadual de Campinas, Instituto de Física, Departamento de Raios Cósmicos e Cronologia, CP 6165, 13084-971, Campinas, SP, Brazil*
- 12 *Universidade Sao Paulo, Instituto de Física, Departamento de Física Experimental, CP 66318, 05315-970, and Instituto Astronomico e Geofisico, Rua do Matao 1226, 05508-900, Sao Paulo, SP, Brasil*
- 13 *Centro Brasileiro de Pesquisas Fisicas, Rua Dr. Xavier Sigaud 150 22290-180 Rio de Janeiro, RJ, Brasil*
- 14 *Universidade Federal Fluminense, Campus da Praia Vermelha, 24210-340 Niteroi, RJ, Brasil*
- 15 *Av. Brigadeiro Trompowski, s/nº, Prédio da Reitoria, 2º andar, Cidade Universitaria. Rio de Janeiro/RJ - CEP 21941-590*
- 16 *Universidade Federal da Bahia, Campus da Onkina, 40210-340 Salvador, BA, Brasil*
- 17 *Av. Universitária, s/n - Km 03 da BR 116, Campus Universitario, CEP: 44031-460, Feira de Santana - BA - Brasil*
- 18 *Universidade. Estadual do Sudoeste Bahiano (UESB), Brazil*
- 19 *Institute of Physics (FZU) of the Academy of Sciences of the Czech Republic*
- 20 *Institute of Particle and Nuclear Physics, Faculty of Mathematics and Physics, Charles University, Prague, Czech Rep.*
- 21 *Laboratoire AstroParticule et Cosmologie, Collège de France and IN2P3/CNRS and Université Paris 7, 75005 Paris, France*
- 22 *Laboratoire de Physique Nucléaire et de Hautes Energies, Université Paris 6 & 7 and IN2P3/CNRS, 75005 Paris, France*
- 23 *Institut de Physique Nucléaire, Université Paris-Sud and IN2P3/CNRS, 91400 Orsay, France*
- 24 *Laboratoire de l'Accélérateur Linéaire, Université Paris-Sud and IN2P3/CNRS, 91400 Orsay, France*
- 25 *Laboratoire d'Astrophysique de l'Observatoire de Besançon, Université de Franche-Comté and INSU/CNRS, 25010 Besançon, France*
- 26 *Forschungszentrum Karlsruhe GmbH, Institut für Kernphysik (FZK-IK), 76021 Karlsruhe, Germany*
- 27 *Forschungszentrum Karlsruhe GmbH, Institut für Prozessdatenverarbeitung und Elektronik (FZK-IPE), 76021 Karlsruhe, Germany*
- 28 *Universität Karlsruhe (TH), Institut für Experimentelle Kernphysik (IEKP), 76128 Karlsruhe, Germany*
- 29 *Universität Wuppertal, Fachbereich Physik, Gaußstr 20, D-42119, Wuppertal, Germany*
- 30 *Max Planck Institut für Radioastronomie, 53121 Bonn, Germany*
- 31 *Dipartimento di Fisica dell'Università and INFN, Corso Italia 57, 95129 Catania, Italy*
- 32 *Dipartimento di Fisica and INFN, L'Aquila, Italy*

- 33 *Dipartimento di Fisica and INFN, Via Celoria 16, 20133 Milano, Italy*
- 34 *Dipartimento di Fisica and INFN, Via Cintia 2, 80123 Napoli, Italy*
- 35 *Università di Roma II “Tor Vergata” and INFN Roma II, Via della Ricerca Scientifica 1, 00133 Roma, Italy*
- 36 *Dipartimento di Fisica Sperimentale and INFN Torino, Via P. Giuria 1, 10125 Torino, Italy*
- 37 *Istituto di Fisica dello Spazio Interplanetario, sezione di Torino and Dipartimento di Fisica Generale dell'Università and INFN Torino, Via P. Giuria 1, 10125 Torino, Italy*
- 38 *INFN, Laboratori Nazionali del Gran Sasso, Italy*
- 39 *Università degli Studi di Lecce - Dipartimento di Fisica - Via Arnesano, 73100 Lecce (Italy)*
- 40 *Benemérita Universidad Autónoma de Puebla (BUAP), Ap. Postal J-48, 72500 Puebla, Puebla, Mexico*
- 41 *Centro de Investigación y de Estudios Avanzados del IPN (CINVESTAV), Physics Dept., POB 14-740, 07000 Mexico D.F., Mexico*
- 42 *Universidad Michoacana de San Nicolás de Hidalgo (UMSNH), Apdo. Postal 2-82, 58040 Morelia, Michoacan, Mexico*
- 43 *Universidad Nacional Autónoma de México (UNAM), Apdo. Postal 70-542, 04510 Mexico D.F., Mexico*
- 44 *PO Box 2, 7990 AA Dwingeloo, The Netherlands*
- 45 *PO Box 72, 9700 AB Groningen, The Netherlands*
- 45a *NIKHEF, POB 41882, 1009 DB Amsterdam, The Netherlands*
- 46 *P.O. Box 9102, 6500 HC Nijmegen, The Netherlands*
- 47 *Institute of Nuclear Physics, ul. Radzikowskiego 152, 31-342 Krakow, Poland*
- 48 *University of Lodz, Division of Experimental Physics, ul. Pomorska 149/153, 90-236 Lodz, Poland*
- 49 *Nova Gorica Polytechnic, Laboratory for Astroparticle Physics, Vipavska 13, POB 301, 5001 Nova Gorica, Slovenia*
- 50 *Departamento de Física de Partículas, Universidad de Santiago de Compostela, Spain*
- 51 *UNIVERSIDAD DE ALCALÁ, Pza. San Diego, s/n - 28801, Alcala de Henares (Madrid)*
- 52 *Universidad Complutense de Madrid, Ciudad Universitaria - 28040 Madrid*
- 53 *University of Oxford. University Offices, Wellington Square, Oxford OX1 2JD*
- 54 *School of Electrical & Electronic Engineering, University of Leeds, LS2 9JT, UK*
- 55 *University of Leeds, Department of Physics and Astrophysics, Leeds, LS2. 9JT, UK*
- 56 *Case Western Reserve University, Dept. of Physics, Cleveland, OH 44106, USA*

- 57 *Clemson University, 105 Sikes Hall, Box 345124, Clemson, South Carolina 29634-5124 USA*
- 58 *Colorado State University, Department of Physics, Fort Collins, CO 80523, USA*
- 59 *Fermilab, MS367, POB 500, Batavia, IL 60510-0500, USA*
- 60 *Louisiana State University, Department of Physics and Astronomy, Baton Rouge, LA 70803-4001, USA*
- 61 *Michigan Technological University, Department of Physics, 1400 Townsend, Houghton, MI 49931-1295, USA*
- 62 *Northeastern University, Department of Physics, 110 Forsyth Street, Boston, MA 02115-5096, USA*
- 63 *Ohio State University, 2400 Olentangy River Road, Columbus, OH 43210-1061, USA*
- 64 *Pennsylvania State University, Dept. of Physics, 104 Davey Laboratory, University Park, PA 16802, USA*
- 65 *University of California, Los Angeles (UCLA), Department of Physics and Astronomy, Los Angeles, CA 90095, USA*
- 66 *University of Chicago, Enrico Fermi Institute, 5640 S. Ellis, Chicago, IL 60637, USA*
- 67 *University of Colorado, Physics Department, Boulder, CO 80309-0446, USA*
- 68 *University of Minnesota, School of Physics and Astronomy, 116 Church St. SE, Minneapolis, MN 55455, USA*
- 69 *University of Nebraska, Dept. of Physics and Astronomy. 116 Brace Lab, Lincoln, NE 68588-0111, USA*
- 70 *The University of New Mexico, Albuquerque, NM 87131, USA*
- 71 *University of Utah 115 S. 1400 East #201, Salt Lake City, UT 84112-0830, USA*
- 72 *Institute of Nuclear Science and Technology (INST), 5T-160 Hoang Quoc Viet Street, Nghia Do, Cau Giay, Hanoi, Vietnam*